TECHNICAL UNIVERSITY OF CRETE
SCHOOL OF MINERAL RESOURCES
ENGINEERING

PhD Thesis

**"VALORIZATION OF MINING AND METALLURGICAL
WASTES THROUGH ALKALI ACTIVATION"**

Vasiliki Karmali

Mineral Resources Engineer, MSc

Chania, June 2021

Examination Committee

Konstantinos Komnitsas – Supervisor
Professor
School of Mineral Resources Engineering
Technical University of Crete

Michael Galetakis – Advisory committee
Professor
School of Mineral Resources Engineering
Technical University of Crete

Nikolaos Kallithrakas – Kontos – Advisory committee
Professor
School of Mineral Resources Engineering
Technical University of Crete

Anthimos Xenidis
Professor
School of Mining and Metallurgical Engineering
National Technical University of Athens

Iliana Halikia
Professor
School of Mining and Metallurgical Engineering
National Technical University of Athens

Nikolaos Xekoukoulotakis
Assistant Professor
School of Chemical and Environmental Engineering
Technical University of Crete

Konstantinos Tsakalakis
Professor
School of Mining and Metallurgical Engineering
National Technical University of Athens

Vasiliki Karmali

PhD Thesis, "Valorisation of mining and metallurgical wastes through alkali activation"

Abstract

The present PhD thesis aims to study in depth the alkali activation potential of metallurgical and mining wastes, including various types of metallurgical slags and laterite leaching residues, for the production of alkali activated materials (AAMs) with desirable chemical and mineralogical composition, and beneficial properties. AAMs were produced under the optimum synthesis conditions using activating solution consisting of sodium hydroxide (NaOH) and sodium silicate (Na_2SiO_3). The effect of various parameters, namely H_2O/Na_2O and other molar ratios present in the activating solution and the reactive paste, particle size of raw materials, curing temperature and ageing period on the main properties of the produced AAMs, including compressive strength, porosity, water absorption and density was also evaluated. The durability and structural integrity of selected AAMs were investigated after firing at temperatures between 200 and 1000 ℃ for 4 or 6 h, immersion in distilled water and acidic solutions (1 M HCl and 1 M H_2SO_4), and subjection to freeze-thaw cycles for a period of 7-30 days. Several analytical techniques, namely X-ray diffraction (XRD), Fourier-transform infrared (FTIR) spectroscopy and Scanning electron microscopy (SEM-EDS) were used for the identification of the morphology and structure of the raw materials and the produced AAMs.

Regarding alkali activation of a Polish ferronickel slag (PS), it is underlined that the AAMs produced acquired compressive strength that exceeds 65 MPa, while after firing at 400 ℃, the compressive strength increased to 115 MPa, and this indicates that they can be used as fire-resistant materials. On the other hand, the AAMs produced from fayalitic slags resulted before and after plasma treatment, i.e. FS and FSP, acquired lower compressive strength values, namely 45 MPa and 27 MPa, respectively, while mixing them with 50 wt% ferronickel slag (LS) resulted in higher compressive strength, namely 64 MPa (FS50LS50 AAM) and 46 MPa (FSP50LS50 AAM), respectively.

An innovative aspect of this PhD thesis is the production of AAMs from laterite leaching residues, since until the start of the study no references were available in literature on this topic. This by-product has very low inherent alkali activation potential. The experimental results proved that when the leaching residues were mixed with metakaolin or slags they were successfully alkali activated and under the optimum synthesis conditions the produced specimens acquired compressive strength values ranging between 26 MPa and 51 MPa.
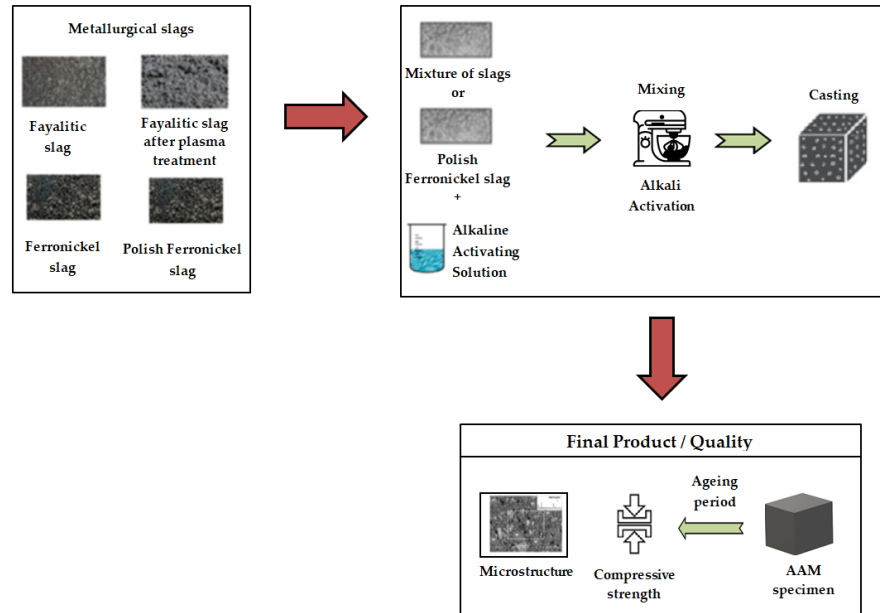
The results of this PhD thesis prove that the valorization or co-valorization of metallurgical wastes is a viable alternative for the production of AAMs with beneficial properties that can be used as binders or in several construction applications, thus improving the sustainability of this industrial sector following the principles of industrial symbiosis and circular economy.

Graphical Abstract

1. Slag–based AAMs

2. Laterite leaching residue–based AAMs

Acknowledgements
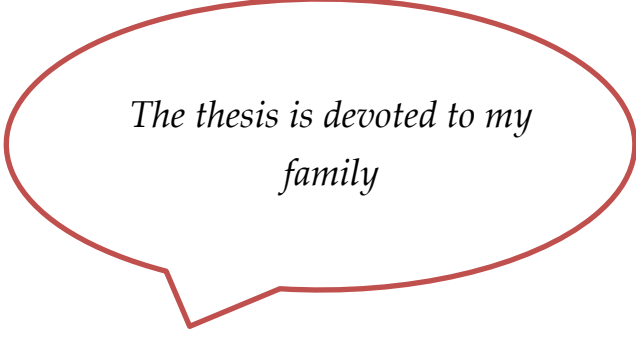
I would like to thank my supervisor, Professor Konstantinos Komnitsas, as well as the members of the advisory committee, Professor Michael Galetakis and Professor Nikolaos Kallithrakas-Kontos, for their valuable guidance throughout this period. I am grateful to my supervisor, for giving me an opportunity to conduct this research but also for our cooperation at both undergraduate and postgraduate levels. I would also to like to thank the other members of the examination committee, Professor Anthimos Xenidis, Professor Iliana Halikia, Assistant Professor Nikolaos Xekoukoulotakis and Professor Konstantinos Tsakalakis for their willingness to evaluate this thesis and for their comments.

I am grateful to the staff of the Laboratories of Ore Processing, and Ceramics and Glass Technology for their continuous help and support. More specifically, I would like to thank Dr. Anna Kritikaki and Mrs. Olga Pantelaki for their invaluable support and encouragement. Special thanks to Dr. Evangelos Petrakis for his continuous help, support, the guidance as well as for reviewing reports and publications. Special thanks to Dr. Antonios Stratakis (Laboratory of Applied Mineralogy) for his help with the mineralogical analyses (XRD). I would also like to thank Professor Nikolaos Kallithrakas-Kontos for his help with the chemical analyses (XRF). I would like to thank Mrs. Eleni Chamilaki (Laboratory of PVT and Core Analysis) for her help with the FTIR analyses. I also thank Mrs. Maria-Liliana Saru (Laboratory of Hydrogeochemical Engineering and Remediation of Soil) for her help with the ICP MS analyses. Special thanks also to my friend Athanasia Soultana (Laboratory of Quality Control-Health and Safety in the Mineral Industry) for her help with the determination of the compressive strength of the specimens. I would also like to thank Dr. Georgios Bartzas (Laboratory of Metallurgy of the School of Mining and Metallurgical Engineering at the National Technical University of Athens) for the time he devoted to SEM analyses as well as for his contribution in the published papers.

Enormous thanks to all my friends for their valuable support and love. Finally, my deepest and warmest gratitude goes to my family for their support, encouragement, understanding and endless love over all these years.

The thesis is devoted to my family

Abbreviations

AAMs	Alkali-Activated Materials
AAL	Atmospheric Acid Leaching
BET	Brunauer-Emmett-Teller
FS	Fayalitic Slag
FSLS	Specimens produced by mixing FS with LS
FSP	Fayalitic slag after plasma treatment
FSPLS	Specimens produced by mixing FSP with LS at ratio 10:90
FTIR	Fourier Transform Infrared
ICP MS	Inductively Coupled Plasma Mass Spectrometry
L	Leaching residues of Polish Laterites
LLR	Leaching residues of Greek Laterites from Agios Ioannis
LLRLS	Specimens produced by mixing LLR with LS
LLRPS	Specimens produced by mixing LLR with PS
LOI	Loss on Ignition
LR	Leaching residues of Greek Laterites from Kopais lake area
1000LR	LR after firing at 1000 ^{o}C
LRMK	Specimens produced by mixing LR after firing at 1000 ^{o}C with MK at ratio
800LR	LR after firing at 800 ^{o}C
LS	Ferronickel Slag
MK	Metakaolin
OPC	Ordinary Portland Cement
PS	Ferronickel Polish Slag
PS120	PS obtained after 120 min of grinding
PS30	PS obtained after 30 min of grinding
PS60	PS obtained after 60 min of grinding
SEM/EDS	Scanning Electron Microscopy/ Energy Dispersive Spectroscopy
XRD	X-Ray Diffraction
XRF	X-Ray Fluorescence
L/S	Liquid to Solid ratio

Publications

<u>In scientific journals</u>

I.   Komnitsas, K.; Bartzas, G.; **Karmali, V.**; Petrakis, E.; Kurylak, W.; Pietek, G.; Kanasiewics, J. Assessment of alkali activation potential of a Polish ferronickel slag. *Sustainability* **2019**, 11, 1863. https://doi.org/10.3390/su11071863.

II.   Komnitsas, K.; Petrakis, E.; Bartzas, G.; **Karmali, V**. Column leaching of low-grade saprolitic laterites and valorization of leaching residues. *Science of the Total Environment* **2019**, 665, 347–357. https://doi.org/10.1016/j.scitotenv.2019.01.381.

III.   Petrakis, E.; **Karmali, V.**; Bartzas, G.; Komnitsas, K. Grinding Kinetics of Slag and Effect of Final Particle Size on the Compressive Strength of Alkali Activated Materials. *Minerals* **2019**, 9, 714. https://doi.org/10.3390/min9110714.

IV.   Komnitsas, K.; Yurramendi, L.; Bartzas, G.; **Karmali, V.**; Petrakis, E. Factors affecting co-valorization of fayalitic and ferronickel slags for the production of alkali activated materials. *Science of the Total Environment* **2020**, 721, 137753. https://doi.org/10.1016/j.scitotenv.2020.137753.

V.   Komnitsas, K.; Bartzas, G.; **Karmali, V.**; Petrakis, E. Factors Affecting Alkali Activation of Laterite Acid Leaching Residues. *Environments* **2021**, 8, 4. https://doi.org/10.3390/environments8010004.

<u>In international conferences</u>

VI.   Komnitsas, K.; Yurramendi, L.; **Karmali, V.**; Petrakis, E.; Aldana, J.L.; Antoñanzas, J. Optimization of alkali activation of fayalitic Slag for the production of inorganic polymers. *ISWA 2019 World Congress*, 7-9 October. **2019**, Bilbao, Spain. https://iswa2019.org/.

VII.   Petrakis, E.; **Karmali, V.**; Komnitsas, K. Effect of particle size on alkali-activation of slag. *ICHPT 2019: 13th International Conference on Hydrometallurgy and Processing Technologies*, 24-25 October **2019**, Istanbul, Turkey. https://waset.org/hydrometallurgy-and-processing-technologies-conference-in-october-2019-in-istanbul.

<u>Participation in international conferences</u>

VIII.   Komnitsas, K.; **Karmali, V.**; Petrakis, E. Co-valorization potential of fayalitic and FeNi slags for the production of alkali activated inorganic polymers. *7th International Conference on Environmental Management, Engineering, Planning and Economics (CEMEPE 2019) and SECOTOX Conference*, 19-24 May **2019,** Mykonos Island, Greece. http://cemepe7.civil.auth.gr/.

Contents

1. **Introduction**

1.1 Background

In recent decades a rapid increase in the produced volumes of metallurgical and mining wastes is observed. Considerable quantities of various types of wastes are used in cement and concrete production and other construction related applications, or disposed of on land or landfills, thus causing various and serious environmental impacts on the soil, surface- and groundwater as well as the atmosphere (Agnello et al., 2018; Bai et al., 2018; Mo et al., 2017; Muñoz et al., 2018). Regarding the Portland cement industry, it is mentioned that is one the most energy intensive industries, consuming 12 % to 15 % of the total industrial energy and is responsible for 7 % to 10 % of the global CO_2 emissions, while aggregate production poses severe environmental problems in surrounding areas (Ali et al., 2011; Chen et al., 2010; Komnitsas, 2011; Wong et al., 2018). According to the Directive 2009/125/EC, the economic value of the produced waste should be calculated prior to its reuse. The valorization or co-valorization of different wastes, such as metallurgical slags, fly ash, construction and demolition wastes leads to environmental benefits and improves the sustainability of the metallurgical and construction sectors, following the principles of zero waste and circular economy (Akcil et al., 2019; Baldassarre et al., 2019; Bartzas and Komnitsas, 2015; Liu et al., 2019; Mastali et al., 2020). Alkali activation is a promising alternative and relatively low-cost technology for the valorization of various industrial wastes and the production of secondary materials, often called alkali-activated materials (AAMs) or geopolymers. These materials have an amorphous to semi-crystalline three-dimensional aluminosilicate microstructure, chemical composition quite similar to zeolites, beneficial physico-chemical properties, higher added value and can be used in the construction sector (Bernal et al., 2010; Davidovits, 1991; Fořt et al., 2018; Gebregziabiher et al., 2016; Ghanbari et al., 2015; Kioupis et al., 2018; Komnitsas et al., 2019a; Mehta and Siddique, 2016; Xu and Van Deventer, 2000). Aluminosilicate raw materials, including a wide range of virgin materials and industrial wastes such as construction and demolition wastes, fly ash, red mud, kaolin or metakaolin, various types of slags (slags from the non-ferrous metallurgy, ground blast furnace slag, ferronickel slag, steel slag, etc.) while mixtures of these can be used for the production of AAMs with tailored properties (Davidovits, 1991; Xu and Van Deventer, 2002; Komnitsas and Zaharaki, 2007). Apart from raw materials rich in silica and alumina, the alkali activation requires the use of strong alkaline solutions, mainly sodium or potassium hydroxide and silicate solutions. Alkaline solutions act as activators to initiate polymerization of Si and Al present in the raw materials and the formation of Si-O-Al-O bonds, while the silicate solution is usually added to balance the Si/Al ratio in the reactive paste. After curing for a few hours at mild temperatures (30-90

°C) the formation of a matrix with beneficial physical, mechanical and thermal properties is achieved (Bernal et al., 2010; Davidovits, 1991; Duxson and Provis, 2008; Gebregziabiher et al., 2016; Khale and Chaudhary, 2007; Peys et al., 2019a; Yip et al., 2005). During the last years, valorization of various wastes through alkali activation has been studied by many researchers and the results of these efforts are reported in the literature (Chen et al., 2016; Cui et al., 2019; Furnali et al., 2018; Heah et al., 2013; Huang et al., 2017; Komnitsas et al., 2007, 2009; Komnitsas, 2016; Maragkos et al., 2009; Marjanović et al., 2015; Mo et al., 2014; Onisei et al., 2012; Pontikes et al., 2013; Provis and Bernal, 2014; Samantasinghar and Singh, 2018; Soultana et al., 2019; Wang et al., 2017; Zaharaki et al., 2016; Zhang et al., 2016a).

In addition, the produced AAMs may be used for the immobilization of heavy metals and hazardous wastes or as adsorbents in various industrial processes (Komnitsas et al., 2013, 2015; Xia et al., 2019). The potential use of AAMs in water and wastewater treatment and in solidification/stabilization of contaminated sediments was investigated in recent studies (Alshaaer et al., 2015; Bumanis et al., 2019; Chen et al., 2019; Luukkonen et al., 2019; Komnitsas, 2016; Wang et al., 2019). The structure and properties of the final products are determined considering several parameters, such as the mineralogical and chemical composition of the raw materials (which usually are characterized by the presence of several mineralogical phases and complex structure), the particle size which determines the specific surface area and the reaction rate, the synthesis conditions (curing temperature, ageing period, etc.), the H_2O/Na_2O and SiO_2/Na_2O ratios in the activating solution and the type of additives used to improve the properties of the produced matrix (Ferone et al., 2013; Görhan and Kürklü, 2014; Hanjitsuwan et al., 2014; Komnitsas et al., 2009, 2015; Mijarsh et al., 2014; Huang et al., 2017; Petrakis et al., 2019; Traven et al., 2019; Tchadjie and Ekolu, 2018).

Therefore, the characteristics of the raw materials, the selection of additives and the experimental conditions are important factors which determine the properties of the final products. In several cases, the final products exhibit beneficial physical, mechanical and thermal properties, namely low permeability and shrinkage, high compressive strength, good resistance to acidic solutions, freeze-thaw cycles and firing, as well as good immobilization potential for several heavy metals (Bernal et al., 2010; Duxson and Provis, 2008; Gebregziabiher et al., 2016; Khale and Chaudhary, 2007; Komnitsas et al., 2007; Krivenko and Kovalchuk, 2007).

1.2 Aims and objective of the thesis

The aim of the present thesis is to study in depth the alkali activation/geopolymerization of different metallurgical/mining wastes, and produce materials with beneficial properties and thus higher added value.

The specific objectives of the thesis are the following:

1. The valorization of different metallurgical and mining wastes namely slags and laterite leaching residues for the production of AAMs.
2. The co-valorization of different slags and other wastes, in order to produce raw materials with desirable chemical and mineralogical composition and beneficial properties.
3. The investigation of the factors, which affect the structure and properties of the produced AAMs. Among others, factors, such as the particle size of the raw materials (and the related specific surface area), the H_2O/Na_2O and SiO_2/Na_2O ratios in the activating solution, the curing temperature, and the ageing period are investigated.

1.3 Novelty of thesis

The innovative aspects of the thesis are the co-valorization of different slags and the production of AAMs from laterite leaching residues.

This thesis contributes to the waste management and valorisation as well as the minimization of the carbon footprint of metallurgical (pyro- and hydro-) industries and the construction sector.

1.4 Outline of the thesis

This thesis is organized into five chapters: Chapter 1, as an introductory chapter, reports the aims and objectives and the contribution of the research thesis. Chapter 2 describes the alkali activation process, the chemistry aspects and reaction mechanisms for the production of AAMs, as well as the factors affecting their properties and potential applications. Chapter 3 describes the raw materials, the synthesis of AAMs and the analytical methods used in this thesis, while Chapter 4 presents and discusses the results. Finally, Chapter 5 presents the conclusions.

2. **Literature review**

2.1 Alkali Activation & Alkali–Activated Materials

2.1.1 Alkali Activation

AAMs are produced through alkali activation which involves the reaction between aluminosilicate materials (solid phase) and a strong alkaline solution (liquid phase) and the formation of a reactive paste, which after curing for a few hours at low temperature (<100 ^{o}C) leads to the formation of a final product with beneficial properties (Bernal et al., 2010; Duxson and Provis, 2008; Khale and Chaudhary, 2007; Komnitsas and Zaharaki, 2007; Peys et al., 2019a; Yip et al., 2005; Davidovits, 1991; Duxson et al., 2007a; Fernández-Jiménez and Palomo, 2005; Fernández-Jiménez et al., 2006; Provis and Van Deventer, 2007). A strong alkaline solution is necessary to increase the dissolution of Si and Al from the precursors and through polycondensation to assist in the formation of three-dimensional cross-linked polysialate structures ([-(Si-O)z-AlO-]n) (Davidovits, 2005; Görhan and Kürklü, 2014; Komnitsas and Zaharaki, 2007).

The alkaline solution consists mainly of sodium hydroxide (NaOH) and sodium silicate (Na_2SiO_3) solution or potassium hydroxide (KOH) and potassium silicate (K_2SiO_3) solutions. In particular, sodium or potassium hydroxide is required for the dissolution of raw materials, while sodium (or potassium) silicate solution is used to balance the Si/Al ratio in the reactive paste and also act as a binder, alkali activator, dispersant or plasticizer (Bernal et al., 2010; Komnitsas and Zaharaki, 2007; Komnitsas et al., 2020; Phair, 2001). Previous studies reported that the type of alkaline activator and its concentration play the most important role in the development of strength and microstructure in the produced AAMs (Cioffi et al., 2003; Ferone et al., 2013; Komnitsas et al., 2009). The most common alkaline activator used in such studies is NaOH, due to its relatively low cost and viscosity compared to KOH (Vickers et al., 2015). Finally, the alkali activation is considered an environment friendly and energy-efficient process and studies have shown that if Ordinary Portland Cement (OPC) is replaced by AAMs the CO_2 emissions can be reduced by 40-80 % (Komnitsas, 2011; Luukkonen et al. 2018a; Provis et al., 2015).

2.1.2 Alkali–Activated Materials

AAMs or geopolymers are a class of inorganic polymers formed by the reaction between an aluminosilicate source and an alkaline activator and have an amorphous three-dimensional polymeric structure consisting of Si-O-Al bonds (Davidovits, 1991, 1999; Duxson and Provis, 2008; Duxson et al., 2007a; Provis et al., 2015; Xu and Van Deventer,

2000). AAMs are considered as environmentally friendly materials, due to their synthesis from industrial by-products or wastes as well as their low energy demand during their production and the associated low CO_2 emissions. Therefore, these materials can be used as substitutes for OPC or alternative low carbon binders in several applications (Mohamed, 2019; Passuello et al., 2017; Scrivener et al., 2016).

In 1940, Purdon used blast furnace slag and NaOH to synthesize new materials (Purdon, 1940). In the 1950s, first Glukhovsky and then Krivenko in Ukraine produced an alkaline aluminosilicate cementious system first called "soil silicates". This alkali-activated system contained hydrated calcium silicate and aluminosilicate phases (Glukhovsky, 1959, 1965, 1989; Krivenko and Kovalchuk, 2007). Davidovits also proposed an one-part geopolymer consisting of aluminosilicate oxide (i.e. metakaolin), sodium or potassium silicate and slag, while later he reported that sodium or potassium silicate could be partially replaced with "synthetic lavas" due to high availability and production issues. Synthetic lava, namely reactive sodium or potassium aluminosilicate glass, could be prepared by mixing volcanic tuff and calcium carbonate, followed by melting at 1200-1350 °C, quenching in water, drying, and grinding (Davidovits, 2020). On the other hand, Ikeda states that three sources are necessary for the alkali activation process, namely raw materials, inactive filler (i.e. kaolinite or metakaolinite) and alkali hydroxide solution (Ikeda, 1998). In particular, raw materials are usually natural (aluminosilicate) sources, such as pozzolans, kaolin and metakaolin, or industrial wastes, such as fly ash, slags, and waste glass, etc. (Elimbri et al., 2011; Komnitsas and Zaharaki, 2007; Sarmin et al., 2014; Xu and Van Deventer, 2002). Kaolin or metakaolin are used for the supply of Al^{3+} ions. Although kaolin and metakaolin are able to be activated by alkaline hydroxide solutions, the rate at which the process occurs depends on the reactivity of the raw aluminosilicate. More specifically, metakaolin dissolution rate is much higher than that of the kaolin due to the higher reactivity in a basic medium. Care should be taken during the selection of the kaolin's calcination temperature because, if the temperature is lower than 700 °C, the produced metakaolin contains unreactive kaolin and exhibits low reactivity, while, if the calcination temperature exceeds 850 °C, crystallization occurs and, as a result, lower amorphicity and reactivity are anticipated. Finally, the use of metakaolin is considered beneficial during alkali activation due to its high amorphous content and its pozzolanic nature (Kakali et al., 2001; Konan et al., 2009; Shvarzman et al., 2003).

2.2 Reaction Mechanisms

The chemical composition of AAMs, which exhibit a partially amorphous microstructure, is similar to zeolites (Abdullah et al., 2011; Xu and Van Deventer, 2000). Several researchers have studied the reaction mechanisms for the production of AAMs (Komnitsas and Zaharaki, 2007; Li et al., 2010; Rees et al., 2008; Zhang et al., 2020a).

Generally, during polymerization, all the reactions occur simultaneously and affect each other due to the multiple components present in the liquid phase. Therefore, these processes are complex compared to the hydration of OPC (Zhang et al., 2011, 2020a).

According to Davidovits (1991, 2005) the AAMs have the following general empirical formula:

$M_n\{(SiO_2)z\text{-}AlO_2\}_n \bullet wH_2O$

where M is a monovalent cation, mainly K^+ and Na^+, or Ca^{2+} which may replace two monovalent cations in the structure; n is the degree of polycondensation; z represents the silicon to the aluminum ratio (Si/Al) which is 1, 2 or >>3 (up to 32) and w is the amount of chemically bound water molecules. The AAMs consist of linked SiO_4 and AlO_4 tetrahedra by sharing the oxygen atoms and are divided into three types depending on the z value, as shown in Figure 2.1. From this Figure, it is observed that the three monomeric units are:

(i) poly-sialate, PS (-Si-O-Al-O-) with Si/Al=2 (Gel 1),

(ii) poly-sialate-siloxo, PSS (-Si-O-Al-O-Si-O-) with Si/Al=2 (Gel 2),

(iii) poly-sialate-disiloxo, PSDS (-Si-O-Al-O-Si-O-Si-O-) with Si/Al=3 (Gel 3) and

(iv) sialate links with Si/Al >>3. The sialate is an abbreviation for silicon-oxo-aluminate Chains and rings are formed and cross-linked together always through a sialate Si-O-Al bridge (Komnitsas, 2011).
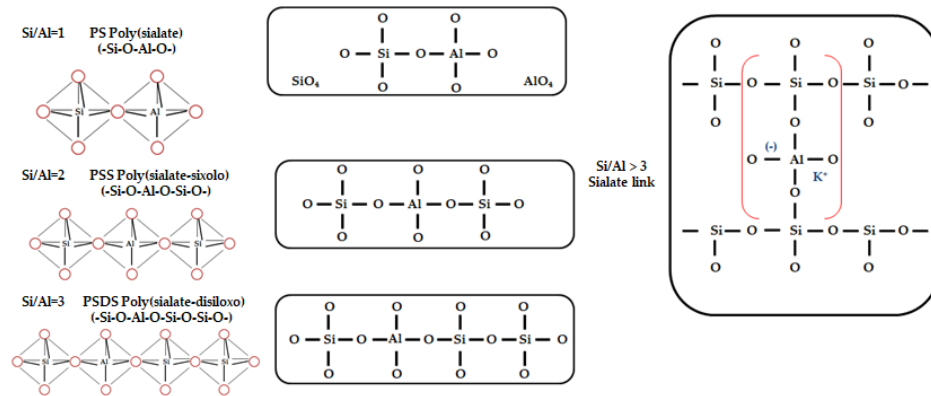
Figure 2.1. AAM structures according to Davidovits (2005).

The reaction mechanism for the production of AAMs involves the following stages, which describe the processes occurring during the transformation of a solid aluminosilicate source into a synthetic material (Davidovits, 1991; Duxson et al., 2007b; Hardjito and Rangan, 2005; Xu and Van Deventer, 2000):

(i) Dissolution: the solid aluminosilicate material is dissolved in the alkaline activator solution (MOH where M: alkali metal, mainly Na or K). More specifically, Si-O and Al-O tetrahedral monomers under the action of the alkali activator are released from the aluminosilicate materials.

(ii) Diffusion or transport: the dissolved Al and Si complexes diffuse from the particle surface into the reaction system. The Si and Al concentrations on the surface of the particles decrease due to the diffusion and so the dissolution process continues, according to the principle of chemical equilibrium.

(iii) Gelation or polycondensation: the formation of the amorphous -Si-O-Al-O- structure (gel) or zeolite crystals due to the polymerization of Al and Si complexes which is assisted by the added silicate solution.

(iv) Re-organization and hardening: the connectivity of the gel network increases and three-dimensional structures starts to form.

(v) Polymerization and hardening: this process can last from a few hours to several weeks depending on the raw materials mineralogy and synthesis conditions.

These stages are shown in Figure 2.2. It is also mentioned that these stages are performed simultaneously, except for the first one which depends on the reaction process. The reaction mechanisms during alkali activation of aluminosilicates have been reported in several earlier studies (Komnitsas et al., 2007; Li et al., 2010; Provis et al., 2014).
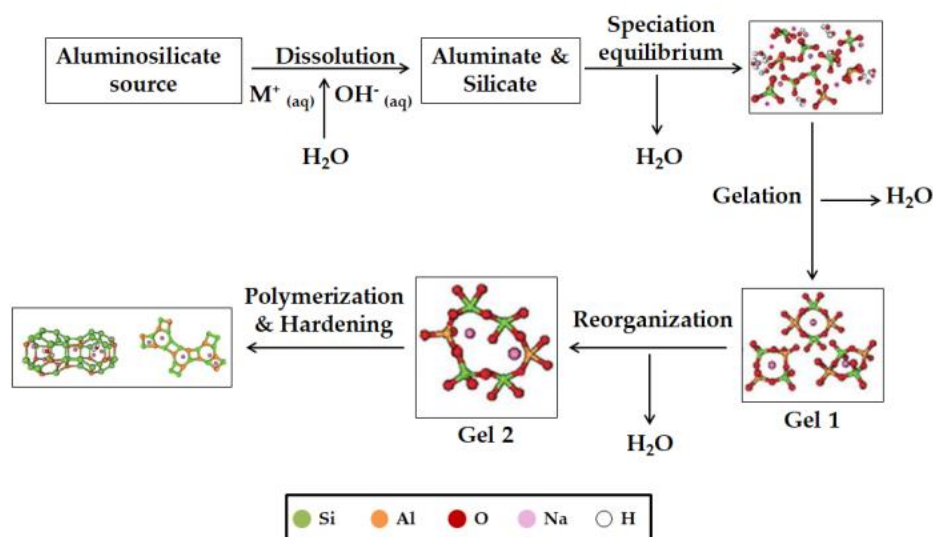
Figure 2.2. Stages of alkali activation process (Shi et al., 2011).

The reaction process results in a three-dimensional structure in which the negative charge of the aluminum units is balanced by the alkali metal, namely Na^+ or K^+. Then, during the gelation process the released water resides in the pores of the gel and plays the role of a reaction medium (Duxson et al., 2007a). However, magnesium, calcium and

iron may also participate in the reactions if they are present in heterogeneous raw materials and may make the overall reaction more complicated (Bernal et al., 2014; Walling et al., 2015).

2.3 Properties & Applications of AAMs

According to Duxson et al. (2007c), the microstructure and properties of AAMs depend on the nature of the raw materials and the formation process. It is known that the raw materials affect the homogeneity of the structure of the produced AAMs and thus their compressive strength and other properties (Subaer and Van Riessen, 2007). Several studies showed that AAMs have excellent physical, mechanical and thermal properties, such as high compressive strength, low shrinkage which prevents the formation of cracks, low permeability to fluids and chloride ions, good acid resistance, thermal stability up to 1000 ^{o}C, and excellent ability to immobilize toxic metals (Azimi et al., 2015; Bakharev et al., 2003; Cheng and Chiu, 2003; Davidovits, 1988; Duxson et al., 2007d; Kamseu et al., 2012; Martin et al., 2015; Sajedi, 2012; Yan et al., 2016; Živica et al., 2011). These properties of AAMs are similar to those of Portland cement, however the differences of both materials are significant. An important difference is the fast hardening of AAMs, which may take place at room temperature and result in acquiring of almost 70 % of the maximum compressive strength within the first 4 h. The final compressive strength is obtained within a period of 28 days and can reach of exceed 100 MPa (Hermann et al., 1999). Therefore, the AAMs are novel materials that may be used as alternatives to organic polymers and inorganic cement in various applications. They can be also used as low energy ceramic tiles (Namkane et al., 2016), protective coatings (Davidovits, 2020), refractory adhesives (Bell et al., 2005), decorative stone artifacts (Won and Kang, 2017), thermal insulating foams (Davidovits, 2020; Łach et al., 2016), hybrid inorganic-organic composites (Li et al., 2005; Zhang et al., 2004), fiber composites, heat resistant components, or for the external strengthening of existing concrete structures (Davidovits, 2020). AAMs find also applications in foundry (Thaarrini and Ramasamy, 2016), automotive and aircraft (Nair et al., 2007), cement and concrete industries (Law et al., 2015) as well as in biotechnological and medicinal applications (Naghsh and Shams, 2017). On the other hand, the environmental applications of AAMs include immobilization of hazardous elements or encapsulation of toxic waste, surface capping of waste dumps, and stabilization of tailing dams (Komnitsas et al., 2013; Van Jaarsveld et al., 1999). Since the AAMs are eco-friendly materials they may be used as alternative binders to replace OPC, for the production of "green" concrete and construction materials with lower carbon footprint (Komnitsas, 2011; Nasvi et al., 2013). In recent years, many studies have focused on the use of AAMs, due to their porous structure, as

adsorbents, for the absorption of heavy metals, such as Cd, Ni, Cu, boron, fluoride, phosphate, NOx, radionuclides ^{137}Cs and ^{90}Sr and dyes, such as methylene blue, methyl violet and methyl orange from wastewaters, as well as novel catalysts and photocatalysts (Ahmaruzzaman, 2010; Al-Harahsheh et al., 2015; Alouani et al., 2018; Fumba et al., 2014; Ge et al., 2015; Zhang et al., 2016b). Also, it is important to mention that the above applications of AAMs depend on their structure which in turn depends mainly on the Si/Al ratio. More specifically, AAMs with Si/Al ratio 1:1 and 3D network are used in low technology applications, namely for the production of building materials, including bricks, ceramics etc., while AAMs with Si/Al ratio of 2:1 and 3D network are used for the production of low CO_2 cements and concrete as well as for radioactive and toxic waste encapsulation. On the other hand, AAMs with Si/Al ratio 3:1 and 2D network are used for fire protection (fiber-glass composite) and as heat resistant composites, between 200 °C and 1000 °C, while AAMs with Si/Al greater that 3:1 and 2D network are used as industrial sealants between 200 °C and 600 °C. Finally, the AAMs with Si/Al ratio between 20:1 and 35:1 and 2D network are used as fire and heat resistant (fiber composites) materials (Davidovits, 2005; Nergis et al., 2018).

2.4 Factors affecting the properties of AAMs

Several factors have been identified as important and affect the mictostructure as well as the mechanical and chemical properties of AAMs. Some of these factors include the type, amount, reactivity and particle size of raw materials (mainly mineralogical and chemical composition), type of activator, liquid-to-solid ratio, curing conditions (i.e. curing temperature, ageing period, etc.), setting time, etc. (Alonso and Palomo, 2001; Gharzouni et al., 2015; Duxson et al., 2005; Granizo et al., 2007; Heah et al., 2012; Kamseu et al., 2014; Komnitsas and Zaharaki, 2007; Kumar and Kumar, 2011; Marjanović et al., 2015; Rattanasak and Chindaprasirt, 2009; Rovnaník, 2010; Xu and Van Deventer, 2000). These factors significantly affect the compressive strength of AAMs and the other properties of raw materials which are the key criterion for their use in various applications in the construction industry (Komnitsas and Zaharaki, 2007; Provis et al., 2005). Therefore, many investigations were focused on the study of these factors. Primarily, the most important factor affecting the synthesis of AAMs is the selection of suitable raw materials which determines the dissolution rate of the contained phases and the release of ions (Na^+, K^+, Ca^{2+}, Mg^{2+}), which participate in the developments of bonds (Duxson and Provis, 2008). During alkali activation, cations play a catalytic role in all stages of alkaline activation and especially during the stage of gel solidification and the development of microstructure of the produced AAMs (Bankowski et al., 2002; Van Jaarsveld, 2000). According to Barbosa et al. (1999), the optimum properties of AAMs are achieved when

the NaOH concentration is sufficient to supply a charge balancing mechanism. On the other hand, the excess of Na may causes the formation of unwanted sodium carbonate due to the atmospheric carbonation. Regarding the presence of Ca, the CaO content of the raw materials may enhance the mechanical properties of the AAMs, as it reduces the microstructure porosity and results in the formation of an amorphous gel rich in Ca, Al and Si (Van Jaarsveld et al., 1998; Xu and Van Deventer, 2002). The positive effect of Ca on the compressive strength of AAMs has been shown in several previous studies (Temuujin et al., 2009a; Xu and Van Deventer, 2000; Yip et al., 2005). In the case that the raw material does not contain sufficient amounts of Ca, it is possible to add $CaCO_3$ and CaO in the form of aqueous suspension to improve the physical and mechanical properties of AAMs. The excess of CaO in the AAMs based on slag is undesirable since the Ca^{2+} ions replace Na^+ ions thus affecting the load balance and as a result AAMs with poor properties are produced (Buchwald et al., 2007; Yip and Van Deventer, 2003).

Another important factor during the synthesis of the AAMs is the particle size distribution of aluminosilicate materials, which is also interrelated with their reactivity. Various studies have reported that finer particle sizes (i.e. $d_{90}<50$ μm) result in increased specific surface area and reactivity of the raw materials, which in tern result in the formation of stronger bonds and the production of AAMs with more beneficial properties (Djobo et al., 2016; Komnitsas et al., 2009; Temuujin et al. 2009b; Tennakoon et al., 2014a; Wei et al., 2017).

The compressive strength of the AAMs, usually depends on the SiO_2/Al_2O_3, $SiO_2/(Al_2O_3+Fe_2O_3)$, and SiO_2/Na_2O molar ratios present in the activating solution, as well as the presence of H_2O. Several studies report that the increase in the SiO_2/Al_2O_3 ratio up to a certain value increases the compressive strength of AAMs (De Silva et al., 2007; Duxson et al., 2007e; Gualtieri et al., 2015; Komnitsas et al., 2015). This is due to the fact that increase of this ratio improves the microstructure of the AAMs. Besides, more Si-O-Si bonds, which are stronger than Si-O-Al and Al-O-Al bonds, are produced when increased SiO_2/Al_2O_3 ratios are present (Lahoti et al., 2018). On the other hand, AAMs produced from materials with high content of Al usually acquire reduced mechanical strength, due to the formation of amorphous rich in Al macromolecular aluminosilicate chains (Komnitsas and Zaharaki, 2007). Optimum ratios of SiO_2/Al_2O_3 have been reported to be between 2.0 and 5.5, or in any case higher than 2.5 (Davidovits, 1999; Provis and Van Deventer, 2014). Other researchers indicated different ranges, for example from 3.3 to 4.5 (Khale and Chaudhary, 2007; Provis et al., 2009). On the contrary, Xu and Van Deventer (2000) mentioned that the SiO_2/Al_2O_3 ratio is not a sufficient factor for the selection of raw materials which are suitable for alkaline activation, due to the complexity of the gel formation and the hardening mechanism of AAMs.

Another ratio that also plays an important role in the properties of the produced AAMs is the $SiO_2/(Al_2O_3+Fe_2O_3)$ ratio. Raw materials rich in Fe could be used for alkaline

activation since Fe^{3+} present as Fe_2O_3 may replace Al^{3+} in the AAM matrix (Lemougna et al., 2014). In the case that slag is used as raw material, Fe is dissolved during alkaline activation, and depending on the synthesis conditions, it forms crystalline hydrated phases on the surface of the grains or colloidal hydrated phases. The formation of crystalline phases usually does not favor the development of strength due to the presence of cracks as a result of moisture release, shrinkage or due to the creation of interfaces. In addition, the SiO_2/Na_2O ratio is also important factor during the synthesis of AAMs, since it may affect the degree of polymerization of dissolved compounds. Generally, as this ratio increases during the alkaline activation, the compressive strength of AAMs also increases (Criado et al., 2007; Leong et al., 2016; Tchakoute et al., 2013). Apart from the above ratios, the H_2O/Na_2O ratio is considered significant during alkaline activation. It is known that low ratio indicates excess of NaOH solution and thus of OH^- ions, which may remain unreacted in the paste and result in the production of AAMs with low compressive strength and other undesired properties. On the contrary, higher ratios may indicate either OH^- ions deficiency or excess of H_2O that remains unreacted in the paste. In each case, the optimum H_2O/Na_2O ratio depends on the mineralogy of the precursors and the reaction rate between the raw materials and the alkaline solution as mentioned in previous studies (Komnitsas et al., 2019a, 2019b, 2020). The presence of H_2O is important during alkaline activation, and it contributes to the absence of cracks in the structure of the produced AAMs (Komnitsas and Zaharaki, 2007). Curing may often need to be carried out at relatively low humidity (i.e. 30 %) and temperature to avoid rapid evaporation of water that results in deterioration of AAMs and inhibits the development of satisfactory mechanical properties (Komnitsas and Zaharaki, 2007; Perera et al., 2007). Generally, the presence of water in the initial compositions is directly linked to the dissolution proess of Si and Al from the raw materials and the formation of bonds (Lee and Van Deventer, 2002; Panias et al., 2007). Additionally, water affects the degree of polymerization, since it is involved in poly-condensation, and is a critical factor for the hardening of the paste. The added water improves the elasticity of the mixture and contributes to the hydrolysis of Al^{3+} and Si^{4+} ions. Besides, it ensures good mixing and homogeneity of the initial paste. Finally, the curing process is a crucial step during the synthesis of AAMs and includes factors such as curing time, temperature and water content. Concerning, the curing time and temperature, the most common temperatures used are 40-80 ^{o}C but may range from room temperature up to 100 ^{o}C for a few hours to some days (Alonso and Palomo, 2001; Aredes et al., 2015; Mo et al., 2014; Tippayasam et al., 2016). In most cases, curing at temperature 30-90 ^{o}C for a few hours, enables the formation of a matrix with beneficial properties (Bernal et al., 2010; Duxson and Provis, 2008; Khale and Chaudhary, 2007; Peys et al., 2019a; Yip et al., 2005). Many studies reported that curing at high temperatures for long period weakens the structure of the AAMs and results in their dehydration and shrinkage; this indicates that in most cases

small amounts of water must be present in order to avoid the formation of cracks and obtain AAMs with sufficient structural integrity (Bakharev, 2005; Khale and Chaudhary, 2007; Van Jaarsveld et al., 2002). Concerning the ageing time, it may vary from several hours to 28 days therefore it is comparable to the respective time required for concrete (Sofi et al., 2007). Longer periods may improve polymerization and result in specimens with higher compressive strength. However, in several cases no significant increase in the compressive strength of the produced AAMs is recorded for a curing period longer than 48 h (Khale and Chaudhary, 2007). The optimum curing period should be selected depending on the type of the raw materials and the desirable properties of the produced AAMs.

3. **Materials and Methods**

3.1 Raw Materials

The materials used in this thesis are metallurgical slags and laterite leaching residues. More specifically, the Polish ferronickel slag (PS) produced after pyrometallurgical treatment of Ni lateritic ores and collected from a waste dump at Szklary Lower Silesia, in south-western Poland (Kierczak et al., 2009); more information for this slag is provided in a previous recent study (Komnitsas et al., 2019a). Furthermore, two types of fayalitic slags were used, namely a fayalitic slag (FS) produced after pyrometallurgical treatment of copper concentrates in a flash smelting furnace in Finland for the production of copper cathodes, copper sulphate and various metal concentrates (Saari et al., 2019), as well as the slag produced after plasma treatment (FSP) of the previous FS. The plasma treatment was carried out at Tecnalia (Spain), https://www.tecnalia.com/en/, in a pilot plant furnace at 1650 ºC, using coke as a reducing agent and calcium hydroxide as flux. It is also noted that except FSP two more materials, a Zn-rich fly ash and a Fe-rich metallic fraction, which are marketable products according to their composition, were produced (Figure 3.1). Finally, in order to assess the co-valorization potential of different slags for the production of AAMs, ferronickel slag (LS) produced at LARCO S.A (Greece) after pyrometallurgical treatment of nickel laterites in electric-arc furnace for the production of ferronickel (FeNi) was used (Komnitsas et al., 2007).
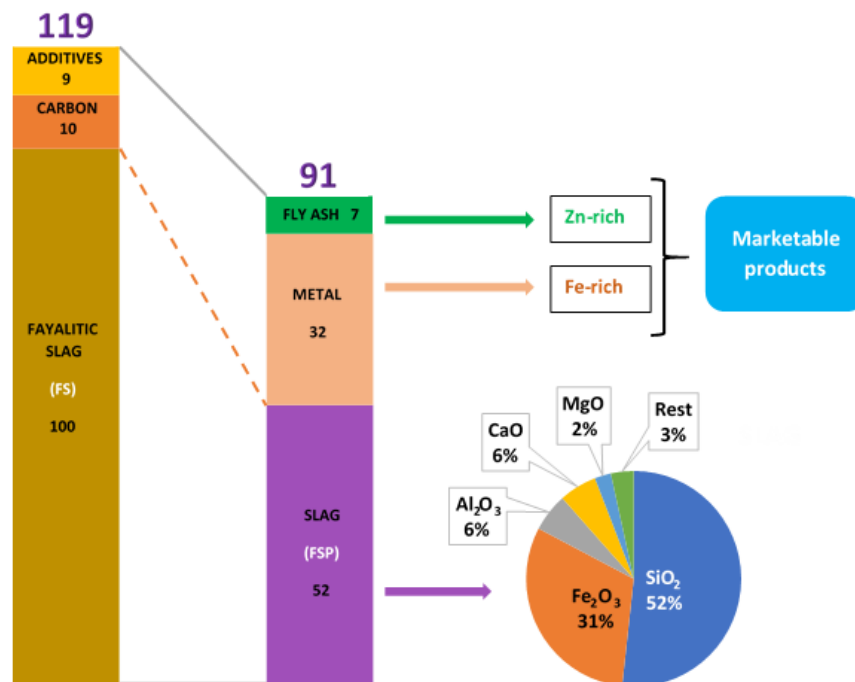
Figure 3.1. Plasma treatment of FS slag for the production of FSP slag and two other marketable products, carried out at Tecnalia, Spain (Komnitsas et al., 2020).

On the other hand, the leaching residues (LR and LLR) were obtained after laboratory column leaching tests using Greek laterites and H_2SO_4 as leaching solution, while leaching residues (L) were obtained after atmospheric acid leaching (AAL) using Polish laterites and H_2SO_4 as leaching solution in a 1-3 L stirred reactors. The experimental conditions used in the column leaching tests of Greek laterites are similar to those described in previous recent studies (Komnitsas et al., 2018, 2019b). In this case, in order to regulate the Si/Al ratio, and increase the reactivity of the starting mixtures during alkaline activation, laterite leaching residues were mixed with ferronickel slags, i.e. PS and LS, or metakaolin (MK) in different proportions. Metakaolin was obtained after calcination of kaolin [$Al_2Si_2O_5(OH)_4$, Fluka] at 750 °C for 2 h in a laboratory oven (N-8L Selecta, Abrera, Spain).

Prior to alkali activation, the raw materials were dried at 80 °C in a laboratory oven (Jeio Tech ON-02G, Seoul, Korea) and then pulverized using a Fritsch-Bico pulverizer (Type UA, Fritsch, Dresden, Germany) until the 90 % passing size (d_{90}) is less than 50 μm for almost all materials used. The particle size distribution was determined using a laser particle size analyzer (Mastersizer S, Malvern Instruments, Malvern, UK). The Brunauer-Emmett-Teller (BET) nitrogen adsorption method was considered for the determination of the specific surface area of the raw materials, using a Quantachrome Nova 2200 analyser, Anton Paar QuantaTec Inc., Boynton Beach, FL, USA.

The particle size distribution (μm) and specific surface area ($m^2 g^{-1}$) of the raw materials used are presented in Table 3.1. It is seen from this data that the 90 % passing size (d_{90}) of almost all materials is less than 50 μm which is considered adequately fine for alkaline activation (Komnitsas et al., 2009). Polish ferronickel slag (PS) was also pulverized to obtain three different particle size fractions after 30, 60 and 120 min of grinding in a ball mill (Sepor, Los Angeles, CA, USA), in order to study the effect of the particle size on the compressive strength of the produced AAMs. More specifically, the d_{90} of the three different PS slag particle sizes obtained after 30, 60 and 120 min of grinding are 154.0 μm, 86.0 μm and 47.0 μm respectively (Table 3.1). It is noted that more details on the grinding process in a ball mill and the grinding products are reported in a previous recent study (Petrakis et al., 2019). Concerning the specific surface area of the raw materials, it is observed that the values range between 1.2 and 65.3 $m^2 g^{-1}$ (Table 3.1). It is well known that the finer particles have larger specific surface and thus the geopolymerization reactions proceed faster and result in the production of AAMs with denser microstructure and better properties (Heah et al., 2011; Komnitsas et al., 2009, 2015; Yahya et al., 2015).

A Bruker-AXS S2 Range Spectroscopic Fluorescence Spectrometer A (XRF-EDS, Bruker, Karlsruhe, Germany) was used for the chemical analysis of raw materials in the form of oxides (Table 3.2). Loss on ignition (LOI) was determined by heating the materials at 1050 °C for 4 h. As seen from this data, all slags contain sufficient amounts of SiO_2 and

Al_2O_3 for successful alkali activation. More specifically, the content of SiO_2 is 30.2, 32.7, 30.1 and 51.8 wt% for PS, LS, FS and FSP slags respectively, while their content of Al_2O_3 is 7.6, 8.3, 2.8 and 5.7 wt%, respectively. It is also observed that the amount of Fe_2O_3 is high for all studied slags, while the CaO content of PS, LS and FSP slags is higher compared to that of FS slag. It is worth noting that the only major difference between ferronickel slags is that PS slag has much higher CaO content (13.0 wt%) compared to LS slag (3.73 wt%). On the other hand, in the same Table, it is observed that the leaching residues mainly consist of SiO_2 and Fe_2O_3, while their low content in Al_2O_3 indicates poor potential for successful alkali activation. Leaching residues of Polish laterite (L) have a high content of SO_3 (30.6 wt%) and this may be due to the atmospheric leaching using sulfuric acid (H_2SO_4). Finally, metakaolin has a high content of SiO_2 (54.2 wt%) and Al_2O_3 (40.3 wt%), thus improved SiO_2/Al_2O_3 ratio and increased reactivity of the initial mixture is anticipated during alkali activation (Table 3.2).

Table 3.1. Particle size distribution and specific surface area of the raw materials.

Raw Materials	Particle size (μm)		Specific surface ($m^2 g^{-1}$)
	d_{90}	d_{50}	
PS	57.5	8.9	2.3
PS30 (30 min of grinding)	154.0	39.9	1.2
PS60 (60 min of grinding)	86.0	23.4	1.6
PS120 (120 min of grinding)	47.0	11.9	2.3
LS	46.0	8.9	1.2
FS	49.0	9.0	3.6
FSP	41.0	5.7	2.8
LR	48.2	9.8	2.1
LLR	31.2	6.1	19.7
L	13.0	2.3	65.3
MK	25.5	8.8	2.4

4. Experimental methodology

For the production of AAMs, the raw materials were mixed with the activating solution under continuous slow stirring in a laboratory mixer for about 10-15 min, to produce a homogenous paste. Then, the fresh paste was cast in metallic cubic molds (5 x 5 x 5 cm^3), which were vibrated for a few minutes to eliminate the presence of air voids in the reactive mass and thus improve the strength and other properties of the final specimens. Pre-curing of the reactive paste was carried out at room temperature (20±0.5 °C) for 4 to 48 h to allow initiation of the alkali activating reactions, development of structural bonds, and sufficient hardening. It is known that the amount of water present in the paste, the

particle size of the raw materials and the strength of the activating solution affect the hardening period of the paste (Soultana et al., 2019).

Table 3.2. Chemical composition (wt%) of raw materials.

(%)	Ferronickel Slags		Fayalitic Slags		Greek laterite leaching residues		Polish laterite leaching residues	Metakaolin
	PS	LS	FS	FSP	LR	LLR	L	MK
Na_2O	0.4	-	0.5	0.6	-	0.6	8.1	1.3
Fe_2O_3	40.6	43.8	57.6	31.0	50.9	37.7	9.0	0.6
SiO_2	30.2	32.7	30.1	51.8	30.8	37.5	23.3	54.2
Al_2O_3	7.6	8.3	2.8	5.7	2.3	4.1	1.2	40.3
Cr_2O_3	1.2	3.1	0.1	0.4	2.5	3.3	0.4	0.02
MgO	1.8	2.8	1.3	2.5	2.1	2	5.9	0.3
NiO	0.9	-	0.2	-	0.1	0.3	0.4	-
K_2O	0.9	-	0.9	1.2	-	0.3	0.01	2.4
TiO_2	0.7	-	0.2	0.3	0.6	0.3	0.01	0.4
CoO	0.03	-	-	-	0.02	0.01	0.02	<0.00097
MnO	0.3	0.4	0.1	0.1	0.3	0.1	0.1	0.01
CaO	13.0	3.7	1.0	5.7	3.7	0.6	17.9	0.1
P_2O_5	0.02		-	-	-	-	0.2	0.5
SO_3	-	0.2	0.4	0.5	-	3	30.6	0.3
ZnO			2.8	0.03	-	-	-	<0.00003
LOI					9.2	10.3	2.9	-
SUM	97.7	95.0	97.9	99.8	99.5	100.0	100.0	100.1

Specimens were then demoulded, sealed in plastic bags to avoid evaporation of the remaining water and remained at room temperature (20 °C±0.5 °C) or placed in a laboratory oven (Jeio Tech ON-02G, Seoul, Korea) and cured at 40-95 °C for 24 or 48 h. After curing, the produced specimens were removed from the oven and allowed to cool at room temperature (20 °C±0.5 °C) for an ageing period of 7 or 28 days. The selection of the curing time was based on previous studies carried out in the laboratory for the production of AAMs with the use of various industrial wastes (Komnitsas et al., 2015, 2019a; Soultana et al., 2019; Zaharaki et al., 2016). Finally, the compressive strength and other selected properties of the produced AAMs were determined. All tests and measurements were carried out in triplicate and mean values are given for each parameter. It is mentioned that the difference in measurements did not exceed ±5 %; with few exceptions. The AAM codes, the selected mixing proportions for materials used and the H_2O/Na_2O and SiO_2/Na_2O ratios in the activating solution are presented in Table 3.3. The mineralogical analysis of raw materials and the selected AAMs was performed using an X-ray Diffractometer (XRD, D8-Advance, Bruker AXS, Karlsruhe, Germany) with a

Cu tube and scanning range from 4° to 70° 2theta (θ), with a step of 0.02° and 0.2 s/step measuring time. Qualitative analysis was carried out using DiffracPlus Software (EVA v. 2006, Bruker, Karlsruhe, Germany) and the PDF database. Fourier Transform Infrared (FTIR) spectroscopy was carried out a PerkinElmer 1000 spectrometer (PerkinElmer, Akron, OH, USA), in the spectra range of 400 to 4000 cm^{-1}. Pellets were produced by mixing a pulverized sample with KBr at a ratio of 1:100 w/w. The identification of the morphology and structure of the raw materials and selected AAMs were identified by Scanning Electron Microscopy (SEM) using a JEOL-6380LV scanning microscope (JEOL ltd., Tokyo, Japan) with an Oxford INCA Energy Dispersive Spectroscopy (EDS) micro analysis system (Oxford, Instruments, Abingdon, UK). In addition, the toxicity of raw materials and the selected AAMs was assessed according to the EN 12457-3 test (EN 12457-3:2002; Van der Sloot et al., 2001), which involved leaching (8 L per kg) of the material in distilled water. The leaching solutions were filtered using 0.45 μm membrane filters and the concentration of the metal ions in the eluate was determined using an Inductively Coupled Plasma Mass Spectrometry (ICP MS, Agilent 7500 cx) equipped with an Agilent ASX-500 Autosampler. Also, the concentration of the metals was expressed as mg kg^{-1} of raw material and compared with existing limits for disposal of wastes in various landfill types (European Commission, 2002).

Table 3.3. Test details and selected molar oxides in the activating solutions.

AAM Code	NaOH	Solid	NaOH pellets	H_2O	Na_2SiO_3	L/S ratio*	H_2O/Na_2O**	SiO_2/Na_2O**
	M	wt%	wt%	wt%	wt%			
PS		82.1	3.8	11.1	3.0	0.2	14.2	0.3
PS120	8	80.0	4.2	12.5	3.3	0.2	14.2	0.3
PS60		80.0	4.2	12.4	3.3	0.2	142	0.3
PS30		80.0	4.2	12.5	3.3	0.2	14.2	0.3
FS		81.0	2.4	7.1	9.5	0.2	17.4	1
FSP	8	81.1	3.6	10.6	4.7	0.2	14.9	0.4
LS		83.2	2.1	6.3	8.4	0.2	17.4	1
FS30LS70		82.6	2.2	6.5	8.7	0.2	17.4	1
FSP30LS70	10	82.4	2.7	6.2	8.7	0.2	14.6	0.9
LR		75.6	3.1	9.1	12.2	0.3	17.4	1
MK	8	52.0	6.0	18.0	24.0	0.7	17.6	1
LR90MK10		75.8	3.1	9.0	12.1	0.3	17.2	1
LLR	10	71.4	4.3	10.0	14.3	0.3	14.8	1
LLR30PS70	8	81.4	4.5	13.2	3.5	0.2	14.1	0.3
LLR30LS70		81.7	2.3	6.8	9.0	0.2	17.4	1
L70MK30	10	51.1	7.5	17.0	24.5	0.7	14.6	1
L80MK20		54.2	7.0	15.9	22.9	0.6	14.6	1

*Liquid-to-solid ratio in the starting mixture, **molar ratios in the activating solution.

In order to study their structural integrity, selected AAMs were subjected to firing at a temperature range of 200-1000 ^{o}C, in a laboratory furnace N-8L Selecta (JP Selecta, Abrera, Spain). The heating rate used was 5 ^{o}C min^{-1}, while the retention time at each temperature varied between 2 and 6 h, depending on each AAM type. In addition, they were immersed in distilled water (H_2O) and acidic solutions (1 mol L^{-1} HCl, 1 mol L^{-1} H_2SO_4) for 7 to 30 days or subjected to freeze-thaw cycles for 7 and 28 days (Standard C1262–10) (ASTM, 2018). More specifically, freezing was performed at –18±5 ^{o}C for 4 h, while thawing carried out at room temperature (20±0.5 ^{o}C) for 12 h (one complete cycle). Finally, the compressive strength and other selected properties of the AAMs were determined. The compressive strength was determined using a MATEST C123N load frame (compression and flexural machine, Matest S.p.A, Treviolo, Bergamo, Italy). The water absorption (%), porosity (%) and apparent density (kg m^{-3}) of selected AAMs were determined according to the standard BS EN 1936:2006 (BSI, 2007).

4. Results and discussion

4.1 Characterization of raw materials

4.1.1 Reactivity of raw materials

The reactivity of raw materials was assessed through leaching tests; 1.0 g of each raw material was added in 100 mL of 8 or 10 mol L^{-1} (M) NaOH solution and leaching was carried out in 250 mL conical flasks under continuous stirring for 24 h at room temperature (20±0.5 ^{o}C). After solid and liquid separation with the use of 0.45 μm pore size membrane filters (PTFE, Chromafil), the Al and Si concentration in solution was determined using ICP. It is known that several studies have focused on the determination of SiO_2/Al_2O_3 molar ratios in the raw materials, thus evaluating their reactivity and subsequently their alkali activation potential (Ascensão et al., 2020; Aughenbaugh et al., 2015; Bumanis et al., 2017; Hertel and Pontikes, 2020; He et al., 2016; Lahoti et al., 2018). Nevertheless, as mentioned in other studies, this ratio mainly indicates their reactivity and does not fully define the actual dissolution of Si and Al ions that participate during alkali activation in the formation of Si-O-Al bonds (Sun et al., 2020; Tennakoon et al., 2014b; Wang et al., 2020a, 2020b; Zhang et al., 2020b).

Table 4.1 shows the reactivity of raw materials, as denoted by the concentration of Si and Al (in mg L^{-1}) and the respective Si/Al molar ratios in solution after alkaline leaching. It is seen from this data that the highest concentration of Si (550.0 mg L^{-1}) and Al (101.5 mg L^{-1}) was obtained after leaching of the finer size of PS slag (PS120). The other ferronickel slag (LS) used in this study, exhibits also high reactivity, as shown by the concentration of Si (335.5 mg L^{-1}) and Al (99.1 mg L^{-1}) in the final solution; comparative results have been also produced in earlier studies (Zaharaki and Komnitsas, 2009). On the contrary, the concentration of Si and especially Al for the FS and FSP slags were much lower (Table 4.1), but their reactivity is considered sufficient for alkali activation. The Si/Al ratios were 5.4, 9.6, 4.2 and 3.4 for PS120, FS, FSP and LS, respectively.

On the other hand, the concentration of Si and Al in solution after leaching of LR, LLR and L residues is very low, thus indicating that their reactivity is not sufficient for alkaline activation. In particular, it is observed that, after alkaline leaching of LR the concentrations of Si and Al in the solution were 20.1 and 2.4 mg L^{-1}, respectively, whereas the calcination of these leaching residues at 800 and 1000 ^{o}C, resulted in a much lower concentration of both elements in the eluate. More specifically, the concentration of Si was 12.9 mg L^{-1} in the solution after calcination of laterite residues at 800 ^{o}C (800LR) and 2.0 mg L^{-1} after calcination at 1000 ^{o}C (1000LR). According to the results of earlier studies, calcination of laterite at temperatures above 800 ^{o}C results in structural modifications and the formation of spinels ($Si_3Al_4O_{12}$) (Kpinsoton et al., 2018; Mascarin, 2018). The Si/Al ratios were 8.4, 21.5 and 5.4 for LR, 800LR and 1000LR, respectively. In addition, it is

noticed from this data that the other leaching residues investigated (LLR), exhibit even lower reactivity, since the concentration of Si and Al in the final solution was 0.9 and 0.1 mg L^{-1}, respectively. The third laterite leaching residues (L) studied exhibited low concentration of Al (0.5 mg L^{-1}) in the solution but much higher Si concentration (59.1 mg L^{-1}). It is mentioned that the Si/Al ratios were 18.1 and 118.2 for LLR residues and L residues, respectively.

Finally, metakaolin (MK) exhibited higher reactivity, as indicated by the concentration of Si and Al in the final solution, which was 58.7 and 41.9 mg L^{-1}, respectively, after alkaline leaching with 8 mol L^{-1} NaOH. It is noted that the alkaline leaching of metakaolin with 10 mol L^{-1} NaOH resulted in slightly increased concentrations of both elements in the final solution as indicated in earlier studies (Komnitsas et al., 2009; Lemougna et al., 2017). The Si/Al ratio was 1.4 for MK.

Table 4.1. Concentration of Si, Al and Si/Al molar ratio in final solution.

Raw material	Si (mg L^{-1})	Al (mg L^{-1})	Si/Al
PS120[a]	550.0	101.5	5.4
PS60[a]	281.5	63.4	4.4
PS30[a]	216.0	57.0	3.8
LS[a]	332.5	99.1	3.4
FS[a]	139.5	14.5	9.6
FSP[a]	100.0	23.9	4.2
LR[a]	20.1	2.4	8.4
800LR[a]	12.9	0.6	21.5
1000LR[a]	2.0	0.4	5.4
LLR[a]	0.9	0.1	18.1
L[b]	59.1	0.5	118.2
MK[a]	58.7	41.9	1.4
MK[b]	61.3	43.4	1.4

a: Leaching with 8 mol L^{-1} NaOH solution for 24 h.

b: Leaching with 10 mol L^{-1} NaOH solution for 24 h.

4.1.2   XRD Analysis

The XRD patterns of ferronickel (PS, LS) and fayalitic (FS, FSP) slags are presented in Figures 4.1 and 4.2, respectively. Magnetite (Fe_3O_4), fayalite (Fe_2SiO_4) and quartz (SiO_2) are the phases detected in PS and LS slags, as shown in Figure 4.1. In addition, the main mineralogical phases present in PS slag are hedenbergite [$Ca(Fe,Mg)(SiO_3)_2$], diopside ($CaMgSi_2O_6$) and hatrurite (Ca_3SiO_5) as a minor phase, while the main mineralogical phases present in LS are anorthite ($CaAl_2Si_2O_8$), chromite ($FeCr_2O_4$), cristobalite (SiO_2), forsterite (Mg_2SiO_4) and tridymite (SiO_2). It is also mentioned that PS and LS slags have high amorphous content (~50 %) denoted by the broad hump shown between 2-Theta 25-40°, as also indicated in previous studies (Komnitsas et al., 2009; Zaharaki et al., 2010).
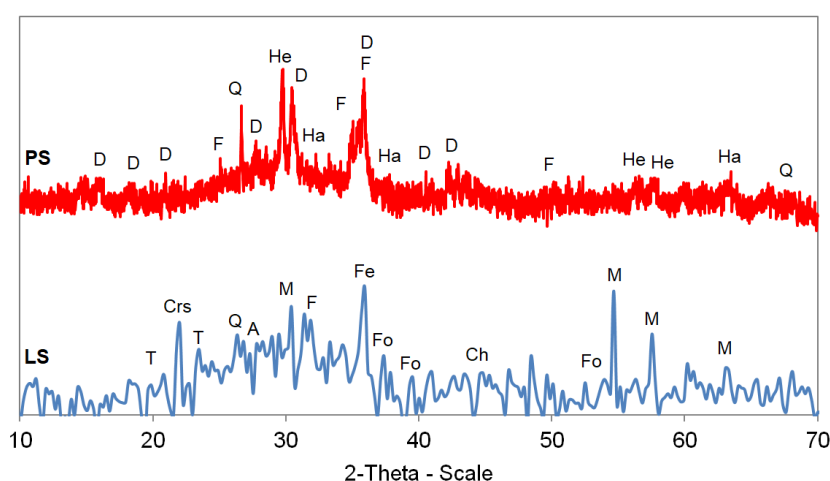
Figure 4.1. XRD patterns of ferronickel slags, namely PS and LS. Phases identified are: anorthite (A), chromite (Ch), cristobalite (Crs), diopside (D), fayalite (F), forsterite (Fo), hatrurite (Ha), hedenbergite (He), magnetite (M), quartz (Q), tridymite (T).

On the other hand, the main mineralogical phases detected in FS slag are magnetite and fayalite, whereas in FSP slag the main phase is clinoferrosilite ($FeSiO_3$) , while graphite (Gr) corresponds to traces of residual carbon due to the carbo-reduction plasma reaction that took place in the pilot plant furnace (Figure 4.2).
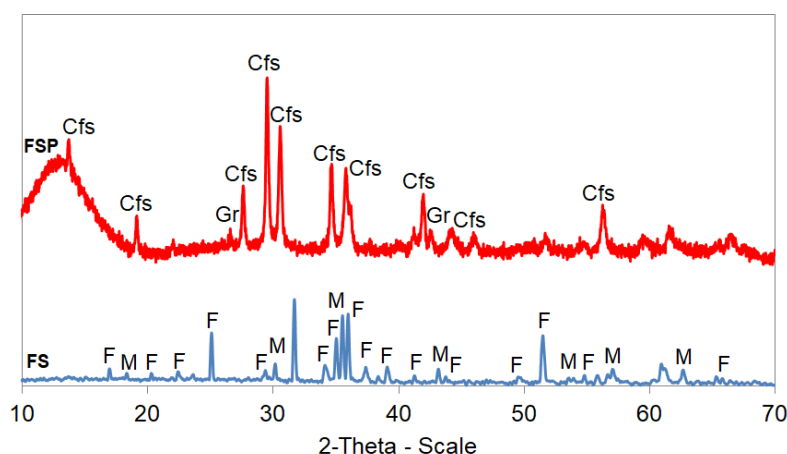
Figure 4.2. XRD patterns of fayalitic slags, namely FS and FSP. Phases identified are: clinoferrosilite (Cfs), fayalite (F), graphite (Gr), magnetite (M).

The mineralogical analysis of all laterite leaching residues, as derived by XRD is presented in Figure 4.3. As seen from the XDR pattern of leaching residues (L) the main mineralogical phases are diopside ($MgCaSi_2O_6$), fayalite (Fe_2SiO_4), talc [$Mg_3Si_4O_{10}(OH)_2$] and zincite (ZnO), while the minor phases are clinochlore [$(Mg,Fe)_5Al(Si_3Al)O_{10}(OH)_8$] and quartz ($SiO_2$). On the other hand, the main mineralogical phases present in the second leaching residues (LR) are quartz (SiO_2) and hematite (Fe_2O_3), while goethite [$FeO(OH)$], clinochlore [$(Mg,Fe)_5Al(Si_3Al)O_{10}(OH)_8$] and lizardite [$(Mg,Fe)_3Si_2O_5(OH)_4$] also exist as minor phases. The main Ni containing phases are chromite (Cr_2O_3 NiO) and willemseite [$(Ni,Mg)_3Si_4O_{10}(OH)_2$]. Finally, in the case of the third leaching residues (LLR), it is seen from the XRD pattern that the main mineralogical phases detected are quartz (SiO_2), goethite ($FeO(OH)$), hematite (Fe_2O_3) and clinochlore ($(Mg,Fe)_5Al(Si_3Al)O_{10}(OH)_8$), while chromite [$(Fe,Mg)Cr_2O_4$], calcite ($CaCO_3$) and cryptomelane ($KMn_8O_{16}$) are minor phases. The main Ni containing phase is willemseite ($(Ni,Mg)_3Si_4O_{10}(OH)_2$). As a result of the acid column leaching of limonitic laterite with the use H_2SO_4 solution, gypsum was also detected in the leaching residues (LR).
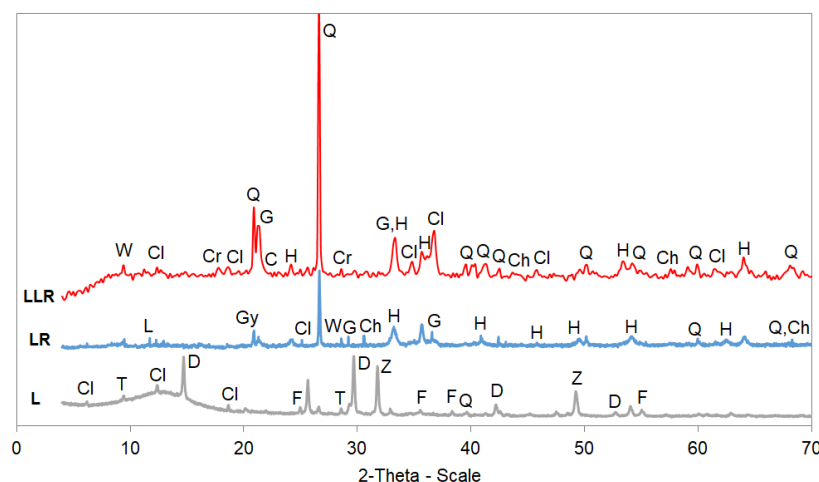
Figure 4.3. XRD patterns of leaching residues of laterites, namely L, LR and LLR. Phases identified are: calcite (C), chromite (Ch), clinochlore (Cl), cryptomelane (Cr), diopside (D), fayalite (F), goethite (G),gypsum (Gy), hematite (H), lizardite (L), talc (T), quartz (Q), willemseite (W), zincite (Z).

4.1.3   FTIR Analysis

The FTIR spectra, over the range 4000-400 cm^{-1}, of PS, LS and FS, FSP slags are illustrated in Figures 4.4 and 4.5, respectively. It is observed that the peak at 472 cm^{-1} in PS is ascribed to the overlapping Si-O-Si and O-Mg-O bending vibrations (Bakharev, 2005; Yang et al., 2014) as shown in Figue 4.4. In line with the XRD data, the bands observed at 828 cm^{-1}, 872 cm^{-1} and 948 cm^{-1} in PS are characteristic peaks of Ca-Fe-Mg-silicate-based slags dominated by fayalite, diopside and hedenbergite (Marangoni et al., 2016; Nazer et al., 2016; Onisei et al., 2018; Peys et al., 2018; Rincón et al., 2018). The first band results from the v1 mode (symmetric stretch), while the others correspond to the asymmetric stretching vibrations of SiO_4 (v3 mode). An additional peak is seen at 668 cm^{-1}, which is associated with the stretching vibrations of Si-O bands of diopside (Zong et al., 2018). The weaker band at 1634 cm^{-1} in PS belongs to the characteristic bending vibrations of H-O-H (Bernal et al., 2015; Liu et al., 2017; Palomo et al., 1999), whereas the band at 3744 cm^{-1} is typical for the OH- stretching region. Concerning the LS slag and in line with XRD results, the narrow band at 505 cm^{-1} is typical of Fe-O stretching vibrations and it is due to the presence of magnetite in raw LS (Muthuvel et al., 2019). The major band observed at 961 cm^{-1} represents the Si-O asymmetric stretching vibrations with its wide broadness indicating the high glassy/vitreous content present in LS slag (Chen et al., 2020; Komnitsas et al., 2009); this band is also observed in FS slag (Figure 4.5). Two narrow bands at 2845 and 2918 cm^{-1} are typical of symmetric and asymmetric -CH_2- stretching vibrations, respectively (Li et al., 2019), while the broad band at 3423 cm^{-1} is ascribed to the presence of water, due to the stretching vibration of O-H bonds (Maragkos et al.,

2009). On the other hand, the band at 457 cm^{-1} in the FS slag is characteristic of fayalitic slags and corresponds to in plane Si-O bending and Al-O linkages as well as bending Si-O-Si and O-Si-O vibrations, as shown in Figure 4.5 (Komnitsas et al., 2013, 2015; Yip et al., 2008). In the same Figure, the peak seen at 575 cm^{-1} in the FS slag is ascribed in the stretching vibrations of T-O-T (T=Si, or Al) bonds, while the bands at 689 cm^{-1} in the FS and 876 cm^{-1} in the FSP are attributed to the bending modes of CO_3^{-2} (Komnitsas et al., 2019a, 2019b). The two bands at 1525 cm^{-1} and 2370 cm^{-1} in the FSP slag are attributed to the atmospheric carbonation (Gao et al., 2014; Komnitsas et al., 2015). Finally, the broad band seen at 1382 cm^{-1} in the FS slag is ascribed to the presence of water, due to bending vibrations of O-H bonds (Maragkos et al., 2009).
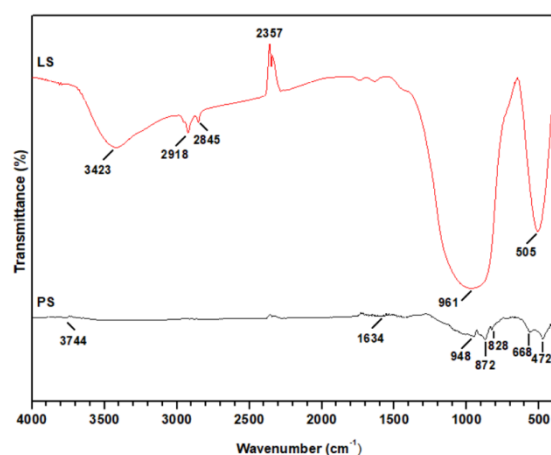
Figure 4.4. FTIR spectra of FeNi slags, namely PS and LS.
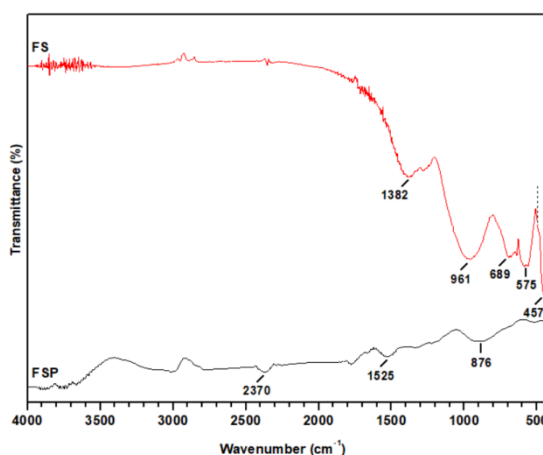
Figure 4.5. FTIR spectra of fayalitic slags, namely FS and FSP.

Figure 4.6 shows the FTIR spectra of all laterite leaching residues. In this case and in line with XRD results (Figure 4.3), the bands at 460 cm^{-1}, 694 cm^{-1}, the double bands at 778 cm^{-1} and 796 cm^{-1}, as well as at 1086 cm^{-1} and 1145 cm^{-1} are characteristic bands attributed to quartz (Criado et al., 2016), while the small bands at 528 cm^{-1} and 910 cm^{-1} are attributed to hematite and goethite, respectively (Komnitsas et al., 2018, 2019b; Lemougna et al., 2017). The band at 460 cm^{-1} seen in all leaching residues is attributed to the bending motions of the Al- and Si-containing phases (Komnitsas et al., 2018; Lemougna et al., 2017). The bands seen at 1086 cm^{-1} and 1102 cm^{-1} in LR residues, 1096 cm^{-1} in L residues and 1108 cm^{-1} in LLR residues correspond to asymmetric stretching vibrations of the silicate tetrahedral network (Komnitsas et al., 2018). In addition, the band present in L residues at 2917 cm^{-1} is assigned to hydrocarbon stretches, while the small bands at 3546 cm^{-1} and 3607 cm^{-1} can be attributed to Fe^{3+}-OH-Fe^{3+} stretching and deformation vibrations (Komnitsas et al., 2018). Finally, the two bands shown at 600 and 650 cm^{-1} in the L residues can be assigned to the formation of calcium-based sulfates, as also indicated by the XRD pattern (Figure 4.3) (Komnitsas et al., 2019b).
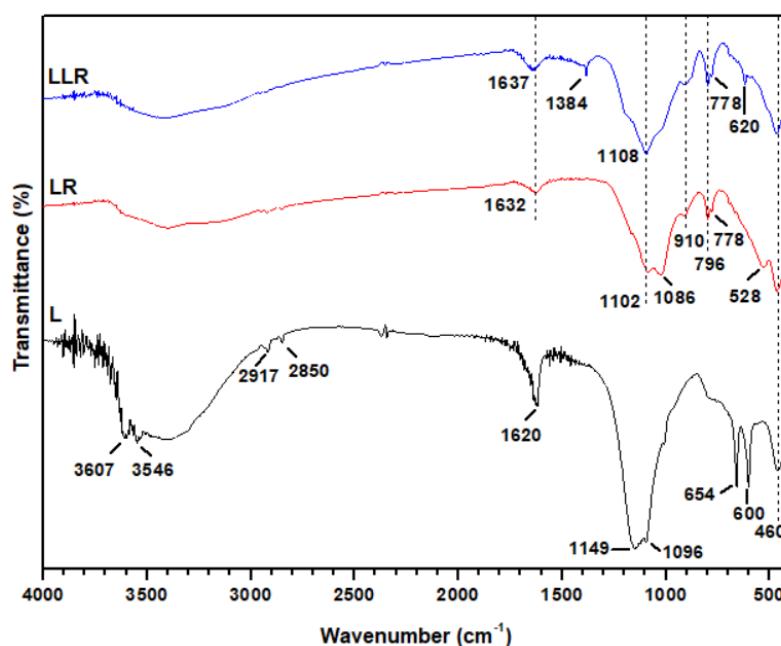
Figure 4.6. FTIR spectra of laterite leaching residues, namely L, LR and LLR.

4.2 Factors affecting valorization of PS slag for the production of AAMs

This section presents the valorization potential of PS slag for the production of AAMs. Selected factors affecting the compressive strength and other properties as well as the structural integrity, morphology and microstructure of the produced AAMs are discussed. More data on this topic are provided in a recent paper (Komnitsas et al., 2019a).

4.2.1 Effect of H_2O/Na_2O molar ratio in the activating solution and curing temperature on the compressive strength of the produced AAMs

Figure 4.7 presents the compressive strength of the produced AAMs after curing for 24 h and ageing for 7 days as a function of H_2O/Na_2O molar ratio in the activating solution and curing temperature (40 or 80 °C). The SiO_2/Na_2O molar ratios in the activating solution are slightly different, and depend on the H_2O/Na_2O ratios used. It also mentioned that the d_{90} (90 % passing) of PS slag used was 57.5 μm (Table 3.1). It is observed that the effect of temperature does not significantly affect the compressive strength for all H_2O/Na_2O ratios tested; this indicates that the process is energy efficient, in terms of heating requirements. It is known that in most cases, the higher curing

temperature accelerates the rate of reactions between the precursors and the activating solution, improves condensation and re-solidification so that more aluminosilicate bonds are formed and a better microstructure is developed, thus a matrix with beneficial mechanical properties is formed, as indicated in earlier studies (Soultana et al., 2019; Zaharaki et al., 2016). It is also known from previous studies that consideration is necessary in order to avoid fast evaporation of water during curing at higher temperature, otherwise incomplete alkali activating reactions are anticipated (Gebregziabiher et al., 2016; Sindhunata et al., 2006; Yuan et al., 2016).
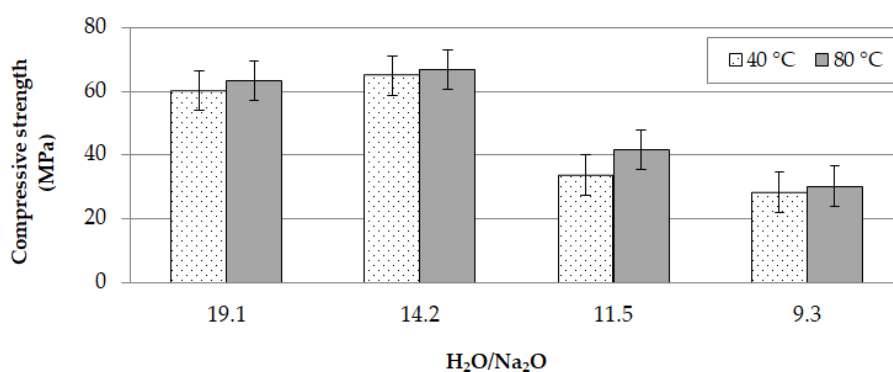
Figure 4.7. Effect of H_2O/Na_2O molar ratio in the activating solution and curing temperature on the compressive strength of the produced the AAMs (pre-curing and curing time 24 h, ageing period 7 days; error bars indicate the standard deviation of measurements obtained from three specimens).

On the other hand, the compressive strength of the produced AAMs increases slightly and reaches the maximum value, i.e. 67.0 MPa, when the H_2O/Na_2O ratio in the activating solution decreases from 19.1 to 14.2; it then drops substantially when lower H_2O/Na_2O ratios are used. It is well known that the low ratios indicate high alkalinity and that OH- ions may remain unreacted and result in the production of specimens with lower strength, while high ratios may indicate either deficiency of OH- ions or excess of water which may also remain unreacted under specific synthesis conditions, as mentioned earlier (section 2.4). However, several studies have reported that an optimum H_2O/Na_2O ratio exists and depends in each case on the mineralogy of the precursor and the rate of the reactions between the raw material and the alkaline solution (Azevedo and Strecker, 2017; Komnitsas et al., 2015; Mo et al., 2017; Soultana et al., 2019). It is also noted that the weight loss of the specimens during curing at 80 ºC, increases from 1.9 % to 3.5 % when lower H_2O/Na_2O ratios are used in the activating solution. Overall, from these results it is concluded that the H_2O/Na_2O ratio in the activating solution is a more important factor compared to the curing temperature during AAMs synthesis.

4.2.2 Effect of particle size on the compressive strength and selected properties of the produced AAMs

Three different particle sizes of PS slag were selected in order to investigate their effect vs. curing temperature on the properties of the produced AAMs. The particle sizes of PS slag studied are presented in Table 3.1, while the other AAMs synthesis conditions were H_2O/Na_2O and SiO_2/Na_2O molar ratios in the activating solution 14.2 and 0.3, respectively, curing time 24 h, ageing period 7 days and constant liquid to solid (L/S) ratio at 0.25; more details are provided in a recent study (Petrakis et al., 2019). It was also observed that the setting time of the paste ranges between 3 and 9 h for the different grinding products tested. The finer particles react faster with the activating solution due to their larger specific surface area and thus the paste requires much shorter setting time compared to the paste consisting of coarser particles (Traven et al., 2019). Figure 4.8 shows the compressive strength of the AAMs produced as a function of particle size and curing temperature (60 or 80 °C). It is seen from this data, that the compressive strength increases from 7.9 to 26.2 MPa (~230 % increase) when the particle size decreases from 154.0 μm to 47.0 μm after curing at 60 °C. Regarding the curing temperature, it is observed that it significantly and positively affects the compressive strength for all particle sizes tested. In particular, when the curing temperature increases to 80 °C and the particle size decreases from 154.0 μm to 47.0 μm, the compressive strength of the produced AAMs increases from 20.2 MPa to 60.8 MPa (~200 % increase).
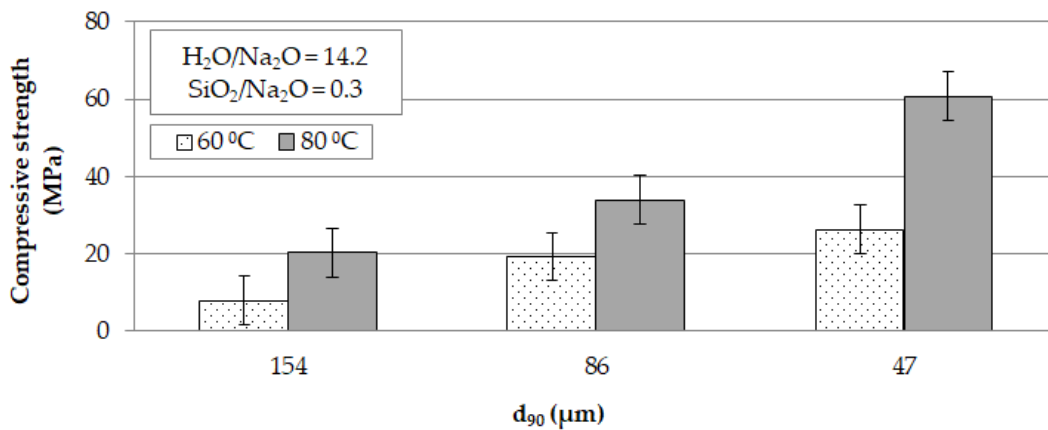
Figure 4.3. Effect of the particle size of PS and curing temperature on the compressive strength of the produced AAMs (curing time 24 h, ageing period 7 days, particle sizes of 154.0, 86.0, 47.0 μm; error bars denote standard deviation of measurements obtained from three specimens.

Other selected properties of the produced AAMs obtained when three different particle sizes were used, namely, apparent density (g cm^{-3}), porosity (%), and water absorption (%) are presented in Table 4.2. This Table also shows the compressive strength of the AAMs produced under the optimum synthesis conditions. It can be seen that all properties vary, however, the main difference was observed for porosity which decreased from 13.5 to 6.7 % with the decrease of the PS slag particle size from 154.0 μm to 47.0 μm, indicating that this property may have a significant effect on the compressive strength of the produced AAMs. A similar trend was also observed for water absorption which decreased from 5.9 to 3.8 % by taking into account the same particle sizes. On the other hand, the apparent density of the AAMs increased from 2.28 to 2.54 g cm^{-3} when the particle size of slag decreased from 154.0 μm to 47.0 μm. Based on these results, it is concluded that when the raw materials are finer, the produced AAMs are denser and stronger. It is mentioned that the shrinkage of AAMs after curing at 60 °C or 80 °C was negligible. Another explanation of the results regarding the alkali activation of slag, when different particle sizes are used, may be due to their different reactivity since higher dissolution of Si and Al takes place when finer particles react and thus higher Si/Al ratios are present in the alkaline solution and participate in alkali activation reactions (Table 4.1). Therefore, the reactivity may predict the magnitude of the anticipated compressive strength values.

Table 4.2. Selected properties of PS-based AAMs produced under the conditions 14.2 H$_2$O/Na$_2$O, curing temperature 80 °C, curing time 24 h, ageing period 7 days.

AAM Code	Particle size, d$_{90}$ (μm)	Compressive Strength (MPa)	Apparent Density (g cm^{-3})	Porosity (%)	Water Absorption (%)
PS30	154.0	20.2	2.3	13.5	5.9
PS60	86.0	33.8	2.4	10.6	4.5
PS120	47.0	60.8	2.5	6.7	3.8

Finally, the effect of pre-curing, curing and ageing period on the compressive strength of the produced AAMs was also investigated and the results are presented in detail in a previous recent study (Komnitsas et al., 2019a). It is mentioned that the ageing period practically did not affect the compressive strength of the produced AAMs, while the longer curing time, when high H$_2$O/Na$_2$O ratio and temperature was used, had an adverse effect on the compressive strength.

4.2.3   Structural Integrity of AAMs

The structural integrity of PS-based AAMs produced was investigated after firing them for a period of 6 h, at a temperature range of 200-1000 ^{o}C (Figure 4.9) and after immersion in distilled water (H$_2$O), 1 M HCl and 1 M H$_2$SO$_4$ for 7, 15 and 30 days (Figure 4.10). The AAMs used were produced under the optimum conditions, namely particle size of PS, 57.5 μm (90 % passing); H$_2$O/Na$_2$O ratio, 14.2; SiO$_2$/Na$_2$O ratio, 0.3; curing temperature, 80 ^{o}C; pre-curing and curing time, 24 h; ageing period, 7 days. Control specimens were also tested for comparison. In addition, Table 4.3 shows the evolution of compressive strength (MPa), as well as some selected properties, namely shrinkage (%), weight loss (%) and apparent density (g cm^{-3}) after firing PS-based AAMs at 200, 400, 600, 800 and 1000 ^{o}C for 6 h.

Figure 4.9 shows that the integrity of AAMs after firing them up to 400 ^{o}C is very good since the compressive strength increases substantially, from 90.2 to 115.2 MPa whereas it decreases sharply after firing at higher temperature. Similar behavior has also been observed in a previous study (Onisei et al., 2015), which indicates that the fayalitic slag-based AAMs exhibited after firing at 500 ^{o}C an increase in compressive strength by almost 30 % to 105 MPa, regardless of the addition of 5 % or 10 % analytical grade Al$_2$O$_3$ in the initial mixture. In this case, the formation of new phases, including laihunite due to oxidation of fayalite, sodium aluminum silicate (NaAlSiO$_4$), hematite, magnetite and spinel hercynite (FeAl$_2$O$_4$), resulted in increase of compressive strength. However, in our case and in line with XRD data (Figure 4.11d), no new visible major mineralogical phases in AAMs fired at 400 ^{o}C were detected, whereas the increase in compressive strength could be attributed to the increase in the quantity of several phases (Figure 4.11d). The compressive strength of the AAMs after firing at 1000 ^{o}C was extremely low, while the specimens showed a volumetric expansion of 7.1 % (Table 4.3) and were severely damaged. Zaharaki et al. (2010) mention that firing at very high temperatures results in a sharp drop in compressive strength, due to dehydroxylation of silanol (Si-OH) and aluminol (Al-OH) groups that causes development of cracks and pores. An earlier study (Duxson et al., 2007d) reported that the increase of shrinkage occurs stepwise in four temperature regions. More specifically, in Region I, at temperatures below 100 ^{o}C, the increase in shrinkage is attributed to the release of free water. Then, in Region II, between 100-250 ^{o}C, shrinkage occurs due to pore water released from the formed gel, whereas in Region III between 250-600 ^{o}C, due to the loss of bound hydroxyls, and in Region IV, at a higher temperature than 700 ^{o}C, due to a viscous sintering-like process.
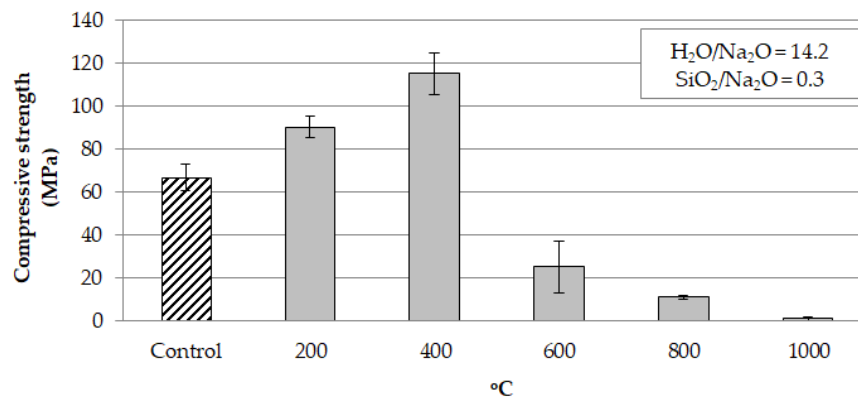
Figure 4.9. Compressive strength of selected AAMs after firing between 200 and 1000 °C for 6 h; synthesis conditions: pre-curing and curing time 24 h, curing temperature 80 °C, ageing period 7 days; the compressive strength of control AAM was determined after ageing period of 7 days; error bars indicate the standard deviation of measurements obtained from three specimens.

Other factors that contributed to the increase in strength after firing at 400 °C are the volumetric shrinkage by 4.8 % (Table 4.3), which is the highest at this temperature, and the increase in density to 2.7 g cm^{-3}. These properties were not determined for the AAMs fired at 1000 °C, since as mentioned earlier, they suffered severe damage. The increase in strength of the AAMs produced after firing at 400 °C is a very important finding and shows that they can be potentially used as fire-resistant materials and replace or coat concrete in specific construction applications, as for example in tunnels, thus allowing more time for rescue teams to intervene in case of fire (Komnitsas et al., 2019a). Similar, but noticeably smaller increase was also reported in earlier studies investigating the potential of a Greek ferronickel slags for the production of AAMs (Zaharaki and Komnitsas, 2012; Zaharaki et al., 2010).

Table 4.3. Selected properties of the fired PS-based specimens.

Temperature (°C)	Compressive strength (MPa)	Shrinkage (%)	Mass Loss (%)	Apparent Density (g cm^{-3})
200	90.2	4.0	5.1	2.2
400	115.2	4.8	7.3	2.7
600	25.2	3.6	9.6	2.0
800	10.9	2.2	10.2	1.8
1000	2.0	-7.1	ND*	NM

* ND: Not Determined

On the other hand, as seen in Figure 4.10, the AAMs after immersion in distilled water, 1M HCl and 1M H_2SO_4 solutions exhibit also good behavior for a period of 7, 15 and 30 days. The compressive strength of control specimens is also provided for comparison. More specifically, it is seen that the immersion of specimens in distilled water, even for a long period of 30 days, has a relatively minor effect on their compressive strength. Also, the specimens retain very good strength, varying between 33.8 MPa and 36.5 MPa, when immersed in 1M HCl and 1M H_2SO_4 solutions for a period of 30 days. The maximum mass loss of the specimens immersed in distilled water, H_2SO_4 and HCl solutions was 0.9 %, 3.2 % and 5.6 % respectively, which is considered as low to very low in all cases. It is also mentioned that the final pH of the solutions containing distilled water, HCl and H_2SO_4 after immersion of the specimens for 30 days was 11.0, 2.7 and 1.7 respectively. These results indicate that the AAMs respond well and exhibit very good structural integrity in aggressive environments.
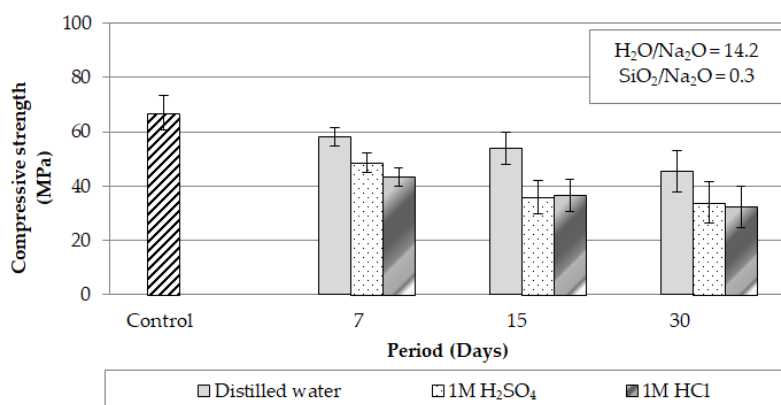
Figure 4.10. Compressive strength of selected AAMs after immersion in distilled water or acidic solutions for a period of 7 to 30 days; synthesis conditions: pre-curing and curing time 24 h, curing temperature 80 °C, ageing period 7 days; the compressive strength of control AAM was determined after ageing period of 7 days; error bars indicate the standard deviation of measurements obtained from three specimens.

4.2.4 Morphology–Microstructure of raw PS and selected PS-based AAMs

Figure 4.11 presents the XRD patterns of selected AAMs, namely the control AAMs, which were produced under the optimum symthesis conditions (i.e. H_2O/Na_2O, 14.2; SiO_2/Na_2O, 0.3; curing temperature, 80 °C; pre-curing and curing time, 24 h; ageing period, 7 days) as well as of those immersed in 1 mol L^{-1} HCl for 30 days or fired at 400 °C for 6 h, and the patterns of the raw PS for comparison. It is seen that no new visible major mineralogical phases for the selected AAMs were detected. However, the intensities of mineralogical phases of fayalite, hedenbergite and diopside increased in the

AAMs after firing at 400 °C and this may explain the noticeable increase of its compressive strength.
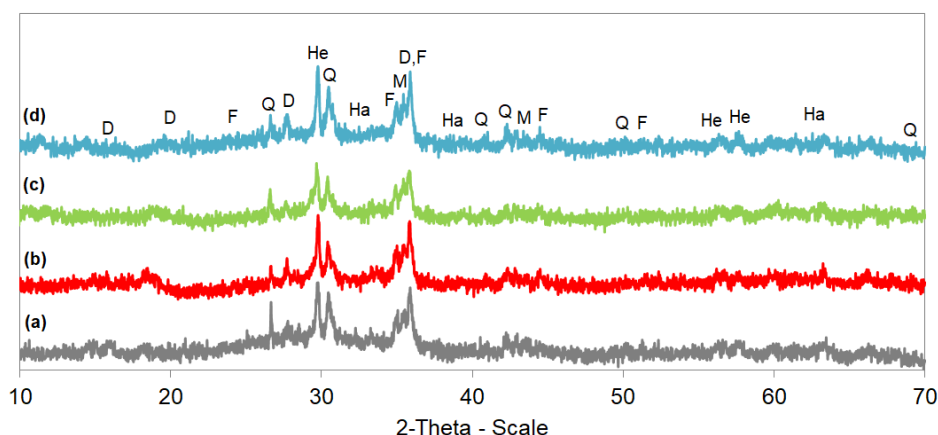
Figure 4.11. XRD pattens of **(a)** raw PS **(b)** AAM control, **(c)** AAM after immersion in 1M HCl for 30 days and **(d)** AAM after firing at 400 °C for 6 h. Phases identified are: diopside (D), fayalite (F), hatrurite (Ha), hedenbergite (He), magnetite (M), quartz (Q).

Figure 4.12 presents the FTIR spectra of selected AAMs, namely the control AAM, which was produced under the optimum synthesis conditions (i.e. H_2O/Na_2O, 14.2; SiO_2/Na_2O, 0.3; curing temperature, 80 °C; pre-curing and curing time, 24 h; ageing period, 7 days) as well as of those immersed in 1M HCl for 30 days or fired at 400 °C for 6 h, and the pattern of the raw PS for comparison. The peak seen at 472 cm^{-1} in the control AAM is ascribed to the overlapping Si-O-Si and O-Mg-O bending vibrations (Bakharev, 2005; Yang et al., 2014). It is seen that this band disappears after firing at 400 °C (Figure 4.12d), thus indicating that phase transformations took place and resulted in the increase of the compressive strength. The strong single peak at 1016 cm^{-1} shown in the control AAM (Figure 4.12b) reveals the formation of reaction products after exposure of AAMs to highly alkaline solution (Komnitsas et al., 2009, 2019b; Mužek et al., 2012). The structural reorganization as result of the alkaline activation is more noticeable by the broader bands shown in the same region (800-1200 cm^{-1}) for the AAMs immersed in HCl solution or fired at 400 °C (Figure 4.12c,d, respectively). The sharper peaks seen at 1650 cm^{-1}, 1636 cm^{-1} and 1644 cm^{-1} in selected AAMs (Figure 4.12b-d) belong to the characteristic bending vibrations of H-O-H (Bernal et al., 2015; Liu et al., 2017; Palomo et al., 1999). The intense absorption bands at ~1410 cm^{-1} and ~1490 cm^{-1} shown only in the AAMs are attributed to stretching vibrations of O-C-O bonds due to carbonation of the remaining Na-silicate (Abdullah et al., 2012; Liu et al., 2017). Finally, the bands observed in raw PS and control AAM at 3744 cm^{-1} and 3756 cm^{-1}, respectively (Figure 4.12a,b) are typical for the OH-stretching region, as previously mentioned. However, the presence of water is more evident in all AAMs since a quite wide absorption band region appeared between 3000

cm^{-1} and 3700 cm^{-1} belonging to stretching vibrations of OH groups (Rincón et al., 2018), due to the hydration processes that took place during alkali activation.
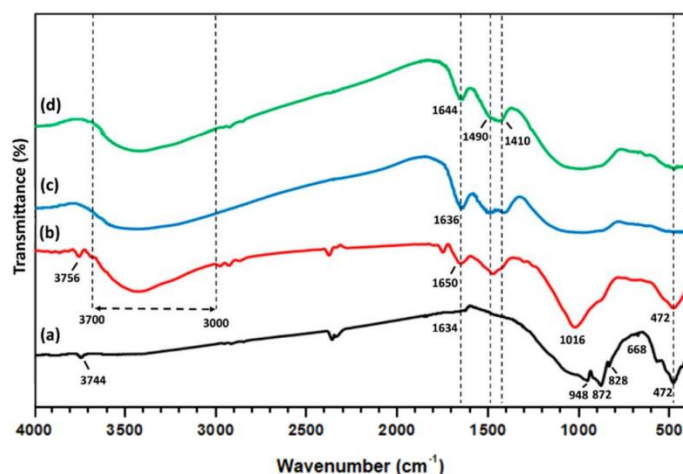
Figure 4.12. FTIR spectra of **(a)** raw PS **(b)** AAM control, **(c)** AAM after immersion in 1M HCl for 30 days and **(d)** AAM after firing at 400 °C for 6 h.

As shown in XRD analysis, SEM examination of the PS surface by SEM/EDS (Figure 4.13a) revealed a glassy morphology with sharp edges that is heterogeneous in size and dominated by large quartz, diopside and weathered fayalite crystals (>50 m long) along with small spherical grains (<15 μm) of magnetite. According to EDS point analyses, other (inter)metallic phases such as chromite ($FeCr_2O_4$) and awaruite (Ni_3Fe) were also detected in minor quantities as small single intergrown drops and inclusions, respectively (Kierczak et al., 2009). Furthermore, several parallel laths/seams of Cr-spinel (~2 m thick) embedded in clinopyroxene (diopside) matrix were identified containing up to 5.2 % Cr.

After alkali activation of slag under the conditions of H_2O/Na_2O 14.2, SiO_2/Na_2O 0.3, curing temperature 80 °C, pre-curing and curing time 24 h and ageing period 7 days (control AAM) (Figure 4.13b) or firing at 400 °C (Figure 4.13c,d), a moderate to highly homogenous and dense glassy matrix (dark color) is formed between PS grains (bright color) and observed in the geopolymeric gel for both AAMs produced. The geopolymeric gel in the control AAM displayed a quite smooth surface mostly comprised of unreacted/unaffected quartz particles and an inorganic matrix (P1) containing Ca, Al, Si, Fe, Mg and Na, provided from the alkaline activator or solubilised from PS slag. As a result of the NaOH solution attack in the slag, deterioration of reacted diaspore, fayalite and chromite particles is clearly observed. In addition, based on elemental analysis, several Ni-Fe sulfides grains scattered/dispersed and aggregated in the geopolymeric matrix were found containing up to 60 % Ni. A higher magnification image of a Ni-Fe sulfide grain shown in Figure 4.13b, indicates that awaruite (Ni_3Fe) occurs as inclusion along with Ni_3S_2 within the mixed Ni-Fe sulfide matrix. Regarding the AAM produced

47

after firing at 400 °C, SEM analysis indicated a more homogenous structure filled with aggregated slag particles smaller in size (~10 μm) compared to the control AAM. This evidence is the synergistic result of alkaline solution attack along with the oxidation of PS after firing at 400 °C (Komnitsas et al., 2019a).
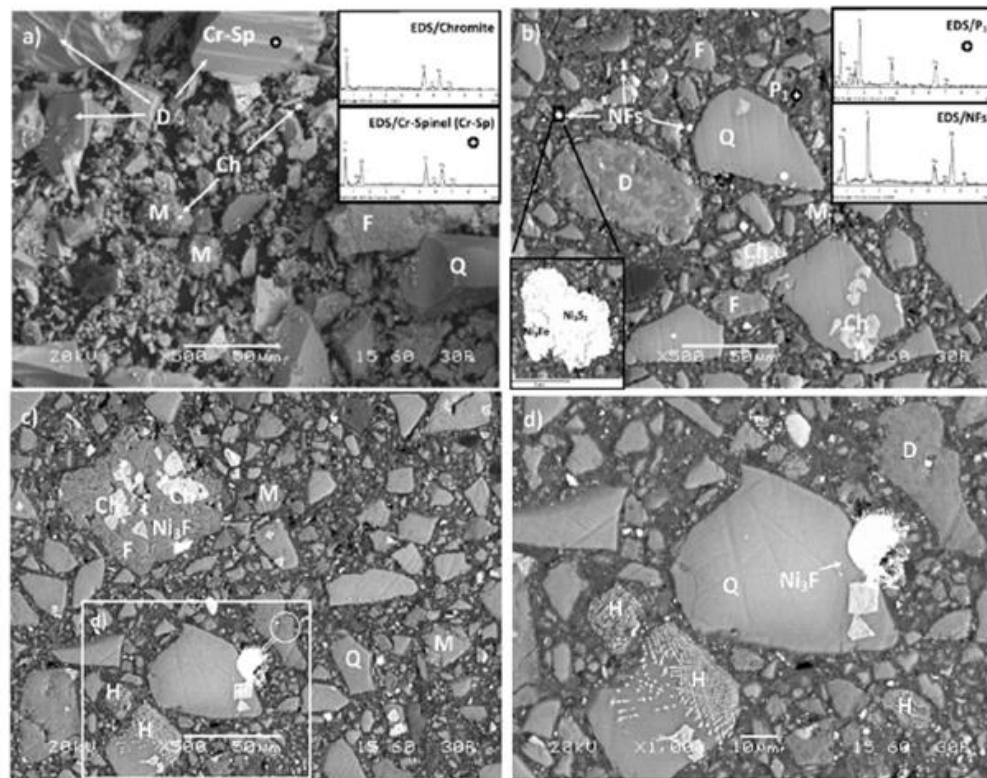
Figure 4.13. Back-scattered electron images of **(a)** raw PS surface and cross-sections of selected AAMs after **(b)** alkali activation with H_2O/Na_2O 14.2 and **(c,d)** firing at 400 °C. EDS spectra show in several spot locations the presence of inter (metallic) phases, the formation of mixed aggregates and newly formed phases (Q: Quartz, D: Diaspore, F: Fayalite, M: Magnetite, H: Hematite, NFs: Ni-Fe sulfides, Ch: Chromite, Cr-Sp: Cr-Spinel).

4.2.5 Toxicity of AAMs

The toxicity of the raw PS, control AAM and control AAM after firing at 400 °C was assessed according to the EN 12457-3 test. The dissolution rates of the metals were expressed as mg kg^{-1} and compared with existing limits for disposal of wastes in various landfill types; these limits are presented in Table 4.4. The raw PS exhibited reasonable toxicity in terms of Ni (6.3 mg kg^{-1}) and slight for total Cr (0.6 mg kg^{-1}), by considering its chemical and mineralogical analyses (Kierczak et al. 2009). On the other hand, the control

AAM exhibited no toxicity at all since the dissolution rates of all heavy metals were below the lower limits, which are indicated by the EN 12457-3 test for wastes accepted at landfills for inert wastes. However, the control AAM after its firing at 400 °C exhibited an increase in the dissolution rates of Ni, As and total Cr, namely 2.2, 1.2 and 2.4 mg kg^{-1} respectively, exceeding the lower limit values indicated by the EN 12457-3 test (Table 4.4) (EN 12457-3:2002; Van der Sloot et al., 2001). So, the alkali activation not only contributes to the production of AAMs with high compressive strength but also binds or traps potentially hazardous elements in a stable matrix and thus reduces their dissolution rate and overall toxicity (Komnitsas et al., 2013). More information on toxicity is presented in a previous recent study (Komnitsas et al., 2019a).

Table 4.4. Limit values for disposal of wastes in various landfill types.

Element	*Limit values* *			
	For wastes accepted at landfills for inert wastes	For non hazardous wastes	For hazardous wastes accepted at landfills for non-hazardous wastes	For wastes accepted at landfills for hazardous wastes
	mg kg^{-1}			
Al				
Cr	0.5	10	10	50
Mn				
Fe				
Ni	0.4	10	10	40
Cu	2	50	50	100
Zn	4	50	50	200
As	0.5	2	2	25
Mo	0.5	10	10	30
Cd	0.04	1	1	5
Pb	0.5	10	10	50

* Council Decision 19 December 2002 (2002/33/EC). Note: Shaded parts indicate elements that exceed specific limits.

4.2.6   Conclusions

The experimental results show that the PS-based AAMs produced under the optimum conditions, namely H$_2$O/Na$_2$O ratio 14.2 in the activating solution, SiO$_2$/Na$_2$O ratio 0.3 in the activating solution, curing temperature 80 °C, pre-curing and curing time 24 h and ageing period 7 days, acquired high compressive strength exceeding 65.0 MPa. An interesting aspect during alkali activation of this slag is that in the reactive paste the wt% addition of Na$_2$SiO$_3$ and the overall L/S ratio were very low, 3 % and ~20 %, respectively. Therefore, the AAMs were produced using a mixture containing a high percentage of

solids and limited addition of chemicals, thus the alkali activation in this case can be characterized as a cost-effective process.

The results also indicate that the compressive strength of the produced AAMs is significantly affected by the slag particle size used. The finer particles of the raw slag have larger surface area and react faster with the activating solution, thus the produced AAMs acquire higher compressive strength. The determination of selected properties of the produced AAMs revealed that porosity and water absorption decreased when the slag particle size decreased, indicating that these properties also affect the compressive strength. As expected, the apparent density (g cm^{-3}) showed an inverse trend. The AAMs produced under the optimum conditions exhibit good structural integrity after firing for 6 h at high temperatures and after immersion in distilled water or acidic solutions (1M HCl and 1M H$_2$SO$_4$).

A novel aspect of this investigation is the increase of the compressive strength of the AAMs after firing at 400 ^{o}C for 6 h, due to phase transformations and the development of a dense and compact structure filled with inclusions of inter (metallic) phases. This behavior indicates that the produced AAMs have beneficial properties and can find several applications in the construction sector, i.e as fire-resistant materials. Finally, the produced AAMs exhibit very low toxicity. So, alkali activation results in the immobilization of hazardous elements present in the raw slag, and thus no adverse effects are anticipated from the use of AAMs.

4.3 Factors affecting co–valorization of FS, FSP and LS slags for the production of AAMs

This section discusses the co-valorization of FS, FSP and LS slags for the production of AAMs. Selected factors affecting the compressive strength and other properties as well as the structural integrity, morphology and the microstructure of produced AAMs are investigated. More results are provided in a recent study (Komnitsas et al., 2020).

4.3.1 Effect of H$_2$O/Na$_2$O molar ratio in the activating solution and ageing period on the compressive strength of the produced AAMs

Figure 4.14 shows the compressive strength of the AAMs produced from FS slag (Figure 4.14a) and FSP slag (Figure 4.14b), after curing at 90 ^{o}C for 24 h, as a function of H$_2$O/Na$_2$O molar ratio in the activating solution and ageing period. The SiO$_2$/Na$_2$O molar ratio in the activating solution was kept constant at 1.0. As seen in Figure 4.14a, the compressive strength of FS-based AAMs decreases from 26.5 MPa to 14.8 MPa, when the

H_2O/Na_2O ratio in the activating solution decreases from 21.6 to 14.8, while the ageing period, between 7 to 28 days, has only a minor beneficial effect on the compressive strength of the produced AAMs. The maximum compressive strength (28.0 MPa) was recorded when the H_2O/Na_2O ratio was 21.6 after a curing period of 28 days. On the other hand, the decrease in H_2O/Na_2O ratio from 19.5 to 11.5 resulted in a noticeable increase in the compressive strength of the produced FSP-based AAMs (Figure 4.14b). On the other hand, when the H_2O/Na_2O ratio decreased to 11.9, the maximum compressive strength recorded was 19.5 MPa. It is noted that the SiO_2/Na_2O molar ratio in alkaline solution was kept constant at 0.4. As in the previous case, the effect of the ageing period was negligible. The H_2O/Na_2O ratios play major role during alkali activation, as already mentioned. The FS-based AAMs exhibit better alkali activation potential and this may be explained by considering their mineralogy as well as the leaching of Si and Al from the raw materials in alkaline conditions (Table 4.1). As seen in Table 4.1, FS exhibits higher activation potential since its Si/Al ratio in the alkaline solution is more than two times higher compared to the respective ratio obtained after leaching of FSP slag. It is also possible that the reactivity of FSP slag was reduced after plasma treatment.
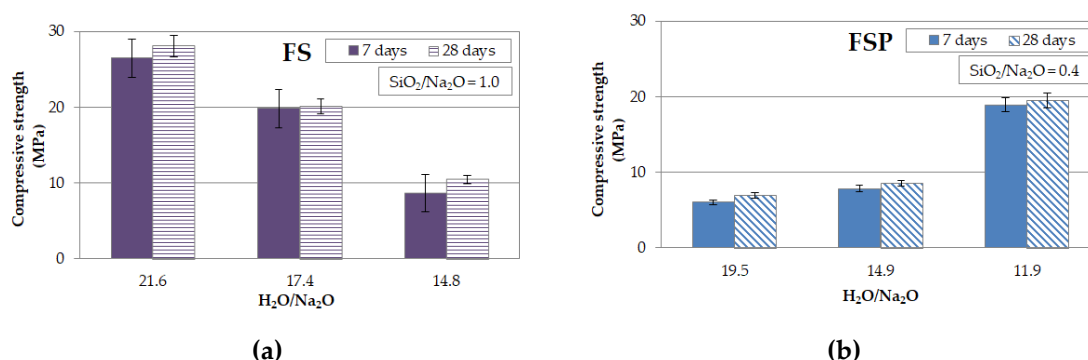
Figure 4.14. Effect of H_2O/Na_2O molar ratio in the activating solution and ageing period on the compressive strength of **(a)** FS- and **(b)** FSP-based AAMs (pre-curing time 6 h, curing temperature 90 °C, curing time 24 h; error bars indicate the standard deviation of measurements obtained from three specimens).

Finally, the effect of curing temperature (40, 60 and 90 °C) and SiO_2/Na_2O molar ratio in the activating solution on the compressive strength of the produced AAMs was also investigated and the results are presented in detail in a previous recent study (Komnitsas et al., 2020). It is noted that curing temperature has a major beneficial effect on the compressive strength of the AAMs produced from both slags, which increases by more than 5 times with the increase of temperature from 40 to 90 °C. On the other hand, the

decrease of SiO_2/Na_2O ratio resulted in the decrease of compressive strength of the AAMs produced from both slags. The maximum values of the compressive strength obtained were 44.8 MPa for the FS-based AAMs produced using H_2O/Na_2O ratio 22.5 and SiO_2/Na_2O ratio 1.5, whereas for FSP-based AAMs, the maximum compressive strength was 27.2 MPa when the H_2O/Na_2O ratio was 14.6 and the SiO_2/Na_2O 0.9. In both cases, the other synthesis conditions were: pre-curing time 6 h, curing temperature 90 °C for 24 h, ageing period, 7 days.

4.3.2   Potential of co–valorization of FS, FSP and LS slags

In order to assess the potential of slag co-valorization through alkali activation, precursors obtained by mixing FS and FSP slags with different ratios of LS slag were used, since as mentioned earlier (Table 4.1), LS exhibits higher reactivity during alkali activation. Figure 4.15 presents the compressive strength obtained for specimens produced by mixing FS with LS at ratios 10:90, 30:70, 40:60 and 50:50. The synthesis conditions used for the alkali activation of the mixtures were pre-curing time 6 h, curing time 24 h, curing temperature 90 °C and ageing period 7 days. The ratios H_2O/Na_2O and SiO_2/Na_2O in the activating solution were 17.4 and 1.0, respectively. In the same Figure the compressive strength of control specimens produced after alkali activation of each slag, namely FS and LS, are also given for comparison.

Figure 4.15. Effect of mixing proportions of FS and LS on the compressive strength of FSLS-based AAMs (pre-curing time 6 h, curing temperature 90 °C, curing time 24 h, ageing period 7 days; error bars indicate the standard deviation of measurements obtained from three specimens).
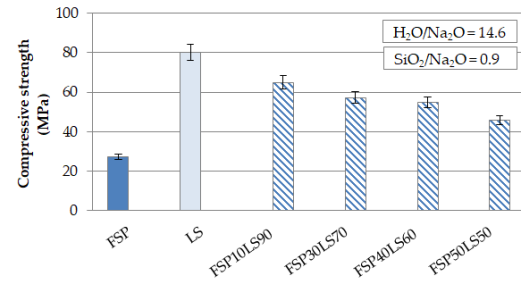
Figure 4.16. Effect of mixing proportions of FSP and LS on the compressive strength of FSPLS-based AAMs (pre-curing time 6 h, curing temperature 90 °C, curing time 24 h ageing period 7 days; error bars indicate the standard deviation of measurements obtained from three specimens).
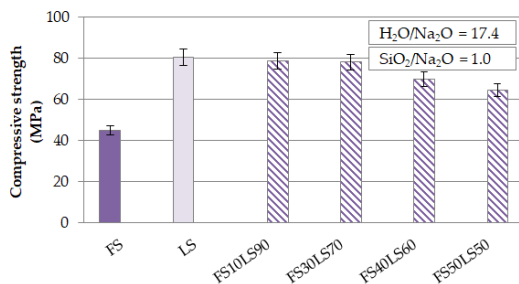
Experimental results prove the beneficial effect of LS addition in the initial mixture on the subsequent alkali activation, given that the AAMs produced after alkali activation of LS acquire a compressive strength of 80.0 MPa. It is seen that the specimens produced after alkali activation of all combinations examined acquire very high compressive strength which reaches 64.3 MPa also in the case when the mixing ratio FS:LS is 50:50. This value is almost 70 % higher compared to the value recorded for the AAM produced using only FS as precursor. It is also important to mention that almost no loss of strength is noted for the specimens produced from FS:LS mixing ratios 10:90 and 30:70. Figure 4.16 presents the compressive strength obtained for specimens produced by mixing FSP with LS at ratios and synthesis conditions similar as in the previous case. In the same Figure the compressive strength of control specimens produced after alkali activation of each slag, namely FSP and LS, are also given for comparison. The ratios H_2O/Na_2O and SiO_2/Na_2O in the activating solution were 14.6 and 0.9, respectively. Experimental results also in this case prove the beneficial effect of LS addition in the initial mixture on the subsequent alkali activation. It is seen that the specimens produced after alkali activation of all combinations tested acquire high compressive strength which reaches 45.8 MPa also in the case when the mixing ratio FSP:LS is 50:50. This value is almost 50 % higher compared to the value recorded for the AAM produced from FSP only. The results of this series prove the high co-valorization potential for both fayalitic and ferronickel slags (Komnitsas et al., 2020).

4.3.3 Structural integrity and selected properties of AAMs FS30LS70 and FSP30LS70

The structural integrity of the FS30LS70 and FSP30LS70 AAMs produced under the optimum conditions (mentioned earlier, section 4.3.2) were assessed after firing at 250, 350 and 500 °C for 6 h, immersion in distilled water (H_2O) and 1M HCl for a period of 7 and 30 days and implementation of freeze-thaw cycles, using −18±5 °C for 4 h and room temperature (20±0.5 °C) for 12 h, as temperature extremes over a period of 7 and 30 days. The compressive strength of the control specimens is also shown for comparison.

Figure 4.17 shows that the response of both AAMs to firing is good and FS30LS70 exhibits better behavior since its initial strength was higher. More specifically, the compressive strength of FS30LS70 specimen increases by ~20 % to 93.9 MPa after firing at 250 °C, due to volumetric shrinkage (5.0 %), and drops slightly by ~12.0 % to 67.2 MPa after firing at higher temperatures up to 500 °C. Similar behavior is seen for FSP30LS70 which after firing at 500 °C retains a compressive strength of 45.0 MPa. The compressive strength after firing at higher temperatures, e.g. 800 °C, drops to less than 15.0 MPa (data not shown), due to phase transformations, deterioration of the structural integrity of the

specimens as a result of the decomposition of Si-O-Al and Si-O-Si bonds, and the development of microcracks. It is thus deduced that AAMs produced after firing can be potentially used as medium fire-resistant materials (Abdel-Ghani et al., 2018; Zaharaki and Komnitsas, 2012; Komnitsas et al., 2019a, 2019b).
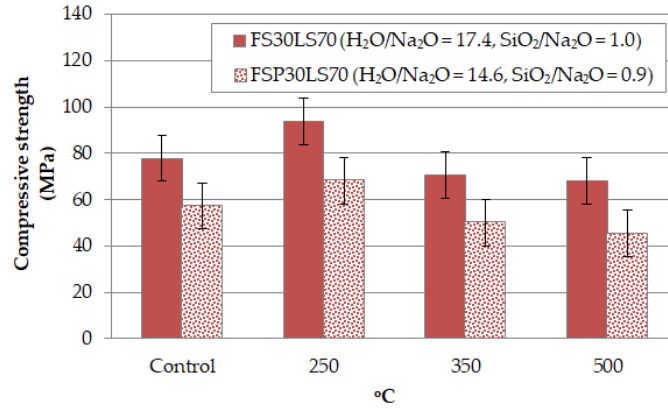
Figure 4.17. Compressive strength of FS30LS70 and FSP30LS70 AAMs after firing between 250 and 500 °C for 6 h; synthesis conditions: pre-curing time 6 h, curing temperature 90 °C, curing time 24 h, ageing period 7 days; the compressive strength of control AAM was determined after ageing period of 7 days; error bars indicate the standard deviation of measurements obtained from three specimens.

On the other hand, both specimens also exhibit very good behavior after immersion in distilled water or 1 M HCl, respectively for a period of 7 and 30 days. More specifically, immersion in distilled water affects only marginally the compressive strength of the specimens, even after a period of 30 days, whereas immersion in HCl solution for 7 days results in a decrease of compressive strength to 65.0 MPa for FS30LS70 (Figure 4.18a) and 45.0 MPa for FSP30LS70 (Figure 4.18b), respectively.

(a)

(b)
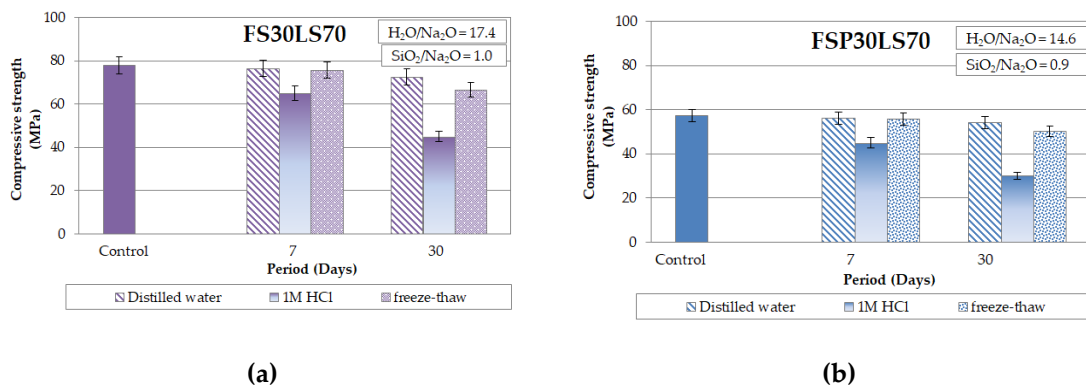
Figure 4.18. Compressive strength of **(a)** FS30LS70 and **(b)** FSP30LS70 AAMs after immersion in distilled water and 1 M (mol L^{-1}) HCl and implementation of freeze-thaw cycles for 7 and 30 days; synthesis conditions: pre-curing time 6 h, curing temperature 90 °C, curing time 24 h and ageing period 7 days; error bars indicate the standard deviation of measurements obtained from three specimens.

Additional retention of both AAMs in HCl solution for 30 days results in higher drop of compressive strength to 45.0 MPa and 30.0 MPa for FS30LS70 and FSP30LS70, respectively. Even though this loss of strength is considered big, it is important to mention that both specimens retain a substantial final strength under such harsh conditions. Regarding the effect of freeze-thaw cycles for 7 and 30 days, it is seen that both specimens respond very well and that the decrease in strength after 30 cycles is only marginal to 66.7 MPa for FS30LS70 (14 % decrease) and 50.2 MPa for FSP30LS70 (12 % decrease), respectively.

Finally, Table 4.5 shows the properties, namely porosity (%), water absorption (%) and density (g cm^{-3}) of selected AAMs, i.e. FS, FSP, LS, FS30LS70, FSP30LS70 as well as of the last two after firing them at 250 ^{o}C and 500 ^{o}C for 6 h. All AAMs examined were produced using the optimum synthesis conditions, as shown in the previous graphs. In this Table the compressive strength of these AAMs is also shown. It is seen from this data that the main differences were observed for porosity and density. It is observed that the porosity of FS specimen was 10.8 % and decreased to 6.3 % for FS30LS70 after firing at 250 ^{o}C. A similar trend was observed for water absorption which decreased from 3.8 % to 3.2 %. On the other hand, by taking into consideration the same AAMs the density increased from 2.3 to 4.3 g cm^{-3}.

Table 4.5. Physical properties of selected AAMs.

AAM Code	Compressive strength (MPa)	Density (g cm^{-3})	Porosity (%)	Water absorption (%)
FS	44.8	2.3	10.8	3.8
FSP	27.2	2.4	9.4	4.0
LS	80.1	2.6	8.0	3.0
FS30LS70 (control)	77.9	2.6	8.6	3.2
FS30LS70 after firing at 250 ^{o}C	93.9	4.3	6.3	3.2
FS30LS70 after firing at 500 ^{o}C	67.2	2.7	10.3	3.9
FSP30LS70 (control)	57.3	3.8	8.5	2.3
FSP30LS70 after firing at 250 ^{o}C	68.3	3.8	8.8	3.8
FSP30LS70 after firing at 500 ^{o}C	45.4	3.4	9.2	3.8

4.3.4   Morphology – Microstructure of raw FS, LS slags and selected AAMs

Figure 4.19 presents the XRD patterns of selected AAMs, namely FS30LS70 before and after firing at 250 °C for 6 h, as well as the patterns of raw FS and LS for comparison. It is observed that the main mineral phases, namely magnetite (Fe_3O_4) and fayalite (Fe_2SiO_4) present in FS30LS70 are also present in the specimen after its firing. It is also observed that silicon containing phases, such as quartz, cristobalite and tridymite present in the raw materials are not detected in the produced AAMs, due to their dissolution after the attack of the raw materials by the activating solution. Finally, it is seen that the intensities of the crystalline phases of fayalite and magnetite present in the produced AAMs are in general lower than the ones present in the raw slags. The lower intensities of these dominant phases in the AAMs indicate that they partially participate in the reactions and thus confirm to some extent the degree of polymerization (Peys et al., 2019b).
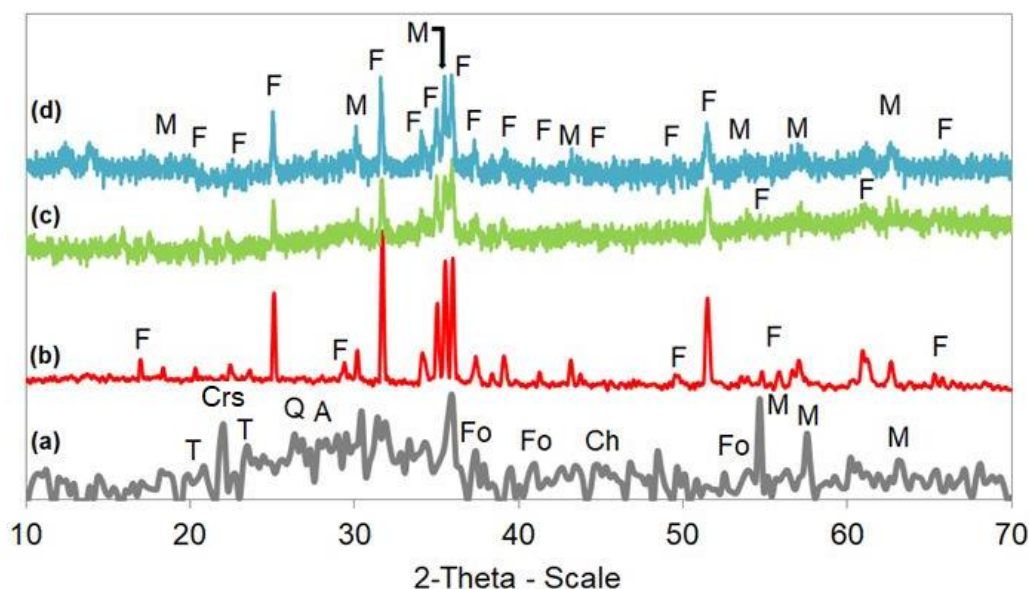
Figure 4.19. XRD patterns of raw **(a)** LS and **(b)** FS slags, as well as AAMs **(c)** FS30LS70 before and **(d)** FS30LS70 after firing at 250 °C for 6 h. Phases identified are: anorthite (A), chromite (Ch), cristobalite (Crs), fayalite (F), forsterite (Fo), magnetite (M), quartz (Q), tridymite (T).

Figure 4.20 presents the FTIR spectra of selected AAMs, namely FS30LS70 before and after firing at 250 °C for 6 h, as well as the FS and LS for comparison. The FTIR spectra of the AAMs indicate that polymerization took place and has resulted in the increase of the compressive strength. In this context and in line with XRD results (Figure 4.19), the disappearance of major bands in the 450-650 cm^{-1} range, which are attributed to characteristic T-O-T (T=Si, or Al) deformation vibrations, suggests that the activating solutions were effective in attacking the glassy content of the raw slags and thus, most of the dissolved aluminosilicates participated in the synthesis of the AAMs (Bernal et al., 2011). Moreover, the FTIR spectra of the AAMs show a slight shift to higher

wavenumbers for most vibration bands compared to raw slags, which is mainly due to the higher Si content in the C-S-H gel and the higher degree of polymerization (Ravikumar and Neithalath, 2012). In particular, a shift of the band at 457 cm^{-1} in the FS slag towards higher wavenumber (465 cm^{-1}) along with a significant reduction in its intensity in the examined AAMs is observed. Another explanation that is proposed, apart from the higher Si content of the inorganic matrix, is that the Fe present in the raw slag partly oxidizes to Fe^{3+} after alkali activation and subsequently decreases the amount of non-bridging oxygens available for the silicate network (Peys et al., 2019a, 2019b; Van De Sande et al., 2020). In this case, higher degree of silicate polymerization is achieved and the Si-O stretching band at 961 cm^{-1} present in the spectra of the raw slags shifts to higher wavenumbers in FS30LS70, i.e. 1017 cm^{-1} and 1021 cm^{-1} before and after firing at 250 $^{\circ}$C for 6 h, respectively. Finally, the weaker bands present at 1630 cm^{-1} and 3423 cm^{-1} in the raw LS which are attributed to the characteristic H-OH- bending and stretching vibrations of O-H are shifted to broader and more intense bands located at 1633 cm^{-1} and 3450 cm^{-1} in both AAMs, respectively.
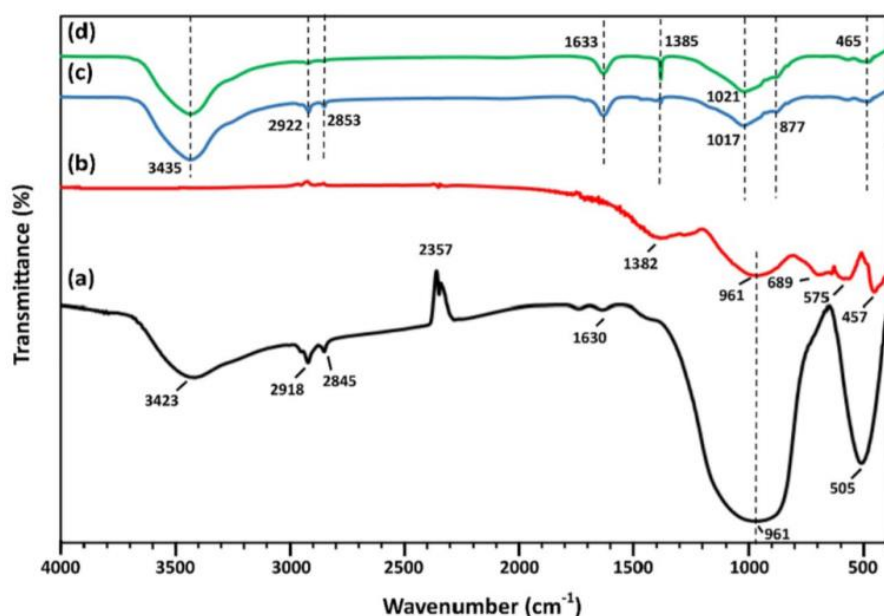
Figure 4.20. FTIR spectra of raw **(a)** LS and **(b)** FS slags, as well as AAMs **(c)** FS30LS70 before and **(d)** FS30LS70 after firing at 250 °C for 6 h.

Back-scattered electron (BSE) images of selected AAMs, namely FS30LS70 before and after firing at 250 $^{\circ}$C for 6 h are shown in Figure 4.21 (a-d). As shown in XRD patterns (Figure 4.19), SEM analysis of the polished AAM surfaces along with EDS point analyses revealed that fayalite and magnetite were the major mineralogical phases identified after alkali activation. Other phases such as chromite occurred as drop-like inclusions, while silicates such as forsterite and quartz were also detected in some places (Figure 4.21b,d).

Regarding the microstructure of both AAMs, no signs of cracks were observed along the cross-sectional interfaces examined as a result of the strong bonds that were formed after the reactions between the slag particles (mostly fayalite) and the alkaline activators (Na_2SiO_3 and $NaOH$). In this context, the presence of inorganic polymeric gels (G1 and G2) containing Ca, Al, Si, Fe, Mg and Na and surrounded by radically dissolved particles of fayalite and quartz after alkali-activation were identified in the specimen before (Figure 4.21b) and after firing (Figure 4.21d), respectively. However, the FS30LS70 AAM presents a microstructure which is characterized by several holes/pores scattered in the inorganic matrix and a greater proportion of unreacted or partially reacted larger particles compared to FS30LS70 after firing at 250 °C for 6 h. After firing, it seems that the voids were filled with inorganic gel as result of the dehydration reactions that took place along with sintering of the unreacted aluminosilicates (Rincón et al., 2018; Xu et al., 2019) and therefore a denser and more homogenous microstructure was finally formed with a continuous and embedded gel matrix. This well-established microstructure justifies the higher compressive strength obtained for the fired AAM (93.9 MPa). Figure 4.21d (zoom of rectangular area of Figure 4.21c) shows in detail the presence of columnar elongated of olivine particles (mixed forsterite/fayalite) and fine to coarse-sized euhedral crystals of anorthite and fayalite embedded in a glassy matrix (Gm) (Lemonis et al., 2015).
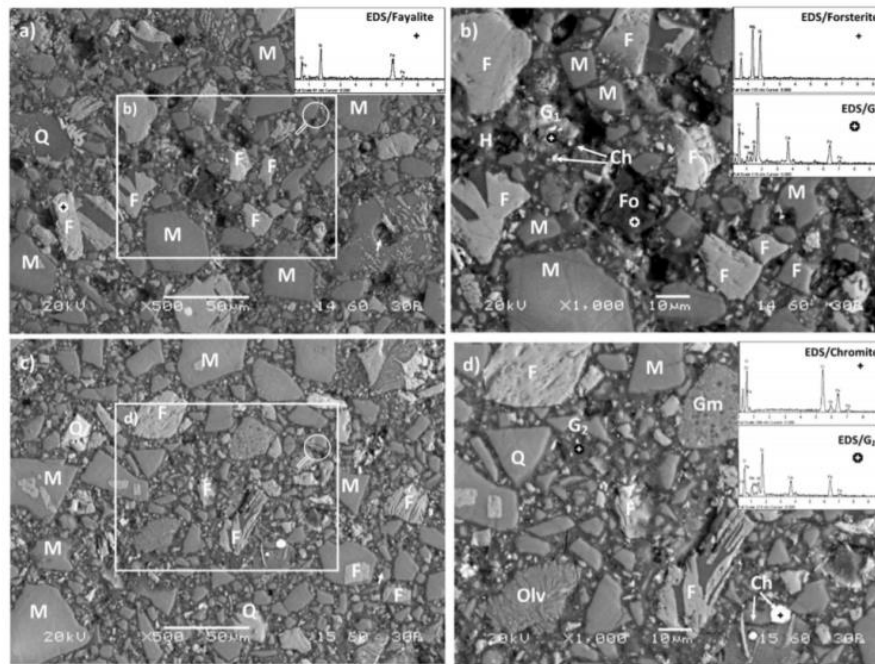
Figure 4.21. SEM-BSE images of polished cross-sections of selected AAMs **(a,b)** FS30LS70 and **(c,d)** FS30LS70 after firing at 250 °C for 6 h. EDS spectra show in several spot locations the presence of metallic and oxide phases, the formation of mixed aggregates and newly formed inorganic gels (Q: Quartz, Fo: Forsterite, F: Fayalite, M: Magnetite, Olv: Olivine, Ch: Chromite, Gm: Glassy matrix, G1:Gel, G2: Gel).

4.3.5   Toxicity of raw FS, FSP and LS slags and produced AAMs

The toxicity of the FS, FSP and LS slags as well as of produced AAMs was assessed according to the EN 12457-3 (2002), TCLP (US EPA, 1992) and NEN 7341 (1995) tests. The only raw material that exhibited some toxicity was the original fayalitic slag (FS) only in terms of Zn, due to its relatively high content of ZnO (2.8 wt%), as shown in Table 3.2. In particular, the Zn dissolution rate was 63 mg kg^{-1} and based on this value, FS as a waste can be only disposed in a landfill that accepts hazardous wastes (Table 4.4). The data from the applications of TCLP and NEN 7341 tests are analyzed in a previous recent study (Komnitsas et al., 2020). So, alkali activation of these wastes apart of their co-valorization and synthesis of new products that can be used as binders or construction materials, also results in reduction of their toxicity, in case it exists.

4.3.6   Conclusions

The experimental results show that under the synthesis conditions: pre-curing time 24 h, curing temperature 90 $^{\circ}$C, curing time 24 h and ageing period 7 days, the maximum values of the compressive strength obtained were 44.8 MPa and 27.2 MPa for FS- and FSP-based AAMs, respectively. The SiO$_2$/Na$_2$O molar ratios used in the activating solution were 1.5 and 0.9 in each case, respectively. The results also show the beneficial effect of co-valorization potential of FS and FSP slags when mixed with LS slag, since the AAMs produced after alkali activation of FS-LS and FSP-LS mixtures at 50:50 ratio acquire compressive strength of 64.3 MPa and 45.8 MPa, respectively; the synthesis conditions were the same as above and the SiO$_2$/Na$_2$O molar ratio in the activating solution was 1.0 and 0.9 for FS- and FSP-based AAMs, respectively. The produced AAMs after alkali activation of slag mixtures also show very good structural integrity after firing up to 500 $^{\circ}$C for 6 h, immersion in distilled water and acidic solution or subjection to freeze-thaw cycles for a period of 7 or 30 days. Finally, all produced AAMs exhibited very low toxicity after the application of EN 12457-3 test. In conclusion, these results confirm that alkali activation is a viable option for the co-valorization of different slags and the production of AAMs with beneficial properties, thus enabling the minimization of these wastes and the reduction of the environmental footprint of the metallurgical sector.

4.4 Comparison of the present study with other studies aiming the production of slag-based AAMs

Table 4.6 compares the results of this PhD thesis with those obtained from other selected studies aiming at the production of AAMs using metallurgical slags.

Table 4.6. Comparison of results of various studies using slag-based AAMs.

Raw Materials	SiO_2/Na_2O molar ratio	Conditions		Compressive strength (MPa)	Reference
		Temperature (^{o}C)	Ageing period (Days)		
Low-calcium slag ferronickel slag	n.r	80	7	~60	Komnitsas et al., 2009
Ferronickel slag	n.r	60 ^{o}C and 70 % relative humidity	2	120	Maragkos et al., 2009
Lead slag and fly ash	n.r	~20	28	47±4	Onisei et al., 2012
Slag with a high Al and Fe content	n.r	ambient temperature	28	5-60	Pontikes et al., 2013
Water granulated fayalitic slag	SiO_2/Na_2O=1.2 and SiO_2/K_2O=1.1	room temperature	28	60 and 70	Onisei et al., 2015
Water quenched fayalitic slag	n.r	20 ^{o}C and 90 % relative humidity	28	31.5	Iacobescu et al. 2017
Blast furnace ferronickel slag	0.5	20±1 ^{o}C and 95±5 % relative humidity	90	70	Wang et al., 2018
Non-ferrous metallurgy slags	1.6 or 2.0	20±1	28	50-53	Van De Sande et al., 2020
Polish ferronickel slag	0.3	80	7	65	This study
Fayalitic and ferronickel slags	1.0	90	7	78.5	This study
Fayalitic Slag after plasma treatment and ferronickel slag	0.9	90	7	65.0	This study

Komnitsas et al. (2009) produced AAMs through alkali activation of low-calcium ferronickel slag, using sodium or potassium hydroxide and sodium silicate solutions as

activators. The produced specimens obtained the highest compressive strength of almost 60 MPa, when the synthesis conditions were 8M NaOH, 8 % Na_2SiO_3, curing temperature of 80 °C for 48 h, and ageing period of 7 days. Also, Maragkos et al. (2009) produced AAMs through alkali activation of ferronickel slag, using sodium hydroxide and sodium silicate solution as activators. The results showed that the optimum synthesis conditions of the produced AAMs, i.e. S/L ratio equal to 5.4 g mL^{-1}, initial NaOH concentration in the aqueous phase equal to 7M and initial SiO_2 concentration in the aqueous phase equal to 4M, curing temperature 60 °C, relative humidity 70 % and ageing period 2 days, resulted in a much higher compressive strength value, namely 120 MPa. On the other hand, Onisei et al. (2012) investigated the synthesis of AAMs using fly ash and primary lead slag with different ratios, and sodium hydroxide and sodium silicate solutions as alkali activators. AAMs produced using a mixture consisting of 70 wt% lead slag and 30 wt% fly ash and acquired compressive strength of 47±4 MPa after curing at 20 °C and ageing period for 28 days. Pontikes et al. (2013) produced AAMs through alkali activation of slag with a high Al and Fe content, cooled in four different ways, namely slag pot, layer, layer+water, and water quenching and used as precursor for the production of AAMs. The paste was cured at ambient conditions and after ageing for 28 days the produced specimens achieved compressive strength which varied between 5 and 60 MPa. Onisei et al. (2015) investigated the production of fayalitic slag-based AAMs and their potential to be used as a heat resistant material. Two different types of activating solutions, i.e. Na-based and K-based also used. The SiO_2/Na_2O and KO_2/Na_2O molar ratios were 1.2 and 1.1, respectively, while the solid/activating solution ratio was kept constant at 5.4 and 5.6 for the samples produced with Na-based and K-based solutions, respectively. The results showed that the produced AAMs acquired compressive strength of 60 MPa and 70 MPa without addition of analytical grade Al_2O_3 in the starting mixture. However, the compressive strength exceeded 100 MPa after firing at 500 °C using K-silicate as activator and regardless of the addition of 5 wt% or 10 wt% analytical grade Al_2O_3 in the initial mixture. Furthermore, Iacobescu et al. (2017) studied the effect of curing conditions on the mechanical properties of fayalitic slag-based AAMs. Specificially, water quenched fayalitic slag was used as precursor, CEN standardised sand as fine aggregate and a mixture of sodium silicate and sodium hydroxide solutions as activator. The pastes cured in a mullfe furnace at 60 °C and relative humidity ~20 %, or at room temperature (20 to 23 °C) and relative humidity ~50 %, or in a humidity chamber at 20 °C with relative humidity ≥90 %. Then, the samples cured at 60 °C were demoulded after 1 day and left to harden for 27 more days. The samples cured at room temperature or in the humidity chamber were demoulded after 4 days, and left to harden for 24 more days. The results showed that the produced AAMs after curing at 20 °C, relative humidity ≥ 90 % and ageing period 28 days acquired compressive strength of 31.5 MPa, a similar value obtained by OPC type CEM I 32.5N after 28 days of curing (i.e. 32.5 MPa),

according to the European Committee for Standardisation EN 197-1 test. Wang et al. (2018) investigated the alkali activation of blast furnace ferronickel slag as a cementitious material, and compared it with alkali-activated blast furnace slag concrete which was used as reference. ISO reference sand and crushed limestone were also used as fine and coarse aggregates, respectively, while sodium hydroxide and industrial water glass used as alkali activators. The mortar samples of blast furnace ferronickel slag produced using SiO_2/Na_2O molar ratio 0.5 after curing at 20±1 ℃ and 95±5 % relative humidity obtained the highest compressive strength (70 MPa) after an ageing period of 90 days. The results also showed that the compressive strength value of alkali-activated blast furnace ferronickel slag mortar is comparable to the alkali-activated blast furnace slag mortar. Finally, Van De Sande et al. (2020) investigated the optimization of non-ferrous metallurgy slags as precursors for the synthesis of AAMs. The synthetic slags were prepared by melting iron (III) oxide, metallic iron, quartz and calcium oxide in an iron crucible placed in an induction furnace while then the melt was heated up to a temperature 100±20 ℃. Sodium silicate solution with molar ratios SiO_2/Na_2O 1.6 or 2.0 and H_2O/Na_2O, 25 were used as activator. The mortars prepared from slags containing more calcium oxide acquired compressive strength of approximately 50 MPa after curing in closed plastic boxes at 20±1 ℃, for an ageing period for 28 days and SiO_2/Na_2O, 2.0 and 1.6, respectively.

In the present study, the produced AAMs after alkali activation of PS, acquired compressive strength of 65.0 MPa. In addition, the produced FSLS- and FSPLS-based AAMs after alkali activation of FS and FSP mixed with 90 wt% LS achieved a high compressive strength of 78.5 and 65.0 MPa, respectively. The SiO_2/Na_2O molar ratios varied from 0.3 to 1.0, depending on the different precursor used. The results of co-valorization of FS and LS slags prove the beneficial effect of LS in the starting mixture as precursor.

4.5 Factors affecting valorization of LR and LLR residues for the production of AAMs

This section presents the alkali activation potential of LR and LLR obtained after column leaching tests of Greek laterites. The experimental conditions used were similar to those described in previous recent studies (Komnitsas et al., 2018, 2019b). It is noted that the LR and LLR exhibit low reactivity, which is not sufficient for alkaline activation as mentioned earlier (section 4.1.1). Therefore, precursors obtained by mixing LR or LLR with different ratios of MK or PS and LS slags were used, in order to assess their co-valorization potential for the production of AAMs with beneficial properties. The factors affecting the compressive strength and other properties as well as the structural integrity,

morphology and microstructure of the produced AAMs were investigated and the results are also presented in this Chapter. More details on the results of the alkali activation of LR are reported in a recent study (Komnitsas et al., 2021).

4.5.1 Effect of curing temperature and H_2O/Na_2O molar ratio in the activating solution on the compressive strength of the produced AAMs

Figure 4.22 presents the compressive strength of the AAMs produced from LR residues (Figure 4.22a) and LLR residues (Figure 4.22b), as a function of curing temperature (40, 60 or 80 ^{o}C for LR-based AMMs and 20, 75 or 95 ^{o}C for LLR-based AAMs) and H_2O/Na_2O ratio in the activating solution (21.2, 17.4 or 14.8 for LR-based AAMs and 17.2 or 14.8 for LLR-based AAMs). Curing and ageing times were 24 h and 7 days respectively, while the SiO_2/Na_2O molar ratio in the activating solution was kept constant at 1.0 in all tests. It is seen from this data that the increase of temperature affects positively the strength of the produced AAMs for all H_2O/Na_2O molar ratios tested. In both cases, it is observed that the compressive strength of LR- and LLR-based AAMs decreases when the H_2O/Na_2O ratio in the activating solution decreases from 17.4 to 14.8 for LR-based AAMs and 17.2 to 14.8 for LLR-based AAMs. This is mainly due to the fact that the lower H_2O/Na_2O ratios indicate excess of OH- ions which may remain unreacted and result in the production of specimens with lower strength, as mentioned earlier (section 2.4). The maximum values of compressive strength acquired were only 1.4 and 10.2 MPa for LR- and LLR-based AAMs, respectively. The experimental results may be explained by considering the low content of Al_2O_3 in the starting materials (Table 3.2), as well as the low concentration of Al ions in alkaline solution, thus confirming the poor potential for successful alkali activation. Nevertheless, LLR exhibits higher activation potential since its Si/Al ratio in the alkaline solution is two times higher compared to the respective ratio obtained after leaching of LR.

Based on this data, precursors obtained by mixing LR with MK and LLR with LS or PS slags with different ratios were used for the production of AAMs with good physical and mechanical properties.

(a)   **(b)**
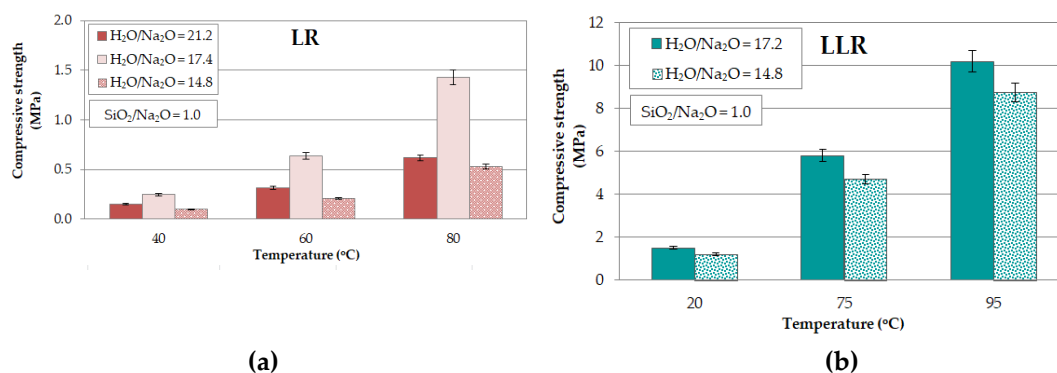
Figure 4.22. Effect of curing temperature and H_2O/Na_2O molar ratio in the activating solution on the compressive strength of **(a)** LR- and **(b)** LLR-based AAMs (pre-curing time 4 h, curing time 24 h and ageing period 7 days; error bars indicate the standard deviation of measurements obtained from three specimens).

4.5.2   Potential of co–valorization of LR residues and MK

In order to assess the co-valorization potential of LR and MK through alkali activation, precursors obtained by mixing LR with MK at ratios 95:5 and 90:10 were used, since as mentioned earlier MK exhibits higher reactivity during alkali activation. Figure 4.23 presents the compressive strength of the AAMs produced by mixing leaching residues, raw and after calcination, with metakaolin. AAMs synthesis conditions were: pre-curing time 4 h, curing temperature 80 ºC for 24 h, and ageing period 7 days. The difference in H_2O/Na_2O molar ratios is due to the slightly different L/S ratios used in each case in the starting mixture to obtain a paste with optimum flowability (Table 3.3), while the SiO_2/Na_2O molar ratio in the activating solution was kept constant at 1. In the same Figure the compressive strength of control specimens produced after alkali activation of each raw material, namely LR and MK, are also given for comparison. Laterite leaching residues were also calcined at 800 and 1000 ºC for 2 h, in order to study the effect of calcination. It is observed that 5 wt% metakaolin addition in the starting mixture resulted in an increase of the compressive strength of LR95MK5 AAMs from 1.4 to 12.3 MPa, while with the increase of metakaolin addition to 10 wt%, the LR90MK10 specimen acquired a much higher compressive strength (45.0 MPa). On the other hand, the AAMs produced after alkali activation of metakaolin (control specimens) achieve a compressive strength of 55.0 MPa. Although both materials had similar grain size (Table 3.1), which is considered beneficial for alkali activation, the value of compressive strength of metakaolin-based AAMs explains its high alkali activation potential and the beneficial effect of its addition in the starting mixture. The higher compressive strength of metakaolin-based AAMs may be also explained by the chemical composition of metakaolin (SiO_2 54.2 wt%, Al_2O_3 40.3 wt%, as shown in Table 3.2), as well as the

concentration of Si and Al in solution after its alkaline leaching (58.7 mg L^{-1} Si and 41.9 mg L^{-1} Al, respectively, as shown in Table 4.1).

In addition, it is seen that calcination of the laterite leaching residues has a detrimental effect on the compressive strength of the produced specimens. However, the specific surface area of calcined laterite residues increased to 15 m^2 g^{-1}, while the dissolution of Si and Al was low due to the occurred phase transformations. Therefore, the low reactivity of calcined laterite leaching residues during alkali activation, as shown in Table 4.1, does not enable the production of specimens with beneficial properties. Finally, the specimens produced from mixtures containing 90 wt% calcined laterite residues at 800 or 1000 °C and 10 wt% metakaolin acquired compressive strength equal to 25.8 and 13.2 MPa, respectively; these values are considered quite good.
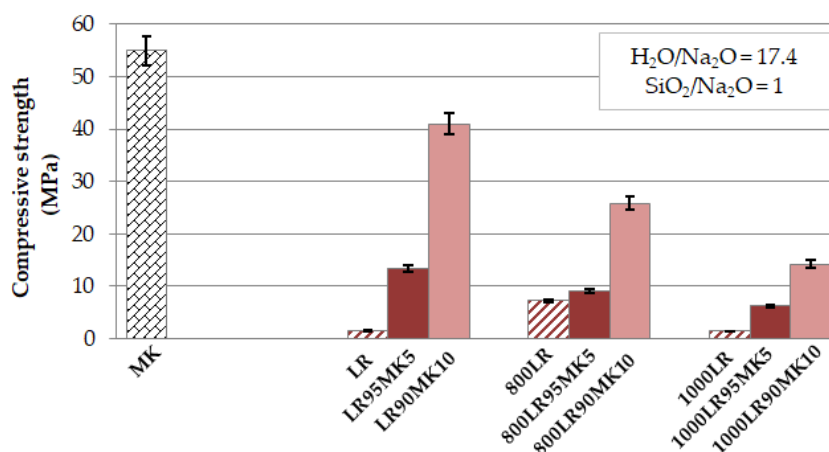
Figure 4.23. Effect of addition of MK (5 wt% and 10 wt%) and calcination of LR on the compressive strength of the produced AAMs (pre-curing time 4 h, curing temperature 80 °C, curing time 24 h, ageing period 7 days, 800LR: LR calcined at 800 °C for 2 h, 1000LR: LR calcined at 1000 °C for 2 h; error bars denote standard deviation of measurements obtained from three specimens).

It is also noted that the effect of pre-curing time (4, 12 and 24 h), curing time (24 and 28 h), as well as the SiO_2/Na_2O molar ratio in the activating solution (0.3, 0.5, 1.0 and 1.6) on the compressive strength of AAM LR90MK10 were also investigated. The data are presented in detail in a previous recent study (Komnitsas et al., 2021). In conclusion, from the experimental data it was observed that the compressive strength decreased with increasing pre-curing and curing time, while the optimum SiO_2/Na_2O molar ratio was equal to 1. The maximum compressive strength of AAM LR90MK10, i.e. 45.0 MPa was obtained when the synthesis conditions used were H_2O/Na_2O and SiO_2/Na_2O molar ratio in the activating solution 17.2 and 1, respectively, pre-curing time 4 h, curing temperature 80 °C for 24 h and ageing period 7 days.

4.5.3 Potential of co–valorization of LLR residues and LS, PS slags – Effect of curing temperature on the compressive strength

The co-valorization potential of LLR and LS, PS slags mixtures through alkali activation was also investigated. Figures 4.24 (a,b) show the compressive strength of AAMs produced by mixing LLR with LS or PS at ratios 50:50 and 30:70 wt% as a function of curing temperature (20, 75, 95 °C). The H_2O/Na_2O and SiO_2/Na_2O molar ratios used for LLR and LS were 17.2 and 1.0, while the respective molar ratios used for LLR and PS were 14.2 and 0.3, respectively. It is known that the difference in H_2O/Na_2O and SiO_2/Na_2O molar ratios in the activating solution is due to the mixtures used in each case, in order to obtain a paste with appropriate viscosity and optimum flowability that can be easily casted. It is also mentioned that the maximum compressive strength obtained under the optimum synthesis conditions for PS- and LS-based AAMs was 80.0 MPa and 86.0 MPa, respectively. It can be seen from Figures 4.24 (a,b) that the specimens produced after alkali activation with 30:70 ratio, regardless of the slag used in the starting mixture obtained high to moderate compressive strength after curing at 95 °C. More specifically, when the LLR:LS ratio in the starting mixture was 30:70 after curing at 95 °C, the compressive strength value acquired was equal to 27.5 MPa (Figure 4.24a), while LLR30PS70 AAMs acquired almost similar compressive strength values, i.e. 50.1 and 50.7 MPa, when the curing temperature was 75 and 95 °C, respectively (Figure 4.24b). Therefore, the AAMs produced after alkali activation of LLR-PS mixtures acquired higher compressive strength, due to the higher reactivity of PS slag (Table 4.1). Based on these results it is deduced that the addition of metallurgical slag in the starting mixture and the curing at higher temperature have beneficial effects on the compressive strength of the produced AAMs, as mentioned in earlier studies (Komnitsas et al., 2020; Soultana et al., 2019).

(a) **(b)**
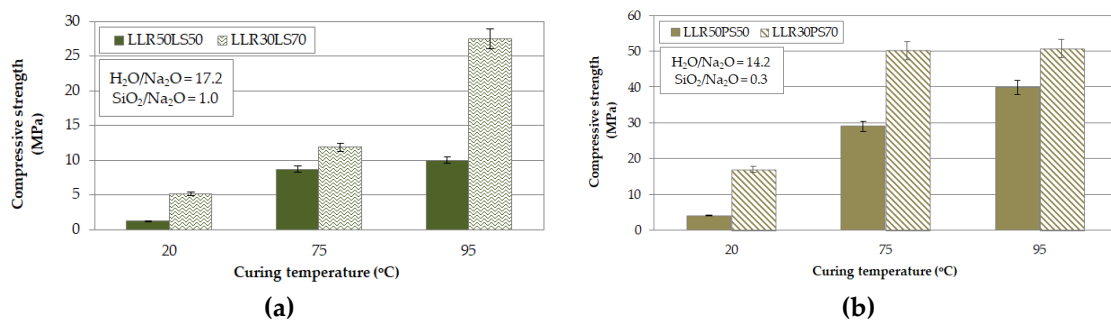
Figure 4.24. Effect of curing temperature on the compressive strength of (a) LLR50LS50, LLR30LS70 AAMs and (b) LLR50PS50, LLR30PS70 AAMs (pre-curing and curing time 24 h, ageing period 7 days; error bars denote standard) deviation of measurements from two specimens).

4.5.4   Structural integrity of AAMs LR90MK10, LLR3LS70 and LLR30PS70

The structural integrity of LR90MK10, LLR30LS70 and LLR30PS70 AAMs produced using the optimum synthesis conditions was also assessed after firing for a period of 2 h or 4 h at a temperature range between 200 and 1000 $^{\circ}$C and after immersion in distilled water and acidic solution (1 mol L^{-1} HCl) for 7 and 30 days.

Figure 4.25 shows the evolution of the compressive strength of LR90MK10 AAM after firing, while the compressive strength of the control specimen, which was not subjected to firing, is also shown for comparison. It is observed from this data that the compressive strength decreases gradually with the increase in firing temperature and the minimum value of strength after firing at 800 $^{\circ}$C was 23.1 MPa, which is considered high. Other factors that contributed to the decrease in compressive strength of fired AAMs are the weight loss (%), the volumetric shrinkage (%) and the water absorption (%) which increase gradually, while the apparent density (g cm^{-3}) decreases slightly with increasing firing temperature, as shown in a recent study (Komnitsas et al., 2020). More specifically, the fired specimen at 800 $^{\circ}$C obtained the lowest compressive strength and apparent density, i.e. 23.1 MPa and 1.8 g cm^{-3}, respectively, as well as the highest weight loss (12.1 %), volumetric shrinkage (7.5 %), porosity (27.2 %) and water adsorption (14.8 %). Figure 4.26 shows the evolution of the compressive strength of LLR30LS70 and LLR30PS70 AAMs after firing. The compressive strength of the control specimens is also shown for comparison.
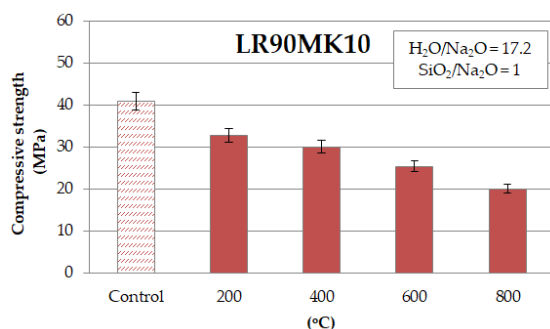
Figure 4.25. Compressive strength of LR90MK10 AAM after firing between 200 and 800 $^{\circ}$C for 2 h; synthesis conditions: pre-curing time 4 h, curing temperature 80 $^{\circ}$C, curing time 24 h and ageing period 7 days; error bars indicate the standard deviation of measurements obtained from three specimens.
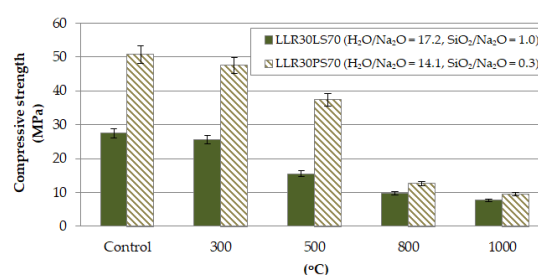
Figure 4.26. Compressive strength of LLR30LS70 and LLR30PS70 AAMs after firing between 300 and 1000 $^{\circ}$C for 4 h; synthesis conditions: pre-curing and curing time 24 h, curing temperature 95 $^{\circ}$C and ageing period 7 days; error bars indicate the standard deviation of measurements obtained from three specimens.

In this case, the response of both AAMs to firing up to 300 $^{\circ}$C is much better since their compressive strength decreases slightly, while at higher firing temperatures drops sharply. More specifically, the value of the compressive strength of LLR30PS70 was 47.5

MPa (6.3 % decrease) after firing at 300 °C, due to volumetric shrinkage 5.0% and weight loss 10.7 %. On the other hand, the minimum compressive strength recorded was 9.5 MPa (81.2 % decrease) after firing at 1000 °C, due to increased volumetric shrinkage (16.4 %) and weight loss (14.3 %). Similar behavior is seen for LLR30LS70 specimen which after firing at 300 °C retains an acceptable compressive strength value of 25.5 MPa, while a much lower value, i.e. 7.7 MPa, was recorded after its firing at 1000 °C. These results contradict those obtained for slags-based AAMs, which after firing at 250 °C (FS30LS70 and FSP30LS70 AAMs) and 400 °C (PS-based AAMs) for 6 h acquired a higher compressive strength, as previously mentioned (sections 4.2.3 and 4.3.3).

Figure 4.27 shows the compressive strength of LR90MK10 AAMs after immersion in distilled water or acidic solution (1 mol L^{-1} HCl) for 7 and 30 days. The compressive strength of the control specimen is also provided for comparison. As seen from this data the greater compressive strength loss (72.3 %, 12.5 MPa) was recorded for the specimens immersed in 1 mol L^{-1} HCl for 30 days, whereas the specimens immersed in distilled water for the same period exhibited lower loss (23.3 %, 34.5 MPa). The values of the compressive strength after immersion of the specimens in distilled water for 7 and 30 days were much higher, i.e 37.5 MPa and 34.5 MPa, respectively. It is also mentioned that an increase in the solution pH was observed after immersion for 30 days; pH increased from 7.6 to 10.8 after immersion in distilled water, whereas a lower increase from 1.3 to 2.3 observed after immersion in 1 mol L^{-1} HCl. A similar trend was noted in a previous study (Soultana et al., 2019).
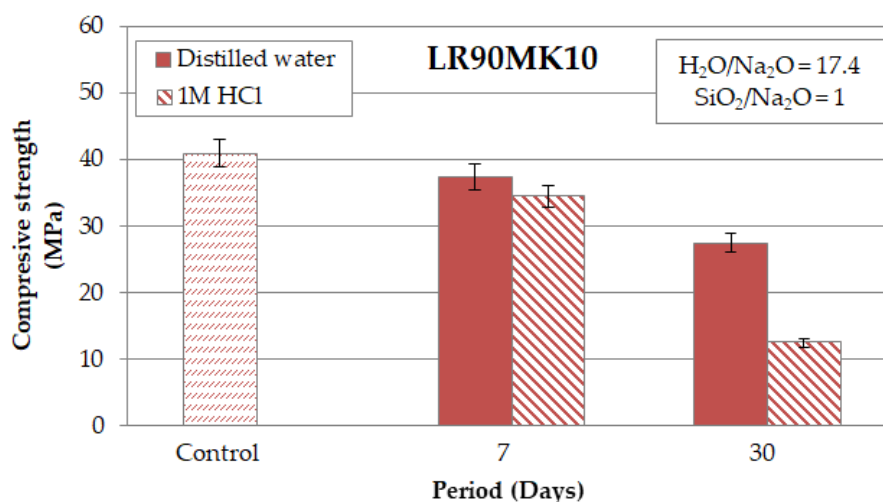
Figure 4.27. Compressive strength of LR90MK10 AAMs after immersion in distilled water and 1 M (mol L^{-1}) HCl for 7 and 30 days; synthesis conditions: pre-curing time 4 h, curing time 24 h, curing temperature 80 °C, ageing period 7 days; error bars indicate the standard deviation of measurements obtained from three specimens.

Figure 4.28 presents the evolution of compressive strength of LLR30LS70 and LLR30PS70 AAMs when immersed in distilled water or acidic solution (1 mol L^{-1} HCl) for 7 days, while the compressive strength of the control specimen is also given for comparison. It is seen that for both AAMs, the maximum decrease in strength was observed after their immersion in 1 mol L^{-1} HCl. In particular, the compressive strength of LLR30LS70 and LLR30PS70 AAMs was 15.4 MPa (44.0 % decrease) and 39.1 MPa (22.9 % decrease), respectively, while after immersion in distilled water lower drop in strength was noticed (22.5 MPa and 40.4 MPa, respectively). Finally, it is mentioned that even though the loss in strength for both AAMs after exposure in such harsh conditionsis considered moderate to big, their values are considered sufficient.
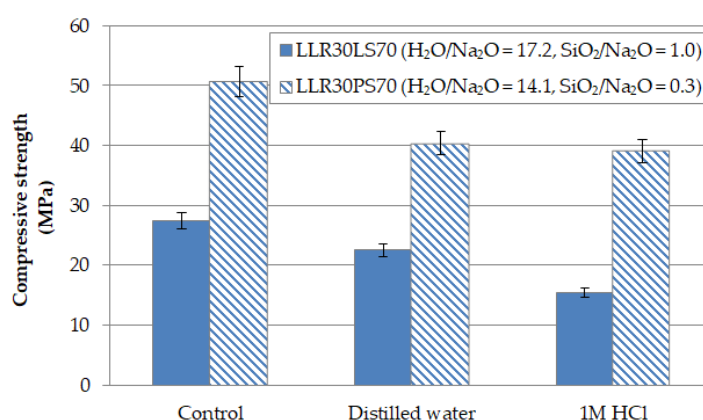
Figure 4.28. Compressive strength of LLR30LS70 and LLR30PS70 AAMs after immersion in distilled water and 1 M (mol L^{-1}) HCl for 7 days; synthesis conditions: pre-curing and curing time 24 h, curing temperature 95 °C, ageing period 7 days; error bars indicate the standard deviation of measurements obtained from three specimens.

Table 4.7 presents the density (g cm^{-3}), porosity (%) and water absorption (%) of selected AAMs, produced under the optimum synthesis conditions, as indicated in the previous graphs.

Table 4.7. Physical properties of selected AAMs.

AAM Code	Compressive strength (MPa)	Density (g·cm^{-3})	Porosity (%)	Water absorption (%)
LR	1.4	1.8	36.8	20.7
LR90MK10	42.5	2.3	21.3	9.1
LLR	10.2	2.1	15.4	5.5
LLR30LS70	27.5	2.4	11.0	4.6
LLR30LS70 after firing at 300 °C	25.5	2.4	17.6	7.5
LLR30PS70	50.7	2.7	9.7	3.8
LLR30PS70 after firing at 300 °C	37.5	2.3	22.6	10.0

In this Table, the compressive strength of selected AAMs is also presented. It is seen that the LR-based AAMs obtained the lowest compressive strength (1.2 MPa) and density (1.8 g cm^{-3}), as well as the highest porosity (36.8 %) and water absorption (20.7 %). AAMs with 10 wt% metakaolin (LR90MK10) acquired high compressive strength (42.5 MPa) and thus exhibited lower porosity (from 36.8 % to 21.3 %), and water absorption (from 20.7 % to 9.1 %), and increased density (2.3 g cm^{-3}). In addition, the main difference between porosity and water absorption was observed for the LLR and LLR30PS70 specimens. More specifically, the porosity was 15.4 % for the LLR specimen and decreased to 9.7 % for the LLR30PS70 specimen. A similar trend was observed for water absorption which decreased from 5.5 % to 3.8 %. On the other hand, for the same AAMs the density increased from 2.1 to 2.7 g cm^{-3}.

4.5.5   Morphology–Microstructure of LR, LLR residues and selected AAMs

Figures 4.29-4.31 present the XRD patterns of laterite leaching residues (LR, LLR), metakaolin (MK), ferronickel slags (PS, LS) and selected AAMs. The main mineralogical phases present in the LR residues were described in Figure 4.3 (section 4.1.2), while the main mineralogical phases present in the XRD pattern of metakaolin were quartz and muscovite. A broad amorphous hump between 2-Theta 17° and 40° is also observed (Figure 4.29b). After alkali activation, the peaks of quartz and hematite slightly increased in LR AAM compared to their intensity in the LR residues (Figure 4.29c), thus confirming that these phases do not participate in alkali activation reactions (Lemougna et al., 2017). On the contrary, the addition of 10 wt% metakaolin in the initial mixture (LR90MK10 AAM), as explained earlier, resulted in the dissolution of sufficient Si and Al ions that participate in alkali activation reactions and the development of the geopolymeric network. This is confirmed by the intensity of the peaks of the crystalline phases in LR90MK10 AAM, which is significantly lower compared to that present in leaching residue LR (Figure 4.29d). It is also mentioned that the LR90MK10 AAM acquired the higher compressive strength (45.0 MPa), which is explained by considering the broad hump shown between 2-Theta 17° and 40° in the XRD pattern of LR90MK10 (Figure 4.29d) that is typical for metakaolin-based AAMs (Yi et al., 2020). Figure 4.29e presents the XRD pattern of LR90MK10 after firing at 800 $^\circ$C for 2 h. In this case, it is observed that the amorphous hump is more apparent, but the center of the hump shifted towards lower 2-Theta, i.e 27° and 26.5° for LR10MK90 AAM before and after firing, respectively. According to the results of a previous study, this decrease suggests partial depolymerization of metakaolin after firing at 800 $^\circ$C and then reorganization of its structure which results in a decrease of compressive strength at 23.1 MPa (Tchakouté et al., 2016).
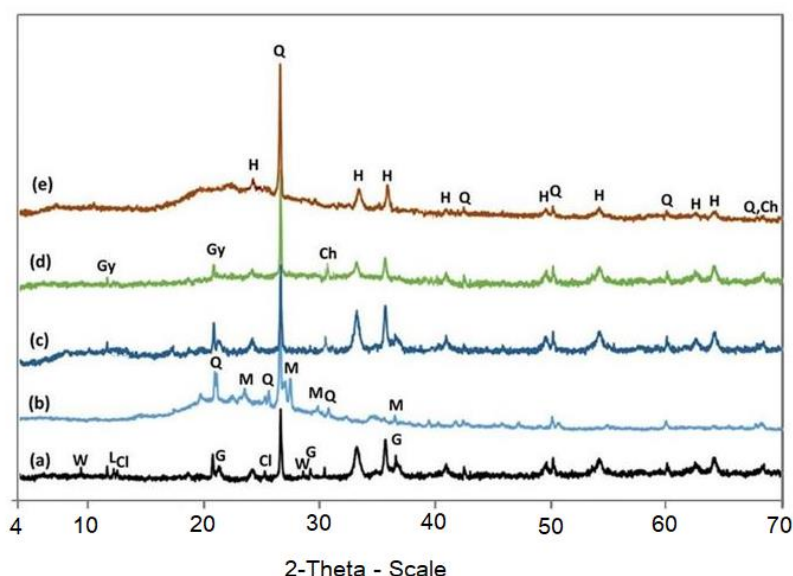
Figure 4.29. XRD patterns of **(a)** leaching residues LR, **(b)** MK and AAMs produced using **(c)** only laterite leaching residues (LR AAM), as well as by mixing **(d)** LR and MK at mass ratio 90:10 (LR90MK10 AAM) and **(e)** LR90MK10 after firing at 800 ºC for 2 h. Phases indentified are: chromite (Ch), clinochlore (Cl), goethite (G), gypsum (Gy), hematite (H), quartz (Q), lizardite (L), muscovite (M), willemseite (W).

Figure 4.30 presents the XRD patterns of LLR30LS70 AAM which was produced under the optimum synthesis conditions, as well as the patterns of leaching residues LLR and LS slag for comparison. After alkali activation, it is seen that the mineralogical phases of fayalite and magnetite are either not detected or exhibit lower intensity (Figure 4.30c), indicating that they partially participate in the alkali activation reactions (Peys et al., 2019b). It is also observed that the silicon containing phases, i.e. quartz, cristobalite and tridymite, as well as the phases of clinochlore and hematite present in the raw materials exhibit lower intensities in the LLR30LS70 AAM, due to the reaction of Si and Al with the strong alkaline solution to form aluminosilicate bonds, resulting in the production of specimens with beneficial properties and high compressive strength (Zaharaki et al., 2010). On the contrary, the crystalline phases of fosterite and anorthite present in the raw slag (Figure 4.30a) are not detected in LLR30LS70 AAM (Figure 4.30c), due to their dissolution after the attack of the raw materials by the activating solution.
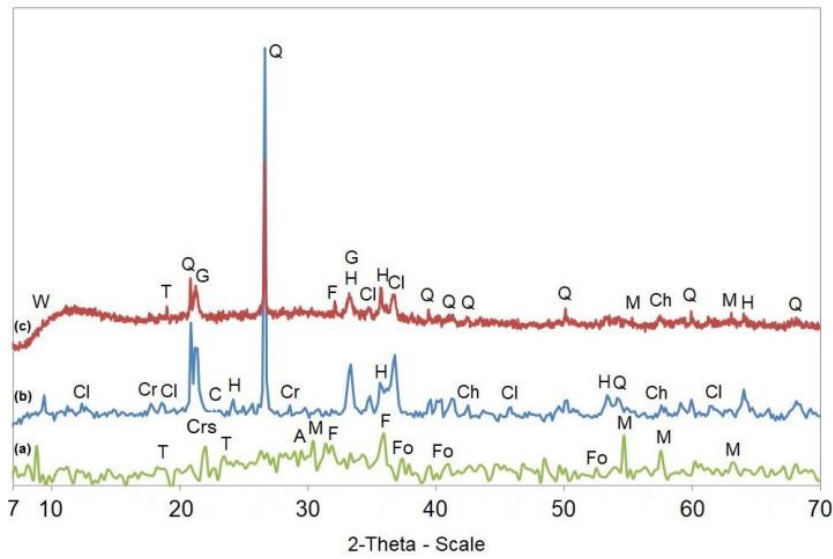
Figure 4.30. XRD patterns of **(a)** LS slag, **(b)** leaching residues LLR and **(c)** LLR30LS70 AAM. Phases indentified are: anorthite (A), calcite (C), chromite (Ch), clinochlore (Cl), cristobalite (Crs),cryptomelane (Cr), fayalite (F), fosterite (Fo), goethite (G), hematite (H), magnetite (M), quartz (Q), tridymite (T), willemseite (W).

On the other hand, Figure 4.31 presents the XRD patterns of the AAM produced after mixing leaching residues LLR and PS slag at mass ratio 30:70 under the optimum synthesis conditions, as well as the patterns of the raw materials. In this case, it is observed that the intensity of crystalline phases present in the PS slag or LLR residues, i.e diopside, hendebergite, fayalite (Figure 4.31a), quartz and clinochlore (Figure 4.31b) is lower in the produced LLR30PS70 AAM. However, the reduction of these intensities is anticipated, as mentioned in earlier cases.
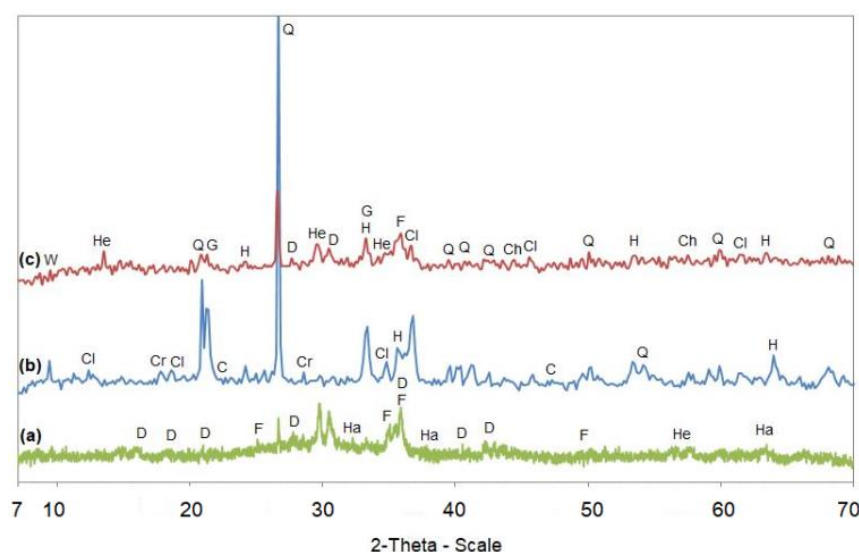
Figure 4.31. XRD patterns of **(a)** PS slag, **(b)** leaching residues LLR and **(c)** LLR30PS70 AAMs. Phases indentified are: calcite (C), chromite (Ch), clinochlore (Cl), cryptomelane (Cr), diopside (D), fayalite (F), goethite (G), hatrurite (Ha), hedenbergite (He), hematite (H), magnetite (M), quartz (Q), willemseite (W).

The FTIR spectra, over the range 4000-400 cm^{-1} of laterite leaching residues (LR, LLR), ferronicklel slags (PS, LS) and selected AAMs are presented in Figures 4.32-4.34. It is seen that the AAMs exhibit different vibrations belonging to Al- and Si-containing phases and Si-O-Si bonds.

First, the spectra of AAMs produced by leaching residues LR (LR AAM), as well as by mixing leaching residues LR with metakaolin at mass ratio 90:10 (LR90MK10 AAMs) before and after firing are presented in Figure 4.32. The characteristic bands at 460 cm^{-1}, the double bands at 778 cm^{-1} and 796 cm^{-1}, 1086 cm^{-1} and 1102 cm^{-1} which are attributed to quartz and the small band at 528 cm^{-1}, which is attributed to hematite are present in the leaching residues LR (Figure 4.32a), remained almost unaffected after alkali activation in the LR AAM (Figure 4.32b). This confirms the low reactivity of LR during alkali activation. A clear difference in the shape, position and intensity of the bands in the spectrum of LR90MK10 AAM in comparison to LR AAM is observed in the region of 450-1250 cm^{-1} (Figure 4.32c). This difference is due to vibrations belonging to Al-, Fe, Si-containing phases in the raw materials or binder, i.e. leaching residues and metakaolin, and the respective Si-O-Si, Fe-O-Si and Si-O-Al bonds formed in the produced alkali activated matrices. In this case, the band present at 460 cm^{-1} in the leaching residues LR and LR AAM (Figure 4.32a,b) and shifted to 466 cm^{-1} in LR90MK10 AAM (Figure 4.32c) is probably attributed to the bending motions of the Al- and Si-containing phases (Komnitsas et al., 2018; Lemougna et al., 2017). In addition, the band seen at 528 cm^{-1} in the LR AAM was shifted at a higher wavenumber, 538 cm^{-1} in LR90MK10 AAM, while the band observed at 910 cm^{-1} disappeared in the LR90MK10 AAMs before and after

firing at 800 °C, possibly due to enhanced dissolution of Fe ions from the crystalline phase of hematite and goethite, respectively, that were present in the laterite leaching residues and their subsequent participation in the alkali-activated reactions (Kaze et al., 2018a, 2020). Moreover, the major difference between LR residues and LR90MK10 AAMs is due to the shifting of the pair of strong bands at 778 cm^{-1} and 796 cm^{-1} observed in LR AAM and leaching residues LR, which are associated with the asymmetric stretching vibrations of the Si–O Al bonds, towards lower wavenumber (770 cm^{-1} and 788 cm^{-1}), thus indicating the formation of inorganic gel in LR90MK10 AAM (Kaze et al., 2018b, 2020). The displacement of the band located at 1086 cm^{-1} in LR AAM to a lower wavenumber (1078 cm^{-1}) in LR90MK10 AAM, is due to the dissolution of aluminosilicate phases present in the laterite leaching residues and their subsequent polymerization during alkali-activation. The bands at ~1410 cm^{-1} and ~1490 cm^{-1}, present only in the LR90MK10 AAM are attributed to asymmetric vibrations of O-C-O bonds due to the formation of carbonation products from the reaction between the alkali-activated silicates and the atmospheric CO_2 during the curing period (Kaze et al., 2020). The weaker peak at 1632 cm^{-1} in the LR AAM shifted at 1648 cm^{-1} in the LR90MK10 AAM; this shift is due to the characteristic bending vibrations of H-O-H (Ricciotti et al., 2017). The presence of water is more evident in LR90MK10 since a quite wide absorption band region appeared between 3000 cm^{-1} and 3700 cm^{-1} belonging to stretching vibrations of OH groups (Rincón et al., 2018), as result of the hydration processes that took place during alkali activation. Finally, in the LR90MK10 AAM, a structural reorganization is observed after firing at 800 °C, which is indicated by the very broad band shown in the region of 800-1200 cm^{-1} as result of the stretching vibrations of the Si(Al)–O groups (Figure 4.32d) (Lemougna et al., 2017). This change in the polymeric matrix, along with the incomplete dihydroxylation, represented by a narrower band region between 3000 cm^{-1} and 3700 cm^{-1} compared to LR90MK10 AAM, results in lower compressive strength (Adesanya et al., 2020). This data is also analyzed in a recent study (Komnitsas et al., 2021).
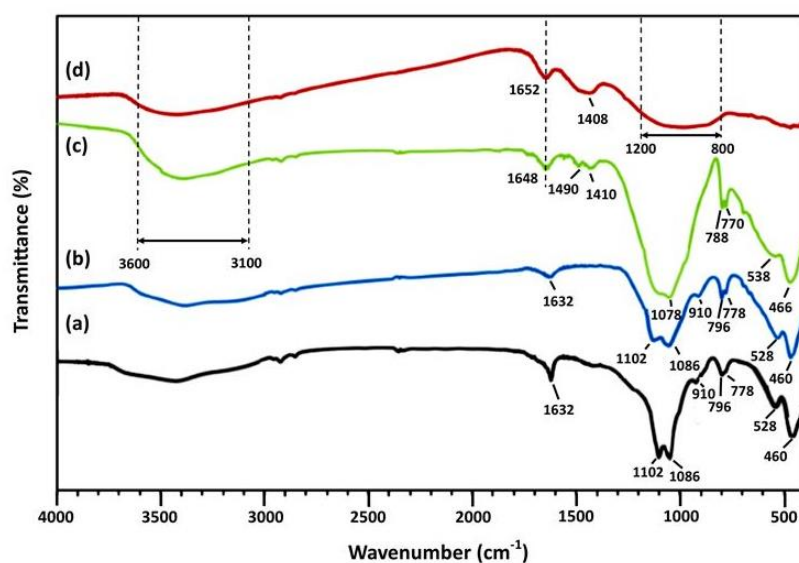
Figure 4.32. FTIR spectra of **(a)** leaching residues LR and AAMs produced using **(b)** only leaching residues (LR AAM) as well as by mixing **(c)** leaching residues and metakaolin at mass ratio 90:10 (LR90MK10) and **(d)** LR90MK10 after firing at 800 °C for 2 h.

Figure 4.33 presents the FTIR spectra of AAMs produced by mixing leaching residues LLR and LS slag at mass ratio 30:70 (LLR30LS70) as well as the precursors (i.e. LS slag and LLR residues), while the FTIR spectra of AAMs produced by mixing leaching residues LLR and PS slag at mass ratio 30:70 (LLR30PS70) and the corresponding precursors (i.e. PS slag and LLR residues) are presented in Figure 4.34.

A clear difference in the shape, position and depth of the bands of all precursors compared to both AAMs can be seen in the spectra of LLR30LS70 AAM (Figure 4.33c) and LLR30PS70 AAM (Figure 4.34c) in the region of 800-3450 cm^{-1}. After alkali activation, it is observed that the bands at 460 cm^{-1}, 620 cm^{-1}, and 796 cm^{-1} present in the LRR remained unaffected in both AAMs (Figures 4.33c, 4.34c), thus confirming the low reactivity of LLR during alkali activation; the same bands remained unaffected after alkali activation of LR, as previously proved (Figure 4.32).
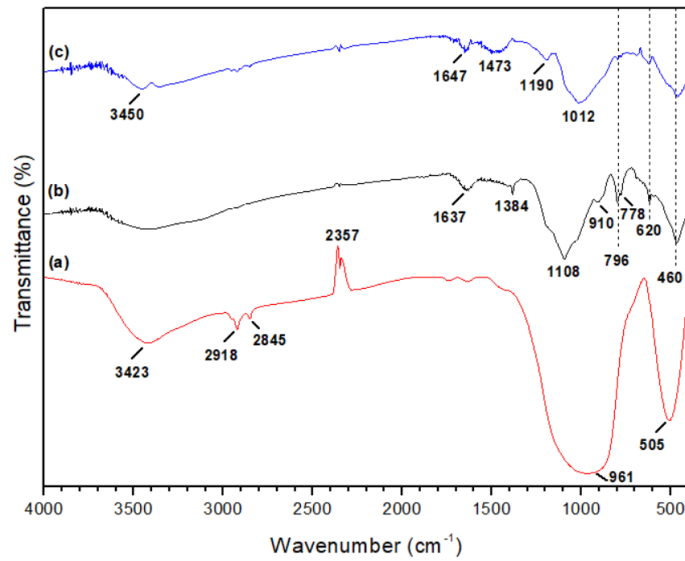
Figure 4.33. FTIR spectra of **(a)** LS slag and **(b)** leaching residues LLR as well as AAMs produced by mixing **(c)** leaching residues LLR and LS slag at mass ratio 30:70 (LLR30LS70).
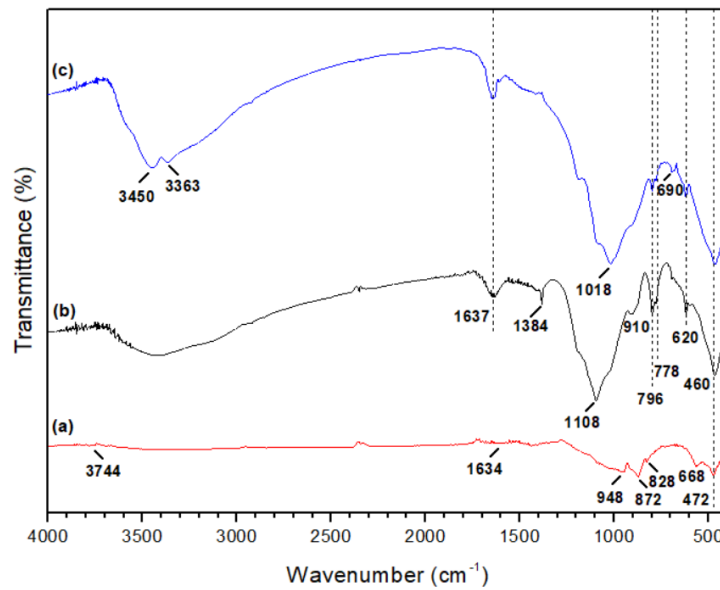
Figure 4.34. FTIR spectra of **(a)** PS slag and **(b)** leaching residues LLR as well as AAM produced by mixing **(c)** leaching residues LLR and PS slag at mass ratio 30:70 (LLR30PS70).

However, the small band at 690 cm^{-1} shown only in the LLR30PS70 AAM (Figure 4.34c) can be attributed to Fe-O and Si-O stretching and deformation vibrations (Kaze et al., 2018c). The bands at 1012 cm^{-1} and 1018 cm^{-1} in the LLR30LS70 (Figure 4.33c) and LLR30PS70 AAMs (Figure 4.34c) respectively, which are characteristic peaks of the inorganic polymer network can be attributed to the asymmetric stretching of Si-O-T bonds (T=Fe, Al or Si) (Kaze et al., 2017). Moreover, the band at 1473 cm^{-1}, present only in

the LLR30LS70 AAM (Figure 4.33c) is attributed to stretching vibrations of O-C-O bonds, due to carbonation of the remaining Na-silicate or unreacted alkali ions (Liu et al., 2017). Finally, the bands at 1634 cm^{-1}, 1637 cm^{-1} and 3423 cm^{-1} in the raw LS and PS slags (Figures 4.33a, 4.34a), which are attributed to the stretching and bending vibrations of H-O-H are shifted to 1647 cm^{-1} and 3450 cm^{-1} in both AAMs, thus indicating the presence of absorbed water in the pores of the hydrated polymeric framework (Adesanya et al., 2020).

4.5.6 Toxicity of LR, LLR residues and selected AAMs

This section investigates the toxicity of LR90MK10, LLR30LS70 and LLR30PS70 AAMs produced under the optimum synthesis conditions as well as the precursors, i.e. laterite leaching residues (LR, LLR) and ferronickel slags (PS and LS), using the EN 12457-3 test. The leaching residues of laterites exhibited noticeable toxicity in terms of Ni and Cr. More specifically, the dissolution rate of Ni was 256.5 and 719.5 mg kg^{-1} for LR and LLR, respectively, while the dissolution rate of Cr was 213.4 mg kg^{-1} for LLR. These values are much higher than the limits which are indicated by the EN 12457-3 test for wastes accepted at landfills for hazardous wastes (Table 4.4). It is also observed that Cu and Zn exceeded marginally the toxicity limits in case of disposal in landfills for inert and non-hazardous wastes (Table 4.4). Several other elements such as Al, Mn and Fe exhibited increased dissolution rates, but no limits exist for these elements in the EN 12457-3 test. The dissolution rate of some metals was anticipated to be high since laterite leaching residues were produced after leaching of the ore with a strong acidic medium. On the contrary, the raw PS and LS slags exhibited much lower toxicity compared to the laterite leaching residues. The only exception observed was in the case of PS slag where Ni (6.3 mg kg^{-1}), and Cr (0.6 mg kg^{-1}) dissolution rates exceeded the lowest limits set by the EN 12457-3 test (Table 4.4). The fact that the slags were produced after pyrometallurgical treatment of the ore at high temperature (~1450 $^{\circ}$C) and the presence of oxides explains their reduced toxicity.

After alkali activation, the dissolution rates of heavy metals for LR90MK10 and LLR30LS70 AAMs were below the toxicity limits, while LLR30PS70 AAM exhibited dissolution rate for Ni (0.4 mg kg^{-1}) equal to the limit set for disposal in landfills for inert wastes (Table 4.4). So, alkali activation of these wastes results in a reduction of their toxicity and the production of matrices with beneficial properties. Finally, it is well known from previous studies that after alkali activation the hazardous elements are trapped in the matrix and exhibit low release potential as indicated by the application of the EN 12457-3 or the US EPA test (Zhang et al., 2020c; Gijbels et al., 2019; Komnitsas et al., 2013; Wang et al., 2018).

4.5.7 Conclusions

The experimental results prove the potential of co-valorization of laterite leaching residues with the addition of metakaolin or ferronickel slags as well as the main factors affecting the production of AAMs with beneficial properties. The raw laterite leaching residues cannot be alkali activated and the compressive strength obtained was very low, namely 1.4 MPa and 10.2 MPa for LR- and LLR-based AAMs, respectively. On the contrary, the AAMs produced after alkali activation of LR-MK, LLR-LS and LLR-PS mixtures with mass ratios 90:10, 30:70 and 30:70 respectively, obtained much higher compressive strength, i.e. 45.0 MPa for LR90MK10, 27.5 MPa for LLR30LS70 and 50.7 MPa for LLR30PS70. The use of metakaolin which was produced after the calcination of kaolin at 750 °C resulted in a material with high amorphous content which is appropriate for alkali activation. The use of ferronickel slags is also considered beneficial due to their high reactivity by considering that the compressive strength obtained for LS- and PS-based AAMs were 86.0 MPa and 80.0 MPa, respectively. On the other hand, calcination of the leaching residues LR at 800 °C and 1000 °C has no beneficial effect on alkali activation. Furthermore, the AAMs produced under the optimum synthesis conditions also maintained good structural integrity after firing for a period of 2 h or 4 h at a temperature range between 200 and 1000 °C and immersion in distilled water or acidic solution (1M HCl) for 7 and 30 days. These results are important since it is the first time that the alkali activation potential of laterite leaching residues and the main factors affecting the compressive strength of the produced AAMs are investigated. Therefore, the AAMs produced after alkali activation of LLR-PS mixtures acquired very high compressive strength, due to the high reactivity of PS slag. Based on these results, it is deduced that the addition of both metallurgical slags in the starting mixture and the use of higher curing temperature have a beneficial effect on the compressive strength of the produced AAMs. It is also underlined that the produced AAMs exhibit very low toxicity, as indicated by the application of EN 12457-3 test and this results in immobilization of the hazardous elements present in the initial wastes. Finally, it was proven that the valorization of laterite leaching residues through alkali activation results in the production of higher added value products which may be used as binders or construction elements (see below in section 4.9).

4.6 Factors affecting co–valorization of L residues with MK for the production of AAMs

This section presents the alkali activation potential of leaching residues (L) which obtained after atmospheric acid leaching (AAL) of Polish laterites using H_2SO_4 as leaching solution in a 1-3 L stirred reactor. It is noted that the laterite leaching residues

exhibit low reactivity, which is not sufficient for alkali activation as mentioned earlier in section 4.1.1. Therefore, precursors obtained by mixing L with different ratios of MK were used, in order to produce AAMs with beneficial properties. Factors affecting the compressive strength and other selected properties are discussed. The structural integrity, morphology and microstructure of selected AAMs were also investigated and are presented in this Chapter.

4.6.1 Effect of H_2O/Na_2O molar ratio in the activating solution and ageing period on selected properties of the produced AAMs

In order to assess the potential of co-valorization of L residues and MK through alkali activation, precursors obtained by mixing L with different ratios of MK were used, since as mentioned earlier MK exhibits higher reactivity (Table 4.1). Figure 4.35 presents the compressive strength obtained for specimens produced by mixing L with MK at mass ratios 20:80 (L20MK80 AAM) (Figure 4.35a) and 30:70 (L30MK70 AAM) (Figure 4.35b) as a function of H_2O/Na_2O molar ratio (21.4, 17.3, 14.6) in the activating solution and ageing period (7 and 28 days). The difference in H_2O/Na_2O ratio in the activating solution is due to the slightly different S/L ratios used. The synthesis conditions used for alkali activation of the mixtures were pre-curing 4 h, curing temperature 60 °C and curing time 24 h. The SiO_2/Na_2O ratio in the activating solution was 1.0 in both cases. It is mentioned that the alkali activation of raw leaching residues was not investigated, because they contain low amounts of Al_2O_3 and SiO_2. So, MK was added to regulate the SiO_2 and Al_2O_3 ratio and increases the reactivity of the starting mixture during alkali activation.

It is seen from the experimental results that the increase of MK content in the starting mixture resulted in an increase in the compressive strength of the produced AAMs. More specifically, as the H_2O/Na_2O ratio in the activating solution decreased, the compressive strength of both AAMs increased significantly. On the contrary, the ageing period had practically no effect on the compressive strength of both AAMs. The maximum compressive strength obtained was 26.2 MPa for L20MK80 AAM using H_2O/Na_2O and SiO_2/Na_2O ratios 14.6 and 1.0, respectively and after pre-curing period 4 h, curing temperature 60 °C for 24 h and ageing period 28 days.
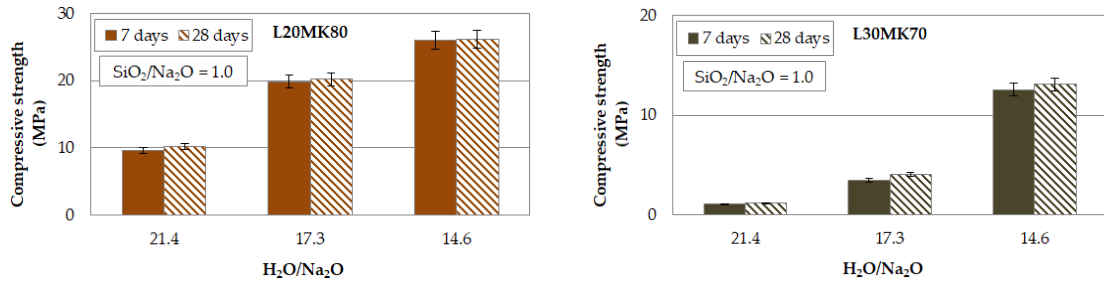
Figure 4.35. Effect of H_2O/Na_2O molar ratio in the activating solution and ageing period on the compressive strength of **(a)** L20MK80 and **(b)** L30MK70 AAMs (pre-curing time 4 h, curing temperature 60 °C, curing time 24 h; error bars indicate the standard deviation of measurements obtained from three specimens).

In order to further explain these findings, the physical properties, i.e. water absorption (%), porosity (%) and density (g cm^{-3}), of L20MK80 and L30MK70 AAMs were determined and are presented in Table 4.8. It is seen from this data that the differences in all properties of AAMs were negligible, thus justifying the slight difference in their compressive strength values. In particular, porosity and water absorption were 7.0 % and 4.2 % respectively for L20MK80 AAM and increased to 7.3 % and 4.5 % respectively for L30MK70 AAM, while the opposite trend was observed for density which decreased slightly from 1.7 to 1.6 g cm^{-3}.

Table 4.8. Physical properties of selected AAMs[1]

AAMs Code	Compressive strength (MPa)	Porosity (%)	Water Absorption (%)	Apparent Density (g cm^{-3})
L20MK80	25.9	7.0	4.2	1.7
L30MK70	17.6	7.3	4.5	1.6

[1]H_2O/Na_2O = 14.6, SiO_2/Na_2O = 1.0, curing at 40 °C for 24 h and ageing for 7 days

4.6.2 Effect of curing temperature on the compressive strength of the produced AAMs

Figure 4.36 presents the compressive strength of L20MK80 and L30MK70 AAMs as a function of curing temperature (40, 60, 80 and 95 °C). In all tests, the curing time and ageing period was 24 h and 7 days respectively, whereas the H_2O/Na_2O and SiO_2/Na_2O ratios were 14.6 and 1.0 respectively. It is observed that increase in temperature from 40 to 60 °C slightly affects the compressive strength of both AAMs, while a further increase above 60 °C results in a decrease in compressive strength. These results are opposite to those obtained so far for the effect of temperature on the compressive strength of the

produced AAMs. This behavior may be explained by the rapid loss of water in the reactive paste during curing above 60 °C which causes the development of microcracks and affects the microstructure of the produced AAMs.
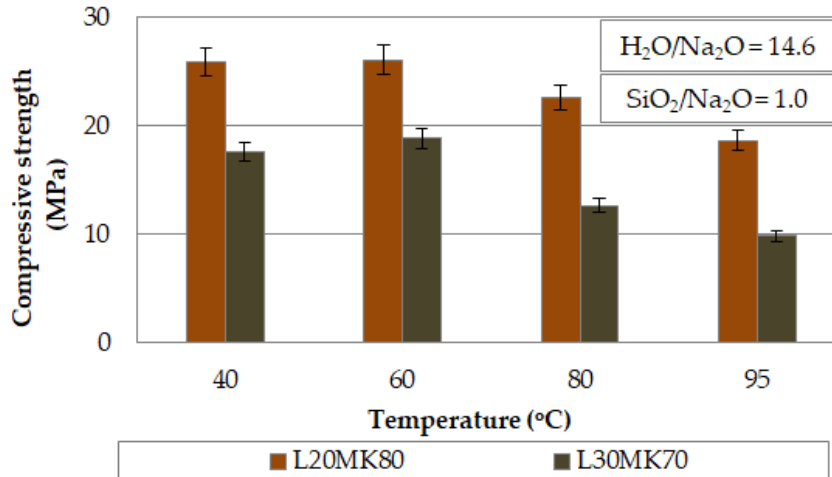
Figure 4.36. Effect of curing temperature on the compressive strength of L20MK80 and L30MK70 AAMs (pre-curing time 4 h, curing time 24 h, ageing period 7 days; error bars indicate the standard deviation of measurements obtained from three specimens).

4.6.3 Structural integrity of L20MK80 AAM

The structural integrity of L20MK80 AAM was assessed after firing for a period 2 h at a temperature range between 200 and 800 °C and after immersion in distilled water (H_2O) and acidic solution (1M HCl) for 7 and 30 days. The control AAM was produced under the optimum conditions, namely H_2O/Na_2O molar ratio 14.6; SiO_2/Na_2O molar ratio 1.0; curing temperature 40 °C; ageing period 7 days.

Table 4.9 shows the compressive strength (MPa), the weight loss (%) and the volumetric shrinkage (%) of L20MK80 AAM after durability testing. It is mentioned that the compressive strength of the control specimen was 25.9 MPa.

Table 4.9. Selected properties of L20MK80 AAM after durability tests.

Durability test	Period	Compressive strength (MPa)	Weight loss (%)	Shrinkage (%)
Control AAM[1]	-	25.9	-	-
Firing at 200 °C	2 h	20.4	0.4	3.5
Immersion in H_2O	7 days	21.8	0.2	3.1
Immersion in 1M HCl	7 days	12.0	0.9	4.7

[1] Curing at 40 °C, ageing for 7 days, H_2O/Na_2O = 14.7, SiO_2/Na_2O = 1.0

As seen in Table 4.9, the compressive strength of L20MK80 AAM decreased after the implementation of all durability tests. The only determined value (20.4 MPa) was the one obtained after firing at 200 ℃, because the specimens fired at higher temperatures, i.e 400-800 ℃, suffered severe damage and almost disintegrated. This may be explained by the phase transformations occurred and the resulting deterioration of their structural integrity after firing at high temperature (Zaharaki et al., 2010). On the contrary, the specimen exhibited better behavior after immersion in distilled water for a period of 7 days, whereas the decrease in its compressive strength was noticeable after immersion in HCl for the same period. The minimum value of 12.0 MPa was obtained after immersion in HCl. Moreover, the AAM immersed in HCl exhibited the highest weight loss (0.9 %) and volumetric shrinkage (4.7 %), whereas after immersion in distilled water exhibited the lowest weight loss (0.2 %) and volumetric shrinkage (3.1 %); these values are considered as low to very low in all cases.

Several studies pertinent to the structural integrity of AAMs using as precursors various types of slags or construction and demolition wastes (i.e. bricks and tiles) have been carried out. Komnitsas et al. (2015) showed that the final compressive strength of tile-based AAMs was severely affected when subjected to freeze-thaw cycles for 1 or 2 months. Soultana et al. (2019) showed that the compressive strength of AAMs produced using a mix ratio of 50 wt% metallurgical slag and 50 wt% brick wastes (B50S50 AAM) slightly decreased after their immersion in 1M HCl solution or distilled water for 30 days. Weight loss and volumetric shrinkage values after immersion in 1M HCl solution were 3.5 % and 8 % respectively, while after immersion in distilled water the values were much lower, 0.5 % and 0.7 % respectively. Komnitsas et al. (2021) showed that the weight loss of AAMs produced using marble waste and metakaolin at a mass ratio of 0.3 was higher (12 %) after their immersion in 1 mol/L NaCl solution over a period of 30 days, while immersion in distilled water for the same period resulted in lowerweight loss (8 %). Mohamed (2019) showed that the alkali-activated slag concrete demonstrates generally better resistance to freeze-thaw compared to OPC. Luukkonen et al. (2018b) studied the freeze-thaw resistance of blast furnace slag mortar specimens and showed that they could withstand 120 cycles.

4.6.4   Morphology–Microstructure of L residues and selected AAMs

The XRD patterns of L residues, MK and selected AAMs produced under the optimum synthesis conditions are shown in Figure 4.37.
After alkali activation, the crystalline phases of quartz, fayalite, zincite, talc, muscovite and clinochlore were evident in both AAMs, while diopside was not detected. It is observed a slight increase in the peaks' intensity of clinochlore and talc, while the phases

of quartz, fayalite and zincite appear with lower intensities, in both AAMs. The decrease of intensity of some peaks is due to metakaolin addition in the starting mixture due to its high alkali activation potential, as explained earlier (section 4.5.5) in the case of the LRMK-based AAMs. So, the specimens produced from L and MK with mixing ratio 20:80 (L20MK80 AAM) exhibit lower intensities of mineralogical phases, due to their increased amorphicity as results from the reactions between Si and Al ions, which are present in sufficient amounts, with the strong alkaline solution and the formation of aluminosilicate bonds; this results in the production of specimens with beneficial properties, which justifies the relatively higher compressive strength acquired by L20MK80 AAM (25.9 MPa). It is seen that the XRD patterns of both AAMs exhibit a hump between 2-Theta 17° and 40° which is typical for metakaolin based-AAMs, as mentioned earlier (section 4.5.5) in the case of the LRMK-based AAMs.
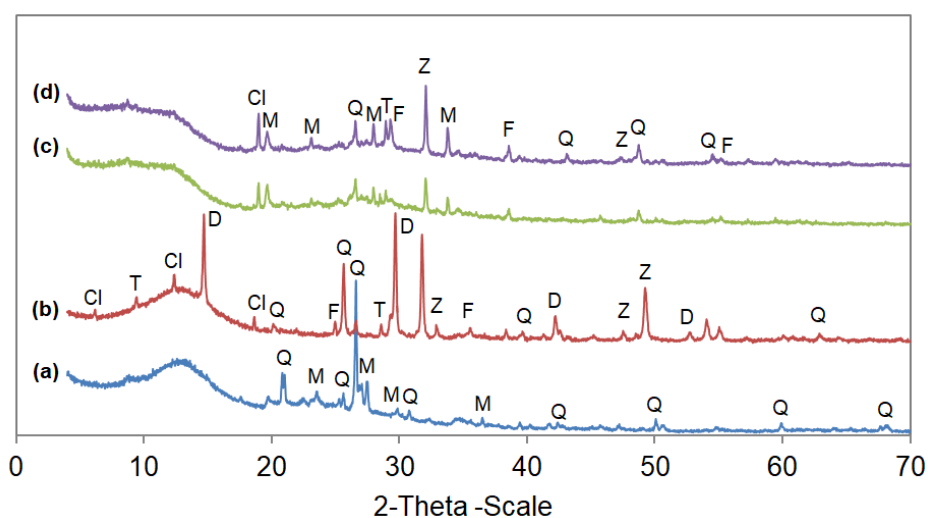
Figure 4.37. XRD patterns of **(a)** metakaolin (MK), **(b)** leaching residues L and AAMs produced by mixing **(c)** laterite leaching residues and metakaolin at mass ratio 20:80 (L20MK80) and **(d)** laterite leaching residues and metakaolin at mass ratio 30:70 (L30MK70). Phases indentified are: clinochlore (Cl), diopside (D), fayalite (F), muscovite (M), quartz (Q), talk (T), zincite (Z).

Figure 4.38 presents the FTIR spectra of AAMs produced by mixing leaching residues L and metakaolin at mass ratios 20:80 (L20MK80) and 30:70 (L30MK70) as well as the leaching residue L for comparison. After alkali activation of L, it is observed that the characteristic band at 460 cm^{-1} which is attributed to quartz remained unaffected, due to the relative inertness of quartz in the alkaline system. The weaker bands between 600 and 800 cm^{-1} in both AAMs are attributed to Si-O-Al deformation vibrations (Ricciotti et al., 2017). In addition, the small bands at 868 cm^{-1} in the L20MK80 AAM (Figure 4.38b) and 873 cm^{-1} in the L30MK70 AAM (Figure 4.38c) can be attributed to the out-of-plane bending vibrations of the carbonate ions (Kaze et al., 2020). The band at 1015 cm^{-1} seen in both AAMs (Figure 4.38b,c) is attributed to the asymmetric stretching of Si-O-Fe, Si-O-Al

and Si-O-Si bonds. This band is a characteristic peak of the inorganic polymer network (Kaze et al., 2017). Moreover, the broad bands at ~1418 cm^{-1} and 1460 cm^{-1} in the L30MK70 and L20MK80 AAMs respectively, are attributed to asymmetric stretching vibrations of O-C-O bonds due to the formation of carbonation products from the reaction between the alkali-activated silicates and the atmospheric CO_2 during the curing period (Kaze et al., 2020). The broad bands at ~3400 cm^{-1} and ~1630 cm^{-1} in both AAMs (Figure 4. 38a,b) are due to O-H stretching and bending vibrations of adsorbed molecular water in the pores of the hydrated polymeric framework (Adesanya et al., 2020).
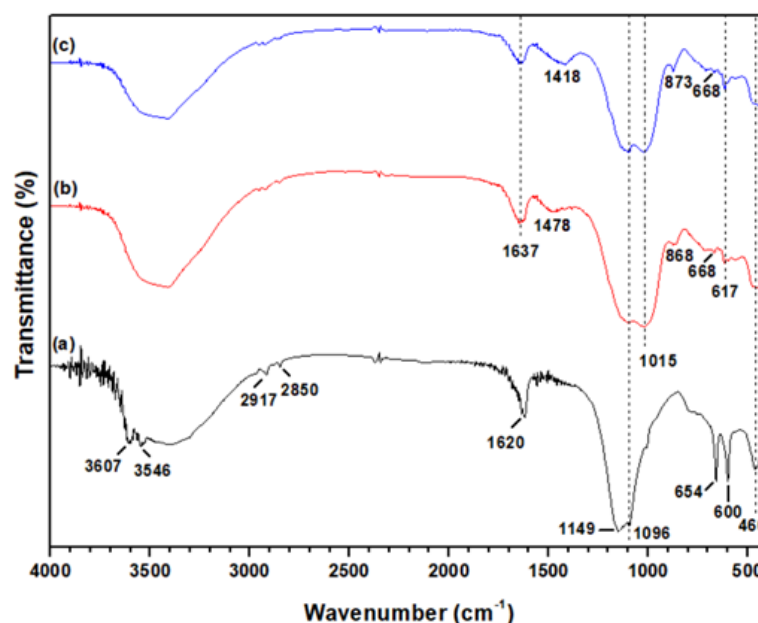
Figure 4.38. FTIR spectra of **(a)** leaching residues L and AAMs produced by mixing **(b)** L and MK at mass ratio 20:80 (L20MK80) and **(c)** L and MK at mass ratio 30:70 (L30MK70).

4.6.5 Toxicity of L residues and selected AAMs

This section investigates the toxicity of L20MK80 and L30MK70 AAMs produced under the optimum synthesis conditions as well as the raw leaching residues L, using the EN 12457-3 test. The results show that the toxicity of Polish laterite leaching residues is noticeable in terms of Ni. More specifically, the dissolution rate of Ni was 449.4 mg kg^{-1} and this value is much higher than the limits set even for disposal of this waste in a landfill for hazardous wastes (Table 4.4). The dissolution rate for Zn was equal to the limit set for disposal in landfills for inert wastes.

After alkali activation, both produced AAMs exhibited extremely low toxicity, except for the dissolution rate of Cr which was 0.86 and 0.60 mg kg^{-1} for L20MK80 and L30MK70 AAMs, respectively. Additionally, the L20MK80 AAM exhibited dissolution rate for Ni

equal to 0.64 mg kg^{-1}, thus exceeding the toxicity limit indicated for disposal in landfills for inert wastes (Table 4.4). Therefore, alkali activation of this laterite leaching residue results in the production of new products and the substantial reduction of their toxicity.

4.6.6   Conclusions

The experimental results show the beneficial effect of co-valorization potential of laterite leaching residues L when mixed with metakaolin, due to its high amorphous content and its pozzolanic nature during alkali activation. AAMs produced from L-MK mixtures at mass ratios 30:70 (L30MK70 AAM) and 20:80 (L20MK80 AAM) acquire compressive strength of 17.6 MPa and 25.9 MPa, respectively. The H_2O/Na_2O molar ratio in the activating solution is a crucial parameter during alkali activation since higher H_2O/Na_2O ratios indicate excess of water which may remain unreacted under specific synthesis conditions and thus AAMs with poor mechanical properties are produced. On the contrary, the ageing period has practically no effect on the compressive strength of the produced AAMs, whereas the curing temperature when exceeds 60 $^{\circ}$C results in a decrease of the compressive strength, due to the rapid loss of water from the reactive paste. The results also indicate that the L20MK80 AAM produced under the optimum synthesis conditions (using molar ratios H_2O/Na_2O, 14.6 and SiO_2/Na_2O, 1.0; pre-curing time, 4 h; curing temperature, 40 $^{\circ}$C, curing time, 24 h and ageing period, 7 days) exhibited sufficient structural integrity after firing at 200 $^{\circ}$C for 2 h or after immersion in distilled water and 1M HCl for 7 days. Furthermore, useful insights on the beneficial effect of metakaolin addition in the initial mixture during alkali activation of laterite leaching residues were provided from XRD and FTIR analyses. Moreover, both AAMs exhibited low toxicity, as indicated by the application of the EN 12457-3 test. In conclusion, these findings prove that alkali activation may be used for the co-valorization of laterite leaching residues and metakaolin and the production of AAMs with beneficial properties which may be used as binders or construction elements (see below in section 4.9).

4.7 Comparison of the results of this PhD thesis with those produced in earlier studies

Table 4.10 compares the results of this PhD thesis, which are related to the alkali activation of laterite leaching residues (i.e LR, LLR and L), with those obtained in earlier studies aiming at the alkali activation of lateritic materials.

Gualtieri et al. (2015) synthesized AAMs by mixing calcined laterite (700 °C for 2 h) with metakaolin, using as activators H_3PO_4 or NaOH and Na_2SiO_3 solution. The produced

specimens acquired low compressive strength, 4 MPa, when the curing temperature was 60 °C after an ageing period of 28 days. Phummiphan et al. (2016) produced AAMs by mixing marginal lateritic soil with fly ash at a mass ratio 70:30, using NaOH and Na_2SiO_3 solutions as activators. The produced specimens acquired compressive strength of 7.1 MPa after curing at 27-30 °C and ageing for 7 days. Lemougna et al. (2017) prepared AAMs by mixing calcined laterite (700 °C for 2 h) with slag, using as activator NaOH and Na_2SiO_3 solutions.

Table 4.10. Comparison of results obtained from previous studies for the production of laterite-based AAMs.

Raw Materials	SiO_2/Na_2O molar ratio	Conditions		Compressive strength (MPa)	Reference
		Temperature (°C)	Ageing period (Days)		
Laterite (calcined at 700 °C for 2 h) and metakaolin	3.0	60	28	4	Gualtieri et al., 2015
Marginal lateritic soil and fly ash	5.6	27-30	7	7.1	Phummiphan et al., 2016
Laterite (calcined at 700 °C for 2 h), slag	1.6	25	28	65	Lemougna et al., 2017
Iron - rich laterite (calcined at 700 °C for 4 h and bagasse fibers	1.4	room temperature	28	14-50	Nkwaju et al., 2019
Laterite (calcined at 600 °C), and metahalloysite (calcined halloysite clay at 600 °C)	0.75	25±3	28	45	Kaze et al., 2020
Greek laterite leaching residues and metakaolin	1.0	80	7	45	This study
Greek laterite leaching residues and Polish ferronickel slag	0.3	95	7	51	This study
Greek laterite leaching residues and metallurgical ferronickel slag	1.0	95	7	26	This study
Polish laterite leaching residues and metakaolin	1.0	60	28	26	This study

The results showed that the replacement of laterite by 50 % slag resulted in increase of compressive strength to 65 MPa after curing at 25 °C and ageing for 28 days. Nkwaju et al. (2019) produced AAMs from iron-rich laterite and sugarcane bagasse fibers using Na_2SiO_3 solution. Prior to the production of AAMs the iron-rich laterite was calcined at 700 °C for 4 h. The compressive strength achieved for the produced specimens was 50 MPa and 14 MPa without and with the addition of 7.5 wt% fibers, respectively, after curing at room temperature and ageing for 28 days. Kaze et al. (2020) produced AAMs using calcined laterite and meta-halloysite as precursors and NaOH and Na_2SiO_3 solutions, as activators. The laterite was calcined at 600 °C, while the meta-halloysite was obtained by calcining the clay fraction of halloysite at 600 °C for 4 h. The produced AAMs acquired a compressive strength of 45 MPa after curing at 25±3 °C and ageing for 28 days.

In the present thesis, the produced AAMs which were produced by mixing laterite leaching residues LR with 10 wt% metakaolin acquired a quite high compressive strength, 41 MPa. On the other hand, the co-valorization of LLR with PS and LS slags at mass ratio of 30:70 resulted in the production of AAMs with compressive strength of almost 50 and 26 MPa, respectively. Furthermore, alkali activation of laterite leaching residues L with the addition of MK at mass ratio of 20:80 resulted in the production of AAMs with compressive strength of 26 MPa. The SiO_2/Na_2O molar ratios varied from 0.3 to 1.0, due to the different mineralogy and properties of the starting mixtures. Finally, the results show that the addition of metakaolin or slags results in the successful alkali activation and co-valorization of by-products with low reactivity and the production of AAMs with beneficial properties.

4.8 Effect of selected molar ratios of oxides present in the reactive paste

In order to further explain the role of synthesis conditions on the alkali activation of the raw materials tested, selected molar ratios of oxides present in the reactive paste were calculated and presented in Table 4.11. In this Table, the compressive strength of AAMs is also given for comparison. The effect of the H_2O/Na_2O molar ratio in the activating solution is a crucial factor and may indicate the compressive strength of the produced AAMs for each raw material used. Moreover, the $(SiO_2+Al_2O_3)/Na_2O$ ratio in the reactive paste may predict the degree of hydrolysis and dissolution of Si and Al which polymerize and polycondensate. It is known that lower or higher ratios indicate excess or deficiency of the activating solution, resulting in the production of AAMs with lower compressive strength (Tuyan et al., 2018). Regarding the slags valorization, it is observed that AAMs produced from mixtures rich in Al_2O_3 (Table 3.2), thus with lower SiO_2/Al_2O_3

and higher $(SiO_2+Al_2O_3)/Na_2O$ ratios, obtained higher compressive strength, because the higher content of Al_2O_3 in the reactive paste promotes the dissolution of Al and subsequently the rate of alkali activation reactions.The actual required amounts of SiO_2 and Al_2O_3 for these reactions depend on the reactivity of the mineralogical phases present in the raw materials tested. For example, it is seen from Table 4.11, that the FS30LS70 AAM obtained much higher compressive strength (77.9 MPa), compared to the value obtained (44.8 MPa) for FS-based AAM, due to the increased reactivity of LS slag (Table 4.1). Similar behavior is seen in AAMs produced from mixtures of laterite leaching residues (LR, LRR and L) and PS, LS slags or MK.

Table 4.11. Selected oxides molar ratios in the reactive paste of selected AAMs.

AAM Code	Compressive strength (MPa)	NaOH (M)	SiO_2/Al_2O_3	$(SiO_2+Al_2O_3)/Na_2O$	Fe_2O_3/Na_2O	Fe_2O_3/CaO
PS	67.0		7.0	8.6	3.7	1.1
LS	80.1	8	7.2	14.9	6.1	4.1
FS	44.8	6	20.2	13.8	8.5	20.2
FSP	27.2	10	16.3	15.1	3.0	1.9
FS30LS70	77.9	8	8.9	13.1	6.1	5.8
FSP30LS70	57.3	10	8.9	11.3	5.3	5.8
LR	1.43		26.0	8.4	4.4	4.8
MK	55.0	8	2.8	6.7	0.02	2.1
LR90MK10	41.0		10.4	9.3	3.9	4.8
LLR	10.2	10	17.8	6.8	2.1	22.0
LLR30PS70	51.0		8.7	7.4	2.9	1.5
LLR30LS70	28.0	8	9.0	13.2	5.0	5.3
L30MK70	17.6		3.4	4.2	0.1	0.2
L20MK80	25.9	10	3.1	5.1	0.1	0.2

More specifically, the compressive strength of LLR30PS70 AAM increased by 80 % to 51.0 MPa compared to the compressive strength (10.2 MPa) of the AAM produced after alkali activation of leaching residues LR. This behavior is justified both by the reactivity of PS slag (Table 4.1) and the values of the SiO_2/Al_2O_3 and $(SiO_2+Al_2O_3)/Na_2O$ ratios in the reactive paste. In addition, the effect of the molar ratios Fe_2O_3/Na_2O and Fe_2O_3/CaO during alkali activation was also investigated. The role of Fe cannot be easily elucidated although its content is high in several slags of the non-ferrous and steel industry. According to Komnitsas et al. (2019a), the Fe_2O_3/Na_2O ratio in the activating solution decreases as the molarity of NaOH solution increases during the production of PS slag-

based AAMs. Recent studies investigating the behavior of Fe mention that Fe^{2+} may be oxidized to Fe^{3+} during alkaline activation in the inorganic polymer binder, or incorporated into the polysialate (Si-O-Al) as network modifier or even participate in carbonation reactions (Onisei et al., 2018; Peys et al., 2018). In our case, no efflorescence was noticed on any of the produced specimens. Apart from the amorphous content, the alkali activation of iron-rich raw materials with lower Ca content, results in the formation of a stronger bonding network due to the formation of Fe-O-Si-O-Fe linkages (Komnitsas et al., 2009; Peys et al., 2019c). This is confirmed by our data, which show that the Fe_2O_3/CaO ratio is higher for LS specimens compared to the respective ratio for PS specimens, and thus the compressive strength value of LS based AAMs is higher (81.0 MPa).

These findings indicate that when these ratios obtain optimum values, the produced AAMs which acquire higher compressive strength. More specifically, optimum values of SiO_2/Al_2O_3 ratio range between 7.0-20.2 for slag-based AAMs and 2.8-26.0 for laterite leaching residue-based AAMs. On the other hand, optimum ratios of $(SiO_2+Al_2O_3)/Na_2O$ range between 8.6 and 15.1 or 4.2 and 13.2 for AAMs produced from slags and laterite leaching residues, respectively. In addition, optimum ratios of Fe_2O_3/Na_2O range between 3.0 and 8.5, while optimum ratios of Fe_2O_3/CaO between 1.1 and 20.2 for slags-based AAMs. The same ratios range between 0.1-5.0 and 0.2-22.0 for laterite leaching residue-based AAMs.

4.9 Potential application of produced AAMs in the construction industry

This section investigates the potential application of the produced AAMs as alternative materials in the construction industry. More specifically, it compares the properties of selected AAMs with those of concrete as well as with the requirements of load-bearing and engineering bricks.

4.9.1 Comparison of produced slag-based AAMs with high-performance concrete

Concrete is the most important material of the construction sector, due to its availability, low cost, high structural performance and ability to take any shape or size. However, concrete is responsible for environmental impacts, since its production emits high volumes of CO_2 in the atmosphere. It is well known that OPC is the main binder in concrete and its production is one the most energy intensive processes, since it consumes

12 % to 15 % of the total industrial energy requirements and is responsible for 7 % to 10 % of the global CO_2 emissions, while aggregate production poses severe environmental problems in surrounding areas, as previously mentioned in section 1.1. There are several types of concrete suitable for numerous uses, such as reinforced concrete, lightweight concrete, high-strength concrete, high-performance concrete (HPC) and precast concrete (Kosmatka et al., 2003). Several studies have indicated that AAMs can be used as an alternative binder to replace OPC in several applications (Mohamed, 2019; Passuello et al., 2017; Komnitsas, 2011; Nasvi et al., 2013). Table 4.12 presents the compressive strength (MPa) and water absorption (%) of AAMs produced from only PS or LS slags, by mixing FS and LS slags at mass ratio 30:70 (FS30LS70) as well as after firing PS, FS30LS70, and FSP30LS70 AAMs at 400 or 250 °C.; the compressive strength and water absorption of HPC are also given for comparison (Kosmatka et al. 2003). It is seen from this Table that the compressive strength values of almost all selected AMMs are similar or exceed the strength of HPC (70 MPa), while the values of water absorption (%) of selected AAMs are within the water absorption limits for HPC. It is important to mention that the compressive strength of HCP reaches 70 MPa after 28 days, while the slag-based AAMs obtained a similar or higher value after 7 days. In addition, it is observed that the liquid to solid ratios used for the production of the AAMs are quite similar to the minimum value of water to cementing materials ratio used for HPC. Therefore, the produced AAMs can be used in similar applications as HPC including tunnels, bridges and tall buildings.

Table 4.12. Comparison of selected properties of HPC and slag-based AAMs.

Properties	High-Performance concrete	AAMs			Fired AAMs		
		PS	LS	FS30LS70	PS (400 °C)	FS30LS70 (250 °C)	FSP30LS70 (250 °C)
Compressive strength (MPa)[a]	70	67	80	78	115	94	68
Water absorption (%)	2 % to 5 %	4	3	3	4	3	4
w/c[b] or L/S[c] ratio	0.20-0.45	0.2	0.2	0.2	0.2	0.2	0.2

[a] measured after 7 and 28 days for AAMs and HPC, respectively, [b]water to cementing materials ratio for HPC, [c]liquid-to-solid ratio in the starting mixture for AAMs.

In addition, one important difference between AAMs and concrete production is the raw materials used in each case. More specifically, limestone which is heated at 1450 °C is the

major raw material used in cement production to produce clinker and is then blended with additives. On the other hand, AMMs rely on minimally processed natural materials and industrial by-products or wastes and their curing takes place at low temperatures (30-90 ^{o}C) for 24 or 48 h. Moreover, AAMs exhibit similar properties to those of Portland cement, such as permeability, low alkali aggregate expansion, low shrinkage, excellent resistance to acids, sulphates, corrosion and freeze-thaw cycles (Komnitsas, 2011; Lemougna et al., 2011; Leonelli et al., 2009; Temuujin et al., 2011). The role of water during alkali activation is different than its role in hydration reactions taking place during Portland cement production. In particular, water facilitates workability of the initial reactive paste during AAM production, but it is not incorporated in the resulting structure and thus it is not involved in the main chemical reactions and is expelled during curing and subsequent drying. This has a significant impact on the mechanical and chemical properties of alkali activated (geopolymer) concrete (Davidovits, 2020). Finally, as most studies indicate the production of AAMs has lower impact on global warming than OPC concrete and therefore their use as alternative to OPC will improve the sustainability of the wider construction industry (Damineli et al., 2010; Huseien and Shah, 2020; Komnitsas, 2011; Robayo-Salazar et al., 2018; Singh and Middendorf, 2020).

4.9.2 Comparison of produced slag- or laterite residue-based AAMs with load-bearing and engineering bricks

The compressive strength of slags-based AAMs produced in this PhD thesis under the optimum synthesis conditions and the requirements for load-bearing and engineering bricks according to different classification categories (BS 3921:1965) are presented in Figure 4.39. It can be seen from this data that almost all produced AAMs exceed the requirements of the Category 7 (48.3 MPa) for load-bearing bricks. More specifically, FS- and FSP-based AAMs satisfy the requirements of Categories 5 (34.5 MPa) and 3 (20.7 MPa), respectively. It is also observed that the LS-based AAMs satisfy the requirements of the Category 10 (69.0 MPa) for load-bearing bricks. On the other hand, the FS30LS70 and FSP30LS70 AAMs produced from FS or FSPand LS slags satisfy the requirements of higher Categories, namely Category 10 (69.0 MPa) and Category 7 (48.3 MPa) respectively, compared to AAMs which produced only from FS or FSP slags. Moreover, AAMs retain sufficient structural integrity after firing at higher temperatures, while their final compressive strength increased. In particular, the compressive strength of the PS AAMs increased substantially after firing up to 400 ^{o}C, reached 115.2 MPa, and meets the requirements of Category 15 (103.5 MPa). The compressive strength of FS30LS70 and FSP30LS70 AAMs after their firing at 250 ^{o}C satisfy the requirements of Category 10 (69.0 MPa). On the other hand, the produced AAMs can be used as engineering bricks of

Categories A and B. It is observed from Figure 4.39 that all AAMs satisfy the requirements of Category B since the compressive strength is greater than 48.3 MPa and water absorption is less than 7.0 %. Finally, the fired AAMs as well as the PS and FS30LS70 AAMs can be also used as engineering bricks of Category A; their compressive strength is 69.0 MPa and water absorption is 4.0 %. It is also mentioned that PS-based AAMs maintain sufficient structural integrity even after immersion in distilled water and acidic solutions (1M HCl and 1M H_2SO_4) for 30 days. Their final compressive strength (see Figure 4.10) satisfies the requirements of Categories 4 and 5. Similar behavior was observed for FS30LS70 and FSP30LS70 AAMs which after immersion in distilled water for 30 days retain compressive strength values which satisfy the requirements of Categories 10 (69.0 MPa) and 7 (48.3 MPa), respectively, while the compressive strength after their immersion in 1M HCl exceeds the requirements of Categories 5 (34.5 MPa) and 4 (27.6 MPa), respectively (see Figures 4.18a,b).
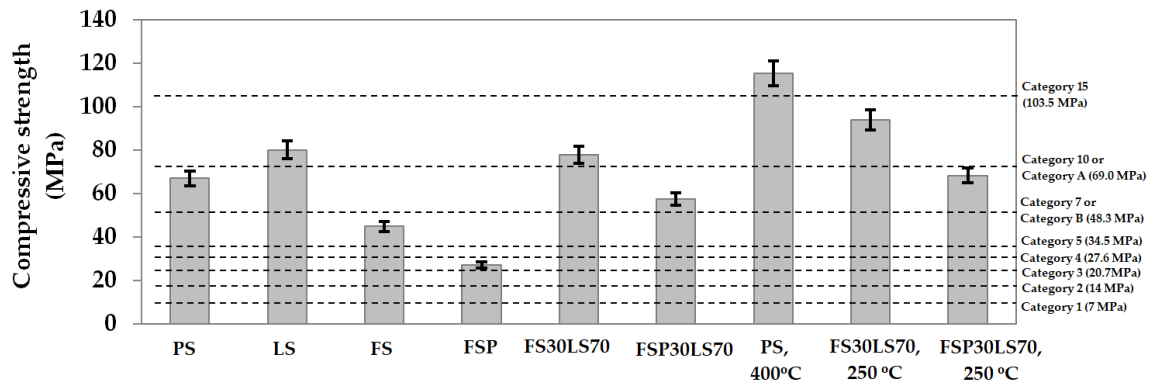
Figure 4.39. Comparison of the compressive strength of slags-based AAMs, with the limits proposed for different classification categories according to BS 3921:1965 (error bars represent the standard deviation of three measurements).

Figure 4.40 shows the compressive strength of LR-, LLR- and L-based AAMs, L20MK80, LR90MK10, LLR30LS70 and LLR30PS70 AAMs (sections 4.5.2, 4.5.3, and 4.6.2), before and after firing at 800 °C, as well as the requirements for load-bearing bricks (BS 3921:1965). It is mentioned that concrete loses its structural integrity after firing at temperature higher than 800 °C (Lahoti et al., 2019). It can be seen from this data that AAMs produced by mixing leaching residues LR or L with MK at mass ratio 90:10 (LR90MK10 AAM) and 20:80 (L20MK80 AAM) exceed the requirements of Categories 5 (34.5 MPa) and 3 (20.7 MPa) for load-bearing bricks, respectively. AAMs obtained by mixing leaching residues LLR with LS or PS slags at ratio 30:70 (LLR30LS70 and LLR30PS70 AAMs) also satisfy the requirements of specific Categories for load-bearing bricks. In particular, LLR30LS70 AAMs meet the requirements of Category 4 (27.6 MPa), while the compressive strength of LLR30PS70 AAMs meets the requirements of Category

7 (48.3 MPa) for load-bearing bricks. In addition, all AAMs maintain sufficient structural integrity even after high temperature firing at 800 °C, since their final compressive strength values satisfy at least the requirements of Categories 2 (14.0 MPa) for LR90MK10 and 1 (7.0 MPa) for LLR30LS70 and LLR30PS70 AAMs. It is also mentioned that LR90MK10, L20MK80, LLR30LS70 and LLR30PS70 AAMs maintain sufficient structural integrity after immersion in distilled water and 1M HCl for 7 days, since their final compressive strength (see Figure 4.27 and Table 4.9) satisfy the requirements of Categories 1-5.

In conclusion, these findings prove that the alkali activation is an advantageous process for the valorization or co-valorization of large volumes of metallurgical slags and laterite leaching residues and the production of sustainable building materials or binders with beneficial properties and durability.
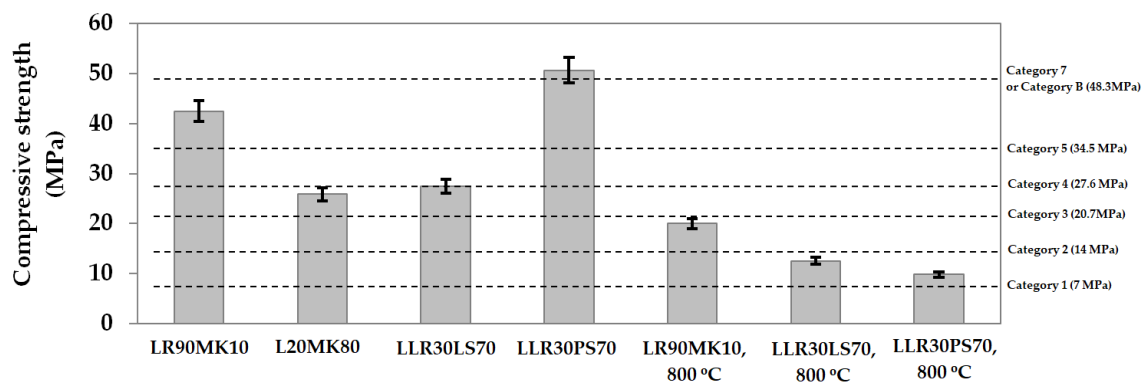

Figure 4.40. Comparison of the compressive strength of laterite leaching residue-based AAMs with the limits proposed for different classification categories according to BS 3921:1965 (error bars represent the standard deviation of three measurements).

5. **Summary and concluding remarks**

The present PhD thesis investigates in depth the alkali activation potential of various types of metallurgical slags and laterite leaching residues.

The experimental results show that the produced PS -based AAMs exhibited compressive strength that exceeds 65 MPa under the conditions H_2O/Na_2O and SiO_2/Na_2O ratios in the activating solution 14.2 and 0.3 respectively, curing temperature 80 ^{o}C, pre-curing and curing time 24 h and ageing period 7 days. Furthermore, they exhibited good structural integrity when subjected to high firing temperature for 6 h or immersed in distilled water or acidic solution (1M HCl and 1M H_2SO_4) for a period of 7-30 days. A novel aspect of this investigation is the increase of the compressive strength of the AAMs after firing at 400 ^{o}C for 6 h, due to the development of a dense and compact microstructure. These results indicate that the produced AAMs may find several applications in the construction sector, including their use as fire-resistant materials. It is also noted that they exhibit very low toxicity after the application of EN 12457-3 test, and thus alkali activation results in immobilization of hazardous elements present in the raw slag and no adverse effects are anticipated from their use.

FS- and FSP-based AAMs produced under the optimum synthesis conditions, namely pre-curing time 24 h, curing temperature 90 ^{o}C, curing time 24 h and ageing period 7 days, reached maximum compressive strength 44.8 MPa and 27.2 MPa, respectively. It is also mentioned that the SiO_2/Na_2O molar ratios in the activating solution were 1.5 and 0.9 in each case, respectively.

AAMs produced after alkali activation of FS-LS and FSP-LS mixtures at 50:50 ratio acquire compressive strength of 64.3 MPa and 45.8 MPa, respectively; the synthesis conditions were the same as in the previous case and the SiO_2/Na_2O molar ratios in the activating solution were 1.0 and 0.9 for FS- and FSP-based AAMs, respectively. In addition, AAMs produced after alkali activation of slag mixtures showed very good structural integrity after firing up to 500 ^{o}C for 6 h, immersion in distilled water and acidic solution or subjection to freeze-thaw cycles for a period of 7 or 30 days. All produced AAMs exhibited very low toxicity.

Another novel aspect of this thesis is the study of the alkali activation potential of laterite leaching residues. LR and LLR residues were alkali activated after calcination at 800 and 1000 ^{o}C, or after the addition of metakaolin or metallurgical slags at different mass ratios, in order to increase the reactivity of the starting mixture. The experimental results show that the raw LR and LLR residues cannot be actually alkali activated and the compressive strength obtained is very low to low, namely 1.4 MPa and 10.2 MPa for LR- and LLR-based AAMs, respectively. On the contrary, the AAMs produced from LR-MK, LLR-LS, and LLR-PS mixtures with mass ratios 90:10, 30:70, and 30:70 respectively, obtained much higher compressive strength, i.e. 45.0 MPa for LR90MK10, 27.5 MPa for LLR30LS70, and 50.7 MPa for LLR30PS70. The AAMs maintained good structural

integrity after firing for a period of 2 h or 4 h at a temperature range between 200 and 1000 ^{o}C and immersion in distilled water or 1M HCl for 7 and 30 days, while calcination of the LR residues at 800 and 1000 ^{o}C had no beneficial effect on alkali activation. Addition of MK, PS or LS in the starting mixture resulted in the production of AAMs with higher compressive strength. It is also underlined that the AAMs exhibited very low toxicity indicating the successful immobilization of hazardous elements present in the initial wastes.

In addition, the experimental results prove the successful alkali activation of laterite leaching residues L and metakaolin mixtures. More specifically, LR-MK mixtures at mass ratio 30:70 and 20:80 resulted in the production of AAMs with compressive strength values 17.6 MPa and 25.9 MPa, respectively.

Finally, it is concluded that the AAMs produced from slags have properties in terms of strength and durability similar to high-performance concrete and can be used in demanding applications. Apart from the above applications, the produced AAMs may be used as binders or construction elements, because they meet the requirements for load-bearing and engineering bricks for different classification categories.

Finally, the findings of this PhD thesis prove that alkali activation can be used for the (co)valorization of hazardous wastes, thus improving the sustainability and minimizing the environmental impacts of the metallurgical industry in line with circular economy and zero-waste principles.

References

1. Abdel-Ghani, N.T.; Elsayed, A.H.; AbdelMoied, S. Geopolymer synthesis by the alkali-activation of blast furnace steel slag and its fire-resistance. *HBRC Journal* **2018**, 14 (2), 159–164. https://doi.org/10.1016/j.hbrcj.2016.06.001.

2. Abdullah, M.M.A.; Kamarudin, H.; Bnhussain, M.; Khairul Nizar, I.; Mastura, W.I.W. Mechanism and Chemical Reaction of Fly Ash Geopolymer Cement-A Review. *International Journal of Pure and Applied Sciences and Technology* **2011**, 6 (1), 35–44. www.ijopaasat.in.

3. Abdullah, M.M.A.B.; Hussin, K.; Bnhussain, M.; Ismail, K.N.; Yahya, Z.; Abdul Razak, R. Fly Ash-based Geopolymer Lightweight Concrete Using Foaming Agent. *International Journal of Molecular Sciences* **2012**, 13 (6), 7186–7198. https://doi.org/10.3390/ijms13067186.

4. Adesanya, E.; Ohenoja, K.; Yliniemi, J.; Illikainen, M. Mechanical trans-formation of phyllite mineralogy toward its use as alkali-activated binderprecursor. *Minerals Engineering* **2020**, 145, 106093. https://doi.org/10.1016/j.mineng.2019.106093.

5. Agnello, A.C.; Potysz, A.; Fourdrin, C.; Huguenot, D.; Chauhan, P.S. Impact of pyrometallurgical slags on sunflower growth, metal accumulation and rhizosphere microbial communities. *Chemosphere* **2018**, 208, 626–639. https://doi.org/10.1016/j.chemosphere.2018.06.038.

6. Ahmaruzzaman, M. A review on the utilization of fly ash. *Progress in Energy and Combustion Science* **2010**, 36 (3), 327–363. https://doi.org/10.1016/j.pecs.2009.11.003.

7. Akcil, A.; Agcasulu, I.; Swain, B. Valorization of waste LCD and recovery of critical raw material for circular economy: A review. *Resources, Conservation and Recycling* **2019**, 149, 622–637. https://doi.org/10.1016/j.resconrec.2019.06.031.

8. Al-Harahsheh, M.S.; Al Zboon, K.; Al-Makhadmeh, L.; Hararah, M.; Mahasneh, M. Fly ash based geopolymer for heavy metal removal: A case study on copper removal. *Journal of Environmental Chemical Engineering* **2015**, 3 (3), 1669–1677. https://doi.org/10.1016/j.jece.2015.06.005.

9. Ali, M.B.; Saidur, R.; Hossain, M.S. A review on emission analysis in cement industries. *Renewable and Sustainable Energy Reviews* **2011**, 15 (5), 2252–2261. https://doi.org/10.1016/j.rser.2011.02.014.

10. Alonso, S.; Palomo, A. Alkaline activation of metakaolin and calcium hydroxide mixtures: influence of temperature, activator concentration and solids ratio. *Materials Letters* **2001**, 47 (1–2), 55–62. https://doi.org/10.1016/S0167-577X(00)00212-3.

11. Alouani, M.EL; Alehyen, S.; Achouri, M.EL; Taibi, M. Removal of Cationic Dye-Methylene Blue-from Aqueous Solution by Adsorption on Fly Ash-based Geopolymer. *Journal of Materials and Environmental Sciences* **2018**, 9 (1), 32–46. https://doi.org/10.26872/jmes.2018.9.1.5.

12. Alshaaer, M.; Zaharaki, D.; Komnitsas, K. Microstructural characteristics and adsorption potential of zeolitic tuff-metakaolin geopolymers. *Desalination Water Treatment* **2015**, 56 (2), 338–345. https://doi.org/10.1080/19443994.2014.938306.

13. Aredes, F.G.M.; Campos, T.M.B.; Machado, J.P.B.; Sakane, K.K.; Thim, G.P.; Brunelli, D.D. Effect of cure temperature on the formation of metakaolinitebased geopolymer. *Ceramics International* **2015**, 41 (6), 7302–7311. https://doi.org/10.1016/j.ceramint.2015.02.022.

14. Ascensão, G.; Marchi, M.; Segata, M.; Faleschini, F.; Pontikes, Y. Reaction kinetics and structural analysis of alkali activated Fe-Si-Ca rich materials. *Journal of Cleaner Production* **2020**, 246, 119065. https://doi.org/10.1016/j.jclepro.2019.119065.

15. ASTM (American Society for Testing and Materials), 2018. C1262-10 Standard Test Method for Evaluating the Freeze-Thaw Durability of Dry Cast Segmental Retaining Wall

Units and Related Concrete Units. ASTM International, West Conshohocken, PA 2018. Retrieved from. www.astm.org.

16. Aughenbaugh, K.L.; Williamson, T.; Juenger, M.C.G. Critical evaluation of strength prediction methods for alkali-activated fly ash. *Materials and Structures* **2015**, 48 (3), 607–620. https://doi.org/10.1617/s11527-014-0496-z.

17. Azevedo, A.G.D.S.; Strecker, K. Brazilian fly ash based inorganic polymers production using different alkali activator solutions. *Ceramics International* **2017**, 43 (12), 9012–9018. https://doi.org/10.1016/j.ceramint.2017.04.044.

18. Azimi, E.A.; Abdullah, M.M.A.B.; Yun Ming, L.; Heah, C.Y.; Hussin, K.; Aziz, I.H. Review of geopolymer materials for thermal insulating applications. *Key Engineering Materials* **2015**, 660, 17–22. https://doi.org/10.4028/www.scientific.net/KEM.660.17.

19. Bai, T.; Song, Z.-G.; Wu, Y.-G.; Hu, X.-D.; Bai, H. Influence of steel slag on the mechanical properties and curing time of metakaolin Geopolymer. *Ceramics International* **2018**, 44 (13), 15706–15713. https://doi.org/10.1016/j.ceramint.2018.05.243.

20. Bakharev, T. Geopolymeric materials prepared using Class F fly ash and elevated temperature curing. *Cement and Concrete Research* **2005**, 35 (6), 1224–1232. https://doi.org/10.1016/j.cemconres.2004.06.031.

21. Bakharev, T.; Sanjayan, J.G.; Chen, Y.-B. Resistance of alkali-activated slag concrete to acid attack. *Cement and Concrete Research* **2003**, 33 (10), 1607–1611. https://doi.org/10.1016/S0008-8846(03)00125-X.

22. Baldassarre, B.; Schepers, M.; Bocken, N.; Cuppen, E.; Korevaar, G.; Calabretta, G. Industrial Symbiosis: towards a design process for eco-industrial clusters by integrating Circular Economy and Industrial Ecology perspectives. *Journal of Cleaner Production* **2019**, 216, 446–460. https://doi.org/10.1016/j.jclepro.2019.01.091.

23. Bankowski, P.; Zou, L; Hodges, R.J.; Singh, P.S.; Trigg, M. Brown coal fly ash stabilisation by inorganic polymers. In: Lukey, G.C. (Ed.), Proceedings of International Conference Geopolymers, Melbourne, Australia, 28–29 October 2002 (in CD-ROM). Geopolymer Institute.

24. Barbosa, V.F.F; Mackenzie, K.J.D.; Thaumaturgo, C. Synthesis and characterization of sodium polysialate inorganic polymer based on alumina and silica. In: Davidovits, J., Davidovits, R., James, C. (Eds.), Proceedings of the 2nd International Conference on Geopolymer, Saint Qunentin, France, 30 June 30–2 July 1999; pp. 65–78.

25. Bartzas, G.; Komnitsas, K. Life cycle assessment of ferronickel production in Greece. *Resources, Conservation & Recycling* **2015**, 105, 113–122. https://doi.org/10.1016/j.resconrec.2015.10.016.

26. Bell, J.; Gordon, M.; Kriven, W.M. Use of Geopolymeric Gements as a Refractory Adhesive for Metal and Ceramic Joins. *Ceramic Engineering and Science Proceeding* **2005**, 26 (3), 407–413. https://doi.org/10.1002/9780470291238.ch46.

27. Bernal, S.A.; de Gutierrez, R.M.; Provis, J.L.; Rose, V. Effect of silicate modulus and metakaolin incorporation on the carbonation of alkali silicate-activated slags. *Cement and Concrete Research* **2010**, 40, 898–907. https://doi.org/10.1016/j.cemconres.2010.02.003.

28. Bernal, S.A.; Provis, J.L.; Rose, V.; Mejía de Gutierrez, R. Evolution of binder structure in sodium silicate-activated slag-metakaolin blends. *Cement and Concrete Composites* **2011,** 33 (1), 46–54. https://doi.org/10.1016/j.cemconcomp.2010.09.004.

29. Bernal, S.A.; Rodríguez, E.D.; de Gutiérrez, R.M.; Provis, J.L. Performance at high temperature of alkali-activated slag pastes produced with silica fume and rice husk ash based activators. *Material de Construcción* **2015**, 65 (318), e049. http://dx.doi.org/10.3989/mc.2015.03114.

30. Bernal, S.A.; San Nicolas, R.; Myers, R.J.; Mejía de Gutiérrez, R.; Puertas, F.; van Deventer J.S.J.; Provis, J.L. MgO content of slag controls phase evolution and structural changes induced by accelerated carbonation in alkali-activated binders. *Cement Concrete Research* **2014**, 57, 33–43. https://doi.org/10.1016/j.cemconres.2013.12.003.

31. British Standards Institute. BS EN 12457-3: *Characterisation of waste. Leaching. In Compliance Test for Leaching of Granular Waste Materials and Sludges. Two Stage Batch Test at a Liquid to Solid Ratio of 2 L/kg and 8 L/kg for Materials with a High Solid Content and with a Particle Size below 4 mm (without or with Size Reduction)*; British Standards Institue: London, UK, 2002.

32. BSI (British Standards Institute), 2007. BS EN 1936: *Natural Stone Test Methods. Determination of Real Density and Apparent Density and of Total and Open Porosity*; NP EN 1936:2006. 2007. BSI, London, UK.

33. Buchwald, A.; Hilbig, H.; Kaps, Ch. Alkali-activated metakaolin-slag blends-performance and structure in dependence of their composition. *Journal of Materials Science* **2007**, 42 (9), 3024–3032. https://doi.org/10.1007/s10853-006-0525-6.

34. Bumanis, G.; Novais, R.M.; Carvalheiras, J.; Bajare, D.; Labrincha, J.A. Metals removal from aqueous solutions by tailored porous waste-based granulated alkali-activated materials. *Applied Clay Science* **2019**, 179, 105147. https://doi.org/10.1016/j.clay.2019.105147.

35. Bumanis, G.; Vitola, L.; Bajare, D.; Dembovska, L.; Pundiene, I. Impact of reactive SiO_2/Al_2O_3 ratio in precursor on durability of porous alkali activated materials. *Ceramics International* **2017**, 43 (7), 5471–5477. https://doi.org/10.1016/j.ceramint.2017.01.060.

36. Chen, C.; Habert, G.; Bouzidi, Y.; Jullien, A. Environmental impact of cement production: Detail of the different processes and cement plant variability evaluation. *Journal of Cleaner Production* **2010**, 18 (5), 478–485. https://doi.org/10.1016/j.jclepro.2009.12.014.

37. Chen, L.; Wang, L.; Cho, D.-W.; Tsang, D.C.W.; Tong, L.; Zhou, Y.; Yang, J.; Hu, Q.; Poon, C.S. Sustainable stabilization/solidification of municipal solid waste incinerator fly ash by incorporation of green materials. *Journal of Cleaner Production* **2019**, 222, 335–343. https://doi.org/10.1016/j.jclepro.2019.03.057.

38. Chen, L.; Wang, Z.; Wang, Y.; Feng, J. Preparation and Properties of Alkali Activated Metakaolin-Based Geopolymer. *Materials* **2016**, 9 (9), 767. https://doi.org/10.3390/ma9090767.

39. Chen, W.; Peng, R.; Straub, C.; Yuan, B. Promoting the performance of one-part alkali-activated slag using fine lead-zinc mine tailings. *Construction and Building Materials* **2020**, 236, 117745. https://doi.org/10.1016/j.conbuildmat.2019.117745.

40. Cheng, T.W.; Chiu, J.P. Fire-resistant geopolymer produced by granulated blast furnace slag. *Minerals Engineering* **2003**, 16 (3), 205–210. https://doi.org/10.1016/S0892-6875(03)00008-6.

41. Cioffi, R.; Maffucci, L.; Santoro, L. Optimization of geopolymers synthesis by calcinations and polycondensation of a kaolinitic residue. *Resources Conservation and Recycling* **2003**, 40 (1), 27–38. https://doi.org/10.1016/S0921-3449(03)00023-5.

42. Criado, M.; Aperador, W.; Sobrados, I. Microstructural and Mechanical Properties of Alkli Activated Colombian Raw Materials. *Materials* **2016**, 9 (3), 158. https://doi.org/10.1007/s10971-016-3983-6.

43. Criado, M.; Fernández-Jiménez, A.; de la Torre, A.G.; Aranda, M.A.G.; Palomo A. An XRD study of the effect of the SiO_2/Na_2O ratio on the alkali activation of fly ash. *Cement and Concrete Research* **2007**, 37 (5), 671–679. https://doi.org/10.1016/j.cemconres.2007.01.013.

44. Cui, Y.; Wang, D.; Wang, Y.; Sun, R.; Rui, Y. Effect of the $n(H_2O:Na_2O_{eq})$ ratio on the geopolymerization process and microstructures of fly ash-based geopolymers *Journal of Non-Crystalline Solids* **2019**, 551, 19–28. https://doi.org/10.1016/j.jnoncrysol.2018.12.033.

45. Damineli, B.L.; Kemeid, F.M.; Aguiar, P.S.; John, M. Measuring the eco-efficiency of cement use. *Cement and Concrete Composites* **2010**, 32, 555-62. https://doi.org/10.1016/j.cemconcomp.2010.07.009.

46. Davidovits J. Geopolymer Chemistry and Properties, In Proceedings of the 1st International Conference on Geopolymer, Compiegne, France, 1–3 June 1988; vol. 1, pp. 25–48.

47. Davidovits, J. Chemistry of Geopolymeric Systems, Terminology. In: Davidovits, J., Orlinski, J. (Eds.), Proceedings of the Second International Conference on Geopolymers, Saint-Quentin, France, 28–29 June 1999; pp. 9–40.

48. Davidovits, J. Geopolymer Chemistry & Applications, 5th edition, *Institut Géopolymère, Saint-Quentin* **2020**.

49. Davidovits, J. Geopolymer chemistry and sustainable development. The Poly(sialate) terminology: a very useful and simple model for the promotion and understanding of green-chemistry. Proceedings of Geopolymere Conference, Geopolymer Institute, Saint-Quentin, France 2005; pp. 9-15.

50. Davidovits, J. Geopolymers-Inorganic Polymeric New Materials. *Journal of Thermal Analysis* **1991**, 37 (8), 1633–1656. https://doi.org/10.1007/BF01912193.

51. De Silva, P.; Sagoe-Crenstil, K.; Sirivivatnanon, V. Kinetics of geopolymerization: Role of Al_2O_3 and SiO_2. *Cement and Concrete Research* 2007, 37 (4), 512–518. https://doi.org/10.1016/j.cemconres.2007.01.003.

52. Directive 2009/125/EC of the European Parliament and of the Council of 21 October 2009 establishing a framework for the setting of ecodesign requirements for energy-related products.

53. Djobo, J.N.Y.; Elimbi, A.; Tchakouté, H.K.; Kumar, S. Mechanical activation of volcanic ash for geopolymer synthesis: effect on reaction kinetics, gel characteristics, physical and mechanical properties. *RSC Advances* **2016**, 6 (45), 39106–39117. http://doi.org/10.1039/C6RA03667H.

54. Duxson, P.; Fernández-Jiménez, A.; Provis, J.L.; Lukey, G.C.; Palomo, A.; van Deventer, J.S.J. Geopolymer technology: the current state of the art. *Journal of Materials Science* **2007a**, 42 (9), 2917–2933. http://dx.doi.org/10.1007/s10853-006-0637-z.

55. Duxson, P.; Lukey, G.C.; Van Deventer, J.S.J. Characteristics of thermal shrinkage and weight loss in Na-geopolymer derived from metakaolin. *Journal of Materials Science* **2007c**, 42 (9), 3044–3054.

56. Duxson, P.; Lukey, G.C.; van Deventer, J.S.J. Physical evolution of Na-geopolymer derived from metakaolin up to 1000 °C. *Journal of Materials Science* **2007b**, 42 (9), 3044–3054. https://doi.org/10.1007/s10853-006-0535-4.

57. Duxson, P.; Mallicoat, S.W.; Lukey, G.C.; Kriven, W.M.; van Deventer, J.S.J. The effect of alkali and Si/Al ratio on the development of mechanical properties of metakaolin-based geopolymers. *Colloids and Surfaces A: Physicochemical and Engineering Aspects* **2007e**, 292 (1), 8–20. https://doi.org/10.1016/j.colsurfa.2006.05.044.

58. Duxson, P.; Provis, J.L. Designing Precursors for Geopolymer Cements. *Journal of the American Ceramic Society* **2008**, 91 (12), 3864–3869. https://doi.org/10.1111/j.1551-2916.2008.02787.x.

59. Duxson, P.; Provis, J.L.; Lukey, G.C., van Deventer, J.S.J. The role of inorganic polymer technology in the development of 'green concrete'. *Cement and Concrete Research* **2007d**, 37 (12), 1590–1597. https://doi.org/10.1016/j.cemconres.2007.08.018.

60. Duxson, P.; Provis, J.L.; Lukey, G.C.; Mallicoat, S.W.; Kriven, W.M.; van Deventer, J.S.J. Understanding the relationship between geopolymer composition, microstructure and mechanical properties. *Colloids and Surfaces A: Physicochemical and Engineering Aspects* **2005**, 269 (1–3), 47–58. https://doi.org/10.1016/j.colsurfa.2005.06.060.

61. Elimbri, A.; Tchakoute, H.K.; Njopwouo, D. Effect of calcination temperature of kaolinite clays on the properties of geopolymer cements. *Construction and Building Materials* **2011**, 25 (6), 2805–2812. https://doi.org/10.1016/j.conbuildmat.2010.12.055.

62. European Commission (EC). Council Decision 2003/33/EC of 19 December 2002 Establishing Criteria and Procedures for the Acceptance of Waste at Landfills Pursuant to Article16 of and Annex II to Directive 1999/31/EC; European Commission: Brussels, Belgium, 2003. Available online: https://eur-lex.europa.eu/legalcontent/EN/TXT/PDF/?uri=CELEX:32003D0033&from=EN (accessed on 9 November 2018).

63. European Commission. Directive 2006/21/EC of the European Parliament and of the Council of 15 March 2006 on the Management of Waste from Extractive Industries and Amending Directive 2004/35/EC, Official Journal of the European Union, L 102/15-33, 11.4.2006. Available online: https://eur-lex.europa.eu/ resource.html?uri=cellar:c370006a-063e-4dc79b0552c37720740c.0005.02/DOC_1&format=PDF (accessed on 14 October 2018).

64. European Commission-IPPC Bureau. Reference Document on Best Available Techniques for Management of Tailings and Waste-Rock in Mining Activities; European Union: Brussels, Belgium, 2009; Available online: http://eippcb.jrc.ec.europa.eu/reference/BREF/mmr_adopted_0109.pdf (accessed on 14 October 2018).

65. Fernández-Jiménez, A.; de la Torre, A.G.; Palomo, A.; López-Olmo, G.; Alonso, M.M.; Aranda, M.A.G. Quantitative determination of phases in the alkaline activation of fly ash. Part II: Degree of reaction. *Fuel* **2006**, 85 (14–15), 1960–1969. https://doi:10.1016/j.fuel.2006.04.006.

66. Fernández-Jiménez, A.; Palomo, A. Composition and microstructure of alkali activated fly ash binder: Effect of the activator. *Cement and Concrete Research* **2005**, 35 (10), 1984–1992. https://doi:10.1016/j.cemconres.2005.03.003.

67. Ferone, C.; Colangelo, F.; Roviello, D.; Asprone, D.; Menna, C.; Balsamo, A.; Prota, A.; Cioffi, R.; Manfredi, G. Application-Oriented Chemical Optimization of a Metakaolin Based Geopolymer. *Materials* **2013**, 6 (5), 1920-1939. https://doi.org/10.3390/ma6051920.

68. Fořt, J.; Vejmelková, E.; Koňáková, D.; Alblová, N.; Čáchová, M.; Keppert, M.; Rovnaníková, P.; Černý, R. Application of waste brick powder in alkali-activated aluminosilicates: Functional and environmental aspects. *Journal Cleaner Production* **2018**, 194, 714–725. https://doi.org/10.1016/j.jclepro.2018.05.181.

69. Fumba, G.; Essomba, J.S.; Tagne, G.M.; Nsami, J.N.; Bélibi, P.D.B.; Mbadcam, J.K. Equilibrium and kinetic adsorption studies of methyl orange from aqueous solutions using kaolinite, metakaolinite and activated geopolymer as low cost adsorbents. *Journal of Academia and Industrial Research (JAIR)* **2014**, 3 (4), 156. www.jairjp.com.

70. Furnali, E.; Maschio, S.; Magnan, M.; Aneggi, E.; Andreatta, F.; Lekka, M.; Lanzutti, A.; Fedrizzi, L. Synthesis and characterization of geopolymers containing blends of unprocessed steel slag and metakaolin: The role of slag particle size. *Ceramics International* **2018**, 44 (5), 5226–5232. https://doi.org/10.1016/j.ceramint.2017.12.131.

71. Gao, K.; Lin, K.-L.; Wang, D.; Hwang, C.-L.; Shiu, H.-S.; Chang, Y-M.; Cheng, T.-W. Effects SiO_2/Na_2O molar ratio on mechanical properties and the microstructure of nano-SiO_2 metakaolin-based geopolymers. *Construction and Building Materials* **2014**, 53, 503–510. https://doi.org/10.1016/j.conbuildmat.2013.12.003.

72. Ge, Y.; Yuan, Y.; Wang, K.; He, Y.; Cui, X. Preparation of geopolymer-based inorganic membrane for removing Ni2+ from wastewater. Journal of Hazardous Materials 2015, 299, 711–718. http://dx.doi.org/10.1016/j.jhazmat.2015.08.006.

73. Gebregziabiher, B.S.; Thomas, R.J.; Peethamparan, S. Temperature and activator effect on early-age reaction kinetics of alkali-activated slag binders. *Construction and Building Materials* **2016**, 133, 783–793. https://doi.org/10.1016/j.conbuildmat.2016.03.098.

74. Ghanbari, M.; Hadiana, A.M.; Nourbakhsh, A.A. Effect of processing parameters on compressive strength of metakaolinite based geopolymers: Using DOE approach. *Procedia Materials Science* **2015**, 11, 711–716. https://doi.org/10.1016/j.mspro.2015.11.047.

75. Gharzouni, A.; Joussein, E.; Samet, B.; Baklouti, S.; Rossignol, S. Effect of the reactivity of alkaline solution and metakaolin on geopolymer formation. Journal of Non-Crystalline Solids **2015**, 410, 127–134. https://doi.org/10.1016/j.jnoncrysol.2014.12.021.

76. Gijbels, K.; Landseberger, S.; Samyn, P.; Iacobescu, R.I.; Pontikes, Y.; Schreurs, S.; Schroeyers, W. Radiological and non-radiological leaching assessment of alkali-activated materials containing ground granulated blast furnace slag and phosphogypsum. *Science of the Total Environment* **2019**, 660, 1098-1107. https://doi.org/10.1016/j.scitotenv.2019.01.089.

77. Glukhovsky, V.D. *Soil Silicates, Their Properties, Technology and Manufacturing and Fields of Application*. Civil Engineering Institute, Kiev, 1965.

78. Glukhovsky, V.D. *Soil Silicates*. USSR: Gostroiizdat Publish, Kiev, 1959

79. Glukhovsky, V.D. Some Aspects of Admixtures and Industrial By-Products on the Durability of Concrete. In: Proceedings of the 2nd International Seminar on Gothenburg, Sweden, 26–27 June 1989; pp. 53–62.

80. Görhan, G.; Kürklü, G. The influence of the NaOH solution on the properties of the fly ash-based geopolymer mortar cured at different temperatures. *Composites: Part B* **2014**, 58, 371-377. https://doi.org/10.1016/j.compositesb.2013.10.082.

81. Granizo, M.L.; Blanco-Varela, M.T.; Martinez-Ramirez, S. Alkali activation of metakaolins: parameters affecting mechanical, structural and microstructural properties. *Journal of Materials Science* **2007**, 42 (9), 2934–2943. https://doi.org/10.1007/s10853-006-0565-y.

82. Gualtieri, M.L.; Romagnoli, M.; Pollastri, S.; Gualtieri, A.F. Inorganic polymers from laterite using activation with phosphoric acid and alkaline sodium silicate solution: Mechanical and microstructural properties. *Cement and Concrete Research* **2015,** 67, 259–270. https://doi.org/10.1016/j.cemconres.2014.08.010.

83. Hanjitsuwan, S.; Hunpratub, S.; Thongbai, P.; Maensiri, S.; Sata, V.; Chindaprasirt, P. Effects of NaOH concentrations on physical and electrical properties of high calcium fly ash geopolymer paste. *Cement and Concrete Composites* **2014,** 45, 9-14. https://doi.org/10.1016/j.cemconcomp.2013.09.012.

84. Hardjito, D.; Rangan, B. V. Development and properties of low-calcium fly ash-based geopolymer concrete. Curtin University of Technology, Perth, Australia, 2005.

85. He, P.; Wang, M.; Fu, A.; Jia, D.; Yan, S.; Yuan, J.; Xu, J.; Wang, P.; Zhou, Y. Effects of Si/Al ratio on the structure and properties of metakaolin based geopolymer. *Ceramics International* **2016**, 42 (13), 14416–4422. https://doi.org/10.1016/j.ceramint.2016.06.033.

86. Heah, C.Y.; Kamarudin, H.; Al Bakri, A.M.M.; Bnhussain, M.; Lugman, M.; Khairul Nizar, I.; Ruzaidi, C.M.; Liew, Y.M. Study on solids-to-liquid and alkaline activator ratios on kaolin-based geopolymers. *Construction and Building Materials* **2012**, 35, 912–922. https://doi.org/10.1016/j.conbuildmat.2012.04.102.

87. Heah, C.Y.; Kamarudin, H.; Mustafa Al Bakri, A.M.; Bnhussain, M.; Luqman, M.; Khairul Nizar, I.; Ruzaidi, C.M.; Liew, Y.M. Kaolin-based geopolymers with various NaOH concentrations. *International Journal of Minerals Metallurgy and Materials* **2013**, 20 (3), 313. https://doi.org/10.1007/s12613-013-0729-0.

88. Heah, C.Y.; Kamarudin, H.; Mustafa, A.L.; Bakri, A.M.; Binhussain, M.; Luqman, M.; Khairul Nizar, I.; Ruzaidi, C.M.; Liew, Y.M. Effect of Curing Profile on Kaolin-based Geopolymers. *Physics Procedia* **2011**, 22, 305–311. https://doi.org/10.1016/j.phpro.2011.11.048.

89. Hermann, E. C.; Kunze, R.; Gatzweiler, G.; Kießig, J. Davidovits. Solidification of various radioactive residues by géopolymère with special emphasison long-term-stability, Part I: Laboratory investigations Part II: Pilot-scale experiment, In Proceedings of the 2nd International Conference on Geopolymer, Saint Qunentin, France, 30 June–2 July 1999; pp. 211-228.

90. Hertel, T.; Pontikes, Y. Geopolymers, inorganic polymers, alkali-activated materials and hybrid binders from bauxite residue (red mud)-Putting things in perspective. *Journal of Cleaner Production* **2020,** 120610. https://doi.org/10.1016/j.jclepro.2020.120610.

91. Huang, Y.; Wang, Q.; Shi, M. Characteristics and reactivity of ferronickel slag powder. *Construction and Building Materials* **2017**, 156, 773–789. https://doi.org/10.1016/j.conbuildmat.2017.09.038.

92. Huseien, G. F.; Shah, K. W. Durability and life cycle evaluation of self-compacting concrete containing fly ash as GBFS replacement with alkali activation. *Construction and Building Materials* **2020**, 235, 117458. https://doi:10.1016/j.conbuildmat.2019.117458.

93. Iacobescu, R. I.; Cappuyns, V.; Geens, T.; Kriskova, L.; Onisei, S.; Jones, P. T.; Pontikes, Y. The influence of curing conditions on the mechanical properties and leaching of inorganic polymers made of fayalitic slag. *Frontiers of Chemical Science and Engineering* **2017,** 11 (3), 317–327. https://doi.org/10.1007/s11705-017-1622-6.

94. Ikeda, K. Consolidation of mineral powders by the geopolymer binder technique for materials use. *Journal of the Mining and Materials Processing Institute of Japan* **1998**, 114, 497–500 (in Japanese).

95. , 8, 4. https://doi.org/10.3390/environments8010004.

96. Kakali, G.; Perrraki, T.; Tsivilis, S.; Badogiannis, E. Thermal Treatment of Kaolin: The Effect of Mineralogy on the Pozzolanic Activity. *Applied Clay Science* **2001**, 20, 73–80. https://doi.org/10.1016/S0169-1317(01)00040-0.

97. Kamseu, E.; Cannio, M.; Obonyo, E.A.; Tobias, F.; Bignozzi, M.C.; Sglavo, V.M.; Leonelli, C. Metakaolin-based inorganic polymer composite: effects of fine aggregate composition and structure on porosity evolution, microstructure and mechanical properties. *Cement and Concrete Composites* **2014**, 53, 258–269 https://doi.org/10.1016/j.cemconcomp.2014.07.008.

98. Kamseu, E.; Nait-Ali, B.; Bignozzi, M.C.; Leonelli, C.; Rossignol, S.; Smith, D.S. Bulk composition and microstructure dependence of effective thermal conductivity of porous inorganic polymer cements. *Journal of the European Ceramic Society* **2012**, 32 (8), 1593–1603. https://doi.org/10.1016/j.jeurceramsoc.2011.12.030.

99. Kaze, C.R.; Beleuk à Moungam, L.M.; Cannio, M.; Rosa, R.; Kamseu, E.; Melo, U.C.; Leonelli, C. Microstructure and engineering properties of $Fe_2O_3(FeO)$-Al_2O_3-SiO_2 based geopolymer composites. *Journal of Cleaner Production* **2018c**, 849–859. https://doi.org/10.1016/j.jclepro.2018.07.171.

100. Kaze, C.R.; Djobo, J.N.Y.; Nana, A.; Tchakoute, H.K.; Kamseu, E.; Melo, U.C.; Leonelli, C.; Rahier, H. Effect of silicate modulus on the setting, mechanical strength and microstructure of iron-rich aluminosilicate (laterite) based-geopolymer cured at room temperature. *Ceramics International* **2018a**, 44, 21442–21450. https://doi.org/10.1016/j.ceramint.2018.08.205.

101. Kaze, C.R.; Tchakoute, H.K.; Mbakop, T.T.; Mache, J.R.; Kamseu, E.; Melo, U.C.; Leonelli, C. Synthesis and properties of inorganic polymers (geopolymers) derived from Cameroon–meta–halloysite. *Ceramics International* **2018b**, 44, 18499–18508. https://doi.org/10.1016/j.ceramint.2018.07.070.

102. Kaze, C.R.; Venyite, P.; Nana, A.; Juvenal, D.N.; Tchakoute, H.K.; Rahier, H.; Kamseu, E.; Melo, U.C.; Leonelli, C. Meta-halloysite to improve compactness in iron-rich laterite-

based alkali activated materials. *Materials Chemistry and Physics* **2020**, 239, 122268. https://doi.org/10.1016/j.matchemphys.2019.122268.

103. Kaze, R.C.; Beleuk à Moungam, L.M.; Fonkwe Djouka, M.L.; Nana, A.; Kamseu, E.; Chinje Melo, U.F.; Leonelli, C. The corrosion of kaolinite by iron minerals and the effects on geopolymerization. *Applied Clay Science* **2017**, 138, 48–62. https://doi.org/10.1016/j.clay.2016.12.040.

104. Khale, D.; Chaudhary, R. Mechanism of geopolymerization and factors influencing its development: a review. *Journal of Materials Science* **2007**, 42 (3), 729–746. https://doi.org/10.1007/s10853-006-0401-4.

105. Kierczak, J.; Neel, C.; Puziewicz, J.; Bril, H. The mineralogy and weathering of slag produced by the smelting of lateritic Ni ores, Szklary, Southwestern Poland. *The Canadian Mineralogist* **2009**, 47 (3), 557–572. https://doi.org/10.3749/canmin.47.3.557.

106. Kioupis, D.; Kavakakis, C.; Tsivilis, S.; Kakali, G. Synthesis and characterization of porous fly ash-based geopolymers using Si as foaming agent. *Advances in Materials Science and Engineering* **2018**. https://doi.org/10.1155/2018/1942898.

107. Komnitsas, K. Co-valorization of marine sediments and construction & demolition wastes through alkali activation. *Journal of Environmental. Chemical Engineering* **2016**, 4 (4), 4661–4669. https://doi.org/10.1016/j.jece.2016.11.003.

108. Komnitsas, K. Potential of geopolymer technology towards green buildings and sustainable cities. *Procedia Engineering* **2011**, 21, 1023–1032. https://doi.org/10.1016/j.proeng.2011.11.2108.

109. Komnitsas, K.; Bartzas, G.; Karmali, V.; Petrakis, E. Factors Affecting Alkali Activation of Laterite Acid Leaching Residues. *Environments*

110. Komnitsas, K.; Bartzas, G.; Karmali, V.; Petrakis, E.; Kurylak, W.; Pietek, G.; Kanasiewics, J. Assessment of alkali activation potential of a Polish ferronickel slag. *Sustainability* **2019a**, 11, 1863. https://doi.org/10.3390/su11071863.

111. Komnitsas, K.; Petrakis, E.; Bartzas, G.; Karmali, V. Column leaching of low-grade saprolitic laterites and valorization of leaching residues. *Science of the Total Environment* **2019b**, 665, 347–357. https://doi.org/10.1016/j.scitotenv.2019.01.381.

112. Komnitsas, K.; Petrakis, E.; Pantelaki, O.; Kritikaki, A. Column Leaching of Greek Low-Grade Limonitic Laterites. *Minerals* **2018**, 8, 377. https://doi.org/10.3390/min8090377.

113. Komnitsas, K.; Yurramendi, L.; Bartzas, G.; Karmali, V.; Petrakis, E. Factors affecting co-valorization of fayalitic and ferronickel slags for the production of alkali activated materials. *Science of the Total Environ*ment **2020**, 721, 137753. https://doi.org/10.1016/j.scitotenv.2020.137753.

114. Komnitsas, K.; Zaharaki, D. Geopolymerisation: A review and prospects for the minerals industry. *Minerals Engineering* **2007**, 20 (14), 1261–1277. https://doi.org/10.1016/j.mineng.2007.07.011.

115. Komnitsas, K.; Zaharaki, D.; Bartzas, G. Effect of sulphate and nitrate anions on heavy metal immobilisation in ferronickel slag geopolymers. *Applied Clay Science* **2013**, 73, 103–109. https://doi.org/10.1016/j.clay.2012.09.018.

116. Komnitsas, K.; Zaharaki, D.; Perdikatsis, V. Effect of synthesis parameters on the compressive strength of low-calcium ferronickel slag inorganic polymers. *Journal of Hazardous Materials* **2009**, 161 (2–3), 760–768. https://doi.org/10.1016/j.jhazmat.2008.04.055.

117. Komnitsas, K.; Zaharaki, D.; Perdikatsis, V. Geopolymerisation of low calcium ferronickel slags. *Journal of Materials Science* **2007**, 42 (9), 3073–3082. https://doi.org/10.1007/s10853-006-0529-2.

118. Komnitsas, K.; Zaharaki, D.; Vlachou, A.; Bartzas, G.; Galetakis, M. Effect of synthesis parameters on the quality of construction and demolition wastes (CDW) geopolymers. *Advanced Powder Technology* **2015**, 26 (2), 368-376. https://doi.org/10.1016/j.apt.2014.11.012.

119. Konan, K.L.; Peyratout, C.; Smith, A.; Bonnet, J.-P.; Rossignol, S.; Oyetola, S. Comparison of surface properties between kaolin and metakaolin in concentrated lime solutions. *Journal of Colloid and Interface Science* **2009**, 339, 103–109. https://doi.org/10.1016/j.jcis.2009.07.019.

120. Kosmatka, S.H.; Kerkhoff, B.; Panerese, W.C. Design and Control of Concrete Mixtures. EB001, 14th edition, *Portland Cement Association*, Skokie, Illinois, USA, **2003.**

121. Kpinsoton, G.M.R.; Karoui, H.; Richardson, Y.; Koffi, B.N.D.S.; Yacouba, H.; Motuzas, J.; Drobek, M.; Lawane Gana, A. New insight into the microstructure of natural calcined laterites and their performance as heterogeneous Fenton catalyst for methylene blue degradation. *Reaction Kinetics, Mechanisms and Catalysis* **2018**, 124, 931–956. https://doi.org/10.1007/s11144-018-1406-0.

122. Krivenko, P.V.; Kovalchuk, G.Y. Directed synthesis of alkaline aluminosilicate minerals in a geocement matrix. *Journal of Materials Science* **2007**, 42 (9), 2944–2952. https://doi.org/10.1007/s10853-006-0528-3.

123. Kumar, S.; Kumar, R. Mechanical activation of fly ash: Effect on reaction, structure and properties of resulting geopolymer. *Ceramics International* **2011**, 37 (2), 533–541. https://doi.org/10.1016/j.ceramint.2010.09.038.

124. Łach, M.; Komiejenko, K.; Mikuła, J. Thermal insulation and thermally resistant materials made of geopolymer foams. *Procedia Engineering* **2016**, 151, 410–416. https://doi.org/10.1016/j.proeng.2016.07.350.

125. Lahoti, M.; Tan, K.H.; Yang, E.-H. A critical review of geopolymer properties for structural fire-resistance applications. *Construction and Building Materials* **2019**, 221, 514–526. https://doi.org/10.1016/j.conbuildmat.2019.06.076.

126. Lahoti, M.; Wong, K.K.; Yang, E.-H.; Tan, K.H. Effects of Si/Al molar ratio on strength endurance and volume stability of metakaolin geopolymers subject to elevated temperature. *Ceramics International* **2018**, 44 (5), 5726–5734. https://doi.org/10.1016/j.ceramint.2017.12.226.

127. Law, D.W.; Adam, A.A.; Molyneaux, T.K.; Patnaikuni, I.; Wardhono, A. Long term durability properties of class F fly ash geopolmer concrete. *Materials and Structures* **2015**, 48 (3), 721–731. http://dx.doi.org/10.1617/s11527-014-0268-9.

128. Lee, W.K.W.; Van Deventer, J.S.J. Structural reorganization of class F fly ash in alkaline silicate solutions. *Colloids and Surfaces A: Physicochemical and Engineering Aspects* **2002**, 211 (1), 49-66. https://doi.org/10.1016/S0927-7757(02)00237-6.

129. Lemonis, N.; Tsakiridis, P.E.; Katsiotis, N.S.; Antiohos, S.; Papageorgiou, D.; Katsiotis, M.S.; Beazi-Katsioti, M. Hydration study of ternary blended cements containing ferronickel slag and natural pozzolan. *Construction and Building Materials* **2015**, 81, 130–139. https://doi. org/10.1016/j.conbuildmat.2015.02.046.

130. Lemougna, P.N.; MacKenzie, K.J.D.; Melo, U.F.C. Sythesis and thermal properties of inorganic polymers (geopolymers) for structural and refractory applications from volcanic ash. *Ceramic International* **2011**, 37 (8), 3011–3018. https://doi.org/10.1016/j.ceramint.2011.05.002.

131. Lemougna, P.N.; Madi, A.B.; Kamseu, E.; Melo, U.C.; Delplancke, M.-P.; Rahier H. Influence of the processing temperature on the compressive strength of Na activated lateritic soil for building applications. *Construction and Building Materials* **2014**, 65, 60–66. https://doi.org/10.1016/j.conbuildmat.2014.04.100.

132. Lemougna, P.N.; Wang, K.-t.; Tang, Q.; Kamseu, E.; Billong, N.; Melo, U.C.; Cui, X.-m. Effect of slag and calcium carbonate addition on the development of geopolymer from indurated laterite. *Applied Clay Science* **2017**, 148, 109–117. https://doi.org/10.1016/j.clay.2017.08.015.

133. Leong, H.Y.; Ong, D.E.L; Sanjayan, J.G.; Nazari, A. The effect of different Na$_2$O and K$_2$O ratios of alkali activator on compressive strength of fly ash based-geopolymer. *Construction and Building Materials* **2016**, 106, 500–511. https://doi.org/10.1016/j.conbuildmat.2015.12.141.

134. Li, C.; Sun, H.; Li, L. A review: The comparison between alkali-activated slag (Si+Ca) and metakaolin (Si+Al) cements. *Cement and Concrete Research* **2010**, 40 (9), 1341–1349. https://doi.org/10.1016/j.cemconres.2010.03.020.

135. Li, Q.; Yang, Y.; Yang, K.; Chao, Z.; Tang, D.; Tian, Yi; Wu, F.; Basheer, M.; Yang, C. The role of calcium stearate on regulating activation to form stable, uniform and flawless reaction products in alkali-activated slag cement. *Cement and Concrete Research* **2019**, 103, 242–251. https://doi.org/10.1016/j.cemconcomp.2019.05.009.

136. Li, Z.; Zhang, Y.; Zhou, X. Short Fiber Reinforced Geopolymer Composites Manufactured by Extrusion. *Journal of Materials in Civil Engineering* **2005**, 17 (6), 624–631. https://doi.org/10.1061/(ASCE)0899-1561(2005)17:6(624).

137. Liu, Y.; Zhang, K.; Feng, E.; Zhao, H.; Liu, F. Synthesis of geopolymer composites from a mixture of ferronickel slag and fly ash. IOP Conference Series: Materials Scence and Engineering **2017**, 182, 012038. https://doi.org/10.1088/1757-899X/182/1/012038.

138. Liu, Z.; Wang, J.; Jiang, Q.; Cheng, G.; Li, L.; Kang, Y.; Wang, D. A green route to sustainable alkali-activated materials by heat and chemical activation of lithium slag. *Journal of Cleaner Production* **2019**, 225, 1184–1193. https://doi.org/10.1016/j.jclepro.2019.04.018.

139. Luukkonen, T.; Abdollahnejad, Z.; Yliniemi, J.; Kinnunen, P.; Illikainen, M. One-part alkali-activeated materials: A review. *Cement and Concrete Research* **2018a**, 103, 21–34. https://doi.org/10.1016/j.cemconres.2017.10.001.

140. Luukkonen, T.; Abdollahnejad, Z.; Yliniemi, J.; Kinnunyn, P.; Illikainen, M. Comparison of alkali and silica sources in one-part alkali-activated blast furnace slag mortar. *Journal of Cleaner Production* **2018b**, 187, 171–179. https://doi.org/10.1016/j.jclepro.2018.03.202.

141. Luukkonen, T.; Heponiemi, A.; Runtti, H.; Pesonen, A.; Yliniemi, J.; Lassi, U. Application of alkali-activated materials for water and wastewater treatment: a review. *Reviews in Environmental Science and Biotechnology* **2019**, 18 (2), 271–297. https://doi.org/10.1007/s11157-019-09494-0.

142. Maragkos, I.; Gianopoulou, I.P.; Panias, D. Synthesis of ferronickel slag-based geopolymers. *Minerals Engineering* **2009**, 22 (2), 196–203. https://doi.org/10.1016/j.mineng.2008.07.003.

143. Marangoni, M.; Arnout, L.; Machiels, L.; Pandelaers, L.; Bernardo, E.; Colombo, P.; Pontikes, Y.; Jantzen, C. Porous, sintered glass-ceramics from inorganic polymers based on fayalite slag. *Journal of the American Ceramic Society* **2016**, 99 (6), 1985–1991. https://doi.org/10.1111/jace.14224.

144. Marjanović, N.; Komljenović, M.; Baščarević, Z.; Nikolić, V.; Petrović, R. Physico-mechanical and microstructural properties of alkali-activated fly ash-blast furnace slag blends. *Ceramics International* **2015** 41 (1), 1421–1435 https://doi.org/10.1016/j.ceramint.2014.09.075.

145. Martin, A.; Pastor, J.Y.; Palomo, A.; Fernández-Jiménez, A. Mechanical behaviour at high temperature of alkali-activated aluminosilicates (geopolymers). *Construction and Building Materials* **2015**, 93, 1188–1196. https://doi.org/10.1016/j.conbuildmat.2015.04.044.

146. Mascarin, L. Characterization and Thermodynamic Modelling of Alkali-Activated Calcined Clays: Potentiality of Cameroon's Laterites as Eco-Sustainable Binders. Master's Thesis, Department of Geosciences, University of Padua, Padova, Italy, 19 July 2018.

147. Mastali, M.; Shaad, K.M.; Abdollahnejad, Z.; Falah, M.; Kinnunen, P.; Illikainen, M. Towards sustainable bricks made with fiber-reinforced alkali-activated desulfurization slag mortars incorporating carbonated basic oxygen furnace aggregates. *Construction and Building Materials* **2020**, 232, 117258. https://doi.org/10.1016/j.conbuildmat.2019.117258.

148. Mehta, A.; Siddique, R. An overview of geopolymers derived from industrial by-products. *Construction and Building Materials* **2016**, 127, 183–198. https://doi.org/10.1016/j.conbuildmat.2016.09.136.

149. Mijarsh, M.J.A.; Megat Johari, M.A.; Ahmad, Z.A. Synthesis of geopolymer from large amounts of treated palm oil fuel ash: application of the Taguchi method in investigating the main parameters affecting compressive strength. *Construction and Building Materials* **2014**, 52, 473–481. https://doi.org/10.1016/j.conbuildmat.2013.11.039.

150. Mo, B.-h.; He, Z.; Cui, X.-m.; He, Y.; Gong, S.-y. Effect of curing temperature on geopolymerization of metakaolin-based geopolymers. *Applied Clay Science* **2014**, 99, 144–148. https://doi.org/10.1016/j.clay.2014.06.024.

151. Mo, L.; Zhang, F.; Deng, M.; Jin, F.; Al-Tabbaa, A.; Wang, A. Accelerated carbonation and performance of concrete made with steel slag as binding materials and aggregates. *Cement and Concrete Composites* **2017**, 83, 138–145. https://doi.org/10.1016/j.cemconcomp.2017.07.018.

152. Mohamed, O.A. A review of durability and strength characteristics of alkaliactivated slag concrete. *Materials* **2019**, 12 (8), 1198. https://doi.org/10.3390/ma12081198.

153. Muñoz, I.; Cifrian, E.; Andrés, A.; San Miguel, G.; Ruiz, D.; Viguri, J.R. Analysis of environmental benefits associated with the incorporation of Waelz slag into fired bricks using LCA. *Construction and Building Materials* **2018**, 168, 178–186. https://doi.org/10.1016/j.conbuildmat.2018.02.108.

154. Muthuvel, I.; Gowthami, K.; Thirunarayanan, G.; Suppuraj, P.; Krishnakumar, B.; do Nascimento Sobral, J.F.; Swaminathan, M. Graphene oxide-$Fe_2V_4O_{13}$ hybrid material as highly efficient hetero-Fenton catalyst for degradation of methyl orange. *International Journal of Industrial Chemistry* **2019**, 10, 1–11. https://doi.org/10.1007/s40090-019-0173-8.

155. Mužek, M.N.; Zelić, J.; Jozić, D. Microstructural characteristics of geopolymers based on alkali-activated fly ash. *Chemical and Biochememical Engineering Quarterly* **2012**, 26 (2), 89–95. Available online: http://pierre.fkit.hr/hdki/cabeq/pdf/26_2_2012/Cabeq%202012-02_3.pdf (accessed on 24 November 2018).

156. Naghsh, M.; Shams, K. Synthesis of a kaolin-based geopolymer using a novel fusion methods and its application in effective water softening. *Applied Clay Science* **2017**, 146, 238–245. http://dx.doi.org/10.1016/j.clay.2017.06.008.

157. Nair, B.G.; Zhao, Q.; Cooper, R.F. Geopolymer matrices with improved hydrothermal corrosion resistance for high-temperatures applications. *Journal of Materials Science* **2007**, 42 (9), 3083–3091. https://doi.org/10.1007/s10853-006-0526-5.

158. Namkane, K.; Naksata, W.; Thiansem, S.; Sooksamiti, P.; Arqueropanyo, O.-a. Utilization of coal botton ash as raw material for production of ceramic floor tiles. *Environmental Earth Sciences* **2016**, 75 (5), 386. https://doi.org/10.1007/s12665-016-5279-0.

159. Nasvi, M.C.M.; Ranjith, P.G.; Sanjayan, J. The permeability of geopolymer at down-hole stress conditions: application for carbon dioxide sequestration wells. *Applied Energy* **2013**, 102, 1391–1398. https://doi.org/10.1016/j.apenergy.2012.09.004.

160. Nazer, A.; Payá, J.; Borrachero, M.V.; Monzó, J. Use of ancient copper slags in Portland cement and alkali activated cement matrices. *Journal of Environmental Management* **2016**, 167, 115–123. https://doi.org/10.1016/j.jenvman.2015.11.024.

161. NEN 7341, 1995. Leaching Characteristics of Solid Earthy and Stony Building and Waste Materials-leaching Tests: Determination of the Availability of Inorganic Components for

Leaching. 1st ed. Nederlands Normalisatie Instituut (NNI), Delft, the Netherlands ICS 13.030-70;91.100.

162. Nergis, D.D.B.; Abdullag, M.M.A.B.; Vizureanu, P.; Tahir, M.F.M. Geopolymers and Their Uses: Review. *IOP Conference Series: Materials Science and Engineering* **2018**, 374, 012019. https://doi.org/10.1088/1757-899X/374/1/012019.

163. Nkwaju, R.Y.; Djobo, J.N.Y.; Nouping, J.N.F.; Huisken, P.W.M.; Deutou, J.G.N.; Courard, L. Iron-rich laterite-bagasse fibers based geopolymer composite: Mechanical, durability and insulating properties. *Applied Clay Science* **2019**, 183, 105333. https://doi.org/10.1016/j.clay.2019.105333.

164. Onisei, S.; Douvalis, A.P.; Malfliet, A.; Peys, A.; Pontikes, Y. Inorganic polymers made of fayalite slag: On the microstructure and behavior of Fe. *Journal of the American Ceramic Society* **2018**, 101 (6), 2245–2257. https://doi.org/10.1111/jace.15420.

165. Onisei, S.; Malfliet, A.; Gutierrez-Campos, D.; Blanplain, B.; Pontikes, Y. Synthesis and high temperature transformations of Fe-rich inorganic polymers. In Proceedings of the 4th International Slag Valorization Symposium, Leuven, Belgium, 15–17 April 2015; pp. 243–248. Available online: http://www.slagvalorisation-symposium.eu/2015/images/papers/SVS2015-Onisei.pdf (accessed on 21 November 2018).

166. Onisei, S.; Pontikes, Y.; Van Gerven, T.; Angelopoulos, G.N.; Velea, T.; Predica, V.; Moldovan, P. Synthesis of inorganic polymers using fly ash and primary lead slag. *Journal of Hazardous Materials* **2012**, 205–206, 101–110. https://doi.org/10.1016/j.jhazmat.2011.12.039.

167. Palomo, A.; Grutzeck, M.W.; Blanco, M.T. Alkali activated fly ashes-A cement for the future. *Cement and Concrete Research* **1999**, 29 (8), 1323–1329. https://doi.org/10.1016/S0008-8846(98)00243-9.

168. Panias, D.; Giannopoulou, I.P; Perraki T. Effect of synthesis parameters on the mechanical properties of fly ash-based geopolymers. *Colloids and Surfaces A: Physicochemical and Engineering Aspects* **2007**, 301 (1–3), 246–254. https://doi.org/10.1016/j.colsurfa.2006.12.064.

169. Passuello, A.; Rodríguez, E.D.; Hirt, E.; Longhi, M.; Bernal, S.A.; Provis, J.L.; Kirchheim, A. P. Evaluation of the potential improvement in the environmental footprint of geopolymers using waste-derived activators. *Journal of Cleaner Production* **2017**, 166, 680–689. https://doi.org/10.1016/j.jclepro.2017.08.007.

170. Perera, D.S.; Uchida, O.; Vance, E.R.; Finnie, K.S. Influence of curing schedule on the integrity of geopolymers. *Journal of Materials Science* **2007**, 42 (9), 3099–3106. https://doi.org/10.1007/s10853-006-0533-6.

171. Petrakis, E.; Karmali, V.; Bartzas, G.; Komnitsas, K. Grinding Kinetics of Slag and Effect of Final Particle Size on the Compressive Strength of Alkali Activated Materials. *Minerals* **2019**, 9, 714. https://doi.org/10.3390/min9110714.

172. Peys, A.; Douvalis, A.P.; Hallet, V.; Rahier, H.; Blanpain, B.; Pontikes, Y. Inorganic polymers from CaO-FeOx-SiO$_2$ Slag: the start of oxidation of Fe and the formation of a mixed valence binder. *Frontiers of Materials* Science **2019b**, 6, 212. https://doi.org/10.3389/fmats.2019.00212.

173. Peys, A.; Douvalis, A.P.; Siakati, C.; Rahier, H.; Blanpain, B.; Pontikes, Y. The influence of air and temperature on the reaction mechanism and molecular structure of Fe-silicate inorganic polymers. *Journal of Non-Crystalline Solids* **2019a**, 526, 119675. https://doi.org/10.1016/j.jnoncrysol.2019.119675.

174. Peys, A.; White, C.E.; Olds, D.; Rahier, H.; Blanpain, B.; Pontikes, Y. Molecular structure of CaO-FeOx-SiO$_2$ glassy slags and resultant inorganic polymer binders. *Journal of the American Ceramic Society* **2018**, 101, 5846–5857. https://doi.org/10.1111/jace.15880.

175. Peys, A.; White, C.E.; Rahier, H.; Blanpain, B.; Pontikes, Y. Alkali-activation of CaO-FeO$_x$-SiO$_2$: Formation mechanism from in-situ X-ray total scattering. *Cement and Concrete Research* **2019**, 122, 179–188. https://doi.org/10.1016/j.cemconres.2019.04.019.

176. Phair, J.W. Compositional effects and microstructure of fly ash based geopolymers. PhD Thesis, Department of Chemical Engineering, University of Melbourne, Victoria, Australia, 2001.

177. Phummiphan, I.; Horpibulsuk, S.; Sukmak, P.; Chinkulkijniwat, A.; Arulrajah, A.; Shen, S.-L. Stabilisation of marginal lateritic soil using high calcium fly ash-based geopolymer. *Road Materials and Pavement Design* **2016**, 17 (4), 877–891. http://dx.doi.org/10.1080/14680629.2015.1132632.

178. Pontikes, Y.; Machiels, L.; Onisei, S.; Pandelaers, L.; Geysen, D.; Jones, P.T.; Blanpain, B. Slags with a high Al and Fe content as precursors for inorganic polymers. *Applied Clay Science* **2013**, 73, 93–102. https://doi.org/10.1016/j.clay.2012.09.020.

179. Provis, J.L.; Bernal, S.A. Geopolymers and Related Alkali-Activated Materials. *Annual Review of Materials Researh* **2014**, 44, 299–327. https://doi.org/10.1146/annurev-matsci-070813-113515.

180. Provis, J.L.; Fernández-Jiménez, A.; Kamseu, E.; Leonelli, C.; Palomo, A. Binder chemistry -Low-calcium alkali-activated materials,. *Alkali Activated Materials* **2014**, 93–123. https://doi.org/10.1007/978-94-007-7672-2_4.

181. Provis, J.L.; Lukey, G.C.; van Deventer, J.S.J. Do geopolymers actually contain nanocrystalline zeolites? A reexamination of existing results. *Chemistry of Materials* **2005**, 17 (12), 3075–3085. https://doi.org/10.1021/cm050230i.

182. Provis, J.L.; Palomo, A; Shi, C. Advances in understanding alkali-activated materials. *Cement and Concrete Research* **2015**, 78, 110–125. https://doi.org/10.1016/j.cemconres.2015.04.013.

183. Provis, J.L.; Van Deventer, J.S.J. Alkali-Activated Materials: State-of-the-art Report. RILEM TC 224-AAM, Springer, Dordrecht 2014.

184. Provis, J.L.; van Deventer, J.S.J. Geopolymerisation kinetics. 1. In situ energy-dispersive X-ray diffractometry. *Chemical Engineering Science* **2007**, 62 (9), 2309–2317. https://doi.org/10.1016/j.ces.2007.01.027.

185. Provis, J.L.; Yong, C.Z.; Duxson, P.; van Deventer, J.S.J. Correlating mechanical and thermal properties of sodium silicate-fly ash geopolymers. *Colloids and Surfaces A: Physicochemical and Engineering Aspects* **2009**, 336 (1–3), 57–63. https://doi.org/10.1016/j.colsurfa.2008.11.019.

186. Purdon, A. The action of alkalis on blast-furnace slag. *Journal of the Society of Chemical Industry* **1940**, 59, 191–202.

187. Rattanasak, U.; Chindaprasirt, P. Influence of NaOH solution on the synthesis of fly ash geopolymer. *Minerals Engineering* **2009**, 22 (12) 1073–1078. https://doi.org/10.1016/j.mineng.2009.03.022.

188. Ravikumar, D.; Neithalath, N. Effects of activator characteristics on the reaction product formation in slag binders activated using alkali silicate powder and NaOH. *Cement and Concrete Composites*, **2012**, 34 (7), 809–818. https://doi.org/10.1016/j.cemconcomp.2012.03.006.

189. Rees, C.A.; Provis, J.L.; Lukey, G.C.; Deventer J.S. The mechanism of geopolymer gel formation investigated through seeded nucleation. *Colloids and Surfaces A: Physicochemical and Engineering Aspects* **2008**, 318 (1–3), 97–105. https://doi.org/10.1016/j.colsurfa.2007.12.019.

190. Ricciotti, L.; Molino, A.J.; Roviello, V.; Chianese, E.; Cennamo, P.; Roviello, G. Geopolymer Composites for Potential Applications in Cultural Heritage. *Environments* **2017**, 4, 91. https://doi.org/10.3390/environments4040091.

191. Rincón, A.; Desideri, D.; Bernardo, E. Functional glass-ceramic foams from 'inorganic gel casting' and sintering of glass/slag mixtures. *Journal of Cleaner Production* **2018**, 187, 250–256. https://doi.org/10.1016/j.jclepro.2018.03.065.

192. Robayo-Salazar, R.; Mejía-Arcila, J.; Mejía de Gutiérrez, R.; Martínez, E. Life cycle assessment (LCA) of an alkali-activated binary concrete based on natural volcanic pozzolan: A comparative analysis to OPC concrete. *Construction and Building Materials* **2018**, 176, 103–111. https://doi:10.1016/j.conbuildmat.2018.05.017.

193. Rovnaník, P. Effect of curing temperature on the development of hard structure of metakaolin based geopolymer. *Construction and Building Materials* **2010**, 24 (7), 1176–1183 https://doi.org/10.1016/j.conbuildmat.2009.12.023.

194. Saari, V.; Latostenmaa, P.; Yliniemi, J.; Ohenoja, K. Boliden Harjavalta copper and nickel smelter-review of smelter operations, slags and slag valorization studies. 6th International Slag Valorisation Symposium, Mechelen, Belgium, 1–5 April 2019, Retrieved from. www.slag-valorisation-symposium.eu.

195. Sajedi, F. Effect of curing regime and temperature on the compressive strength of cement-slag mortars. *Construction and Building Materials* **2012**, 36, 549–556. https://doi.org/10.1016/j.conbuildmat.2012.06.036.

196. Samantasinghar, S.; Singh, S.P. Effect of synthesis parameters on compressive strength of fly ash-slag blended geopolymer. *Construction and Building Materials* **2018**, 170, 225–234. https://doi.org/10.1016/j.conbuildmat.2018.03.026.

197. Sarmin, S.N.; Welling, J.; Krause, A.; Shalbafan, A. Investigated the Possibility of Geopolymer to Produce Inorganic-Bonded Wood Composites for Multifunctional Construction Material-A Review. *BioResources* **2014**, 9 (4), 7941–7950.

198. Scrivener, K.L.; John, V.M.; Gartner, E.M. Eco-efficient cements: Potential, economically viable solutions for a low-CO₂, cement-based materials industry. *UNEP: United Nations Environment Program* **2016**. Available online: https://www.devalt.org/Pdf/L2_SixThemePdfs/2016-UNEPReport-Complete4 (1).pdf.

199. Shi, C.; Fernández-Jiménez, A.; Palomo, A. New cements for the 21st century: The pursuit of an alternative to Portland cement. *Cement and Concrete Research* **2011**, 41 (7), 750–763. https://doi.org/10.1016/j.cemconres.2011.03.016.

200. Shvarzman, A.; Kovler, K.; Grader, G.S.; Shter, G.E. The effect of dehydroxylation/amorphization degree on pozzolanic activity of kaolinite. *Cement and Concrete Research* **2003**, 33, 405–416. https://doi.org/10.1016/S0008-8846(02)00975-4.

201. Sindhunata; Van Deventer, J.S.J.; Lukey, G.C.; Xu, H. Effect of curing temperature and silicate concentration on fly-ash-based geopolymerization. *Industrial and Engineering Chemistry Research* **2006**, 45 (10), 3559–3568. https://doi.org/10.1021/ie051251p.

202. Singh, N.B.; Middendorf, B. Geopolymers as an alternative to Portland cement: An overview. *Construction and Building Materials* **2020**, 237, 117455. https://doi.org/10.1016/j.conbuildmat.2019.117455.

203. Sofi, M.; van Deventer, J.S.J.; Mendis, P.A.; Lukey, G.C. Engineering properties of inorganic polymer concretes (IPCs). *Cement and Concrete Research* **2007**, 37 (2), 251–257. https://doi.org/10.1016/j.cemconres.2006.10.008.

204. Soultana, A.; Valouma, A.; Bartzas, G.; Komnitsas, K. Properties of inorganic polymers produced form brick waste and metallurgical slag. *Minerals* **2019**, 9, 551. https://doi.org/10.3390/min9090551.

205. Subaer; van Riessen, A. Thermo-mechanical and microstructural characterisation of sodium-poly(sialate-siloxo) (Na-PSS) geopolymers. *Journal of Materials Science* **2007**, 42(9), 3117-3123. https://doi.org/10.1007/s10853-006-0522-9.

206. Sun, J.; Zhang, Z.; Zhuang, S.; He, W. Hydration properties and microstructure characteristics of alkali-activated steel slag. *Construction and Building Materials* **2020,** 241, 118141. https://doi.org/10.1016/j.conbuildmat.2020.118141.

207. Tchadjie, L.N.; Ekolu, S.O. Enhancing the reactivity of aluminosilicate materials toward geopolymer synthesis. *Journal of Materials Science* **2018**, 53, 4709–4733. https://doi.org/10.1007/s10853-017-1907-7.

208. Tchakoute, H.K.; Elimbi, A.; Yanne, E.; Djangang, C.N. Utilization of volcanic ashes for the production of geopolymers cured at ambient temperature. *Cement and Concrete Composites* **2013**, 38, 75–81. https://doi.org/10.1016/j.cemconcomp.2013.03.010.

209. Tchakouté, H.K.; Rüscher, C.H.; Kong, S.; Kamseu, E.; Leonelli, C. Comparison of metakaolin-based geopolymer cements from commercial sodium waterglass and sodium waterglass from rice husk ash. *Journal of Sol-Gel Science and Technology* **2016**, 78, 492–506. https://doi.org/10.1007/s10971-016-3983-6.

210. Temuujin, J.; Minjigmaa, A.; Rickard, W.; Lee, M.; Williams, I.; van Riessen, A. Preparation of metakaolin based geopolymer coatings on metal substrates as thermal barriers. *Applied Clay Science* **2009a**, 46 (3), 265–270. https://doi.org/10.1016/j.clay.2009.08.015.

211. Temuujin, J.; Williams R.P.; van Riessen, A. Effect of mechanical activation of fly ash on the properties of geopolymer cured at ambient temperature. *Jouranl of Materials Processing Technology* **2009b**, 209 (12–13), 5276–5280. https://doi.org/10.1016/j.jmatprotec.2009.03.016.

212. Tennakoon, C.; De Silva, P.; Sagoe-Crentsil, K.; Sanjayan, J.G. Influence and role of feedstock Si and Al content in Geopolymer synthesis. *Journal of Sustainable Cement-Based Materials* **2014b**, 4 (2), 129–39. https://doi.org/10.1080/21650373.2014.979264.

213. Tennakoon, C.; Nazari, A.; Sanjayan, J.G.; Sagoe-Crentsil, K. Distribution of oxides in fly ash controls strength evolution of geopolymers. *Construction and Building Materials* **2014a**, 71, 72–82. https://doi.org/10.1016/j.conbuildmat.2014.08.016.

214. Thaarrini, J.; Ramasamy, V. Properties of Foundry Sand, Ground Granulated Blast Fyrnace Slag and Botton Ash Based Geopolymers under Ambient Conditions. *Periodica Polytechnica Civil Enginnering* **2016**, 60 (2), 159–168. https://doi.org/10.3311/PPci.8014.

215. Tippayasam, C.; Balyore, P.; Thavorniti, P.; Kamseu, E.; Leonelli, C.; Chindaprasirt, P.; Chaysuwan, D. Potassium alkali concentration and heat treatment affected metakaolin-based geopolymer. *Construction and Building Materials* **2016**, 104, 293–297. https://doi.org/10.1016/j.conbuildmat.2015.11.027.

216. Traven, K.; Češnovar, M.; Ducman, V. Particle size manipulation as an influential parameter in the development of mechanical properties in electric arc furnace slag-based AAM. *Ceramics International* **2019**, 45 (17), Part B, 22632–22641. https://doi.org/10.1016/j.ceramint.2019.07.296.

217. Tuyan, M.; Andiç-Çakir, Ö.; Ramyar, K. Effect of alkali activator concentration and curing condition on strength and microstructure of waste clay brick powder-based geopolymer. *Composites Part B: Engineering*, **2018**, 135, 242–252. https://doi.org/10.1016/j.compositesb.2017.10.013.

218. US EPA, 1992. TCLP (Toxicity Characteristics Leaching Procedure), Method 1311, Revision 2, July 1992.

219. Van De Sande, J.; Peys, A.; Hertel, T.; Rahier, H.; Pontikes, Y. Upcycling of non-ferrous metallurgy slags: Identifying the most reactive slag for inorganic polymer construction materials. *Resources, Conseration and Recycling* **2020**, 154, 104627. https://doi.org/10.1016/j.resconrec.2019.104627.

220. Van der Sloot, H.A.; Hjelmar, O.; Bjerre Hansen, J.; Woitke, P.; Lepom, P.; Leschber, R.; Bartet, B.; Debrucker , N. *Validation of CEN/TC 292 Leaching Tests and Eluate Analysis Methods prEN 12457 1-4, ENV 13370 and ENV 12506 in Co-Operation with CEN/TC 308*;

ECN: Petten, Netherlands, 2001. Available online: https://publicaties.ecn.nl/PdfFetch.aspx?nr=ECN-C--01-117 (accessed on 9 November 2018).

221. Van Jaarsveld, J.G.S. The physical and chemical characterisation of fly ash based geopolymers. PhD Thesis, Department of Chemical Engineering, University of Melbourne, Victoria, Australia, 2000.

222. Van Jaarsveld, J.G.S., Van Deventer, J.S.J.; Lukey, G.C. The effect of composition and temperature on the properties of fly ash and kaolinite based geopolymers. *Chemical Engineering Journal* **2002**, 89 (1–3), 63–73. https://doi.org/10.1016/S1385-8947(02)00025-6.

223. Van Jaarsveld, J.G.S.; Van Deventer, J.S.J.; Lorenzen, L. Factors affecting the immobilisation of metals in geopolymerised fly ash. *Metallurgical and Materials Transactions B–Process Metallurgy and Materials Processing Science* **1998**, 29 (1), 283–291. https://doi.org/10.1007/s11663-998-0032-z.

224. Van Jaarsveld, J.G.S.; Van Deventer, J.S.J.; Schwartzman, A. The potential use of geopolymeric materials to immobilize toxic metals: Part II. Material and leaching characteristics. *Minerals Engineering* **1999**, 12 (1), 75–91. https://doi.org/10.1016/S0892-6875(98)00121-6.

225. Vickers, L.; van Riessen, A.; Rickard, W.D.A. Precursors and Additives for Geopolymer Synthesis. *Springer Singapore in Fire-Resistant Geopolymers* **2015**, 17-37. https://doi.org/10.1007/978-981-287-311-8_2.

226. Walling S.A; Kinoshita; H.; Bernal, S.A.; Collier, N.C.; Provis, J.L. Structure and properties of binder gels formed in the system $Mg(OH)_2$-SiO_2-H_2O for immobilisation of Magnox sludge. *Dalton Transactions* **2015**, 44 (17), 8126–8137. https://doi.org/10.1039/c5dt00877h.

227. Wang, D.; Wang, Q.; Zhuang, S.; Yang, J. Evaluation of alkali-activated blast furnace ferronickel slag as a cementitious material: Reaction mechanism, engineering properties and leaching behaviors. *Construction and Building Materials* **2018**, 188, 860-873. https://doi.org/10.1016/j.conbuildmat.2018.08.182.

228. Wang, K.; Lemougna, P.N.; Tang, Q.; Li, W.; He, Y.; Cui, X. Low temperature depolymerization and polycondensation of a slag-based inorganic polymer. *Ceramics International* **2017**, 43 (12), 9067–9076. https://doi.org/10.1016/j.ceramint.2017.04.052.

229. Wang, L. Chen, L., Tsang, D.C.W., Zhou, Y., Rinklebe, J., Song, H., Kwon, E.E., Baek, K., Sik Ok, Y. Mechanistic insights into red mud, blast furnace slag, or metakaolin assisted stabilization/solidification of arsenic-contaminated sediment. *Environment International* **2019**, 133, 105247. https://doi.org/10.1016/j.envint.2019.105247.

230. Wang, R.; Wang, J.; Dong, T.; Ouyang, G. Structural and mechanical properties of geopolymers made of aluminosilicate powder with different SiO_2/Al2O3 ratio: Molecular dynamics simulation and microstructural experimental study. *Construction and Building Materials* **2020b**, 240, 117935. https://doi.org/10.1016/j.conbuildmat.2019.117935.

231. Wang, Y.; Liu, X.; Zhang, W.; Li, Z.; Zhang, Y.; Li, Y.; Ren, Y. Effects of Si/Al ratio on the efflorescence and properties of fly ash based geopolymer. *Journal of Cleaner Production* **2020a**, 244, 118852. https://doi.org/10.1016/j.jclepro.2019.118852.

232. Wei, B.; Zhang, Y.; Bao, S. Preparation of geopolymers from vanadium tailings by mechanical activation. *Construction and Building Materials* **2017**, 145, 236–242. https://doi.org/10.1016/j.conbuildmat.2017.03.234.

233. Won, J.; Kang, S. Dependence of alkali activator coating on aggregates upon mechanical strength of geopolymer/aggregates composites. *Journal of Ceramic Processing Research* **2017**, 18 (2), 166–171.

234. Wong, C.L.; Mo, K.H.; Yap, S.P.; Alengaram, U.J.; Ling, T.C. Potential use of brick waste as alternate concrete-making materials: A review. *Journal of Cleaner Production* **2018**, 195, 226–239. https://doi.org/10.1016/j.jclepro.2018.05.193.

235. Xia, M.; Muhammad, F.; Zeng, L.; Li, S.; Huang, X.; Jiao, B.; Shiauc, Y.; Li, D. Solidification/stabilization of lead-zinc smelting slag in composite based geopolymer. *Journal Cleaner Production* **2019**, 209, 1206–1215. https://doi.org/10.1016/j.jclepro.2018.10.265.

236. Xu, H.; Van Deventer, J.S.J. Geopolymerization of multiple minerals. *Minerals Engineering* **2002**, 15 (12), 1131–1139. https://doi.org/10.1016/S0892-6875(02)00255-8.

237. Xu, H.; Van Deventer, J.S.J. The geopolymerisation of alumino-silicate minerals. *International Journal of Mineral Processing* **2000**, 59 (3), 247–266. https://doi.org/10.1016/s0301-7516(99)00074-5.

238. Xu, Y.; Yang, B.; Liu, X.; Gao, S.; Li, D.; Mukiza, E.; Li, H.. Investigation of the medium calcium based non-burnt brick made by red mud and fly ash: durability and hydration characteristics. *International Journal of Minerals Metallurgy and Materials* **2019**, 26 (8), 983–991. https://doi.org/10.1007/s12613-019-1814-9.

239. .Yi, C.; Boluk, Y.; Bindiganavile, V. Enhancing alkali-activation of metakaolin-based geopolymers using dry water. *Journal of Cleaner Production* **2020**, 258, 120676. https://doi.org/10.1016/j.jclepro.2020.120676.

240. Yahya, Z.; Abdullah, M.M.A.B.; Hussin, K.; Ismail, K.N.; Razak, R.A.; Sandu, A.V. Effect of Solids-To-Liquids, Na_2SiO_3-To-NaOH and Curing Temperature on the Palm Oil Boiler Ash (Si+Ca) Geopolymerisation System. *Materials* **2015**, 8 (5), 2227–2242. https://doi.org/10.3390/ma8052227.

241. Yan, D.; Chen, S.; Zeng, Q.; Xu, S.; Li, H. Correlating the elastic properties of metakaolin-based geopolymer with its composition. *Materials and Design* **2016**, 95, 306–318. https://doi.org/10.1016/j.matdes.2016.01.107.

242. Yang, Z.; Lin, Q.; Lu, S.; He, Y.; Liao, G.; Ke, Y. Effect of CaO/SiO_2 ratio on the preparation and crystallization of glass-ceramics from copper slag. *Ceramics International* **2014**, 40 (5), 7297–7305. https://doi.org/10.1016/j.ceramint.2013.12.071.

243. Yip, C.K.; Lukey, G.C.; Provis, J.L.; Van Deventer, J.S.J. Effect of calcium silicate sources on geopolymerisation. *Cement and Concrete Research* **2008**, 38, 554–564. https://doi.org/10.1016/j.cemconres.2007.11.001.

244. Yip, C.K.; Lukey, G.C.; van Deventer, J.S.J. The coexistence of geopolymeric gel and calcium silicate hydrate at the early stage of alkaline activation. *Cement and Concrete Research* **2005**, 35 (9), 1688–1697. https://doi.org/10.1016/j.cemconres.2004.10.042.

245. Yip, C.K.; Van Deventer, J.S.J. Microanalysis of calcium silicate hydrate gel formed within a geopolymeric binder. *Journal of Materials Science* **2003**, 38 (18), 3851-3860. https://doi.org/10.1023/A:1025904905176.

246. Yuan, J.; He, P.; Jia, D.; Yang, C.; Zhang, Y.; Yan, S.; Yang, Z.; Duan, X.; Wang, S.; Zhou, Y. Effect of curing temperature and SiO_2/K_2O molar ratio on the performance of metakaolin-based geopolymers. *Ceramics International* **2016**, 42 (14), 16184–16190. https://doi.org/10.1016/j.ceramint.2016.07.139.

247. Zaharaki, D.; Galetakis, M.; Komnitsas, K. Valorization of construction and demolition (C&D) and industrial wastes through alkali activation. *Construction and Building Materials* **2016**, 121, 686–693. https://doi.org/10.1016/j.conbuildmat.2016.06.051.

248. Zaharaki, D.; Komnitsas, K. Effect of additives on the compressive strength of slag-based inorganic polymers. *Global Nest Journal* **2009**, 11, 137–146. https://doi.org/10.30955/gnj.000585.

249. Zaharaki, D.; Komnitsas, K. Long term behaviour of ferronickel slag inorganic polymers in various environments. *Fresenius Environmental Bulletin* **2012**, 21 (8), 2436–2440.

250. Zaharaki, D.; Komnitsas, K.; Perdikatsis, V. Use of analytical techniques for identification of inorganic polymer gel composition. *Journal of Materials Science* **2010,** 45 (10), 2715–2724. https://doi.org/10.1007/s10853-010-4257-2.

251. Zhang, P.; Gao, Z.; Wang, J.; Guo, J.; Hu, S.; Ling, Y. Properties of fresh and hardened fly ash/slag based geopolymer concrete: A review. *Journal of Cleaner Production* **2020a**, 122389. https://doi.org/10.1016/j.jclepro.2020.122389.

252. Zhang, P.; Muhammad, F.; Yu, L.; Xia, M.; Lin, H.; Huang, X.; Jiao, B.; Shiau, Y.; Li, D. Self-cementation solidification of heavy metals in lead-zinc smelting slag through alkali-activated materials. *Construction and Building Materials* **2020c**, 249, 118756. https://doi.org/10.1016/j.conbuildmat.2020.118756.

253. Zhang, Q.; Ji, T.; Yang, Z.; Wang, C.; Wu, H-c. Influence of different activators on microstructure and strength of alkali-activated nickel slag cementitious materials. *Construction and Building Materials* **2020b**, 235, 117449. https://doi.org/10.1016/j.conbuildmat.2019.117449.

254. Zhang, S.; Gong, K.; Lu, J. Novel modification method for inorganic geopolymer by using water soluble organic polymers. *Materials Letters* **2004**, 58 (7–8), 1292–1296. https://doi.org/10.1016/j.matlet.2003.07.051.

255. Zhang, Y.J.; Li, H.H.; Wang, Y.C., Xu, D.L. Geopolymer microstructure and hydration mechanism of alkali-activated fly ash-based geopolymer. *Advanced Materials Research* **2011**, 374–377, 1481–1484. https://doi.org/10.4028/www.scientific.net/AMR.374-377.1481.

256. Zhang, Y.J.; Yang, M.Y.; Zhang, L.; Zhang, K.; Kang, L. A new graphene/geopolymer nanocomposite for degradation of dye wastewater. *Integrated Ferroelectrics: An International Journal* **2016b**, 171 (1), 38–45. https://doi.org/10.1080/10584587.2016.1171178.

257. Zhang, Z.H.; Zhu, H.J.; Zhou, C.H.; Wang, H. Geopolymer from kaolin in China: An overview. *Applied Clay Science* **2016a**, 119 (1), 31–41. https://doi.org/10.1016/j.clay.2015.04.023.

258. Živica, V.; Balkovic, S.; Drabik, M. Properties of metakaolin geopolymer hardened paste prepared by high-pressure compaction. *Construction and Building Materials* **2011**, 25 (5), 2206–2213. https://doi.org/10.1016/j.conbuildmat.2010.11.004.

259. Zong, Y.; Zhang, X.; Mukiza, E.; Xu, X.; Li, F. Effect of Fly Ash on the Properties of Ceramics Prepared from Steel Slag. *Applied Sciences*. **2018**, 8 (7), 1187. https://doi.org/10.3390/app8071187.

Published Papers

I. Komnitsas, K.; Bartzas, G.; **Karmali, V.**; Petrakis, E.; Kurylak, W.; Pietek, G.; Kanasiewics, J. Assessment of alkali activation potential of a Polish ferronickel slag. *Sustainability* **2019**, 11, 1863. https://doi.org/10.3390/su11071863.

II. Komnitsas, K.; Petrakis, E.; Bartzas, G.; **Karmali, V**. Column leaching of low-grade saprolitic laterites and valorization of leaching residues. *Science of the Total Environment* **2019**, 665, 347–357. https://doi.org/10.1016/j.scitotenv.2019.01.381.

III. Petrakis, E.; **Karmali, V.**; Bartzas, G.; Komnitsas, K. Grinding Kinetics of Slag and Effect of Final Particle Size on the Compressive Strength of Alkali Activated Materials. *Minerals* **2019**, 9, 714. https://doi.org/10.3390/min9110714.

IV. Komnitsas, K.; Yurramendi, L.; Bartzas, G.; **Karmali, V.**; Petrakis, E. Factors affecting co-valorization of fayalitic and ferronickel slags for the production of alkali activated materials. *Science of the Total Environment* **2020**, 721, 137753. https://doi.org/10.1016/j.scitotenv.2020.137753.

V. Komnitsas, K.; Bartzas, G.; **Karmali, V.**; Petrakis, E. Factors Affecting Alkali Activation of Laterite Acid Leaching Residues. *Environments* **2021**, 8, 4. https://doi.org/10.3390/environments8010004.

Assessment of Alkali Activation Potential of a Polish Ferronickel Slag

Konstantinos Komnitsas [1,*] , **Georgios Bartzas** [2] , **Vasiliki Karmali** [1] , **Evangelos Petrakis** [1] , **Witold Kurylak** [3] , **Grzegorz Pietek** [3] **and Jarosław Kanasiewicz** [4]

[1] School of Mineral Resources Engineering, Technical University of Crete, 73100 Chania, Greece; vkarmali@isc.tuc.gr (V.K.); vpetraki@mred.tuc.gr (E.P.)

[2] National Technical University of Athens, School of Mining and Metallurgical Engineering, 15780 Zografos, Athens, Greece; gbartzas@metal.ntua.gr

[3] Instytut Metali Nieżelaznych, ul. Generała Józefa Sowińskiego 5, 44–100 Gliwice, Poland; witoldk@imn.gliwice.pl (W.K.); grzegorz.pietek@imn.gliwice.pl (G.P.)

[4] PROFIMA, ul. Bielawska 6/40, 02-511 Warsaw, Poland; kanasiewicz@interia.pl

* Correspondence: komni@mred.tuc.gr; Tel.: +30-28210-37686

Abstract: In this study, the alkali activation potential of a Polish ferronickel slag (PS), for the production of inorganic polymers (IPs), is investigated. The effect of the main synthesis parameters, i.e., strength of the activating solution, consisting of NaOH and Na_2SiO_3 solutions and affecting $(SiO_2 + Al_2O_3)/Na_2O$ and other important molar ratios in the reactive paste, pre-curing period, curing temperature and time and ageing period was investigated. The structural integrity of the produced specimens was tested after their (i) immersion in distilled water and acidic solutions for a period of 7–30 days, and (ii) firing at temperatures between 200 °C and 1000 °C. Several analytical techniques including X-ray diffraction, X-ray fluorescence, Fourier transform infrared spectroscopy, Differential scanning analysis-Thermogravimetry and Scanning Electron Microscopy were used for the characterization of the produced IPs. Results show that under the optimum synthesis conditions the IPs obtain compressive strength that exceeds 65 MPa. An innovative aspect of this study is that after heating at 400 °C, the specimens acquire compressive strength of 115 MPa and this indicates that they can be also used as fire resistant materials. This study highlights the potential of alkali activation for the valorization of a ferronickel slag and the production of IPs that can be used as binders or in several construction applications, thus improving the sustainability of the metallurgical sector.

Keywords: ferronickel slag; alkali activation; compressive strength; morphology

1. Introduction

Millions of tons of metallurgical slags, containing fine-grained silicate and glassy phases, are produced every year from the non-ferrous, ferrous and steel industry. Today, even though considerable quantities of slags are used in concrete production and other construction applications, large quantities are disposed on land and elsewhere, thus causing various environmental impacts [1–3].

By taking into account that several slags may be considered hazardous under the existing strict environmental regulations [4,5], the development of an integrated management scheme that valorizes slags, produces secondary products with higher added value, minimizes environmental impacts, and improves the sustainability of the metallurgical sector is under investigation [6–9].

Inorganic polymers (IPs) or geopolymers have an amorphous to semi-crystalline three dimensional alumino-silicate microstructure and chemical composition quite similar to zeolites [10,11]. They exhibit low permeability and high-unconfined compressive strength, low shrinkage, good

resistance to acid attack, freeze-thaw cycles and fire, as well as good immobilization potential for several heavy metals within their structure [12–15]. In addition, some studies have been carried out to compare the environmental footprint of geopolymer and Portland concrete [16–18].

Inorganic polymers are produced through alkali activation. The source of IPs includes a broad range of virgin materials and industrial waste [19,20]. The process for the production of IPs starts with the dissolution of Si and Al from raw materials with the action of alkaline solutions and the formation of a gel that, after a relatively short setting time, hardens quickly. The presence of a silicate solution balances the Si/Al atomic ratio in the IP paste and leads to the formation of homogeneous interconnected structures, which define their final physical, mechanical and thermal properties [21–25].

The alkali activation of various types of metallurgical slags, often in mixtures with other industrial wastes, for the production of IPs has been widely studied. The materials produced have diverse properties depending on the characteristics of the source materials, the additives, and the experimental conditions used. In this context, slags with varying content of Fe, Si, Al and Ca have been investigated, including ground granulated blast furnace slag mixed with fly ash [26–28], ferronickel (FeNi) slag [2,29,30] or mixtures of FeNi slag, construction and demolition wastes and red mud [31], mixtures of steel slag and metakaolin or kaolin [32,33], slags from non-ferrous metallurgy [34], and mixtures of fly ash and lead slag [35].

The present experimental study aims to investigate the main factors affecting the alkali activation of an old and subjected to weathering Polish ferronickel slag, assess the structural integrity of the produced IPs when exposed to various environmental conditions, identify their potential toxicity, and determine whether they can be used in construction applications.

2. Materials and Methods

The slag, which was produced after pyrometallurgical treatment of nickel (Ni) lateritic ores, was collected from a waste dump at Szklary, Lower Silesia, in south-western Poland [36]. Mining was initiated in the area after the discovery of nickel deposits in 1890 and lasted until 1983. During the period of 1890–1920, ore was excavated using underground mining, while later surface mining techniques were applied. The Ni content in the ore varied between 1% and 4% in surface and deeper locations, respectively; it is mentioned that in some ore lenses, the Ni content was as high as 12%. During the period of 1955–1983, about 4.6 million tons of ore were excavated, of which 2.9 million tons were treated pyrometallurgically to produce almost 20,000 t of nickel. Today, the mineable deposit is estimated at 14.64 million tons and the Ni that can be produced is estimated at 120 thousand tons; the cut-off grade of Ni in the ore is 0.8%.

The as-received slag was pulverized using a Fritsch-Bico pulverizer and then characterized in terms of mineralogical and chemical composition. The particle size analysis of the ground slag was determined using a Mastersizer S (Malvern Instruments) analyser. A Bruker-AXS S2 Range Spectroscopic Fluorescence Spectrometer A (XRF-EDS) was used for chemical analysis, while the main mineralogical phases were identified through X-ray diffraction (XRD) using a Bruker D8 Advance diffractometer (Cu tube, scanning range from 4° to 70° 2θ, step 0.02° and 2s/step). Fourier transform infrared (FTIR) spectroscopy, using a Perkin Elmer Spectrum 1000 spectrometer, was used for the identification of the functional groups present in solid samples, while a Setaram LabSys Evo, TG-DTA-DSC analyzer was used to carry out differential thermal analysis and Thermogravimetry (DTA/TG). The identification of the morphology and structure of the raw material and the final products were identified by Scanning Electron Microscopy (SEM), using a JEOL 6380LV (USA) microscope equipped with an Oxford INCA energy dispersive X-ray spectrometer (EDS).

For the production of the IPs, the slag was mixed for about 10 min, in a laboratory mixer under continuous slow stirring, with the alkaline activating solution, which was prepared by dissolving sodium hydroxide (NaOH) anhydrous pellets (Sigma Aldrich) in distilled water to obtain the required molarity, namely 6, 8, 10 and 12 mol L^{-1} (M), followed by the addition of sodium silicate solution (Na$_2$O = 7.5 − 8.5%, SiO$_2$ = 25.5 − 28.5%, Merck). The activating solution, which was allowed to

cool for 24 h prior to use, had molar ratios SiO_2/Na_2O equal to 0.37, 0.26, 0.21 and 0.19, while the H_2O/Na_2O molar ratios were 19.03, 14.31, 11.16 and 9.26, respectively. The liquid/solid (L/S) ratio in the initial reactive paste varied slightly between 0.19 and 0.23, depending on the conditions used in each case, to improve the flowability characteristics of the produced paste before casting. A typical average indicative composition of the starting mixture was (in wt%): slag 82%, 8M NaOH solution 15% and Na_2SiO_3 solution 3%; the wt% of Na_2SiO_3 was kept constant in all tests. It is mentioned that these ratios are some of the lowest reported in the literature for similar studies.

The fresh paste was cast in cubic metal moulds of 5 cm edge, which were vibrated for a few minutes to remove air from the reactive mass and thus improve the strength of the final specimens. Pre-curing involved retention of the paste in the moulds at room temperature for a period of 6 h to 48 h to allow initiation of the alkali activating reactions, development of structural bonds and partial solidification. Then, the formed specimens were demoulded, sealed in plastic bags to prevent fast evaporation of the remaining water, cured at 40–80 °C in a laboratory oven (Jeio Tech ON-02G) for 24 or 48 h and allowed to cool. This configuration was based on the results obtained from a large number of previous studies investigating the alkali activation potential of several metallurgical wastes [2,30]. After ageing at room temperature (20 °C) for 7 days or 28 days, the compressive strength of the specimens was determined with the application of a MATEST C123N load frame. All tests were carried out in duplicate.

In order to study the structural integrity of the produced IPs, specimens obtained under the optimum conditions were immersed in distilled water and acidic solutions (1M HCl and 1M H_2SO_4) for 7, 15 and 30 days. Also, the thermal behavior of the IPs was evaluated after firing them in a laboratory oven (N-8L SELECTA) at temperatures between 200 °C and 1000 °C. The heating rate used was 5 °C min^{-1}, while the retention time at each temperature was very long, namely 6 h. The specimens were naturally cooled in the oven prior to determination of their final compressive strength. Each experimental series was also carried out in duplicate.

The determination of the apparent density of selected IPs was carried out in accordance with BS EN 1936 (2006) [37]. Finally, the toxicity of the as-received slag as well as of the IPs produced was assessed by subjecting them to the EN 12457-3 test [38,39], involving leaching of 8 L per kg of material in distilled water for 24 hours. The leaching solutions were filtered using 0.45 μm membrane filters and the concentration of the metals in the eluate was expressed as mg kg^{-1} of dry slag or IP and compared with existing limits for disposal of wastes in various landfill types [40].

3. Results and Discussion

3.1. Slag Characterisation

The particle size distribution of the as-received slag after grinding revealed that the 90% passing size (d_{90}) of the material is 57.50 μm, which is considered adequately fine for efficient alkali activation and the production of IPs, as indicated in previous studies [41].

Table 1 shows the chemical composition of slag in the form of oxides, as derived by XRF. It is observed that the slag contains sufficient amounts of SiO_2 (30.18%) and Al_2O_3 (7.6%) for alkali activation, while the content of Fe_2O_3 and CaO is also high, 40.62% and 13%, respectively.

Table 1. Chemical composition (wt%) of slag.

Fe_2O_3	SiO_2	Al_2O_3	Cr_2O_3	MgO	NiO	K_2O	Na_2O	TiO_2	CoO	MnO	CaO	P_2O_5	Total
40.62	30.18	7.60	1.98	1.80	0.95	0.89	0.44	0.69	0.03	0.28	13.0	0.02	98.48

The quality of this slag is comparable with that of Larco S.A slag, derived from pyrometallurgical treatment of Greek laterites and used in a previous study for the synthesis of IPs [41]. The only major difference is that Larco slag has much lower CaO content, 3.73%.

3.2. Factors Affecting IP Synthesis

3.2.1. Effect of NaOH Molarity, Selected Molar Ratios in the Reactive Paste and Curing Temperature

　　Figure 1 shows the compressive strength of the IPs produced after a curing period of 24 h and an ageing period of 7 days as a function of NaOH molarity (6–12 M) and curing temperature (40 °C or 80 °C). It is seen that the effect of temperature is considered marginal for all NaOH concentrations tested; this indicates, in terms of heating requirements, that the process is energy efficient. On the other hand, the compressive strength of the produced IPs increases slightly and reaches its maximum value, 67.0 MPa, when the NaOH molarity increases from 6 to 8 M, whereas it drops substantially when higher NaOH molarities (10–12 M) are used. The fact that an optimum NaOH concentration exists has been also noted in several earlier studies involving alkali activation of slags and other industrial wastes [3,42,43]. When high NaOH molarity is used, unreacted OH^- may remain in the paste and the produced specimens cannot acquire the maximum strength. Overall, for this specific slag, it is deduced that NaOH molarity is a much more important factor than curing temperature during IP synthesis. Finally, it is mentioned that the water loss during curing at 80 °C is identical (1.9%) when NaOH molarity is 6 mol L^{-1} or 8 mol L^{-1} and increases to 2.5% or 3.1% when the molarity used is 10 mol L^{-1} and 12 mol L^{-1}, respectively.
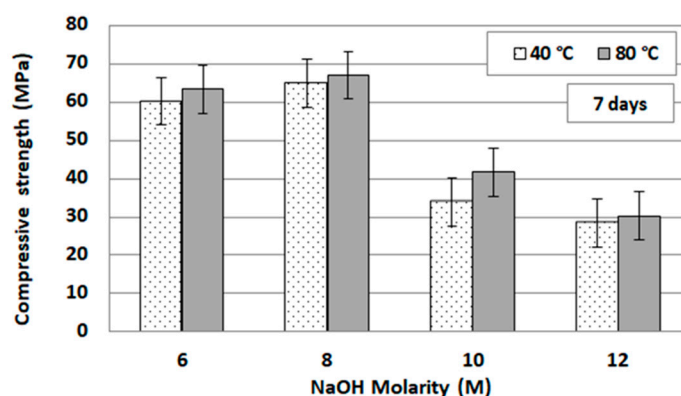
Figure 1. Effect of NaOH molarity in relation to curing temperature on the compressive strength of the produced IPs (curing temperature 40 °C or 80 °C, ageing period seven days, pre-curing and curing time 24h; error bars denote standard deviation of measurements obtained from three specimens).

　　In order to further elucidate these findings, the molar ratios of selected phases present in the initial reactive paste for each NaOH molarity used, are calculated and presented in Table 2. In this table, the compressive strength of IPs cured at 80 °C (shown in Table 1) are also given for comparison.

Table 2. Molar ratios of selected phases present in the reactive paste.

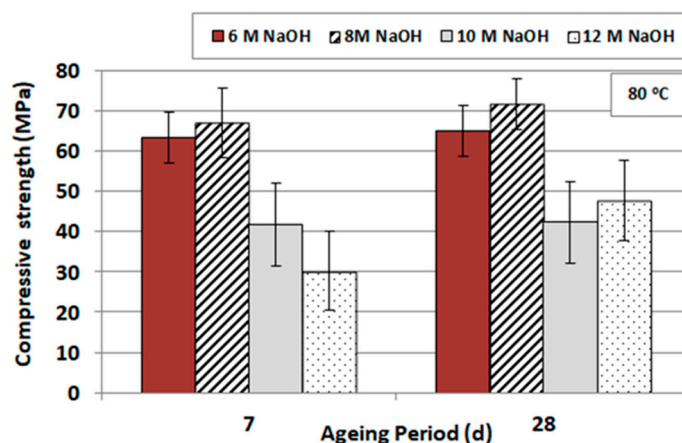| NaOH Molarity (M)	Compressive Strength (MPa) *	$(SiO_2 + Al_2O_3)/Na_2O$	H_2O/Na_2O	Na/Al	Fe_2O_3/Na_2O
6	63.3	11.9	16.3	0.7	5.1
8	67.0	8.6	12.9	0.9	3.7
10	41.7	6.8	10.3	1.2	2.9
12	30.2	6.4	8.5	1.3	2.7

* Curing temperature 80 °C.

　　As shown in Table 2, when the activator concentration increases, given that the wt% addition of Na_2SiO_3 solution is low and identical in all tests, the molar ratios $(SiO_2 + Al_2O_3)/Na_2O$ decrease in the reactive paste and thus higher degree of hydrolysis and dissolution of silicon, aluminium and iron that polymerize/polycondensate to form IPs with higher strength is anticipated. This is confirmed by our data, which show that when the NaOH molarity increases from 6 M to 8 M, the compressive

strength also increases slightly (~5%). Lower molar ratios, obtained when higher NaOH molarities are used, result in excess of activator in the paste, which may not fully react with solid particles or require much longer time for reaction and thus the specimens acquire lower strength. This conclusion is also supported by the values of the Na/Al ratio in the reactive paste. Optimum ratios indicate the presence of sufficient OH^-, which accelerate polycondensation, whereas if ratios get bigger than a specific value, the compressive strength will drop. As mentioned in a recent study and several other research works, an optimum Na/Al ratio close to one is required for the synthesis of IPs with high strength [44]. Regarding the effect of the molar ratio Fe_2O_3/Na_2O, it is seen from Table 2 that obviously this ratio decreases as the molarity of NaOH solution increases. The role of Fe, whose content is high in several slags of the non-ferrous and steel industry, cannot be easily elucidated. Good insights into the behavior of Fe are provided in recent studies, which indicate that Fe^{2+} may be oxidized to Fe^{3+} during alkaline activation in the inorganic polymer binder, or incorporated into the polysialate (Si-O-Al) as network modifier or even participate in carbonation reactions [45,46]. However, in our case, no efflorescence was noticed on any of the produced specimens.

3.2.2. Effect of Ageing Period

Figure 2 shows the effect of ageing period on the compressive strength of the produced IPs. It is seen from this data that the ageing period has practically no effect on the compressive strength and the values obtained are almost identical and within the measurement error; the highest value recorded was 71.4 MPa, when IPs were produced using 8M NaOH after curing at 80 °C and ageing for 28 days. This means that the alkali activation reactions are fast and almost completed during curing and ageing for seven days, in contrast to the reactions involved in concrete production, which progress for a period of 28 days after casting and result in additional strength gain. The only exception shown was in the case where 12 M NaOH solution was used as activating solution and some of the excess NaOH reacts over the remaining period so that the final compressive strength increases to 47.8 MPa after 28 days (58% increase). As mentioned earlier, the only parameter that varied significantly in our tests was the molarity of the NaOH solution, whereas the wt% addition of Na_2SiO_3 was kept equal in all tests and the L/S ratio in the reactive paste was very low. Prolonged ageing periods normally improve compressive strength [2,44], but in our study this was not the case even when different mixing configurations were used (data not shown).

Figure 2. Effect of ageing period (in days) in relation to NaOH molarity on the compressive strength of the produced IPs (curing temperature 80 °C, pre-curing and curing time 24 h; error bars denote standard deviation of measurements obtained from three specimens).
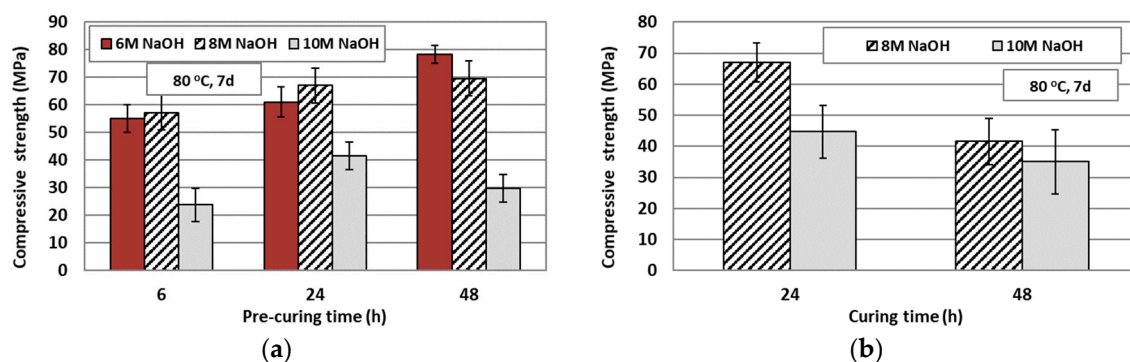
3.2.3. Effect of Pre-Curing and Curing Period

Figure 3a,b show the effect of pre-curing and curing period on the compressive strength of the produced IPs, respectively. The duration of pre-curing defines the extent to which reactions involved

in alkali activation of the raw materials, depending on the L/S ratio and the strength of the activating solution, proceed so that bonds are developed and specimens harden and acquire early strength.

It is seen in Figure 3a that for a pre-curing period of 6 h or 24 h, the produced IPs obtain marginally better compressive strength when 8M NaOH is used. If the pre-curing period becomes 48 h, the use of 6M NaOH results in IPs with higher strength (78.4 MPa), almost 28% increase in comparison with the pre-curing period of 24 h. The use of 10M NaOH results in IPs with lower compressive strength, regardless of the pre-curing period used. Based on this data, we selected 24 h as optimum pre-curing period.

Figure 3b shows that when the molarity of NaOH is 8M, the curing temperature 80 °C and the ageing period 24 h, the optimum curing period is 24 h. The same graph also indicates that longer curing periods, when high molarity and temperature are used, has an adverse effect on the compressive strength of the produced IPs. This loss of strength is mainly linked to (i) the lack of sufficient amount of water, which is necessary for polycondensation reactions and (ii) the presence of unreacted alkaline solution, factors which affect the mobility of ions in the matrix and also create internal stresses [47].

Figure 3. Effect of (**a**) pre-curing time and (**b**) curing time and NaOH molarity on the compressive strength of inorganic polymer (curing temperature 80 °C, curing time 24 h, ageing period seven days; the pre-curing time in (**b**) is 24 h; error bars denote standard deviation of measurements obtained from three specimens).

3.3. Structural Integrity of IPs

3.3.1. Effect of High-Temperature Firing

Figure 4 illustrates the effect of firing of IPs, for a period of 6h, over a temperature range of 200–1000 °C on their compressive strength. The specimens tested were produced using activating solution consisting of 8M NaOH and Na_2SiO_3, curing temperature of 80 °C, curing period 24 h and ageing period seven days. The compressive strength of the control specimen, which was not subjected to firing, is also shown for comparison. In addition, Table 3 shows some selected properties, namely shrinkage (%), mass loss (%) and apparent density (g cm^{-3}) of the fired specimens.

It is seen from this data that the compressive strength of the specimens increases substantially after firing up to 400 °C and then decreases sharply. The increase of the compressive strength after firing at 400 °C to 115 MPa may be attributed to oxidation of fayalite and magnetite of the PS and the increase in the quantity of several phases as shown in the XRD patterns (see below in text). This behavior has also been observed in a study by Onisei et al. [48], where the IPs produced from alkaline activation of a fayalitic slag (Fe_2O_3 49.6%, SiO_2 27.1%, Al_2O_3 6.8%, ZnO 8.4% and CaO 1.6%) exhibited after firing at 500 °C an increase in strength by almost 30% to 105 MPa, regardless of the addition of 5% or 10% analytical grade Al_2O_3 in the starting mixture. This increase in strength was attributed to the formation of new phases, including laihunite [$Fe^{2+}Fe^{3+}_2(SiO_4)_2$] as the result of oxidation of fayalite, as well as sodium aluminum silicate ($NaAlSiO_4$), hematite, magnetite and spinel hercynite ($FeAl_2O_4$). The compressive strength of the IPs after firing at 1000 °C was extremely low, while the specimens showed a volumetric expansion of 7.1% and were severely damaged. This sharp drop in strength after

firing in very high temperatures is due to dehydroxylation of silanol (Si-OH) and aluminol (Al–OH) groups that causes development of cracks and pores [49].
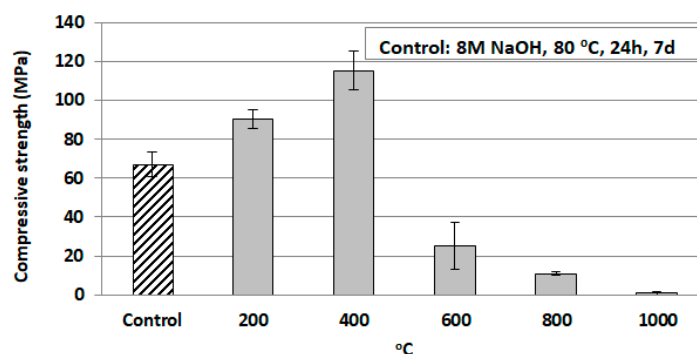
Figure 4. Evolution of compressive strength of selected IPs when fired at high temperatures (the compressive strength of control IP was determined after 7 days of ageing); error bars denote standard deviation of measurements obtained from three specimens.

Table 3. Selected properties of the fired specimens.

| Temperature (°C)	Compressive Strength (MPa)	Shrinkage (%)	Mass Loss (%)	Apparent Density (g cm^{-3})
200	90	4.0	5.1	2.2
400	115	4.8	7.3	2.7
600	25	3.6	9.6	2.0
800	11	2.2	10.2	1.8
1000	2	−7.1	NM [1]	NM

[1] NM: not measured.

Other factors that contributed to the increase in strength after firing at 400 °C are the volumetric shrinkage by 4.8% (Table 3), which is the highest at this temperature, and the increase in density to 2.7 g cm^{-3}. The bigger changes seen, mainly for shrinkage and mass loss, after firing at temperatures higher than 600 °C are mainly due to phase transformations. These properties were not measured for the IP fired at 1000 °C, since as mentioned earlier, it suffered severe damage. The increase in strength of the IPs produced in the present study after firing at 400 °C is a very important finding and shows that they can be potentially used as fire resistant materials and replace or coat concrete in specific construction applications; for example, in tunnels, thus allowing more time for rescue teams to intervene in case of fire. Similar, but noticeably smaller increase was also reported in earlier studies investigating the potential of a Greek ferronickel slag for the production of IPs [49,50].

3.3.2. Effect of Immersion of IPs in Distilled Water or Acidic Solutions

Figure 5 shows the compressive strength of IPs, produced under the conditions of molarity NaOH 8M, heating 80 °C, curing period 24 hours and ageing period seven days, when immersed in distilled water or acidic solutions (1M HCl and 1M H_2SO_4) for 7, 15 and 30 days. The compressive strength of control specimens is also provided for comparison. It is seen that the immersion of IPs in distilled water, even for a period of 30 days, has a relatively minor effect on their compressive strength. Also, the IPs retain a very good strength, varying between 33.8 MPa and 36.5 MPa, even when immersed in 1M HCl and H_2SO_4 solutions for a period of 30 days. The maximum mass loss of the IPs immersed in distilled water, H_2SO_4 and HCl solutions was 0.9%, 3.2% and 5.6% respectively, which is considered as low to very low in all cases. Earlier studies carried out in our laboratory confirm the higher mass loss of various IPs when immersed in HCl solution. It is also mentioned that the final pH of the solutions containing distilled water, HCl and H_2SO_4 after immersion of the specimens for 30 days was 11.0, 2.7 and 1.7 respectively. These results indicate that the IPs respond well and exhibit very good structural integrity in corrosive environments.
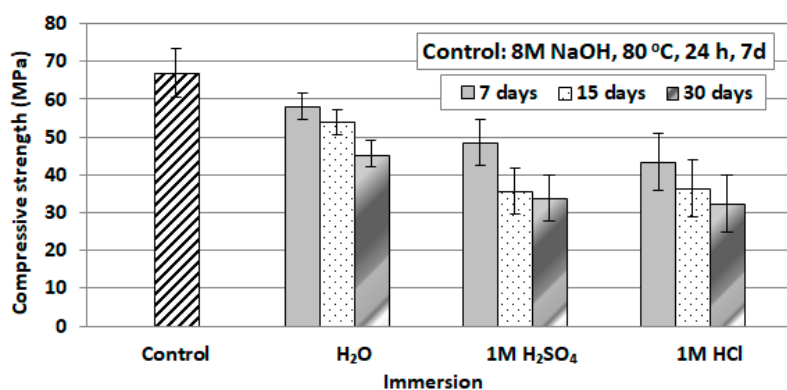
Figure 5. Evolution of the compressive strength of selected specimens immersed in water or acidic solutions for a period of 7 to 30 days (the compressive strength of the control IP is obtained after seven days; error bars denote standard deviation of measurements obtained from three specimens).

### 3.4. Morphology-Microstructure of Inorganic Polymers

Figure 6 presents the XRD pattern of PS and selected IPs, namely the one produced under the conditions of molarity NaOH 8M, curing temperature 80 °C and curing period 24 h, as well as those immersed in 1M HCl for 30 days or fired at 400 °C. It is seen from this figure that the main mineralogical phases present in PS are quartz (SiO_2), hedenbergite ($Ca(Fe,Mg)(SiO_3)_2$), fayalite (Fe_2SiO_4), diopside ($CaMgSi_2O_6$) and magnetite (Fe_3O_4), while hatrurite (Ca_3SiO_5) is present as a minor phase. In addition, PS has a high amorphous content (~45%), which is indicated by the broad hump shown between 2θ 25–40°, and is typical for several metallurgical slags [49,50]. As seen in Figure 6b–d, no new visible major crystalline phases for the selected IPs were detected. However, the intensities of some crystalline phases, namely fayalite, hedenbergite and diopside increases in the IP after firing at 400 °C and this may explain the noticeable increase of its compressive strength.
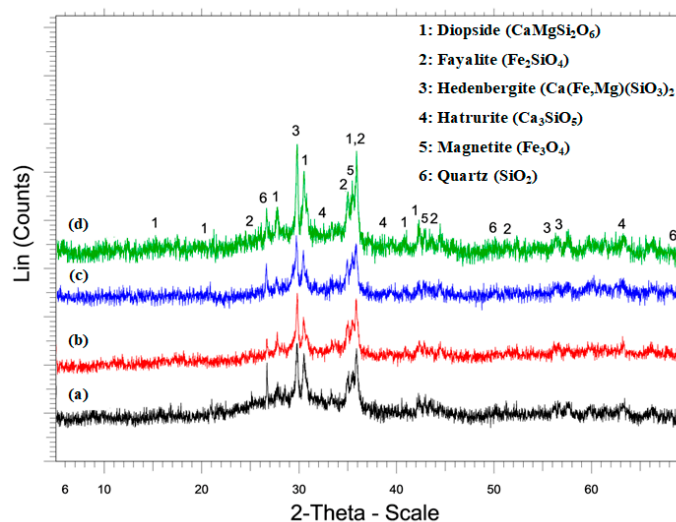
Figure 6. XRD patterns of (**a**) raw PS, (**b**) IP produced after alkali activation with 8M NaOH, (**c**) IP immersed in 1M HCl for 30 days and (**d**) IP fired at 400 °C.

The FTIR spectra of raw PS and selected IPs are shown in Figure 7. In line with the XRD data, the spectrum of the raw PS presents the characteristic peaks of Ca-Fe-Mg-silicate-based slags dominated by fayalite, diopside and hedenbergite, with bands seen at 828 cm^{-1}, 872 cm^{-1} and 948 cm^{-1} [45,46,51–53]. The first band results from the v1 mode (symmetric stretch), while the others correspond to the asymmetric stretching vibrations of SiO_4 (v3 mode). An additional peak associated with the stretching vibrations of Si-O bands of diopside is also seen at 668 cm^{-1} [54]. The peak seen

at 472 cm^{-1} in Figure 7a,b (raw PS and IP produced using 8M NaOH) is ascribed to the overlapping Si-O-Si and O-Mg-O bending vibrations [55,56]. It is seen that this rocking band disappears after firing at 400 °C (Figure 7d), thus indicating that phase transformations took place and may have resulted in the increase of the compressive strength. The strong single peak at 1016 cm^{-1} shown in Figure 7b (IP produced using 8M NaOH) reveals the formation of reaction products in the IPs after exposure to highly alkaline solution [41,57,58]. The structural reorganization as result of the alkaline activation is more noticeable in the broader bands shown in the same region (800–1200 cm^{-1}) for the IPs immersed in HCl solution or fired at 400 °C (Figure 7c,d, respectively). The weaker band at 1634 cm^{-1} in the raw PS and the sharper peaks seen at 1650 cm^{-1}, 1636 cm^{-1} and 1644 cm^{-1} in IPs belong to the characteristic bending vibrations of H-O-H [59–61]. The intense absorption bands at ~1410 cm^{-1} and ~1490 cm^{-1} shown only in the IPs are attributed to stretching vibrations of O-C-O bonds due to carbonation of the remaining Na-silicate [59,62]. Moreover, the notable bands observed in the raw PS and IP produced using 8M NaOH at 3744 cm^{-1} and 3756 cm^{-1}, respectively (Figure 7a,b) are typical for the OH-stretching region. However, the presence of water is more evident in all IPs since a quite wide absorption band region appeared between 3000 cm^{-1} and 3700 cm^{-1} belonging to stretching vibrations of OH groups [52], as result of the hydration processes that took place during alkali activation.
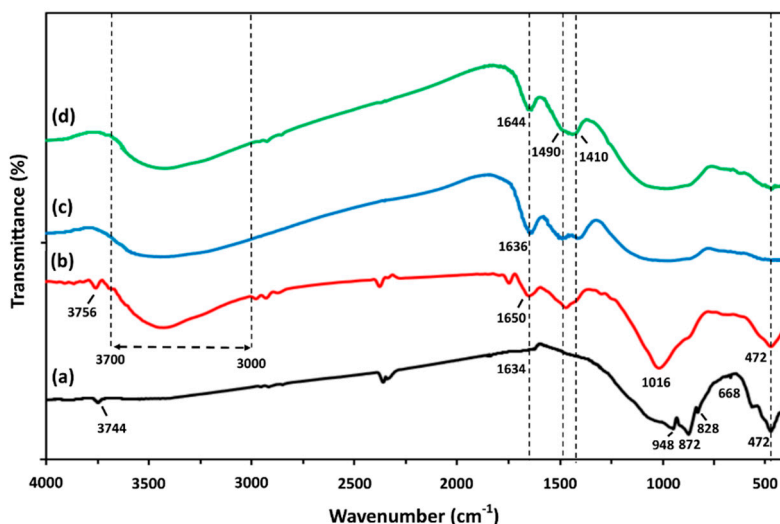
Figure 7. FTIR spectra of (**a**) raw slag, (**b**) IP produced after alkali activation with 8M NaOH, (**c**) IP immersed in 1M HCl for 30 days and (**d**) IP fired at 400 °C.

The behavior of the raw slag and selected IPs, namely the one produced after alkaline activation using 8M NaOH, curing temperature of 80 °C and curing period of 24 h (control IP) as well as after firing at 400 °C was investigated through DTA/TG analysis (Figure 8a–c). In general, TG-curves show that the initial mass of the samples decreases as a result of dehydration of free (below 200 °C) and chemically bound water up to 400 °C for raw PS (Figure 8a) and 570 °C for IPs (Figure 8b,c). More specifically, Figure 8a shows a clearly visible peak at 742 °C associated to significant mass gain (~2.3%) of the PS, which can be attributed to the oxidation of fayalite to hematite and silica [53]. This exo-effect is characterized by a continuous increase in mass for the raw PS and involves a four-stage mechanism, i.e., (i) oxidation of magnetite and formation of metastable spinel (γ-Fe$_2$O$_3$), (ii) transformation of γ-Fe$_2$O$_3$ into the stable α-Fe$_2$O$_3$; (iii) oxidation and decomposition of fayalite (2FeO·SiO$_2$), (iv) decomposition of the residual fayalite and polymorphic transformations of the silicate and iron phases [63]. On the other hand, the endothermic peak shown at 468 °C in the raw PS is related to dehydroxylation/condensation processes [64], which result in a slight mass loss (~0.4%) due to the release of residual moisture.

Figure 8b,c show that similar TG-curves were obtained for the two selected IPs as a result of alkali-activation. The control IP (Figure 8b) shows a weight loss ~7%, observed below 200 °C, which is mainly attributed to the dehydration of the calcium/magnesium-rich silicate gel. The remaining more strongly bound water evaporates after heating above 400 °C and results in an additional 3% weight loss. Heating in higher temperatures results in a minor weight increase (~0.7%), attributed to oxidation reactions that took place in the iron-rich phases i.e., fayalite and magnetite [52,65]. Regarding the IP fired at 400 °C, a four-time lower overall decrease in mass is observed compared to control IP (3.3% vs. 12.1%), thus indicating that more pronounced alkali-activation processes dominated the formation of the geopolymeric gel. The latter also explains the structural stability of this IP, which is reflected by its noticeable increase in strength (115 MPa).
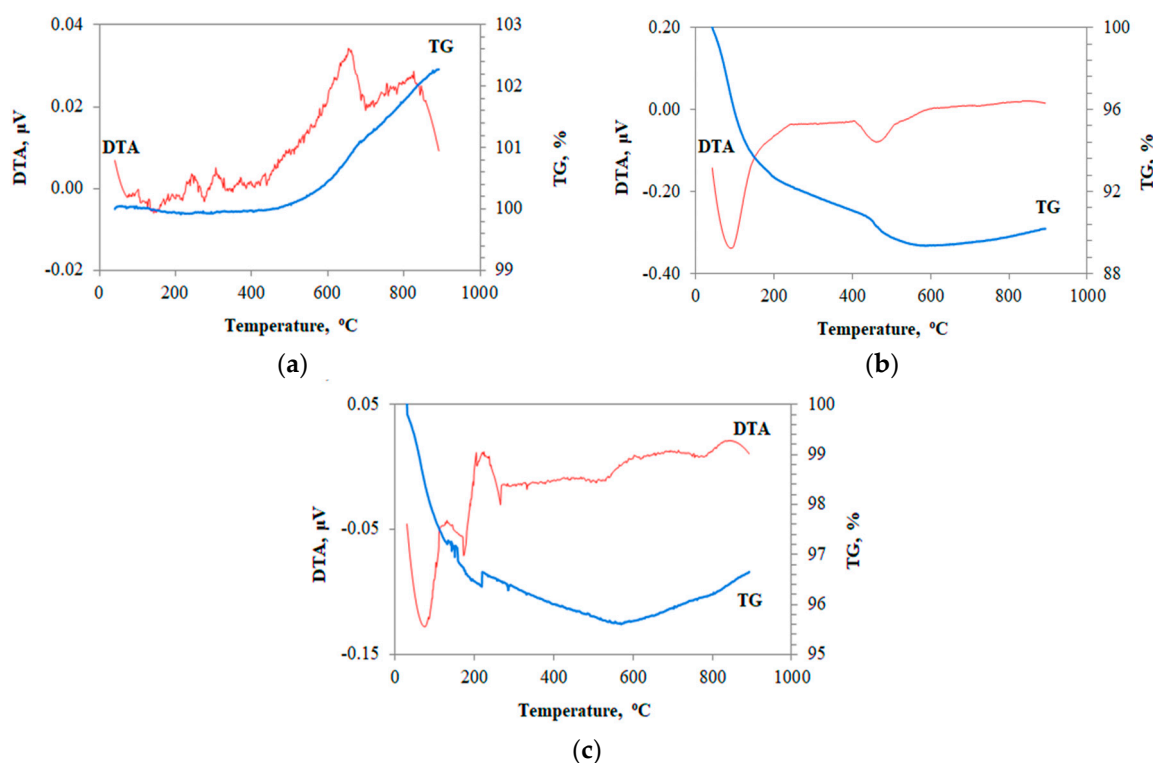
Figure 8. DTA-TG analysis of (**a**) raw slag, (**b**) control IP produced using 8M NaOH and (**c**) IP fired at 400 °C.

As shown in XRD analysis, SEM examination of PS surface by SEM/EDS (Figure 9a) revealed a glassy morphology with sharp edges that is heterogeneous in size and dominated by large quartz, diopside and weathered fayalite crystals (>50 µm long) along with small spherical grains (<15 µm) of magnetite. According to EDS point analyses, other (inter)metallic phases such as chromite ($FeCr_2O_4$) and awaruite (Ni_3Fe) were also detected in minor quantities as small single intergrown drops and inclusions, respectively [36]. Furthermore, several parallel laths/seams of Cr-spinel (~2 µm thick) embedded in clinopyroxene (diopside) matrix were identified containing up to 5.2% Cr.
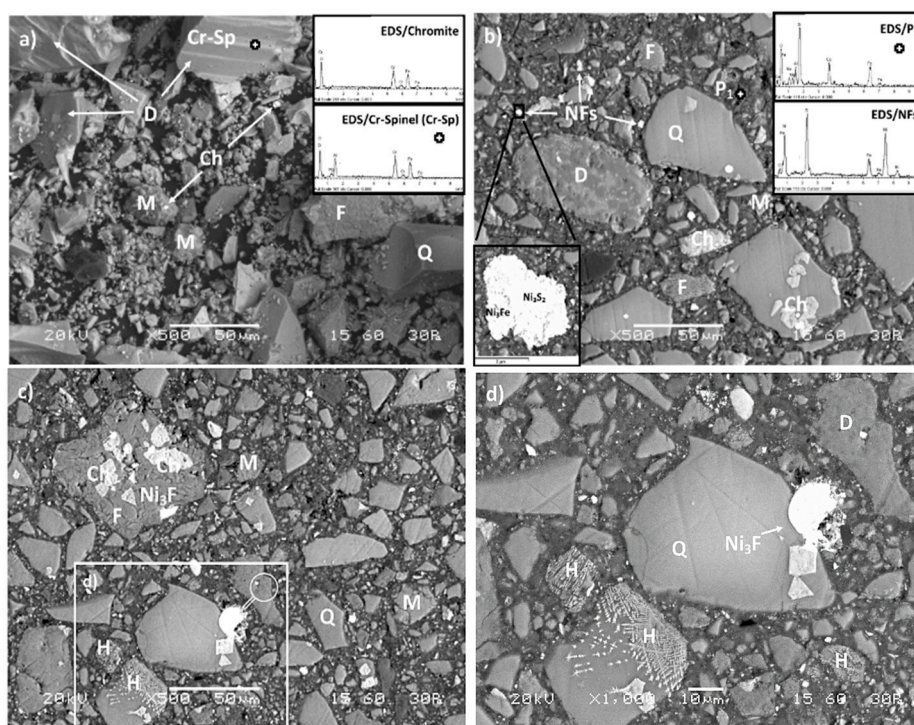
Figure 9. Back-scattered electron images of (**a**) raw PS surface and cross-sections of selected IPs after (**b**) alkali activation with 8M NaOH, and (**c,d**) firing at 400 °C. EDS spectra show in several spot locations the presence of (inter)metallic phases, the formation of mixed aggregates and newly formed phases (Q: Quartz, D: Diaspore, F: Fayalite, M: Magnetite, H: Hematite, NFs: Ni-Fe sulfides, Ch: Chromite, Cr-Sp: Cr-Spinel).

After alkali activation of PS with 8M NaOH at 80 °C (Figure 9b) or firing at 400 °C (Figure 9c,d), a moderate to highly homogenous and dense glassy matrix (dark color) is formed between PS grains (bright color) and observed in the geopolymeric gel for both IPs produced. The geopolymeric gel in the IP produced using 8M NaOH at 80 °C displayed a quite smooth surface mostly comprised of unreacted/unaffected quartz particles and an inorganic matrix (P1) containing Ca, Al, Si, Fe, Mg and Na, provided from the alkaline activator or solubilised from PS. As a result of the NaOH solution attack in the slag, deterioration of reacted diaspore, fayalite and chromite particles is clearly observed. In addition, based on elemental analysis, several Ni-Fe sulfides grains scattered/dispersed and aggregated in the geopolymeric matrix were found containing up to 60% Ni. A higher magnification image of a Ni-Fe sulfide grain shown in Figure 9b, indicates that awaruite (Ni_3Fe) occurs as inclusion along with Ni_3S_2 within the mixed Ni-Fe sulfide matrix.

Regarding the IP produced after firing at 400 °C, SEM analysis indicated a more homogenous structure filled with aggregated slag particles smaller in size (~10 μm) compared to the IP obtained after alkali activation with 8M NaOH at 80 °C. This evidence is the synergistic result of alkaline solution attack along with the oxidation of PS after firing at 400 °C. As seen from Figure 9c and in agreement with DTA/TG analysis, fayalite particles have undergone excessive oxidation and decomposition; this resulted in a compact structure filled with inclusions of inter(metallic) phases such as chromite and Ni_3F. In this context, oxidation of magnetite (Fe_3O_4) present in the PS and transformation into the stable hematite (Fe_2O_3) is clearly visible in the IP after firing at 400 °C. Figure 9d (zoom of rectangular area of Figure 9c) shows in detail the oxidation of magnetite particles and the subsequent dentritic growth of hematite.

3.5. IP Toxicity

Table 4 presents the toxicity of the raw PS as well as of the IPs produced after alkali activation of slag under the conditions of NaOH molarity 8M, curing temperature 80 °C, curing period 24 h, ageing period 7 days, fired at 400 °C.

Table 4. EN 12457-3 results (L/S = 10L kg^{-1}).

Element	Polish Slag (mg kg^{-1})	Inorganic Polymer (mg kg^{-1})		Limit Values (mg kg^{-1}) *			
		Control IP	IP After Firing at 400 °C	For Wastes Accepted at Landfills for Inert Wastes	For Non-Hazardous Wastes	For Hazardous Wastes Accepted at Landfills for Non-Hazardous Wastes	For Wastes Accepted at Landfills for Hazardous Wastes
Fe	32.1	29.1	164.3				
Mn	0.4	0.2	1.0				
Al	9.0	88.4	97.6				
Ni	6.3	0.3	2.2	0.4	10	10	40
Cu	0.1	0.9	0.7	2	50	50	100
Zn	3.6	0.8	2.9	4	50	50	200
As	0.1	0.4	1.2	0.5	2	2	25
Mo	<DL	0.2	0.5	0.5	10	10	30
Cd	<DL	<DL	<DL	0.04	1	1	5
Cr$_{total}$	0.6	0.3	2.4	0.5	10	10	50
Pb	<DL	<DL	<DL	0.5	10	10	50

* Council Decision 19 December 2002 (2003/33/EC). Note: Shaded parts indicate elements that exceed specific limits, DL: Detection Limit.

It is seen from this data that regarding raw PS, the toxicity limits are exceeded by far only for Ni and slightly for total Cr. The solubilization of these two elements is anticipated by considering the chemical and mineralogical analyses of the PS, as given by Kierczak et al. [36]. After alkali activation, the control IP produced exhibits no toxicity at all, even when the lower limits, which are specified by the EN 12457-3 test for wastes accepted at landfills for inert wastes, are taken into account. After firing the control IP at 400 °C, the solubilisation rates of Ni, As, total Cr and As increase and exceed the lower limit values indicated by this test; it is mentioned though that the indicated limit value is only marginally exceeded for As. Finally, it is mentioned that the solubilisation rates of Fe and Al increase noticeably for the IPs produced both at 80 °C and fired at 400 °C, but no limits values are specified for these two elements by the EN 12457-3 test. These results indicate the potential of alkali activation not only to contribute to the production of IPs with high compressive strength, but also to bind or trap potentially hazardous elements in a stable matrix and thus reduce their solubilization rate and overall toxicity [66].

4. Conclusions

The present experimental study investigated the alkali activation potential of an old Polish ferronickel slag for the production of IPs. Under the optimum synthesis conditions, namely, NaOH molarity 8M, curing temperature 80 °C, pre-curing and curing time 24 h and ageing period seven days, the produced IPs exhibited compressive strength that exceeds 65 MPa. In this case, the molar ratio SiO_2/Na_2O of the silicate solution was equal to 0.26, while the molar ratios $(SiO_2 + Al_2O_3)/Na_2O$ and H_2O/Na_2O in the reactive paste were 8.6 and 12.9, respectively. An interesting aspect of the present study is that in the reactive paste, the wt% addition of Na_2SiO_3 and the overall L/S ratio were very low, 3% and ~20% respectively. This means that the IPs are produced using a cost-effective process, involving a mixture containing a high percentage of solids and limited addition of chemicals.

The main novelty of the study is the increase of the compressive strength of the IPs produced under the optimum conditions, after firing them at 400 °C mainly as result of phase transformations and the development of a dense and compact structure filled with inclusions of inter(metallic) phases. After firing at 400 °C, the IPs exhibited volumetric shrinkage of 4.8% and increased density of 2.7 g cm^{-3}. This indicates that the produced IPs have beneficial properties and may find several applications in

the construction sector, including their use as fire-resistant materials. The produced IPs also show very good structural integrity when immersed in water or acidic solutions for a period of 30 days. Finally, it is underlined that alkali activation results in immobilization of hazardous elements present in the raw slag and the production of IPs with very low toxicity, thus no adverse effects are anticipated from their use. The findings of this study prove that alkali activation can be used for the valorization of potentially hazardous wastes, such as metallurgical slags, and the production of high added value materials, thus improving the sustainability and minimizing the environmental impacts of the metallurgical sector.

Author Contributions: K.K.; designed the experiments, critically analyzed results, and reviewed the paper. G.B.; V.K. and E.P. performed a literature search, carried out experiments and analytical techniques, analyzed data, and wrote a first draft of the paper. W.K.; G.P. and J.K.; carried out analytical techniques for the raw materials used.

Conflicts of Interest: The authors declare no conflicts of interest.

References

1. Bai, T.; Song, Z.G.; Wu, Y.G.; Hu, X.D.; Hua, B. Influence of steel slag on the mechanical properties and curing time of metakaolin Geopolymer. *Ceram. Int.* **2018**, *44*, 15706–15713. [CrossRef]

2. Komnitsas, K.; Zaharaki, D.; Perdikatsis, V. Geopolymerisation of low calcium ferronickel slags. *J. Mater. Sci.* **2007**, *42*, 3073–3082. [CrossRef]

3. Mo, L.; Zhang, F.; Deng, M.; Jin, F.; Al-Tabbaa, A.; Wang, A. Accelerated carbonation and performance of concrete made with steel slag as binding materials and aggregates. *Cem. Concr. Compos.* **2017**, *83*, 138–145. [CrossRef]

4. European Commission—IPPC Bureau. *Reference Document on Best Available Techniques for Management of Tailings and Waste-Rock in Mining Activities*; European Union: Brussels, Belgium, 2009; Available online: http://eippcb.jrc.ec.europa.eu/reference/BREF/mmr_adopted_0109.pdf (accessed on 14 October 2018).

5. European Commission. Directive 2006/21/EC of the European Parliament and of the Council of 15 March 2006 on the Management of Waste from Extractive Industries and Amending Directive 2004/35/EC, Official Journal of the European Union, L 102/15-33, 11.4.2006. Available online: https://eur-lex.europa.eu/resource.html?uri=cellar:c370006a-063e-4dc79b0552c37720740c.0005.02/DOC_1&format=PDF (accessed on 14 October 2018).

6. Bartzas, G.; Komnitsas, K. Life cycle assessment of ferronickel production in Greece. *Resour. Conserv. Recycl.* **2015**, *105*, 113–122. [CrossRef]

7. Gee, C.; Ramsey, M.H.; Maskallh, J.; Thornton, I. Mineralogy and weathering processes in historical smelting slags and their effect on the mobilisation of lead. *J. Geochem. Explor.* **1997**, *58*, 249–257. [CrossRef]

8. Pasetto, M.; Baliello, A.; Giacomello, G.; Pasquini, E. Sustainable solutions for road pavements: A multi-scale characterization of warm mix asphalts containing steel slags. *J. Clean. Prod.* **2017**, *166*, 835–843. [CrossRef]

9. Rosales, J.; Cabrera, M.; Agrela, F. Effect of stainless steel slag waste as a replacement for cement in mortars. Mechanical and statistical study. *Constr. Build. Mater.* **2017**, *142*, 444–458. [CrossRef]

10. Davidovits, J. Geopolymers—Inorganic polymeric new materials. *J. Therm. Anal. Calorim.* **1991**, *37*, 1633–1656. [CrossRef]

11. Davidovits, J. Chemistry of Geopolymeric Systems, Terminology. In Proceedings of the Second International Conference on Geopolymers, Saint-Quentin, France, 28–29 June 1999; pp. 9–40.

12. Duxson, P.; Provis, J.L.; Lukey, G.C.; Mallicoat, S.W.; Kriven, W.M.; van Deventer, J.S.J. Understanding the relationship between geopolymer composition, microstructure and mechanical properties. *Colloids. Surf. A Physicochem. Eng. Asp.* **2005**, *269*, 47–58. [CrossRef]

13. Kriven, W.M.; Bell, J.L.; Gordon, M. Microstructure and microchemistry of fully-reacted geopolymers and geopolymer matrix composites. *Ceram. Trans.* **2003**, *153*, 227–250.

14. Krivenko, P.V.; Kovalchuk, G.Y. Directed synthesis of alkaline aluminosilicate minerals in a geocement matrix. *J. Mater. Sci.* **2007**, *42*, 2944–2952. [CrossRef]

15. Komnitsas, K.; Zaharaki, D. Geopolymerisation: A review and prospects for the minerals industry. *Miner. Eng.* **2007**, *20*, 1261–1277. [CrossRef]

16. Duxson, P.; Provis, J.L.; Lukey, G.C.; van Deventer, J.S.J. The role of inorganic polymer technology in the development of 'green concrete'. *Cem. Concr. Res.* **2007**, *37*, 1590–1597. [CrossRef]

17. Habert, G.; Lacaillerie, J.B.E.; Russel, N. An environmental evaluation of geopolymer based concrete production: Reviewing current research trends. *J. Clean. Prod.* **2011**, *19*, 1229–1238. [CrossRef]

18. de Toledo Pereira, D.S.; da Silva, F.J.; Porto, A.B.R.; Candido, V.S.; da Silva, A.C.R.; Filho, F.D.C.G.; Monteiro, S.N. Comparative analysis between properties and microstructures of geopolymeric concrete and portland concrete. *J. Mater. Res. Technol.* **2018**, *7*, 606–611. [CrossRef]

19. Xu, H.; Van Deventer, J.S.J. Geopolymerization of multiple minerals. *Miner. Eng.* **2002**, *15*, 1131–1139. [CrossRef]

20. Provis, J.L.; van Deventer, J.S.J. *Geopolymers: Structures, Processing, Properties and Industrial Applications*; Elsevier: Amsterdam, The Netherlands, 2009; ISBN 9781845694494.

21. Bernal, S.A.; de Gutierrez, R.M.; Provis, J.L.; Rose, V. Effect of silicate modulus and metakaolin incorporation on the carbonation of alkali silicate-activated slags. *Cem. Concr. Res.* **2010**, *40*, 898–907. [CrossRef]

22. Duxson, P.; Provis, J.L. Designing precursors for geopolymer cements. *J. Am. Ceram. Soc.* **2008**, *91*, 3864–3869. [CrossRef]

23. Gebregziabiher, B.S.; Thomas, R.J.; Peethamparan, S. Temperature and activator effect on early-age reaction kinetics of alkali-activated slag binders. *Constr. Build. Mater.* **2016**, *133*, 783–793. [CrossRef]

24. Khale, D.; Chaudhary, R. Mechanism of geopolymerization and factors influencing its development: A review. *J. Mater. Sci.* **2007**, *42*, 729–746. [CrossRef]

25. Yip, C.K.; Lukey, G.C.; van Deventer, J.S.J. The coexistence of geopolymeric gel and calcium silicate hydrate at the early stage of alkaline activation. *Cem. Concr. Res.* **2005**, *35*, 1688–1697. [CrossRef]

26. Nath, P.; Sarker, P.K. Effect of GGBFS on setting, workability and early strength properties of fly ash geopolymer concrete cured in ambient condition. *Constr. Build. Mater.* **2014**, *66*, 163–171. [CrossRef]

27. Wang, K.; Lemougna, P.N.; Tang, Q.; Li, W.; He, Y.; Cui, X. Low temperature depolymerization and polycondensation of a slag-based inorganic polymer. *Ceram. Int.* **2017**, *43*, 9067–9076. [CrossRef]

28. Yan, B.; Yu, Q.L.; Brouwers, H.J.H. Evaluation of slag characteristics on the reaction kinetics and mechanical properties of Na_2CO_3 activated slag. *Constr. Build. Mater.* **2017**, *131*, 334–346. [CrossRef]

29. Huang, Y.; Wang, Q.; Shi, M. Characteristics and reactivity of ferronickel slag powder. *Constr. Build. Mater.* **2017**, *156*, 773–789. [CrossRef]

30. Maragkos, I.; Gianopoulou, I.P.; Panias, D. Synthesis of ferronickel slag-based geopolymers. *Miner. Eng.* **2009**, *22*, 196–203. [CrossRef]

31. Zaharaki, D.; Galetakis, M.; Komnitsas, K. Valorization of construction and demolition (C&D) and industrial wastes through alkali activation. *Constr. Build. Mater.* **2016**, *121*, 686–693. [CrossRef]

32. Furlani, E.; Maschio, S.; Magnan, M.; Aneggi, E.; Andreatta, F.; Lekka, M.; Lanzutti, A.; Fedrizzi, L. Synthesis and characterization of geopolymers containing blends of unprocessed steel slag and metakaolin: The role of slag particle size. *Ceram. Int.* **2018**, *44*, 5226–5232. [CrossRef]

33. Jiao, Z.; Wang, Y.; Zheng, W.; Huang, W. Effect of dosage of sodium carbonate on the strength and drying shrinkage of sodium hydroxide based alkali-activated slag paste. *Constr. Build. Mater.* **2018**, *179*, 11–24. [CrossRef]

34. Pontikes, Y.; Machiels, L.; Onisei, S.; Pandelaers, L.; Geysen, D.; Jones, P.T.; Blanpain, B. Slags with a high Al and Fe content as precursors for inorganic polymers. *Appl. Clay Sci.* **2013**, *73*, 93–102. [CrossRef]

35. Onisei, S.; Pontikes, Y.; Van Gerven, T.; Angelopoulos, G.N.; Velea, T.; Predica, V.; Moldovan, P. Synthesis of inorganic polymers using fly ash and primary lead slag. *J. Hazard. Mater.* **2012**, *205–206*, 101–110. [CrossRef]

36. Kierczak, J.; Neel, C.; Puziewicz, J.; Bril, H. The Mineralogy and weathering of slag produced by the smelting of lateritic Ni ores, Szklary, Southwestern Poland. *Can. Miner.* **2009**, *47*, 557–572. [CrossRef]

37. British Standards Institute. *BS EN 1936: Natural Stone Test Methods. Determination of Real Density and Apparent Density and of Total and Open Porosity*; NP EN 1936:2006; BSI: London, UK, 2007.

38. British Standards Institute. *BS EN 12457-3: Characterisation of waste. Leaching. In Compliance Test for Leaching of Granular Waste Materials and Sludges. Two Stage Batch Test at a Liquid to Solid Ratio of 2 L/kg and 8 L/kg for Materials with a High Solid Content and with a Particle Size below 4 mm (without or with Size Reduction)*; British Standards Institue: London, UK, 2002.

39. van der Sloot, H.A.; Hjelmar, O.; Bjerre Hansen, J.; Woitke, P.; Lepom, P.; Leschber, R.; Bartet, B.; Debrucker, N. *Validation of CEN/TC 292 Leaching Tests and Eluate Analysis Methods prEN 12457 1-4, ENV 13370 and ENV 12506 in Co-Operation with CEN/TC 308*; ECN: Petten, Netherlands, 2001. Available online: https://publicaties.ecn.nl/PdfFetch.aspx?nr=ECN-C--01-117 (accessed on 9 November 2018).

40. European Commission (EC). *Council Decision 2003/33/EC of 19 December 2002 Establishing Criteria and Procedures for the Acceptance of Waste at Landfills Pursuant to Article 16 of and Annex II to Directive 1999/31/EC*; European Commission: Brussels, Belgium, 2003. Available online: https://eur-lex.europa.eu/legalcontent/EN/TXT/PDF/?uri=CELEX:32003D0033&from=EN (accessed on 9 November 2018).

41. Komnitsas, K.; Zaharaki, D.; Perdikatsis, V. Effect of synthesis parameters on the compressive strength of low-calcium ferronickel slag inorganic polymers. *J. Hazard. Mater.* **2009**, *161*, 760–768. [CrossRef] [PubMed]

42. Azevedo, A.G.D.S.; Strecker, K. Brazilian fly ash based inorganic polymers production using different alkali activator solutions. *Ceram. Int.* **2017**, *43*, 9012–9018. [CrossRef]

43. Komnitsas, K.; Zaharaki, D.; Vlachou, A.; Bartzas, G.; Galetakis, M. Effect of synthesis parameters on the quality of construction and demolition wastes (CDW) geopolymers. *Adv. Powder Technol.* **2015**, *26*, 368–376. [CrossRef]

44. Kaze, C.R.; Djobo, J.N.Y.; Nana, A.; Tchakoute, H.K.; Kamseu, E.; Melo, U.C.; Leonelli, C.; Rahier, H. Effect of silicate modulus on the setting, mechanical strength and microstructure of iron-rich aluminosilicate (laterite) based-geopolymer cured at room temperature. *Ceram. Int.* **2018**, *44*, 21442–21450. [CrossRef]

45. Peys, A.; White, C.E.; Olds, D.; Rahier, H.; Blanpain, B.; Pontikes, Y. Molecular structure of CaO–FeOx–SiO2 glassy slags and resultant inorganic polymer binders. *J. Am. Ceram. Soc.* **2018**, *101*, 5846–5857. [CrossRef]

46. Onisei, S.; Douvalis, A.P.; Malfliet, A.; Arne Peys, A.; Pontikes, Y. Inorganic polymers made of fayalite slag: On the microstructure and behavior of Fe. *J. Am. Ceram. Soc.* **2018**, *101*, 2245–2257. [CrossRef]

47. Lemougna, P.N.; Chinje Melo, U.F.; Delplancke, M.-P.; Rahier, H. Influence of the activating solution composition on the stability and thermo-mechanical properties of inorganic polymers (geopolymers) from volcanic ash. *Constr. Build. Mater.* **2013**, *48*, 278–286. [CrossRef]

48. Onisei, S.; Malfliet, A.; Gutierrez-Campos, D.; Blanplain, B. Synthesis and high temperature transformations of Fe-rich inorganic polymers. In Proceedings of the 4th International Slag Valorization Symposium, Leuven, Belgium, 15–17 April 2015; Malfliet, A., Pontikes, Y., Eds.; pp. 243–248. Available online: http://www.slag-valorisation-symposium.eu/2015/images/papers/SVS2015-Onisei.pdf (accessed on 21 November 2018).

49. Zaharaki, D.; Komnitsas, K.; Perdikatsis, V. Use of analytical techniques for identification of inorganic polymer gel composition. *J. Mater. Sci.* **2010**, *45*, 2715–2724. [CrossRef]

50. Zaharaki, D.; Komnitsas, K. Long term behaviour of ferronickel slag inorganic polymers in various environments. *Fresenius Environ. Bull.* **2012**, *21*, 2436–2440.

51. Marangoni, M.; Arnout, L.; Machiels, L.; Pandelaers, L.; Bernardo, E.; Colombo, P.; Pontikes, Y.; Jantzen, C. Porous, sintered glass-ceramics from inorganic polymers based on fayalite slag. *J. Am. Ceram. Soc.* **2016**, *99*, 1985–1991. [CrossRef]

52. Rincón, A.; Desideri, D.; Bernardo, E. Functional glass-ceramic foams from 'inorganic gel casting' and sintering of glass/slag mixtures. *J. Clean. Prod.* **2018**, *187*, 250–256. [CrossRef]

53. Nazer, A.; Payá, J.; Borrachero, M.V.; Monzó, J. Use of ancient copper slags in Portland cement and alkali activated cement matrices. *J. Environ. Manag.* **2016**, *167*, 115–123. [CrossRef] [PubMed]

54. Zong, Y.; Zhang, X.; Mukiza, E.; Xu, X.; Li, F. Effect of Fly Ash on the Properties of Ceramics Prepared from Steel Slag. *Appl. Sci.* **2018**, *8*, 1187. [CrossRef]

55. Bakharev, T. Geopolymeric materials prepared using class F fly ash and elevated temperature curing. *Cem. Concr. Res.* **2005**, *35*, 1224–1232. [CrossRef]

56. Yang, Z.; Lin, Q.; Lu, S.; He, Y.; Liao, G.; Ke, Y. Effect of CaO/SiO2 ratio on the preparation and crystallization of glass-ceramics from copper slag. *Ceram. Int.* **2014**, *40*, 7297–7305. [CrossRef]

57. Komnitsas, K.; Petrakis, E.; Bartzas, G.; Karmali, V. Column leaching of low-grade saprolitic laterites and valorization of leaching residues. *Sci. Total Environ.* **2019**, *665*, 347–357. [CrossRef] [PubMed]

58. Mužek, M.N.; Zelić, J.; Jozić, D. Microstructural characteristics of geopolymers based on alkali-activated fly ash. *Chem. Biochem. Eng. Q.* **2012**, *26*, 89–95. Available online: http://pierre.fkit.hr/hdki/cabeq/pdf/26_2_2012/Cabeq%202012-02_3.pdf (accessed on 24 November 2018).

59. Liu, Y.; Zhang, K.; Feng, E.; Zhao, H.; Liu, F. Synthesis of geopolymer composites from a mixture of ferronickel slag and fly ash. *IOP Conf. Ser. Mater. Sci. Eng.* **2017**, *182*, 012038. [CrossRef]

60. Bernal, S.A.; Rodríguez, E.D.; de Gutiérrez, R.M.; Provis, J.L. Performance at high temperature of alkali-activated slag pastes produced with silica fume and rice husk ash based activators. *Mater. Constr.* **2015**, *65*, e049. [CrossRef]

61. Palomo, A.; Grutzeck, M.W.; Blanco, M.T. Alkali-activated fly ashes: A cement for the future. *Cem. Concr. Res.* **1999**, *29*, 1323–1329. [CrossRef]

62. Bakri, A.M.M.A.; Kamarudin, H.; Bnhussain, M.; Ismail, K.N.; Yahya, Z.; Razak, R.A. Fly Ash-based Geopolymer Lightweight Concrete Using Foaming Agent. *Int. J. Mol. Sci.* **2012**, *13*, 7186–7198. [CrossRef]

63. Gyurov, S.; Marinkov, N.; Kostova, Y.; Rabadjieva, D.; Kovacheva, D.; Tzvetkova, C.; Gentscheva, G.; Ivan Penkov, I. Technological scheme for copper slag processing. *Int. J. Miner. Process.* **2017**, *158*, 1–7. [CrossRef]

64. Mihailova, I.; Radev, L.; Mehandjie, D. Phase composition, structure and catalytic activity in oxidation reactions of fayalite waste from the flotation of copper slag. *J. Chem. Technol. Metall.* **2017**, *52*, 929–939. Available online: https://dl.uctm.edu/journal/node/j2017-5/17_17-69_Irena_p_929-939.pdf (accessed on 14 December 2018).

65. Zuo, Z.; Yu, Q.; Wei, M.; Xie, H.; Duan, W.; Wang, K.; Qin, Q. Thermogravimetric study of the reduction of copper slag by biomass. *Therm. Anal. Calorim.* **2016**, *126*, 481. [CrossRef]

66. Komnitsas, K.; Zaharaki, D.; Bartzas, G. Effect of sulphate and nitrate anions on heavy metal immobilisation in ferronickel slag geopolymers. *Appl. Clay Sci.* **2013**, *73*, 103–109. [CrossRef]

Column leaching of low-grade saprolitic laterites and valorization of leaching residues

Kostas Komnitsas [a,*], Evangelos Petrakis [a], Georgios Bartzas [b], Vassiliki Karmali [a]

[a] Technical University of Crete, School of Mineral Resources Engineering, University Campus, Kounoupidiana, 73100 Chania, Greece
[b] National Technical University of Athens, School of Mining and Metallurgical Engineering, 9 Heroon Polytechniou str., 157 80 Zografos, Athens, Greece

HIGHLIGHTS

- Low grade saprolitic laterites are column leached for the extraction of Ni and Co.
- The presence of Na_2SO_3 has a beneficial effect on Ni and Co extraction.
- The selectivity of leaching is good considering the ratio Ni/Fe in the PLS.
- Leaching residues can be successfully alkali activated.
- The inorganic polymers produced have low toxicity and high compressive strength.

GRAPHICAL ABSTRACT
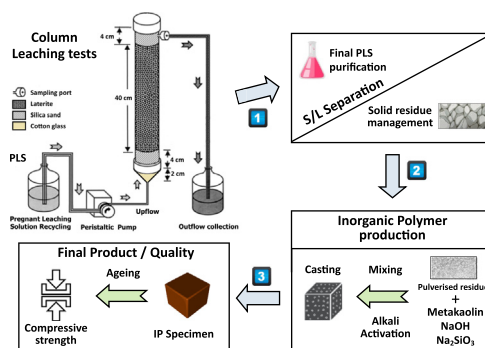
ABSTRACT

Socio-economic data on nickel and cobalt show their importance throughout the entire metal value chain, from mining to end use, disposal and recycling. Thus, the extraction of both metals from primary and secondary raw materials as well as from wastes is currently considered strategically important for the industry and the society. In this paper heap leaching of Greek low-grade saprolitic laterites, with Ni content 0.97%, was investigated. The main parameters studied involved the strength of the H_2SO_4 solution used (49 and 147 g L^{-1}) and the effect of adding sodium sulfite (Na_2SO_3) in the leaching medium. The pregnant leach solution (PLS) was recycled several times during leaching in order to minimize acid consumption. The experimental results showed that within a period of 25 days, and under the optimum conditions (147 g L^{-1} H_2SO_4 and 20 g L^{-1} Na_2SO_3), i) Ni and Co extractions were 72.5% and 47.4%, respectively and ii) Fe and Al co-extractions were 8.7% and 31.3%, respectively. Furthermore, valorization of the leaching residues through alkali activation using NaOH and Na_2SiO_3 and the addition of metakaolin (MK) for the production of inorganic polymers (IPs) was explored. X-ray fluorescence (XRF), X-ray diffraction (XRD), Fourier-transform infrared (FTIR) spectroscopy, Differential scanning calorimetry (DSC/TG) and Scanning electron microscopy (SEM-EDS) were used to characterize the ore, its leaching residues and the IPs. The IPs produced demonstrated high compressive strength, almost 40 MPa and are suitable for a wide range of applications in the construction sector.

© 2019 Elsevier B.V. All rights reserved.

1. Introduction

Nickel and cobalt have excellent physical and chemical properties and thus they are essential for thousands of products. Both metals are

* Corresponding author.
  E-mail address: komni@mred.tuc.gr (K. Komnitsas).

also necessary for the most common types of lithium-ion batteries which power electric vehicles. The annual production and consumption of nickel exceeds two million tonnes. On the other hand, the annual European Union (EU) cobalt production is almost 2300 t, while its demand is about nine times higher and is met by imports from third countries (EU Science Hub, 2019; Nickel Institute, 2019).

Nickel laterites are formed through weathering of underlying parent rocks and the resulting main zones of mineralization include limonites (with high iron and low magnesium content) and saprolites (with high magnesium and low iron content). Saprolites, which are more reactive compared to limonites, are located at the bottom of the deposit and contain nickel-rich serpentines and hydrous magnesium silicates (Luo et al., 2009; Myagkiy et al., 2017). Due to the complexity of the laterite ores and the presence of nickel in several mineral phases, their beneficiation with the use of traditional mineral processing techniques, including gravity-, electrostatic-, magnetic-, and density separation, as well as flotation, is quite inefficient. Selective grinding aiming at separation of the coarse fraction, which normally has a lower Ni content, is rarely successful (Petrakis et al., 2018; Quast et al., 2015).

The continuous depletion of higher grade nickel sulfides and the increasing demand for nickel, which is used in many industrial products including Li-ion battery cathodes in electric vehicles, requires the economical treatment of the huge reserves of nickel laterites (MacCarthy et al., 2015).

Today, most nickel laterites, which represent almost 70% of the global reserves, are low grade (<1.5%) and account for almost 40% of nickel production. These ores are mainly treated pyrometallurgically to produce ferronickel (FeNi) (Pickles and Anthony, 2018). However, due to the high environmental footprint of pyrometallurgical treatment (Bartzas and Komnitsas, 2015; Eckelman, 2010), research efforts are focusing on the development of more economical and eco-friendly hydrometallurgical approaches (Khoo et al., 2017; Norgate and Jahanshahi, 2011; Quast et al., 2013).

The main hydrometallurgical techniques include atmospheric leaching (McDonald and Whittington, 2008), heap leaching (Oxley et al., 2016), high pressure acid leaching (HPAL) (Loveday, 2008; Zhang et al., 2015) and bioleaching (du Plessis et al., 2011; Le et al., 2006). Other alternatives including pre-roasting and acid leaching have been also investigated (Li et al., 2018a, 2018b; Li et al., 2009).

Atmospheric leaching is carried out at ambient temperature in stirred reactors and is often characterized by low selectivity. It involves the use of sulfuric (Luo et al., 2010; Thubakgale et al., 2013), hydrochloric (Guo et al., 2015; Mystrioti et al., 2018) or ammonium chloride-hydrochloric acid mixtures (Li et al., 2018a, 2018b). Bioleaching still requires process optimization in order to improve its efficiency and economics (Chaerun et al., 2017; Jang and Marjorie Valix, 2017).

HPAL, which is carried out with the use of sulfuric acid, nitric acid or ferric chloride, is characterized by high recoveries of Ni and Co, low recoveries of Fe and Al, short leaching times but high operating costs (Liu et al., 2012; Ma et al., 2015; Zhang et al., 2016). An excellent continuous model for sulfuric acid pressure leaching of laterites has been proposed by Rubisov and Papangelakis (2000).

Heap leaching, which is considered a feasible alternative for the treatment of low grade laterite ores, has been intensively investigated over the last years. It is characterized by slower kinetics, longer leaching times, which normally vary between 60 and 100 days, and higher selectivity compared to leaching in stirred reactors (Elliot et al., 2009; Quaicoe et al., 2014; Quast et al., 2013; Watling et al., 2011).

Laterites are treated for >50 years at the pyrometallurgical plant of Larymna, in central Greece, to produce FeNi (Zevgolis et al., 2010). The atmospheric and pressure leaching of Greek laterites was first studied in the '80s (Komnitsas, 1983; Komnitsas, 1988; Kontopoulos and Komnitsas, 1988; Panagiotopoulos et al., 1986). Later, heap leaching was intensively investigated in laboratory and pilot tests (Agatzini-Leonardou and Dimaki, 1994; Agatzini-Leonardou and Zafiratos, 2004; Agatzini-Leonardou et al., 2004; Agatzini-Leonardou et al., 2009).

Recently, by taking into account the gradual depletion of the ore grade and the increased demand for nickel, research efforts have been again initiated (Komnitsas et al., 2018; Mystrioti et al., 2018).

In this context, the main aim of this study was to investigate the efficiency of column leaching with the use of sulfuric acid (H_2SO_4) for the treatment of low-grade Greek saprolitic laterites as well as to study the effect of the addition of sodium sulfite (Na_2SO_3) in the leaching solution on the overall efficiency of the process. The study also aimed to explore the potential of alkali activation for the valorization of leaching residues in order to improve process economics and reduce environmental impacts associated with their disposal.

2. Materials and methods

2.1. Ore

The ore used in this study is a saprolitic laterite (<30 mm, 0.97%wt Ni) which was obtained from Larco S.A mines in Kastoria (Northern Greece). The ore (100 kg) was homogenized by the cone and quartering method and a representative sample of about 1 kg was crushed below 4 mm for the determination of the particle size distribution.

2.2. Leaching tests

Three leaching tests were carried out in laboratory Plexiglas columns, with 5 cm inner diameter and 50 cm height, to study the effect of (i) H_2SO_4 concentration and (ii) the addition of Na_2SO_3 in the leaching solution on Ni, Co and other elements extraction. The column experimental conditions are presented in Table 1. 1000 g of laterite ore (LK) were added in the main column zone so that a bed of 40 cm height was formed. Two 4 cm layers of silica sand were placed at both ends of each column to act as filters. Cotton glass was also added at the bottom of each column to prevent losses of ultra-fine particles and avoid clogging of the columns. The experimental configuration is shown in Fig. 1.

It is important to note that the experimental conditions used were carefully selected based on the results of earlier tests investigating leaching of other Greek saprolitic and limonitic ores (Komnitsas et al., 2018).

Upflow transport of the leaching medium with the use of peristaltic pumps (Masterflex L/S economy variable-speed drive, Cole-Parmer Instrument Co) was considered to enable full contact of the leaching medium with the ore. The leaching solution was pumped from 5 L plastic vessels with a flow-rate of 3 L day^{-1} and collected in the outflow in similar vessels. The duration of each leaching test, which involved daily recycling of the PLS, was 25 days, while at the end of the tests, columns were flushed with distilled water so that the final PLS volume was ~3 L. 10 mL samples from the outflow were initially collected daily and at later stages every 2 or 3 days to measure pH and Eh with the use of a WTW pH 7110 inoLab pH/Eh meter and determine the concentration of Ni, Co, Fe, Ca, Al, Mg and Mn in the PLS by atomic absorption spectroscopy (AAS). Acid consumption was calculated using the titrimetric method proposed by Quaicoe et al. (2014). The efficiency of leaching was determined by taking into account the extraction percentage of the useful elements Ni and Co as well as by calculating the ratios Ni/Fe, Ni/Mg, Ni/Ca and Ni/Al in the PLS, given that Fe, Mg, Ca and Al are the undesirable elements. All leaching tests were carried out in duplicate and mean values are given for all parameters analysed; it is

Table 1
Column experimental conditions.

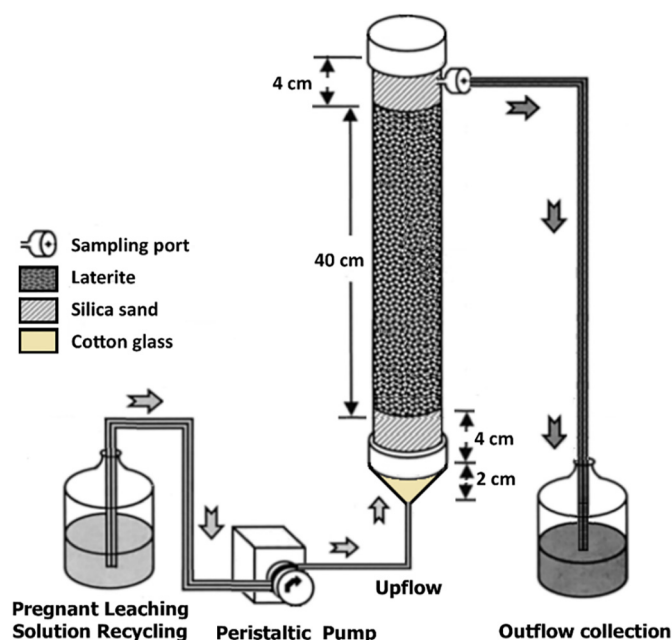| Test no.	H_2SO_4 solution (g L^{-1})	Na_2SO_3 concentration (g L^{-1})
1	49	–
2	147	–
3	147	20

Fig. 1. Experimental configuration of column leaching tests.

mentioned though that the variation of measurements was in all cases around ±1%.

2.3. Valorization of leaching residues

The valorization of the leaching residues (LKr) was investigated through alkali activation. The residues were first dried at 80 °C for 1 day, then pulverized using a FRITSCH BICO pulverizer (d_{90} = 52.4 μm) and added under continuous slow mixing to the activating solution, consisting of NaOH and sodium silicate (Na_2O = 7.5–8.5%, SiO_2 = 25.5–28.5%, Merck). The NaOH solution was prepared by dissolving sodium hydroxide anhydrous pellets (Sigma Aldrich) in distilled water, until the required molarity was obtained. The effect of the addition of metakaolin in the starting mixture (5 and 10%wt) as filler, for the supply of Al^{3+} ions in the inorganic polymer paste, as well as the calcination of the LKr at 800 and 1000 °C in order to increase its reactivity were also examined. Metakaolin was produced after calcining kaolin, $Al_2Si_2O_5$ $(OH)_4$, (Fluka) at 750 °C for 2 h in a SNOL 8,2/1100 oven. Calcination of LKr was carried out for 1 h in the same oven. Loss on ignition (LOI) was determined by heating the materials at 1050 °C for 4 h.

The liquid to solid (L/S) ratio was adjusted in order to improve the flowability of the paste before casting. A typical indicative composition of the mixture included (in %wt): leaching residue 69%, metakaolin 7%, 8 M NaOH solution 12% and Na_2SiO_3 12%. The fresh paste was cast in cubic metal moulds of 5 cm edge, which were vibrated for a few minutes to eliminate the presence of air voids in the reactive mass. The moulds remained at room temperature for 2 h to allow early initiation of the alkali activating reactions, development of structural bonds and early solidification of the paste. Then the specimens were demoulded, sealed in plastic bags to prevent fast evaporation of water, cured at 80 °C in a laboratory oven (Jeio Tech ON-02G) for 24 h and then allowed to cool. This configuration was based on the results obtained from previous studies investigating the alkali activation potential of several metallurgical wastes (Komnitsas et al., 2007; Zaharaki et al., 2016). After ageing at room temperature for 7 days, the compressive strength of the specimens was determined with the use of a MATEST C123N load frame. All tests were carried out in triplicate.

Finally, the toxicity of the leaching residues as well as of the specimens produced after alkali activation was assessed by using the EN 12457-3 test (EN12457-3:2002; van der Sloot et al., 2001), which

involves leaching of material in distilled water (8 L kg^{-1}) for 24 h. The obtained solutions were filtered using 0.45 μm membrane filters and the concentration of the metals in the eluate was expressed as mg kg^{-1} of dry sample and compared with existing limits for disposal of wastes in different landfills (European Commission, 2002). Apart from distilled water a more severe leaching agent, namely an HCl solution with pH 4, was used.

2.4. Use of analytical techniques

After grinding with the use of a FRITSCH-BICO pulverizer, the ore (LK) and the leaching residues (LKr) were chemically and mineralogically characterized using (i) a Bruker-AXS S2 Range type X-ray fluorescence energy dispersive spectrometer (XRF–EDS) and (ii) an X-ray diffractometer (XRD), D8 ADVANCE type (BRUKER-AXS). Chemical analysis of the ore and each leaching residue was also carried out after digestion of 2 g of each sample in aqua regia followed by AAS, with a Perkin Elmer AAnalyst 100 Flame Atomic Absorption Spectrometer. Since the differences observed between XRF and AAS results were minor (±1%), those obtained by XRF are presented in this study. The functional groups in each solid sample were identified by Fourier transform infrared (FTIR) spectroscopy, using a Perkin Elmer Spectrum 1000 spectrometer, while a Setaram LabSys Evo analyzer was used for Differential Scanning Calorimetry and Thermogravimetry (DSC/TG).

Scanning electron microscopy (SEM) and energy dispersive X-ray spectroscopy (EDS) were used to evaluate the morphology of the ore and the solid leaching residues. A JEOL-6380LV scanning microscope (Tokyo, Japan) operating at an accelerating voltage of 20 kV was used. Back-scattered electron (BSE) examinations were carried out on polished sections of the samples embedded in epoxy resin to ensure cohesion of the solid residues.

3. Results and discussion

3.1. Characterization of the ore

The cumulative particle size distribution of the −4 mm LK ore is presented in Fig. 2. The results show that the 80% passing size (d_{80}) is 2.1 mm. The chemical composition (Table 2) confirms that the ore is a saprolitic low grade laterite, with high magnesia and low iron content.

3.2. Leaching efficiency

Fig. 3(a–g) show the percent extraction of Ni, Co, Fe, Mg, Al, Mn and Ca as a function of time. As shown in Fig. (3a) Ni extraction obtained after 25 days of leaching with the use of 49 g L^{-1} H_2SO_4 solution (0.5 M) is low and does not exceed 14% whereas, the increase of acid
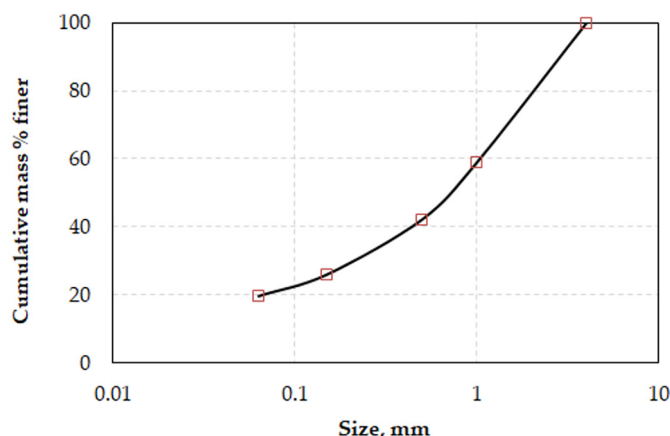

**Fig. 2.** Particle size distribution of Kastoria laterite (LK) ore.

Table 2
Chemical composition (%wt) of LK ore.

| Ni	Co	Fe$_2$O$_3$	SiO$_2$	Al$_2$O$_3$	MgO	MnO	CaO	Cr$_2$O$_3$	LOI[a]
0.97	0.031	21.79	34.44	0.35	17.14	0.33	7.16	0.86	16.8

[a] LOI: loss on ignition.

strength to 147 g L^{-1} H$_2$SO$_4$ (1.5 M) improves Ni extraction to 47%. Cobalt extraction follows a similar trend (Fig. 3b) and increases from 11.3% to 27.9% with the increase in acid strength. Higher extractions of 72.5% and 47.4% for Ni and Co respectively, were obtained when Na$_2$SO$_3$ was added to the leaching solution. It is noteworthy that the increase of Ni

and Co extractions in the presence of Na$_2$SO$_3$ was very fast within 2–4 days (Komnitsas et al., 2018; Luo et al., 2015). In the presence of higher concentrations of Na$_2$SO$_3$ (30 g L^{-1}), the increase of Ni and Co extractions was only marginal (~1%, data not shown). In the presence of H$_2$SO$_4$, Na$_2$SO$_3$ reacts with H$^+$ ions to form the intermediate H$_2$SO$_3$ which dissociates to SO$_2$ (Reaction (1):

$$Na_2SO_3 + H_2SO_4 = Na_2SO_4 + H_2O + SO_2(aq) \qquad (1)$$
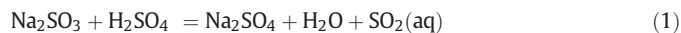
The SO$_2$(aq) from Reaction (1) reacts with iron-based phases (e.g. goethite), as shown in Reaction (2), accelerates Fe extraction and subsequently Ni release from the iron phases (Das and de Lange, 2011). The generation of SO$_2$ is clearly visible in the first days of leaching through
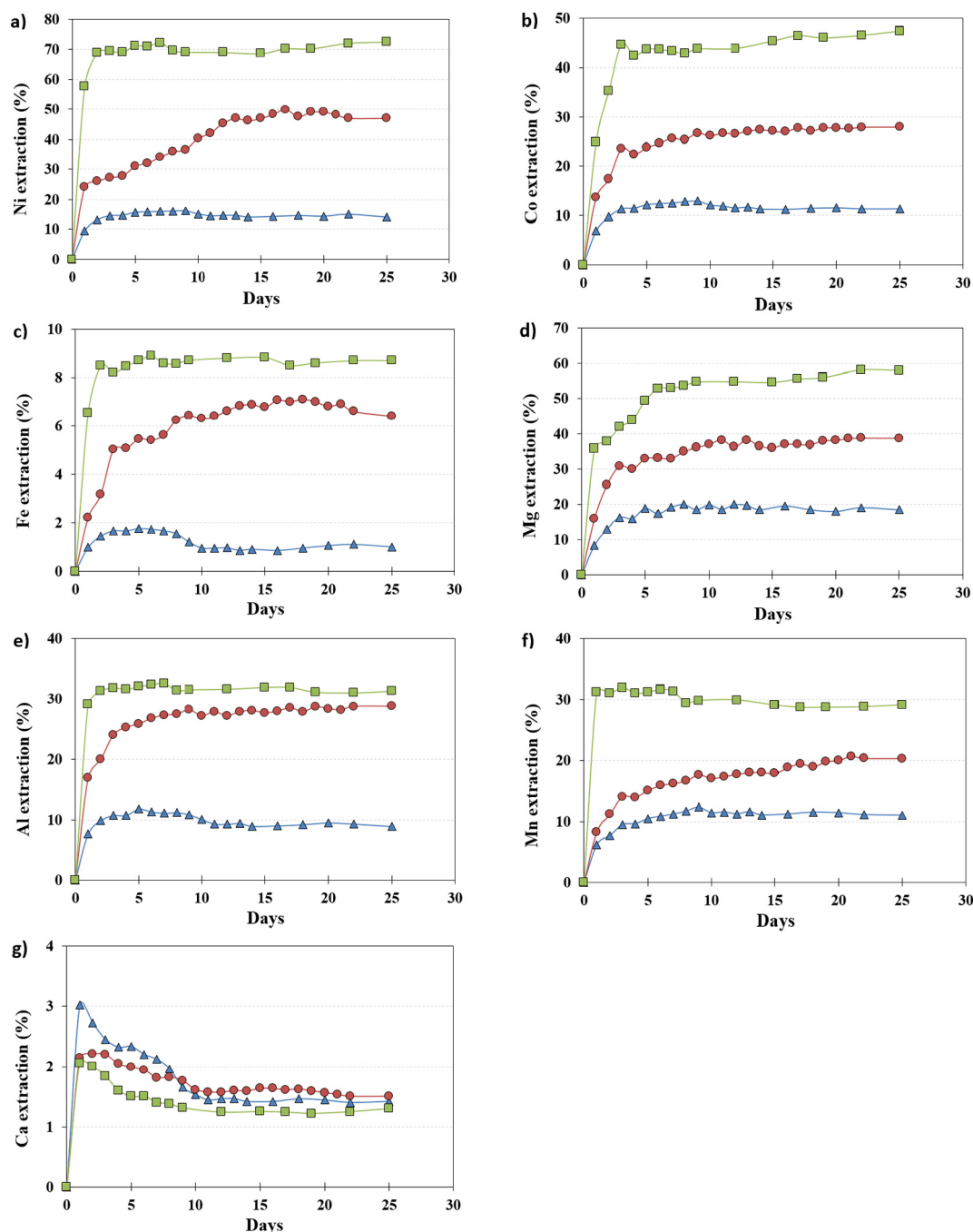

Fig. 3. Evolution of % metal extraction vs. time during LK leaching, ▲: 49 g L^{-1} H$_2$SO$_4$, ●: 147 g L^{-1} H$_2$SO$_4$, ■: 147 g L^{-1} H$_2$SO$_4$ containing 20 g L^{-1} Na$_2$SO$_3$.

Table 3
PLS composition and selectivity of leaching.

Test no.	Ni	Co	Fe	Mg	Ca	Al	Ni/Fe	Ni/Mg	Ni/Ca	Ni/Al
	mg L^{-1}									
1	501	12.9	563	7005	267	61	0.89	0.07	1.88	8.21
2	1600	30.3	3423	14,002	269	186	0.47	0.11	5.95	8.60
3	2825	59.3	5328	24,001	260	233	0.53	0.12	10.87	12.12

Table 5
Comparative results obtained after leaching of a Greek limonitic and saprolitic laterite ore.

Ore type[a]	Ni (%)	H$_2$SO$_4$ (g L^{-1})	Duration (days)	Extraction (%)			Ni/Fe in PLS	Reference
				Ni	Fe	Co		
L	0.58	147	33	60.2	3.9	59.0	0.26	Komnitsas
L	0.58	147[b]	33	73.5	7.9	84.1	0.15	et al., 2018
S	0.97	147	25	47.0	6.4	27.9	0.47	This study
S	0.97	147[b]	25	72.5	8.7	47.4	0.53	

[a] L: limonitic ore, S: saprolitic ore.
[b] Addition of sodium sulfite.

the production of bubbles within the column bed. It is mentioned that in other tests carried out in our laboratory using higher solution flowrates, a synergistic effect of flowrate and bubbles was noted and the ore bed was split in several parts and lifted

$$2FeOOH(s) + 2H^+ + SO_2(aq) = 2Fe^{2+} + SO_4^{2-} + 2H_2O \quad (2)$$
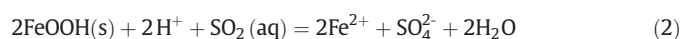
Reaction (2) requires less acid for the dissolution of goethite than Reaction (3) which involves direct leaching of iron-based phases (Georgiou and Papangelakis, 1998)

$$FeOOH(s) + 3H^+ = Fe^{3+} + 2H_2O \quad (3)$$

Fig. 3(c) shows that the extraction of Fe increases in all tests with the increase of acid strength or the addition of Na$_2$SO$_3$ but it remains in general very low (<9%) and thus the selectivity of leaching is improved. The low Fe extraction obtained in these column tests is due to the milder conditions used, namely low temperature and coarser feed size, compared to stirred reactor leaching (Mystrioti et al., 2018).

The maximum co-extraction of other elements, namely Mg, Al, Mn and Ca, which also assesses the selectivity of leaching, was 58%, 31.3%, 29.1% and 1.3%, respectively, as seen in Fig. 3(d–g).

The similar profiles of Ni and Mg extraction indicate that Ni is loosely bound in Ni-containing phases such as lizardite and thus both elements can be leached simultaneously (Luo et al., 2010). On the other hand, the extraction of Ni which is associated to magnetite/maghemite and chromite is difficult since these phases remain practically unleached (Canterford, 1986).

The pH of the leaching solutions was very low in all tests, increased slowly with time but did not exceed the value of 1.5. When the leaching solution contained 147 g L^{-1} H$_2$SO$_4$ and 20 g L^{-1} Na$_2$SO$_3$, Eh values decreased gradually with time from 385 to 282 mV (Komnitsas et al., 2018). The beneficial effect of the reducing agent Na$_2$SO$_3$ in lowering the potential of the leaching reactions and increasing the extraction of nickel contained in the iron phases has been also noticed during atmospheric sulfuric acid leaching of limonitic laterites at temperatures between 30 and 90 °C (Luo et al., 2015). The weight loss recorded during leaching was quite similar in all tests and varied between 16.1% (when a solution with 49 g L^{-1} H$_2$SO$_4$ was used) and 18.8% (when a solution containing 147 g L^{-1} H$_2$SO$_4$ and 20 g L^{-1} Na$_2$SO$_3$ was used).

The concentrations of the main elements (mg L^{-1}) in the PLS are presented in Table 3. This table also compares the selectivity of leaching as defined by the concentration ratios of Ni/Fe, Ni/Mg, Ni/Ca, and Ni/Al. Because low Ni and Co extractions are obtained when 49 g L^{-1} H$_2$SO$_4$ solution is used as leaching medium, the comparison does not include the results of this test. The results indicate that the addition of Na$_2$SO$_3$ in the leaching medium, apart from the fast extraction of Ni, improves also the selectivity of leaching since the ratios Ni/Fe, Ni/Mg, Ni/Ca, and Ni/Al increase by 13%, 9%, 83% and 41%, respectively.

Table 4 presents comparative results of various studies involving column leaching of saprolitic ores, as derived from the related literature. It is seen that the efficiency of leaching depends on Ni grade, ore size, agglomeration of feed, concentration of acid, flowrate of leaching solution and duration of column tests. Apart from these factors, the type of laterite is also crucial during leaching (MacCarthy et al., 2016; McDonald and Whittington, 2008). Table 5 presents the results of the this and a recent similar study that involved column leaching of a Greek limonitic ore (L), with a much lower Ni grade (Komnitsas et al., 2018). These data show that despite the higher extraction of Ni and the lower extraction of Fe from the limonitic ore, a much lower (45–72%) Ni/Fe ratio was recorded in the PLS due to its much lower Ni grade. Also, much higher Co extractions were obtained during leaching of the limonitic ore in all cases studied. The results of earlier laterite column leaching studies showed that for limonitic ores, dissolution of the refractory iron minerals, such as goethite, is required to obtain high Ni and Co extractions, whereas for saprolitic ores the Ni and Co bearing silicate minerals are weakly bound and hence the extraction of both elements contained in them is much easier (Quaicoe et al., 2014; Watling et al., 2011). However, as indicated in an excellent recent study, given the intrinsic mineral heterogeneity of Ni-laterites, a comprehensive mineralogical characterization at the mineral grain scale is required in order to assess the overall leaching behavior of the ore. In the same study it is mentioned that the scale of leaching tests may also affect Ni and Fe selectivity (Hunter et al., 2013).

3.3. Alkali-activation of residues

After heap leaching, the residues are normally transferred to a lined facility, which is called spent ore repository and are reclaimed with the

Table 4
Results of various column leaching studies for saprolitic ores.

Ni content (%)	Particle size (mm)	H$_2$SO$_4$ (g L^{-1})	Duration (days)	Flow rate (L day^{-1})	Extraction (%)			Ni/Fe in PLS	Acid consumption (kg t^{-1} ore)	Reference
					Ni	Fe	Co			
1.94	<15[a]	98	10	4.0	60.0	12.6	45.0	0.7–1.0	510	Agatzini-Leonardou and Zafiratos, 2004
1.20	<20	100	122	31.4	83.9	55.8	55.2	0.11	462	Büyükakinci, 2008
0.92	<15[a]	200	101	2.3	97.0	–	75.0	–	502	Nosrati et al., 2014
0.92	<2[a]	200	100	2.3	90.0	60.0	72.8	0.06	641	Quaicoe et al., 2014
0.97	<4	147	25	2.5	47.0	6.4	27.9	0.47	626.2	This study
0.97	<4	147[b]	25	2.5	72.5	8.7	47.4	0.53	576.8	

[a] Agglomerated feed ore.
[b] + Addition of sodium sulfite.

Table 6
Typical composition of LKr obtained after leaching of laterite ore with 147 g L^{-1} H$_2$SO$_4$ and 20 g L^{-1} Na$_2$SO$_3$.

| Fe$_2$O$_3$	SiO$_2$	Al$_2$O$_3$	MgO	MnO	CaO	Cr$_2$O$_3$	TiO$_2$	LOI[a]	Total
16.43	39.71	0.54	4.45	0.11	7.96	2.35	0.84	27.11	99.5

[a] LOI: loss on ignition.

construction of a vegetative soil cover (Zanbak, 2012). Thus, valorization of the residues and production of added value materials will reduce the overall cost of the process and minimize its environmental impacts.

The chemical analysis of the residues obtained after LK leaching is presented in Table 6. It is seen that while the residues contain sufficient SiO$_2$, the content of Al$_2$O$_3$ remains low.

It is known that alkali activation of Al-Si wastes and residues in relatively low temperature (40–90 °C) results in the formation of dense IPs with chemical composition similar to zeolites and amorphous to semicrystalline three-dimensional alumino-silicate microstructure. The produced materials are mainly called IPs (also known as geopolymers) (Komnitsas and Zaharaki, 2007). Fig. 4 shows the compressive strength of the IPs produced after alkali activation of the residues (LKr) obtained after LK leaching. The effect of the addition of 5 and 10%wt metakaolin as well as the calcination of the residues at 800 and 1000 °C is also presented. These results indicate that (i) the residues obtained after laterite leaching cannot be alkali activated and the compressive strength of the produced specimens merely reaches 1.3 MPa, (ii) mixing with 10%wt metakaolin results in a noticeable increase of the compressive strength of the specimens, to 39 MPa, (iii) calcination of LKr at 800 °C (LKr800) and 1000 °C (LKr1000) has adverse effect on the compressive strength.

LKr have low content of Al (Table 6) and therefore cannot be alkali activated. There is no specific rule about the ratio SiO$_2$:Al$_2$O$_3$ in the starting mixture but this has to be quite high provided that the content of both oxides is sufficient. For example, ferronickel slag produced after pyrometallurgical treatment of the same laterites is well alkali activated since the aforementioned ratio is ~4 (SiO$_2$ 32.74%, Al$_2$O$_3$ 8.32%) (Komnitsas and Zaharaki, 2007). Thus, in order to increase the alkali activation potential of LKr (SiO$_2$:Al$_2$O$_3$ = 73.5, Al$_2$O$_3$ content only 0.54%) an Al source is required. The results show that the addition of 5% and especially 10%wt MK, with an Al$_2$O$_3$ content of ~30% (Kwon et al., 2017;
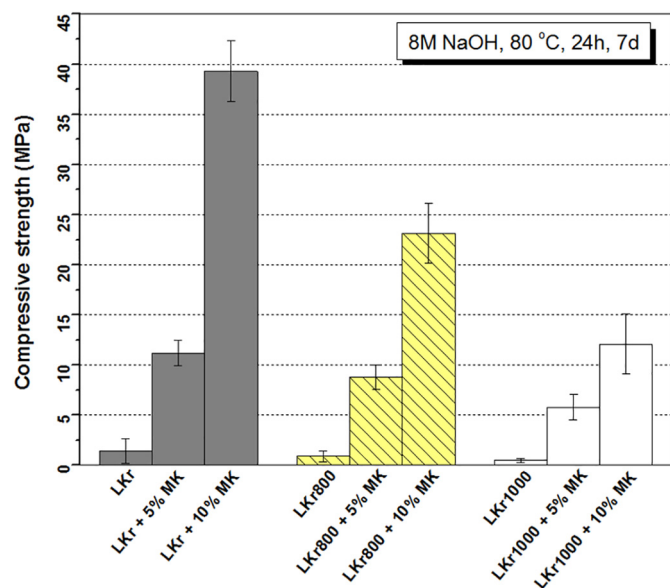
Fig. 4. Effect of the addition of metakaolin (MK) (5 and 10%wt) and calcination on the compressive strength of specimens produced by alkali activation of LKr. Conditions were: 8 M NaOH, heating (at 80 °C for 24 h), curing for 7 days. LKr: Kastoria laterite leaching residue, LKr800: leaching residue calcined at 800 °C, LKr1000: leaching residue calcined at 1000 °C.

Sullivan et al., 2018), improves greatly their alkali activation potential, because calcination of kaolin changes its original crystalline structure. The dehydration starts at about 100–120 °C, then dehydroxylation of the structure takes place and finally metakaolin is produced. The loss of crystallinity weakens the bonds between crystals and the produced metakaolin has sufficient amorphous content and thus exhibits increased reactivity during alkali activation. It is also known that calcination of kaolin transforms the octahedral coordinated Al layers into the more reactive tetrahedral form. It is thus anticipated that Al ions may dissolve more rapidly from metakaolin than from un-calcined kaolin (Komnitsas et al., 2009). The percentage of Na$_2$SiO$_3$ used in the present study was carefully selected after a number of tests in order to balance the SiO$_2$:Al$_2$O$_3$ ratio.

### 3.4. Characterization of the leaching residues

Fig. 5 presents the XRD patterns of LK ore and selected LKr. The main mineralogical phases present in the ore are: quartz (SiO$_2$), goethite (FeO(OH)) and magnesium-bearing silicates, such as lizardite [(Mg,Fe)$_3$Si$_2$O$_5$(OH)$_4$], (clino)chrysotile [Mg$_3$Si$_2$O$_5$(OH)$_4$] and saponite [Ca$_{0.5}$(Mg,Fe)$_3$(Si,Al)$_4$O$_{10}$(O,H)$_2$·4H$_2$O], while the main Ni-bearing phases are nepouite [(Ni,Mg)$_3$Si$_2$O$_5$(OH)$_4$] and chromite (FeCr$_2$O$_4$) as also mentioned in earlier studies (Brand et al., 1998; Proenza et al., 2008). Willemseite [(Ni,Mg)$_3$Si$_4$O$_{10}$(OH)$_2$] and other garnierite minerals may be also sources of Ni in saprolitic ores (Tauler et al., 2009; Villanova-De-Benavent et al., 2017; Zhu et al., 2012). Hematite (Fe$_2$O$_3$) and Talc [Mg$_3$Si$_2$O$_{10}$(OH)$_2$] are also present in the ore as minor mineral phases.

The XRD patterns of the leaching residues, obtained after leaching with H$_2$SO$_4$ solution containing Na$_2$SO$_3$, are shown in Fig. 5(b, c). It is shown that the characteristic peaks of lizardite/nepouite at 2-theta = 12.108 which were present in the initial ore were not present in the leaching residues, indicating that most of these minerals were leached, at least to a degree that does not allow their identification through XRD. On the other hand, the intensities of characteristic peaks of quartz and goethite/hematite increased in the XRD patterns of the residues obtained after H$_2$SO$_4$ leaching, especially in the presence of Na$_2$SO$_3$. H$_2$SO$_4$ leaching without or with the addition of Na$_2$SO$_3$ resulted in the formation in the LKr of bassanite (CaSO$_4$·0.5H$_2$O) or gypsum (CaSO$_4$·2H$_2$O) respectively, due to the relatively high CaO content (7.16%) in the LK ore.

The FTIR spectra of LK and LKr are shown in Fig. 6. In all samples, bending and stretching vibrational bands of Si—O—Si and O—Si—O can be observed at 450–460 cm^{-1} and ~800 cm^{-1}, respectively (Andini et al., 2008). The next peaks, seen only in LKr, between 600 and 667 cm^{-1} are due to the formation of calcium-based sulfates. These results are consistent with the data derived from the corresponding XRD patterns (Fig. 5). Moreover, the characteristic asymmetric stretching vibration of Si—O—T (T=Al or Si) in the LK at 1014 cm^{-1} is shifted toward higher wavenumbers (1092 and 1150 cm^{-1}) in LKr. This upward shift indicates that Si—O bonds dominate LKr due to the destruction/decomposition of the initial Mg-Al-silicate matrix (Baščarević et al., 2013) and the subsequent formation and precipitation of Ca-sulfates. Two small shoulders at 876 cm^{-1} and 2512 cm^{-1} seen in the LK ore along with a weak band at 1422 cm^{-1} can be attributed to stretching vibrations of O—C—O bonds indicating the presence of calcite, as shown in XRD patterns. The decrease of the intensity of the stretching vibration of the inner —OH group at ~3680 cm^{-1} means that most nickel has been extracted from the LK ore (Scholtzová et al., 2003).

Fig. 7 shows the DSC/TG curves for LK and its residues during heating. The low-temperature endothermic peaks seen at 110 °C and 140 °C (Fig. 7(a–c)) are associated with the loss of free water. The endothermic peaks seen between 300 and 315 °C in all samples are attributed to the dehydroxylation of goethite (FeOOH) to form hematite (α-Fe$_2$O$_3$) or the decomposition of other hydroxyls (Elfiad et al., 2018). The endothermic peak at 640 °C for LK (Fig. 7a) shows the
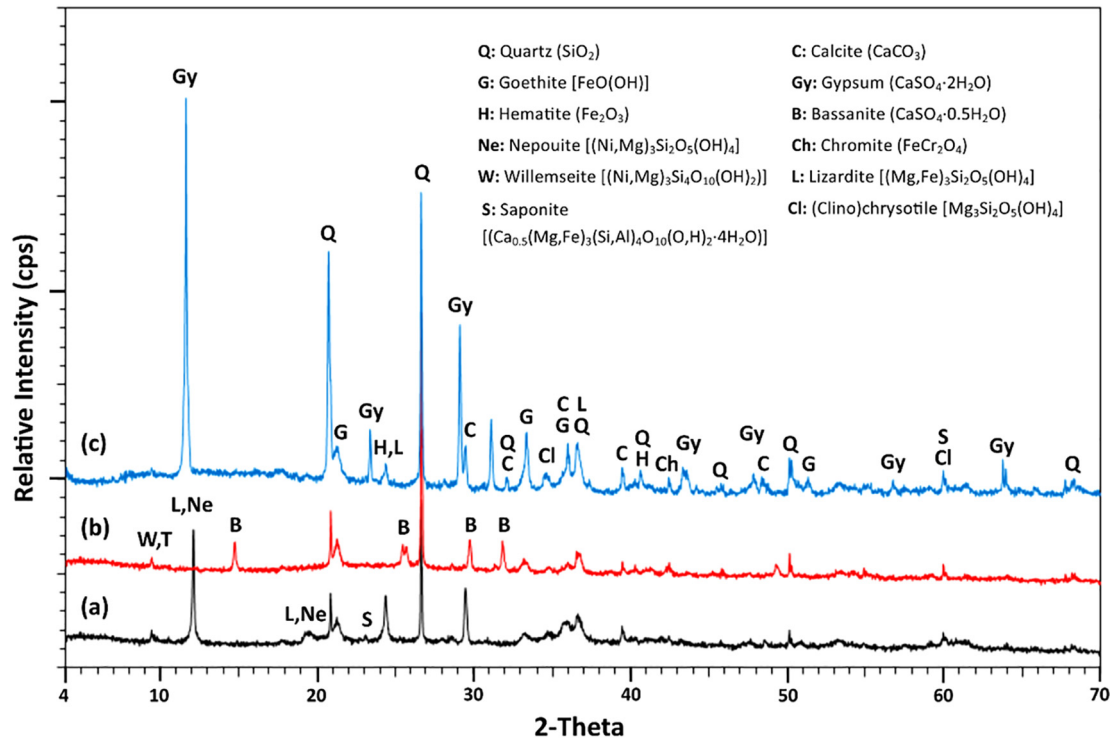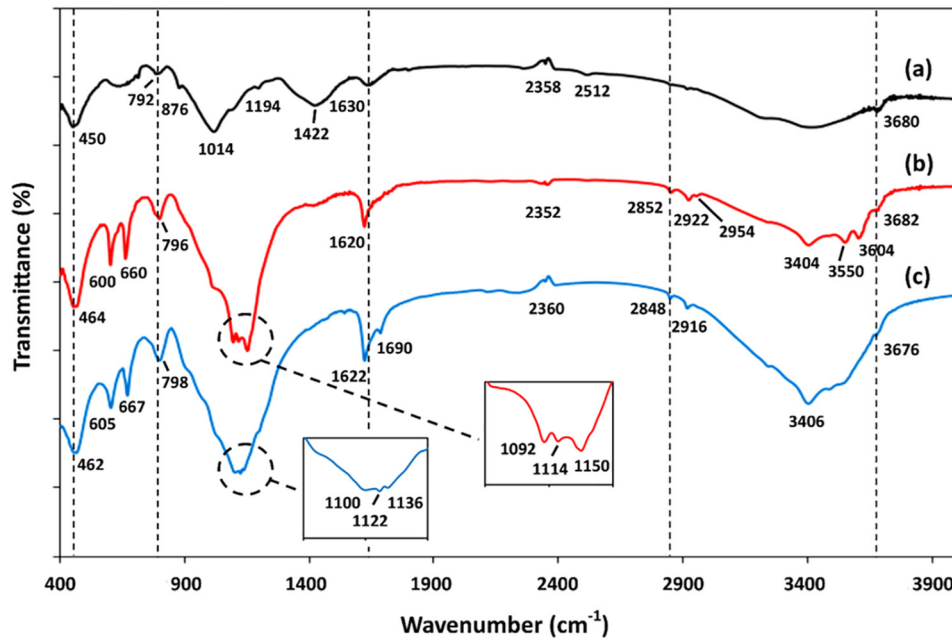
Fig. 5. XRD patterns of (a) LK ore, (b) LKr obtained after leaching with 147 g L^{-1} H$_2$SO$_4$ solution and (c) LKr obtained after leaching with 147 g L^{-1} H$_2$SO$_4$ solution containing 20 g L^{-1} Na$_2$SO$_3$.

decomposition of nickeliferous lizardite which loses its crystal water and transforms to olivine (Febriana et al., 2018; Mu et al., 2018); this peak is not shown in LKr since most lizardite has been leached. The peaks at 590 °C and 840 °C shown in the residues are due to recrystallization of magnesium silicates to forsterite (Mg$_2$SiO$_4$) (Tartaj et al., 2000; Zevgolis et al., 2010).

BSE images of the LK ore and LKr obtained after leaching with H$_2$SO$_4$ solution without and with the addition of Na$_2$SO$_3$ are shown in Fig. 8(a–d).

SEM analysis of the LK ore along with EDS point analyses (Fig. 8(a, b)) revealed that nepouite, chromite and vitreous goethite were the main Ni-bearing mineral phases, containing up to 3.16%, 5.89% and 0.95% Ni, respectively. As shown in XRD patterns, the major mineralogical phases, namely quartz, calcite, and hematite were also detected in the LK ore; other silicates such as talc and clinochrysotile were also detected in some places. Fig. 8(b) (zoom of rectangular area of Fig. 8(a)) shows in detail the presence of nepouite and lizardite along cracks

Fig. 6. FTIR spectra of (a) LK ore, (b) LKr obtained after leaching with 147 g L^{-1} H$_2$SO$_4$ solution, and (c) LKr obtained after leaching with 147 g L^{-1} H$_2$SO$_4$ solution containing 20 g L^{-1} Na$_2$SO$_3$.
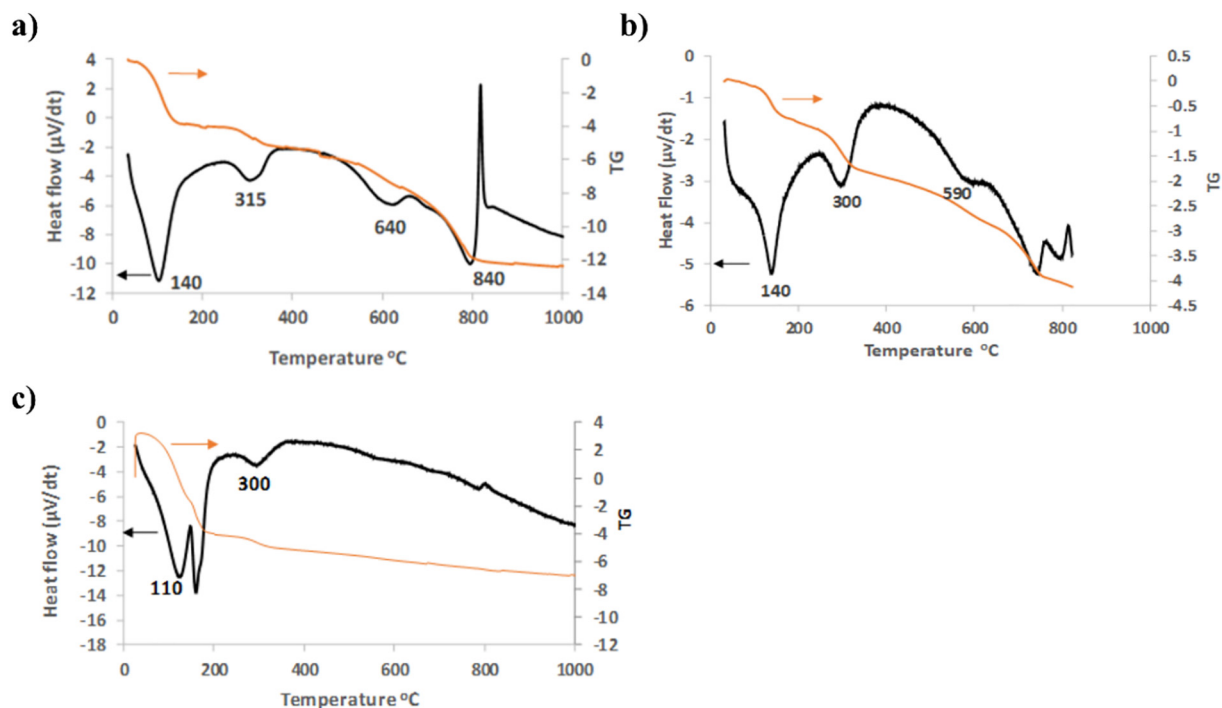
Fig. 7. DSC/TG curves of (a) LK, (b) LKr obtained after leaching with 147 g L^{-1} H$_2$SO$_4$ solution, and (c) LKr obtained after leaching with 147 g L^{-1} H$_2$SO$_4$ solution containing 20 g L^{-1} Na$_2$SO$_3$.
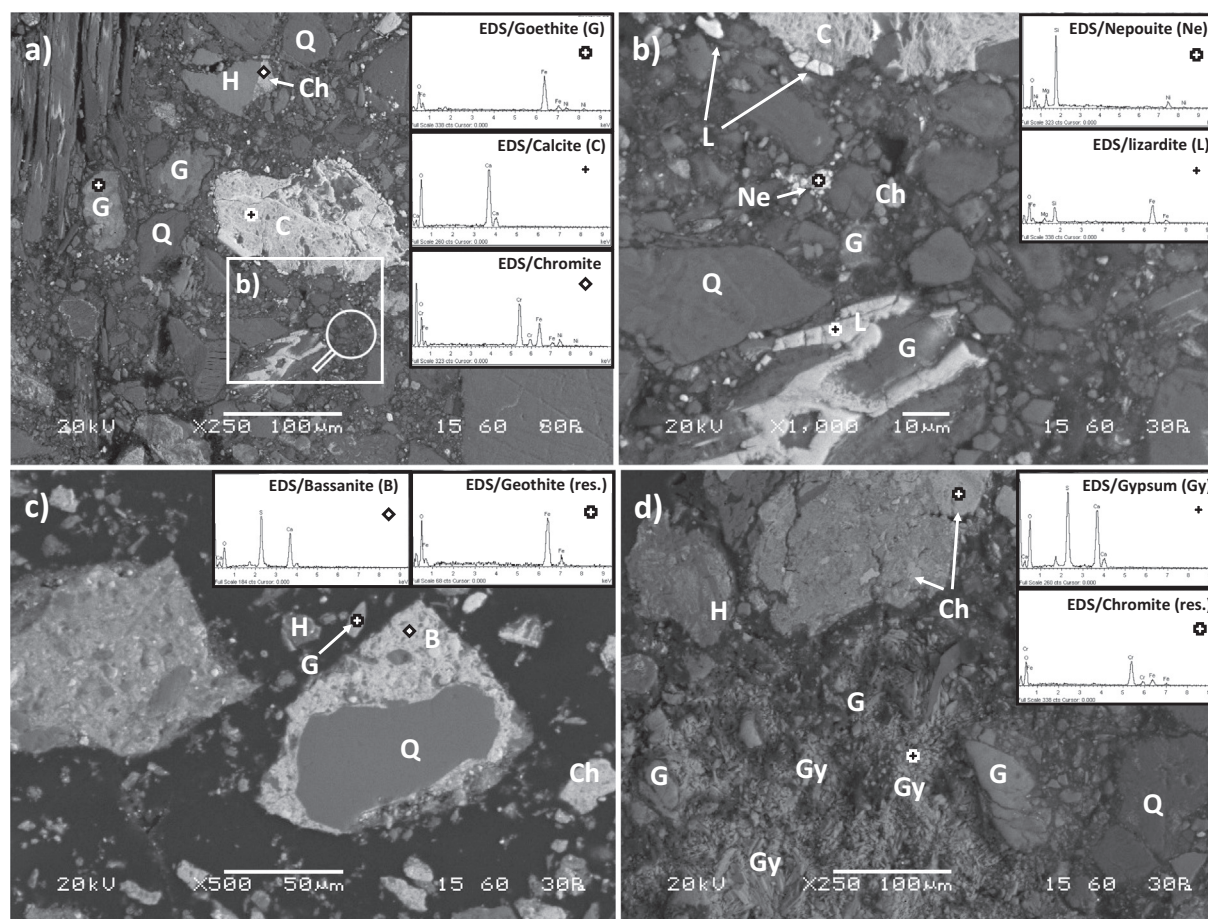

Fig. 8. Back-scattered electron images of the LK ore (a and b) and LKr obtained after leaching with c) H$_2$SO$_4$ and d) H$_2$SO$_4$ with the addition of Na$_2$SO$_3$. EDS spectra show in several spot locations the presence of Ni-bearing mineral phases and the formation of mixed aggregates and newly formed phases after leaching (Q: Quartz, C: Calcite, G: Geothite, H: Hematite, Ne: Nepouite, Ch: Chromite, L: Lizardite, B: Bassanite, Gy: Gypsum).

and grain boundaries. As can be seen in Fig. 8(b), nepouite (Ni-rich an-alogue of lizardite) is observed as flaky-like infillings present at the boundaries between geothite and quartz, while long tabular lizardite crystals were found along shrinkage cracks at the internal space of goe-thite (Zhu et al., 2012) or at the boundaries of calcite. Furthermore, chromite crystals were usually severely cracked and the cracks were filled with Ni-rich goethite.

After LK leaching with H_2SO_4 without or with the addition of Na_2SO_3 (Fig. 8(c, d)), LKr displayed quite smooth edges and surfaces which mostly comprised of newly formed aggregates formed by a large num-ber of small particles of the LK ore that agglomerated (Çetintaş et al., 2018). It is seen that Ni-rich nepouite and calcite were not observed in LKr obtained after leaching, thus indicating that they were both de-pleted after reacting with the leaching medium, while the more refrac-tory particles of hematite, goethite and quartz reacted only partially.

It is important to note that bassanite formed an outer shell of fine crystals often mixed with silicate aggregates adjacent to quartz or iron (oxy)hydroxides surfaces, while gypsum almost dominated the whole interlocking crystalline matrix of the solid residues. Finally, SEM micro-graphs and EDS analyses of LKr also revealed a porous structure for the goethite and chromite particles as a result of the acid attack, which re-sulted in partial or even complete leaching of the contained nickel (Fig. 8(c, d)). The presence of these Ni-free phases and the absence of nepouite indicate that most Ni was extracted from the LK ore during leaching.

3.5. Assessment of toxicity

Table 7 presents the toxicity of LKr as well as of the IPs produced after alkali activation of the leaching residues, as derived from the appli-cation of the EN 12457-3 test.

Regarding LKr it is seen that the toxicity limits are exceeded by far only for Ni, when both distilled water (pH 7.0) or HCl (pH 4.0) are used as leaching solutions. In the second case, the degree of dissolution rate of Ni is almost doubled to 447 mg kg^{-1}. After alkali activation the dissolution rate of Ni from the IPs decreases dramatically to values well below the limits, 1.13 mg kg^{-1}. This indicates the potential of alkali activation not only to result in the production of materials with benefi-cial properties but also to bind or trap potentially hazardous elements in a stable matrix and therefore reduce their solubilization potential (Komnitsas et al., 2013). The results also show that the dissolution of all other elements from the IPs is well below the lowest limits when

the leaching solution is water, thus the specimens present no toxicity according to the EN 12457-3 test. When the leaching solution becomes more aggressive (HCl solution, pH 4) the dissolution of Ni, As and Pb ex-ceeds slightly the lowest limits, thus suggesting that the structural in-tegrity of the produced specimens is very good.

4. Conclusions

This study confirms the potential of column leaching of a low-grade Greek saprolitic laterite for the extraction of Ni and Co. Experimental re-sults indicate that within a very short period, 72.5% of Ni and 47.4% of Co can be extracted from the ore, when leaching is carried out using a solu-tion containing 147 g L^{-1} H_2SO_4 and 20 g L^{-1} Na_2SO_3. Furthermore, it is mentioned that the obtained Fe and Al co-extractions are low, 8.7% and 31.3% respectively, thus indicating that the process is characterized by good selectivity, as also confirmed by the ratios Ni/Fe and Ni/Al in the PLS.

In addition, the beneficial effect of the presence of H_2SO_3 in the leaching medium is due to the fact that the generated SO_2 reacts with iron-based phases, accelerates their dissolution and subsequently re-sults in the extraction of the contained Ni.

Leaching residues can be alkali activated with the use of NaOH and Na_2SiO_3 as activators and the addition of 10 wt% metakaolin so that IPs with high strength, almost 40 MPa, can be produced. These products have very low toxicity and can be used as binders or building materials in several applications in the construction sector.

The approach followed in this study is environment friendly since it treats low grade nickel ores for the production of critical metals such as Ni and Co and thus contributes to raw materials savings, while it valo-rizes successfully the leaching residues and produces IPs with high added value.

Table 7
Toxicity of LKr and IPs according to the EN 12457-3 (L/S = 10 L kg^{-1}) compliance test.

Element	LKr (mg kg^{-1})[a]		IP (mg kg^{-1})[a]		Toxicity limits (mg kg^{-1})[b]			
	H$_2$O (pH 7)	HCl (pH 4)	H$_2$O (pH 7)	HCl (pH 4)	For waste accepted at landfills for inert waste[c]	For nonhazardous waste	For hazardous waste accepted at landfills for non-hazardous waste	For waste accepted at landfills for hazardous waste
Fe	11.53	52.72	9.69	0.04				
Mn	24.16	41.16	0.18	0.50				
Al	30.00	82.64	165.16	382.46				
Ni	256.53	447.11	0.31	1.13	0.4	10	10	40
Cu	1.89	0.31	0.43	0.69	2	50	50	100
Zn	1.89	1.10	0.67	2.51	4	50	50	200
As	0.01	0.02	0.12	1.47	0.5	2	2	25
Mo	0.01	0.32	0.22	0.17	0.5	10	10	30
Cd	<DL	<DL	<DL	<DL	0.04	1	1	5
Cr$_{total}$	0.24	1.07	0.38	1.75	0.5	10	10	50
Pb	<DL	<DL	0.15	3.18	0.5	10	10	50

[a] DL: detection limit.
[b] Council Decision 19 Dec. 2002 (2003/33/EC).
[c] Shaded parts indicate elements that exceed limits.

References

Agatzini-Leonardou, S., Dimaki, D., 1994. Heap leaching of poor nickel laterites by sulphuric acid at ambient temperature. Hydrometallurgy '94. 1994. Springer, Dordrecht, The Netherlands, pp. 193–208. https://doi.org/10.1007/978-94-011-1214-7_11.

Agatzini-Leonardou, S., Zafiratos, I.G., 2004. Beneficiation of a Greek serpentinic nickeliferous ore part II. Sulphuric acid heap and agitation leaching. Hydrometallurgy 74, 267–275. https://doi.org/10.1016/j.hydromet.2004.05.006.

Agatzini-Leonardou, S., Zafiratos, J.G., Spathis, D., 2004. Beneficiation of a Greek serpentinic nickeliferous ore: part I. Mineral processing. Hydrometallurgy 74, 259–265. https://doi.org/10.1016/j.hydromet.2004.05.005.

Agatzini-leonardou, S., Tsakiridis, P.E., Oustadakis, P., Karidakis, T., Katsiapi, A., 2009. Hydrometallurgical process for the separation and recovery of nickel from sulphate heap leach liquor of nickeliferrous laterite ores. Miner. Eng. 22, 1181–1192. https://doi.org/10.1016/j.mineng.2009.06.006.

Andini, S., Cioffi, R., Colangelo, F., Grieco, T., Montagnaro, F., Santoro, L., 2008. Coal fly ash as raw material for the manufacture of geopolymer-based products. Waste Manag. 28, 416–423. https://doi.org/10.1016/j.wasman.2007.02.001.

Bartzas, G., Komnitsas, K., 2015. Life cycle assessment of ferronickel production in Greece. Resour. Conserv. Recycl. 105, 113–122. https://doi.org/10.1016/j.resconrec.2015.10.016.

Baščarević, Z., Komljenović, M., Miladinović, Z., Nikolić, V., Marjanović, N., Žujović, Z., Petrović, A., 2013. Effects of the concentrated NH_4NO_3 solution on mechanical properties and structure of the fly ash based geopolymers. Constr. Build. Mater. 41, 570–579. https://doi.org/10.1016/j.conbuildmat.2012.12.067.

Brand, N.W., Butt, C.R.M., Elias, M., 1998. Nickel laterites: classification and features. J. Aust. Geol. Geophys. 17 (4), 81–88.

Büyükakinci, E., 2008. Extraction of Nickel From Lateritic Ores. (Master of Science Thesis). Middle East Technical University, Turkey https://etd.lib.metu.edu.tr/upload/12609291/index.pdf, Accessed date: 10 November 2018.

Canterford, J.H., 1986. Acid leaching of chromite-bearing nickeliferous laterite from Rockhampton, Queensland. AusIMM Bull. 291 (6), 51–56.

Çetintaş, S., Yildiz, U., Bingöl, D., 2018. A novel reagent-assisted mechanochemical method for nickel recovery from lateritic ore. J. Clean. Prod. 199, 616–632. https://doi.org/10.1016/j.jclepro.2018.07.212.

Chaerun, S.K., Sulistyo, R.S., Minwal, W.P., Mubarok, M.Z., 2017. Indirect bioleaching of low-grade nickel limonite and saprolite ores using fungal metabolic organic acids generated by Aspergillus Niger. Hydrometallurgy 174, 29–37. https://doi.org/10.1016/j.hydromet.2017.08.006.

Das, G.K., de Lange, J.A.B., 2011. Reductive atmospheric acid leaching of West Australian smectitic nickel laterite in the presence of sulphur dioxide and copper(II). Hydrometallurgy 105, 264–269. https://doi.org/10.1016/j.hydromet.2010.10.016.

du Plessis, C.A., Slabbert, W., Hallberg, K.B., Johnson, D.B., 2011. Ferredox: a biohydrometallurgical processing concept for limonitic nickel laterites. Hydrometallurgy 109 (3–4), 221–229. https://doi.org/10.1016/j.hydromet.2011.07.005.

Eckelman, M.J., 2010. Facility-level energy and greenhouse gas life-cycle assessment of the global nickel industry. Resour. Conserv. Recycl. 54, 256–266. https://doi.org/10.1016/j.resconrec.2009.08.008.

Elfiad, A., Galli, F., Djadoun, A., Sennour, M., Chegrouche, S., Meddour-Boukhobza, L., Boffito, D.C., 2018. Natural α-Fe_2O_3 as an efficient catalyst for the p-nitrophenol reduction. Mater. Sci. Eng. B 229, 126–134. https://doi.org/10.1016/j.mseb.2017.12.009.

Elliot, A., Fletcher, H., Li, J., Watling, H., Robinson, D.J., 2009. Heap leaching of nickel laterites-a challenge and an opportunity. In: Budac, J.J., Fraser, R., Mihaylov, I., Papangelakis, V.G., Robinson, D.J. (Eds.), Hydrometallurgy of Nickel and Cobalt 2009, Proceedings of the 39th Annual Hydrometallurgy Meeting Held in the Conjunction With the 48th Annual Conference of Metallurgists; Sudbury, Canada, 23–26 August. 2009. Canadian Institute of Mining, Metallurgy and Petroleum, Montreal, pp. 537–549.

EN12457-3, 2002. Characterization of Waste – Compliance Test for Leaching of Granular Waste Materials and Sludges – Part 3: Two Stage Batch Test at a Liquid to Solid Ratio of 2 l/kg and 8 l/kg for Materials With High Solid Content and With Particle Size Below 4 mm. 2002. European Committee for Standardization, Brussels.

EU Science Hub, 2019. The European Commission's science and knowledge service. https://ec.europa.eu/jrc/en/news/cobalt-potential-bottleneck-transition-electricmobility, Accessed date: 14 January 2019.

European Commission, 2002. Council Decision of 19 December 2002 establishing criteria and procedures for the acceptance of waste at landfills pursuant to Article 16 of and Annex II to Directive 1999/31/EC. https://eur-lex.europa.eu/legal-content/EN/TXT/PDF/?uri=CELEX:32003D0033&from=EN, Accessed date: 10 November 2018.

Febriana, E., Manaf, A., Prasetyo, A.B., Mayangsari, W., 2018. Thermal characteristic of limonite ore upon calcination and reduction. Proceedings of the International Seminar on Metallurgy and Materials (ISMM2017), AIP Conference Proceedings. vol. 1964, p. 020026. https://doi.org/10.1063/1.5038308.

Georgiou, D., Papangelakis, V., 1998. Sulphuric acid pressure leaching of a limonitic laterite: chemistry and kinetics. Hydrometallurgy 49, 23–46. https://doi.org/10.1016/s0304-386x(98)00023-1.

Guo, Q., Qu, J., Han, B., Zhang, P., Song, Y., Qi, T., 2015. Innovative technology for processing saprolitic laterite ores by hydrochloric acid atmospheric pressure leaching. Miner. Eng. 71, 1–6. https://doi.org/10.1016/j.mineng.2014.08.010.

Hunter, H.M.A., Herrington, R.J., Oxley, E.A., 2013. Examining Ni-laterite leach mineralogy & chemistry – a holistic multi-scale approach. Miner. Eng. 54, 100–119. https://doi.org/10.1016/j.mineng.2013.05.002.

Jang, H.-C., Marjorie Valix, M., 2017. Overcoming the bacteriostatic effects of heavy metals on Acidithiobacillus thiooxidans for direct bioleaching of saprolitic Ni laterite ores. Hydrometallurgy 168, 21–25. https://doi.org/10.1016/j.hydromet.2016.08.016.

Khoo, J.Z., Haque, N., Woodbridge, G., McDonald, R., Bhattacharya, S., 2017. A life cycle assessment of a new laterite processing technology. J. Clean. Prod. 142 (4), 1765–1777. https://doi.org/10.1016/j.jclepro.2016.11.111.

Komnitsas, K., 1983. Kinetic Study of Laterite Leaching With Sulfuric Acid at Atmospheric Pressure. (Diploma thesis). National Technical University of Athens (in Greek).

Komnitsas, K., 1988. High Pressure Acid Leaching of Laterites. (PhD thesis). National Technical University of Athens (in Greek, English abstract). https://www.didaktorika.gr/eadd/handle/10442/1521?locale=en, Accessed date: 9 November 2018.

Komnitsas, K., Zaharaki, D., 2007. Geopolymerisation. A review and prospects for the minerals industry. Miner. Eng. 20, 1261–1277. https://doi.org/10.1016/j.mineng.2007.07.011.

Komnitsas, K., Zaharaki, D., Perdikatsis, V., 2007. Geopolymerisation of low calcium ferronickel slags. J. Mater. Sci. 42 (9), 3073–3082. https://doi.org/10.1007/s10853-006-0529-2.

Komnitsas, K., Zaharaki, D., Perdikatsis, V., 2009. Effect of synthesis parameters on the compressive strength of low-calcium ferronickel slag inorganic polymers. J. Hazard. Mater. 161, 760–768. https://doi.org/10.1016/j.jhazmat.2008.04.055.

Komnitsas, K., Zaharaki, D., Bartzas, G., 2013. Effect of sulphate and nitrate anions on heavy metal immobilisation in ferronickel slag geopolymers. Appl. Clay Sci. 73, 103–109. https://doi.org/10.1016/j.clay.2012.09.018.

Komnitsas, K., Petrakis, E., Pantelaki, O., Kritikaki, A., 2018. Column leaching of greek low-grade limonitic laterites. Minerals 8 (9), 377. https://doi.org/10.3390/min8090377.

Kontopoulos, M.A., Komnitsas, K., 1988. Sulphuric acid pressure leaching of low-grade Greek laterites. In: Yulian, Zheng, Jiazhong, Xu (Eds.), Proceedings of the 1st International Symposium on Hydrometallurgy. 1988. Pergamon Press, Oxford, United Kingdom, pp. 140–144 (Beijing, China, 12–15 October).

Kwon, Y.H., Kang, S.H., Hong, A.G., Moon, J., 2017. Intensified pozzolanic reaction on kaolinite clay-based mortar. Appl. Sci. 7, 522. https://doi.org/10.3390/app7050522.

Le, L., Tang, J., Ryan, D., Valix, M., 2006. Bioleaching nickel laterite ores using multi-metal tolerant Aspergillus foetidus organism. Miner. Eng. 19, 1259–1265. https://doi.org/10.1016/j.mineng.2006.02.006.

Li, J., Li, X., Hu, Q., Wang, Z., Zhou, Y., Zheng, J., Liu, W., Li, L., 2009. Effect of pre-roasting on leaching of laterite. Hydrometallurgy 99, 84–88. https://doi.org/10.1016/j.hydromet.2009.07.006.

Li, G., Zhou, Q., Zhu, Z., Luo, J., Rao, M., Peng, Z., Jiang, T., 2018a. Selective leaching of nickel and cobalt from limonitic laterite using phosphoric acid: an alternative for value-added processing of laterite. J. Clean. Prod. 189, 620–626. https://doi.org/10.1016/j.jclepro.2018.04.083.

Li, J., Li, D., Xu, Z., Liao, C., Liu, Y., Zhong, B., 2018b. Selective leaching of valuable metals from laterite nickel ore with ammonium chloride - hydrochloric acid solution. J. Clean. Prod. 179, 24–30. https://doi.org/10.1016/j.jclepro.2018.01.085.

Liu, K., Chen, Q., Yin, Z., Hu, H., Ding, Z., 2012. Kinetics of leaching of a Chinese laterite containing maghemite and magnetite in sulfuric acid solutions. Hydrometallurgy 125–126, 125–136. https://doi.org/10.1016/j.hydromet.2012.06. 001.

Loveday, B.K., 2008. The use of oxygen in high pressure acid leaching of nickel laterites. Miner. Eng. 21, 533–538. https://doi.org/10.1016/j.mineng.2007.11.002.

Luo, W., Feng, Q., Ou, L., Zhang, G., Lu, Y., 2009. Fast dissolution of nickel from a lizardite rich saprolitic laterite by sulphuric acid at atmospheric pressure. Hydrometallurgy 96 (1–2), 171–175. https://doi.org/10.1016/j.hydromet.2008.08.001.

Luo, W., Feng, Q., Ou, L., Zhang, G., Chen, Y., 2010. Kinetics of saprolitic laterite leaching by sulphuric acid at atmospheric pressure. Miner. Eng. 23, 458–462. https://doi.org/10.1016/j.mineng.2009.10.006.

Luo, J., Li, G., Rao, M., Peng, Z., Zhang, Y., Jiang, T., 2015. Atmospheric leaching characteristics of nickel and iron in limonitic laterite with sulfuric acid in the presence of sodium sulfite. Miner. Eng. 78, 38–44. https://doi.org/10.1016/j.mineng.2015.03.030.

Ma, B., Yang, W., Yang, B., Wang, C., Chen, Y., Zhang, Y., 2015. Pilot-scale plant study on the innovative nitric acid pressure leaching technology for laterite ores. Hydrometallurgy 155, 88–94. https://doi.org/10.1016/j.hydromet.2015.04.016.

MacCarthy, J., Nosrati, A., Skinner, W., Addai-Mensah, J., 2015. Acid leaching and rheological behaviour of a siliceous goethitic nickel laterite ore: influence of particle size and temperature. Miner. Eng. 77, 52–63. https://doi.org/10.1016/j.mineng.2014.12.031.

MacCarthy, J., Nosrati, A., Skinner, W., Addai-Mensah, J., 2016. Atmospheric acid leaching mechanisms and kinetics and rheological studies of a low grade saprolitic nickel laterite ore. Hydrometallurgy 160, 26–37. https://doi.org/10.1016/j.hydromet.2015.11.004.

McDonald, R.G., Whittington, B.I., 2008. Atmospheric acid leaching of nickel laterites review: part I. Sulphuric acid technologies. Hydrometallurgy 91, 35–55. https://doi.org/10.1016/j.hydromet.2007.11.009.

Mu, W., Lu, X., Cui, F., Luo, S., Zhai, Y., 2018. Transformation and leaching kinetics of silicon from low-grade nickel laterite ore by pre-roasting and alkaline leaching process. Trans. Nonferrous Metals Soc. China 28 (1), 169–176. https://doi.org/10.1016/s1003-6326(18)64650-3.

Myagkiy, A., Truche, L., Cathelineau, M., Golfier, F., 2017. Revealing the conditions of Ni mineralization in the laterite profiles of New Caledonia: insights from reactive geochemical transport modeling. Chem. Geol. 466, 274–284. https://doi.org/10.1016/j.chemgeo.2017.06.018.

Mystrioti, C., Papassiopi, N., Xenidis, A., Komnitsas, K., 2018. Comparative evaluation of sulfuric and hydrochloric acid atmospheric leaching for the treatment of Greek low grade nickel laterites. In: Davis, B., et al. (Eds.), Extraction 2018. The Minerals, Metals & Materials Series. Springer, Cham, pp. 1753–1764 https://doi.org/10.1007/978-3-319-95022-8_145.

Nickel Institute, 2019. Nickel mining & production. https://www.nickelinstitute.org/about-nickel/, Accessed date: 14 January 2019.

Norgate, T., Jahanshahi, S., 2011. Assessing the energy and greenhouse gas footprints of nickel laterite processing. Miner. Eng. 24 (7), 698–707. https://doi.org/10.1016/j.mineng.2010.10.002.

Nosrati, A., Quast, K., Xu, D., Skinner, W., Robinson, D.J., Addai-Mensah, J., 2014. Agglomeration and column leaching behaviour of nickel laterite ores: effect of ore mineralogy and particle size distribution. Hydrometallurgy 146, 29–39. https://doi.org/10.1016/j.hydromet.2014.03.004.

Oxley, A., Smith, M.E., Caceres, O., 2016. Why heap leach nickel laterites? Miner. Eng. 88, 53–60. https://doi.org/10.1016/j.mineng.2015.09.018.

Panagiotopoulos, N., Agatzini, S., Kontopoulos, A., 1986. Extraction of Nickel and Cobalt From Serpentinic Type Laterites by Atmospheric Pressure Sulfuric Acid Leaching, 115th TMS-AIME Annual Meeting, New Orleans, Paper no A86–30.

Petrakis, E., Karmali, V., Komnitsas, K., 2018. Factors affecting nickel upgrade during selective grinding of low-grade limonitic laterites. Miner. Process. Ext. Metall., 1–10 https://doi.org/10.1080/25726641.2018.1521578.

Pickles, C.A., Anthony, W., 2018. Thermodynamic modelling of the reduction of a saprolitic laterite ore by methane. Miner. Eng. 120, 47–59. https://doi.org/10.1016/j.mineng.2018.02.006.

Proenza, J.A., Lewis, J.F., Galí, S., Tauler, E., Labrador, M., Melgarejo, J.C., Longo, F., Bloise, G., 2008. Garnierite Mineralization From Falcondo Ni-Laterite Deposit (Dominican Republic). 9. Macla, pp. 197–198. http://diposit.ub.edu/dspace/bitstream/2445/107902/1/562923.pdf, Accessed date: 13 November 2018.

Quaicoe, I., Nosrati, A., Skinner, W., Addai-Mensah, J., 2014. Agglomeration and column leaching behaviour of goethitic and saprolitic nickel laterite ores. Miner. Eng. 65, 1–8. https://doi.org/10.1016/j.mineng.2014.04.001.

Quast, K., Xu, D., Skinner, W., Nosrati, A., Hilder, T., Robinson, D.J., Addai-Mensah, J., 2013. Column leaching of nickel laterite agglomerates: effect of feed size. Hydrometallurgy 134–135, 144–149. https://doi.org/10.1016/j.hydromet.2013.02. 001.

Quast, K., Connor, J.N., Skinner, W., Robinson, D.J., Addai-Mensah, J., 2015. Preconcentration strategies in the processing of nickel laterite ores part 1: literature review. Miner. Eng. 79, 261–268. https://doi.org/10.1016/j.mineng.2015.03.017.

Rubisov, D.H., Papangelakis, V.G., 2000. Sulphuric acid pressure leaching of laterites - a comprehensive model of a continuous autoclave. Hydrometallurgy 58 (2), 89–101. https://doi.org/10.1016/s0304-386x(00)00092-x.

Scholtzová, E., Tunega, D., Turi Nagy, L., 2003. Theoretical study of cation substitution in trioctahedral sheet of phyllosilicates. An effect on inner OH group. J. Mol. Struct. (THEOCHEM) 620 (1), 1–8. https://doi.org/10.1016/S0166-1280(02)00320-2.

Sullivan, M.S., Chorzepa, M.G., Hamid, H., Durham, S.A., Kim, S.S., 2018. Sustainable materials for transportation infrastructures: comparison of three commercially metakaolin products in binary, cementitious systems. Infrastructures 3 (3), 17. https://doi.org/10.3390/infrastructures3030017.

Tartaj, P., Cerpa, A., Garcia-Gonzalez, M.T., Serna, C.J., 2000. Surface instability of serpentine in aqueous suspensions. J. Colloid Interface Sci. 231 (1), 176–181. https://doi.org/10.1006/jcis.2000.7109.

Tauler, E., Proenza, J., Galí, S., Lewis, J., Labrador, M., García-Romero, E., 2009. Ni-sepiolite-falcondoite in garnierite mineralisation from the Falcondo Ni-laterite deposit, Dominican Republic. Clay Miner. 44 (4), 435–454. https://doi.org/10.1180/claymin.2009.044.4.435.

Thubakgale, C.K., Mbaya, R.K.K., Kabongo, K., 2013. A study of atmospheric acid leaching of a South African nickel laterite. Miner. Eng. 54, 79–81. https://doi.org/10.1016/j.mineng.2013.04.006.

van der Sloot, H.A., Hjelmar, O., Bjerre Hansen, J., Woitke, P., Lepom, P., Leschber, R., Bartet, B., Debrucker, N., 2001. Validation of CEN/TC 292 Leaching Tests and Eluate Analysis Methods prEN 12457 1-4, ENV 13370 and ENV 12506.

Villanova-De-Benavent, C., Domènech, C., Tauler, E., Galí, S., Tassara, S., Proenza, J., 2017. Fe–Ni-bearing serpentines from the saprolite horizon of Caribbean Ni-laterite deposits: new insights from thermodynamic calculations. Mineral. Deposita 52 (7), 979–992. https://doi.org/10.1007/s00126-016-0683-7.

Watling, H.R., Elliot, A.D., Fletcher, H.M., Robinson, D.J., Sully, D.M., 2011. Ore mineralogy of nickel laterites: controls on processing characteristics under simulated heap-leach conditions. Aust. J. Earth Sci. 58 (7), 725–744. https://doi.org/10.1080/08120099.2011.602986.

Zaharaki, D., Galetakis, M., Komnitsas, K., 2016. Valorization of construction and demolition (C&D) and industrial wastes through alkali activation. Constr. Build. Mater. 121, 686–693. https://doi.org/10.1016/j.conbuildmat.2016.06.051.

Zanbak, C., 2012. Heap leaching technique in mining within the context of best available techniques (BAT), November 2012. http://www.euromines.org/files/mining-europe/mining-techniques/batforheapleaching-feb2013-c.zanbak-euromines.pdf, Accessed date: 7 November 2018.

Zevgolis, E., Zografidis, C., Halikia, I., 2010. The reducibility of the Greek nickeliferous laterites: a review. Miner. Process. Ext. Metall. 119 (1), 9–17. https://doi.org/10.1179/174328509x431472.

Zhang, P., Guo, Q., Wei, G., Meng, L., Han, L., Qu, J., Qi, T., 2015. Extraction of metals from saprolitic laterite ore through pressure hydrochloric-acid selective leaching. Hydrometallurgy 157, 149–158. https://doi.org/10.1016/j.hydromet.2015.08.007.

Zhang, P., Guo, Q., Wei, G., Meng, L., Han, L., Qu, J., Qi, T., 2016. Leaching metals from saprolitic laterite ore using a ferric chloride solution. J. Clean. Prod. 112, 3531–3539. https://doi.org/10.1016/j.jclepro.2015.10.134.

Zhu, D.-Q., Cui, Y., Hapugoda, S., Vining, K., Pan, J., 2012. Mineralogy and crystal chemistry of a low grade nickel laterite ore. Trans. Nonferrous Metals Soc. China 22 (4), 907–916. https://doi.org/10.1016/s1003-6326(11)61264-8.

Grinding Kinetics of Slag and Effect of Final Particle Size on the Compressive Strength of Alkali Activated Materials

Evangelos Petrakis [1],*[iD]**, Vasiliki Karmali** [1]**, Georgios Bartzas** [2][iD] **and Konstantinos Komnitsas** [1][iD]

[1] Technical University of Crete, School of Mineral Resources Engineering, University Campus, Kounoupidiana, 73100 Chania, Greece; vkarmali@isc.tuc.gr (V.K.); komni@mred.tuc.gr (K.K.)

[2] School of Mining and Metallurgical Engineering, National Technical University of Athens, 15780 Zografos, Athens, Greece; gbartzas@metal.ntua.gr

* Correspondence: vpetraki@mred.tuc.gr; Tel.: +30-28210-37608

Abstract: This study aims to model grinding of a Polish ferronickel slag and evaluate the particle size distributions (PSDs) of the products obtained after different grinding times. Then, selected products were alkali activated in order to investigate the effect of particle size on the compressive strength of the produced alkali activated materials (AAMs). Other parameters affecting alkali activation, i.e., temperature, curing, and ageing time were also examined. Among the different mathematical models used to simulate the particle size distribution, Rosin–Rammler (RR) was found to be the most suitable. When piecewise regression analysis was applied to experimental data it was found that the particle size distribution of the slag products exhibits multifractal character. In addition, grinding of slag exhibits non-first-order behavior and the reduction rate of each size is time dependent. The grinding rate and consequently the grinding efficiency increases when the particle size increases, but drops sharply near zero after prolonged grinding periods. Regarding alkali activation, it is deduced that among the parameters studied, particle size (and the respective specific surface area) of the raw slag product and curing temperature have the most noticeable impact on the compressive strength of the produced AAMs.

Keywords: particle size distribution; grinding kinetics; slag; alkali activated materials; compressive strength

1. Introduction

Very large quantities of slags are generated during steel, ferrous- and non-ferrous metal production. Even though a certain share of the produced slag volume is used in the construction sector, large quantities are not properly managed and are considered as sources of environmental pollution. Thus, the development of an integrated management scheme that can transform this resource into valuable products is of great importance [1,2].

Slags are mainly used for cement and concrete production. This utilization option eliminates environmental problems and contributes to the reduction of the environmental footprint of the construction sector. It is known that cement production is one of the most energy intensive processes, since it consumes 12% to 15% of the total industrial energy requirements and is responsible for 7% to 10% of the global CO_2 emissions [3,4]. Other alternative options for slag management include its use in road construction as aggregate [5], and in recent years the production of alkali activated materials (AAMs), called inorganic polymers (IPs) or "geopolymers", can be used as construction materials or binders in the construction sector, thus improving its sustainability [6].

Alkaline activation, which is carried out with the use of NaOH, KOH, and Na_2SiO_3 solutions at relatively low temperature, is considered as a promising option for the management of various waste streams and the production of AAMs (alkali activated materials) exhibiting beneficial physico–chemical and thermal properties [7–12]. The potential of wastes for alkali activation depends on their content of aluminosilicates which defines their reactivity, the strength of the activating solution and the other synthesis conditions, mainly particle size of the raw material used, curing temperature, curing and ageing period [13,14].

So far various types of slags, rich in Ca or Fe, produced from various metal and steel production industries have been successfully alkali activated. Alkali activation involves the use of raw slags or their mixtures with other waste types to regulate their content of aluminosilicates and enable the formation of strong bonds [15–18]. It is mentioned that the produced structures may also exhibit other beneficial properties, including the sorption of contaminants from solutions and immobilization of hazardous ions [19,20].

Slag, prior to its use in most applications, requires grinding which is an energy intensive process, characterized by high CO_2 emissions and increased processing cost. In addition, grinding is a low-efficiency process because a large share of the consumed energy is absorbed by the device and only a small part is used for size reduction [21,22]. Considering these factors, the investigation of grinding kinetics of any raw material, including slag, is an important aspect.

Among the different approaches used to improve grinding efficiency, phenomenological grinding kinetics models based on population balance considerations are used. Population balance modeling is based on two functions, namely the breakage rate and the breakage function [23,24]. Many studies have reported the advantages of these functions [25,26] and the variation of the kinetic model parameters under different mill operating conditions [27–32]. Another important issue associated with the grinding operation is the scale-up of ball mills based on laboratory test work [33].

The determination of the breakage rate for the mass fraction of feed size R is based on the assumption that grinding follows a first-order law as reported in previous studies [22,24], according to Equation (1),

$$\frac{dR}{dt} = -K{\cdot}R \tag{1}$$

where K is the grinding rate constant and t is the grinding time.

Generally, the first-order hypothesis is the most widely used one to describe the grinding process in a ball mill, however, many researchers have observed that, in fact, the breakage rate slows down with increasing grinding time and deviates from the first-order; this breakage is called non-first-order [34–36].

In light of the non-first-order behavior Alyavdin proposed that the following formula (Equation (2)) can be used to describe the grinding process [37,38],

$$R = R_0{\cdot}e^{-K{\cdot}t^M} \tag{2}$$

where R_0 is the mass fraction in the feed, and M is a constant depending on the material properties and grinding conditions.

The present study aims, through batch grinding experiments, to model grinding and evaluate the effect of grinding time on the particle size distribution of the slag products. Then, selected grinding products were alkali activated, and the effect of particle size, specific surface area, curing temperature, and ageing time on the properties of the produced AAMs was assessed. The novelty of the study is that it investigates in depth the grinding kinetics of an industrial waste and the effect of the particle size of the raw material for the production of AAMs, issues that so far have not been systematically investigated.

2. Mathematical Models for the Simulation of PSD

In the literature and also in industrial practice, several models have been tested to simulate mathematically the particle size distribution (PSD) of the grinding products. These include log-normal, logistic, Gates–Gaudin–Schuhmann (GGS) and Rosin–Rammler (RR) distributions, while truncated distributions, e.g., logarithmic distribution, Gaudin–Meloy, log-normal and the truncated version of RR distribution can also be used to describe particulate materials [39,40]. In addition, fractal geometry which is based on the idea of self-similarity is also widely used for describing various complex natural phenomena, including particle size distribution [41,42]. Other studies have used the Swrebec distribution model as an alternative to traditional distributions because of its goodness-of-fit in both coarse and fine size ranges [43,44]. The Rosin–Rammler distribution that was used in the present study is expressed by Equation (3),

$$P = 100 - 100 \cdot \exp\left[-\left(\frac{x}{x'}\right)^n\right] \qquad (3)$$

where x is the screen aperture size, P is the mass or volume (in %) finer than size x, x' is the size modulus (63.2% passing-screen size), and n is the distribution modulus (index of uniformity). The higher the n value the more uniform is the distribution [45]. The RR distribution can be transformed to:

$$loglog\left(\frac{100}{100 - P}\right) = n \cdot logx + (logloge - n \cdot logx') \qquad (4)$$

Equation (4) indicates that if the data follow the RR distribution, the plot of loglog(100/(100-P)) versus log$x$ will be a straight line from which n and x' can be calculated.

The PSD of the grinding products can be also mathematically described by the logistic distribution as follows:

$$P = \frac{100}{1 + \left(\frac{x_{50}}{x}\right)^\lambda} \qquad (5)$$

where x_{50} is the 50% passing-screen size and λ (>0) is the distribution modulus (sharpness index). Equation (5) can be transformed into a straight line as follows:

$$log\left(\frac{100}{P} - 1\right) = -\lambda \cdot logx + (\lambda \cdot logx_{50}) \qquad (6)$$

From the straight line of Equation (6) λ and x_{50} can be calculated.

The GGS model that was used in the present study is expressed by Equation (7),

$$P = 100 \cdot \left(\frac{x}{k}\right)^m \qquad (7)$$

where k is the particle size modulus (maximum particle size) and m is the distribution modulus (index of uniformity). Lower values of m suggest the production of more fines and large particles, while as the value of m increases the distribution gets narrower [45,46].

The GGS model follows a power-law and is therefore equivalent to fractal distribution, as proposed by Turcotte [47]. Logarithmic transformation of Equation (7) results in a linear relationship between log$P$ and log$x$ from which k and m can be determined using linear regression analysis. Then, the fragmentation fractal dimension could be calculated as follows,

$$D = 3 - m \qquad (8)$$

Since simple linear models may not fit the entire dataset, a piecewise approximation could be used for the description of the PSD of the grinding products [48,49]. Based on this, it is assumed that there could be two intervals of particle sizes separated by a critical size. This could mean that the log-transformed data of Equation (7) would yield two straight lines, separated by a breakpoint (logx_b) defined as the transition point between two particle intervals,

$$logP = m_1 \cdot logx + b_1 \cdot (logx \leq logx_b) + m_2 \cdot logx + b_2 \cdot (logx > logx_b) \tag{9}$$

where m_1 and m_2 are the slopes and b_1 and b_2 are the intercepts of the straight lines. Each term in parenthesis represents a logical operation, i.e., if the term is true it will get the value 1, while if it is false it will get the value 0.

3. Materials and Methods

The material used in this study is slag produced from the pyrometallurgical treatment of Ni-bearing silicate ores in Szklary, southwestern Poland [50]. Its chemical composition, as obtained by X-ray fluorescence in the form of oxides is shown in Table 1. The main mineralogical phases present, as obtained by X-ray diffraction (XRD), were quartz (SiO_2), hedenbergite ($Ca(Fe,Mg)(SiO_3)_2$), fayalite (Fe_2SiO_4), diopside ($CaMgSi_2O_6$), and magnetite (Fe_3O_4), while hatrurite (Ca_3SiO_5) is present as a minor phase. More data about the origin and the characteristics of this slag can be found in a previous recent study [2].

The received sample, approximately 200 kg, with a particle size of –100 mm was homogenized by the cone and quarter method, and a representative quantity was crushed to less than 0.850 mm using a Fritsch type jaw crusher (Fritsch pulverisette 1, Fritsch GmbH, Idar-Oberstein, Germany) for primary and a cone crusher (Sepor, Wilmington, NC, USA) for secondary crushing. The particle size distribution of the feed material and grinding product was determined using a Malvern type S Mastersizer (Malvern Instruments, Malvern, UK) (size range: 0.05 to 850 μm) and laser diffraction (LD) technique. LD was also used for the estimation of the specific surface area (SSA) of the feed material and grinding products using Equation (10).

$$S_w = \left(\frac{f}{k}\right) \cdot \frac{1}{\rho_p \cdot D[3,2]} \tag{10}$$

S_w is the specific surface area, ρ_p is the particle density, D[3,2] is the surface area mean (Sauter mean diameter), and f, k are the surface and volume coefficients (for spheres $f/k = 6$).

Table 1. Chemical composition (wt %) of slag.

Fe$_2$O$_3$	SiO$_2$	Al$_2$O$_3$	Cr$_2$O$_3$	MgO	NiO	K$_2$O	TiO$_2$	CoO	MnO	CaO	P$_2$O$_5$	Total
40.62	30.18	7.60	1.98	1.80	0.95	0.89	0.69	0.03	0.28	13.0	0.02	98.01

LD involves the detection of the angular distribution of scattered light produced by a laser beam which passes through a dispersed particulate sample [51]. The data of the angular scattering intensity is then analyzed and the particle sizes are calculated using the Mie theory of light scattering and expressed as the volume equivalent sphere diameter [52,53]. Thus, since LD assumes a specific geometry for the particles without taking into consideration the particle shape, the Brunauer–Emmett–Teller (BET) nitrogen adsorption method (using a Quantachrome Nova 2200 analyser, Anton Paar QuantaTec Inc., Boynton Beach, FL, USA) was considered for the determination of SSA [54].

The techniques used for characterizing raw slag and the produced AAMs are (i) X-ray powder diffraction, for the identification of the mineral phases using a D8 Advance type (-AXS, Karlsruhe, Germany) diffractometer and (ii) X-ray fluorescence, for the chemical analysis using a Bruker S2 Ranger Energy-dispersive ED-XRF (Bruker, Karlsruhe, Germany) Spectrometer. Scanning electron microscopy (SEM) was also used to define the morphology of the raw slag and the grinding products, using a JEOL 6380LV microscope (JEOL Ltd., Tokyo, Japan) equipped with an Oxford INCA energy dispersive X-ray spectrometer (EDS).

Grinding tests were carried out in a ball mill (Sepor, Los Angeles, CA, USA) with dimensions of $L \times D = 166 \times 204$ mm using different grinding times (15, 30, 45, 60, 90, and 120 min) under dry conditions. Stainless steel balls ($\rho_b = 7.85$ g/cm^3) with three different sizes, i.e., 40, 25.4, and

12.7 mm were used as grinding media. The total ball mass was almost constant at each ball size used corresponding to ball filling volume $J = 20\%$, while the material filling volume f_c was 4%. This means that 50% of the interstitial filling U of the void spaces of the balls was filled with material, according to Equation (11). The mill specification data and test conditions are shown in Table 2.

$$U = \frac{f_c}{0.4 \cdot J} \tag{11}$$

Table 2. Mill specification data and test conditions.

Mill	Diameter, D (cm)	20.4
	Length, L (cm)	16.6
	Volume, V (cm^3)	5423
	Operational speed, N (rpm)	66
	Critical speed, N_c (rpm)	93.7
Balls	Diameter, d (mm)	40, 25.4, 12.7
	Number	6, 28, 202
	Weight (g)	1572.7, 1865.7, 1702.4
	Density (g/cm^3)	7.85
	Porosity (%)	40
	Ball filling volume, J (%)	20
Material	Bulk density (g/cm^3)	1.67
	Material filling volume, f_c (%)	4
	Interstitial filling, U (%)	50

The reactivity of the products obtained after 30, 60, and 120 min of grinding was evaluated through leaching of 1.0 g of solids in 100 mL of 8 mol/L (M) NaOH solution for 24 h at ambient temperature (~22 °C) under continuous magnetic stirring. After solid–liquid separation with the use of 0.45 μm pore size membrane filters (PTFE, Chromafil, Macherey-Nagel GmbH and Co. Düren, Germany), the concentration of Al and Si in the eluate was determined using an Agilent 7500cx Inductively Coupled Plasma Mass Spectrometry (ICP-MS) (Agilent Technologies Inc., Santa Clara, CA, United States) equipped with an Agilent ASX-500 Autosampler.

The slag products obtained after 30, 60, and 120 min of grinding were alkali activated using a mixture of sodium hydroxide (NaOH, Sigma Aldrich) and sodium silicate (Na_2SiO_3, Merck) as alkaline activating solution. Pellets (anhydrous) of NaOH dissolved in water to produce solutions with specific molarity, followed by the addition of sodium silicate solution (8 wt % Na_2O, 27 wt % SiO_2, and 65 wt % H_2O). The final solution was allowed to cool at ambient temperature for 24 h and then mixed under continuous stirring with each grinding product to obtain a paste. Six sets of samples were prepared in order to investigate the effect of slag particle size and curing temperature on the properties of the produced AAMs, while the liquid/solid (L/S) ratio was kept constant at 0.25. The composition of the mixture was (wt %): 80% slag, 16.7% 8 M NaOH solution and 3.3% Na_2SiO_3. Under these conditions the molar ratio of H_2O/Na_2O in the reactive paste was 12.9. According to the procedure followed, cubic metal molds (5 cm edge) were filled with the fresh paste and vibrated for compaction and removal of air voids. The molds remained at ambient temperature for a period of 3 to 9 h and when the paste hardened sufficiently the specimens were removed, sealed in plastic bags to avoid moisture loss, and cured for 24 h at either 60 or 80 °C in a laboratory oven (Jeio Tech ON-02G, Seoul, Korea). After curing, specimens were allowed to cool at room temperature, and after the ageing periods of 7 and 28 days the compressive strength was determined using a Matest C123N load frame (Matest S.p.A, Treviolo, Bergamo, Italy). The experimental conditions used in this study were based on the results of a previous study carried out in the laboratory and involving the same slag [2]. All tests and measurements were carried out in triplicate and the average values are provided in this study. Finally, the apparent density, porosity, and water absorption of selected AAMs were determined based on the standard BS EN 1936 [55].

4. Results and Discussion

4.1. Particle Morphology of Raw Slag and Grinding Products

The particle morphology of the raw slag and the grinding products obtained after 30, 60, and 120 min of grinding, as derived with the use of SEM at different magnifications, is shown in Figure 1a–e.
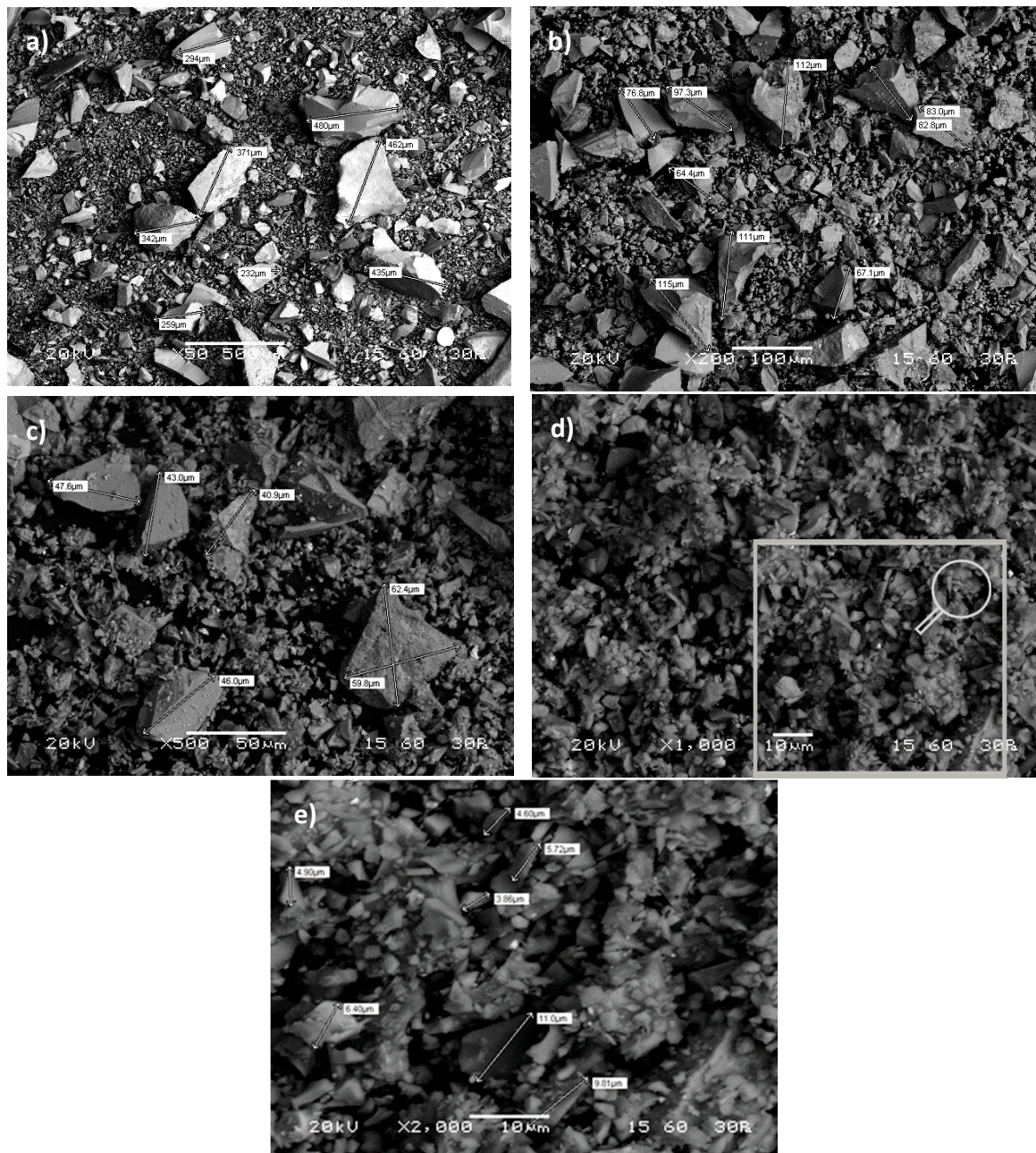

Figure 1. Morphology of particles: (**a**) raw slag, and after (**b**) 30 min, (**c**) 60 min, (**d**,**e**) 120 min of grinding.

The obtained results indicate that, in general, the particles of raw slag have a flat-face, and an irregular and elongated shape, while no spherical particles are observed (Figure 1a). A broad particle size distribution is observed for particles smaller than ~500 µm. With increasing grinding time (30 to 60 min) the particles become progressively finer while their morphology shape remains almost similar (Figure 1b,c).

After prolonged grinding (120 min), even though finer particles are quite irregular, coarser particles tend to become more rounded due to their subjection to attrition (Figure 1d). At this stage, it is seen that particles are distinct and no agglomeration is observed. The evolution of particle morphology during grinding has been investigated in previous studies which reported that the type of material being ground, the mill type, as well as the mode of breakage may have a large impact on the shape of particles produced [56–58].

4.2. Grinding Kinetics Modeling

The particle size distributions of the feed (raw slag) and grinding products as a function of the grinding time are shown in Figure 2. It is seen that the particle size of the grinding product gradually decreases with the increase of grinding time. It is known that the degree to which finer particles are reduced depends on the mill, the material type, and the grinding conditions [58]. Figure 2 also shows that no particle agglomeration was observed even after 120 min of grinding, unlike the findings of previous studies which indicate potential agglomeration after long grinding periods [59,60]; the absence of agglomeration is due to the lack of clay minerals in the feed and is confirmed in Figure 1d which shows that particles are distinct.
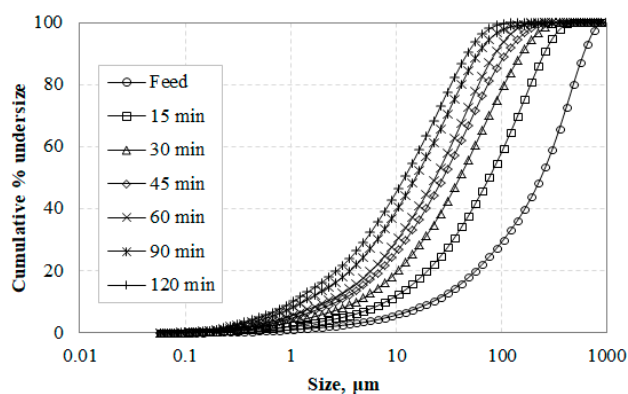

Figure 2. Variation of particle size distribution with grinding time.

In order to investigate the grinding kinetics of the raw slag seven representative sizes (222.3, 65.51, 19.31, 5.69, 1.68, 0.49, and 0.15 µm) were selected, and the remaining volume (%) fraction for each size after various grinding times was determined, as seen in Figure 3. The results indicate that the remaining fraction of each representative size decreases with increasing grinding time and the experimental data can be expressed by Equation (2), which confirms that grinding of slag exhibits non-first-order behavior and the reduction rate of each size is time dependent. The deviation from the first order is more evident for the larger particle sizes which are ground more efficiently than finer particles during grinding. The non-first-order grinding behavior is due to either mill conditions or material properties and has been reported in several earlier studies [22,34,61,62].

Table 3 presents the estimated parameters K and M by fitting the Alyavdin grinding kinetic equation to experimental data. This table also reveals the very good fitting curves, as indicated by the correlation coefficients (R^2) values. Based on the grinding rate constant (K) values, it is confirmed that grinding rate and consequently grinding efficiency increases when the particle size increases, but drops sharply to near zero values after prolonged grinding (Figure 3). The grinding time at which the grinding rate decreases to zero depends on particle size; the larger the particle size the faster the grinding rate drops to zero. M values range between 0.652 and 1.110, indicating deviation from slope unity ($M = 1$) and the first-order grinding kinetics of the population balance model.
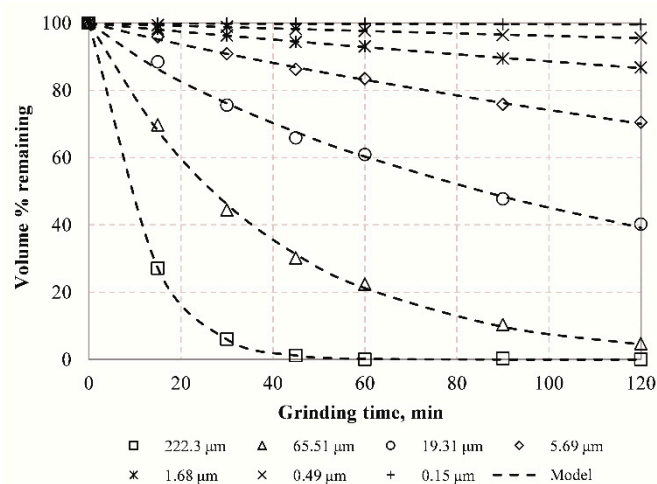
Figure 3. Remaining fraction (% volume) for seven representative sizes vs. grinding time.

Table 3. Parameters of Alyavdin formula (Equation (2)) for seven representative sizes (mm).

Parameter	222.3 mm	65.51 mm	19.31 mm	5.69 mm	1.68 mm	0.49mm	0.15 mm
K	0.0645	0.0255	0.0132	0.0039	0.0015	0.0005	0.0002
M	1.110	1.004	0.890	0.943	0.954	0.952	0.652
R^2 (adj.)	1.000	0.999	0.996	0.997	0.998	0.997	0.850

4.3. Particle Size and Specific Surface Area of Slag Products

The characteristic diameters of the cumulative distributions, i.e. d_{10}, d_{50}, d_{75}, and d_{90}, which refer to particle sizes passing 10%, 50%, 75%, or 90% cumulative undersize, were determined in order to investigate the fineness of the ground products for different grinding times (Table 4). In the LD technique particles are assumed to be spheres and therefore these characteristic diameters are typically the equivalent particle sizes (EPSs). This table also presents the SSA of the slag products determined by either the BET or LD techniques.

Table 4. Equivalent particle size and specific surface area of slag grinding products at different times.

Grinding Time	BET	LD	d_{10}	d_{50}	d_{75}	d_{90}
min	m²/kg	m²/kg	μm	μm	μm	μm
15	930	221.5	7.9	75.9	163.0	252.2
30	1200	316.3	4.2	39.9	88.8	153.8
45	1435	416.2	2.7	27.8	62.5	109.5
60	1598	486.3	2.1	23.4	51.8	86.2
90	2160	681.5	1.3	15.2	35.2	59.9
120	2260	780.4	1.0	11.9	28.1	47.1

The results show that EPSs decrease during grinding, and no agglomeration is observed as indicated by the coarse part of the particle size distributions which continues to shift to finer sizes. This can be also seen from the d_{90} values (Table 4) which continue to decrease during grinding. More specifically, the d_{90} of slag grinding product obtained after 15 min of grinding was 252.2 μm and reduced after prolonged grinding (120 min) to 47.1 μm. Since surface area is intimately linked to particle size, the results of Table 4 show that the specific surface area increases during grinding. By comparing the different techniques, it is revealed that the measured surface areas with BET are almost three times bigger compared to those measured with LD, and this indicates clearly that gas adsorption provides an essential bulk measurement of surface area as it can access surface features close to the size of nitrogen molecules.

In order to investigate the grinding behavior of raw slag, non-linear regression analysis was carried out to correlate the equivalent particle size and grinding time (Figure 4).
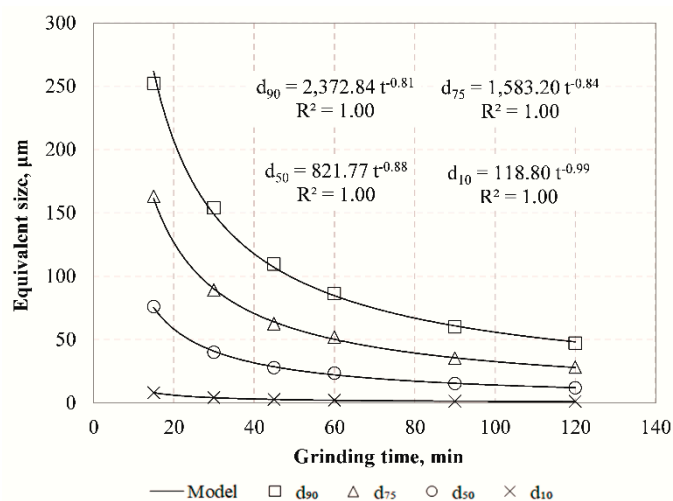

Figure 4. Equivalent particle size of slag products versus grinding time.

The results indicate that with the use of inverse exponential functions very strong correlations are obtained between EPSs and grinding time. It is evident that the reduction rate of particle size is constantly decreasing, and after prolonged grinding the particle size can reach a theoretical constant value which is defined as the grinding limit. This means that there is a product size that cannot be further reduced by the mill and all energy consumed beyond this point is considered as loss. Apart from various parameters affecting grinding limit, namely material type as well as process or machine parameters, its prediction is sensitive to the technique used. Figure 5 presents the evolution of median size (d_{50}) with grinding time in comparison with the particle size determined by the BET method using Equation (10).
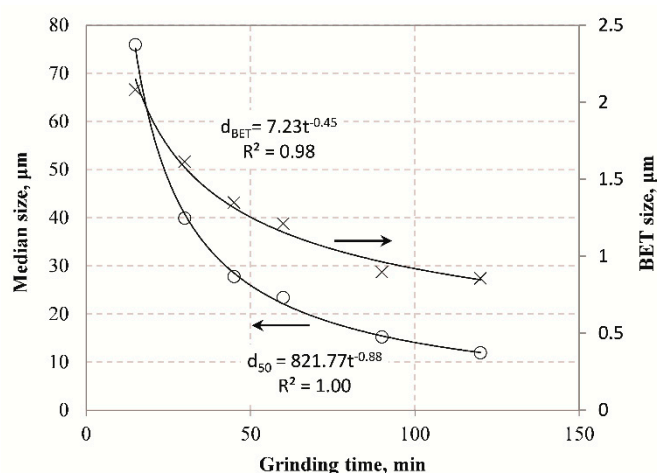

Figure 5. Evolution of median size (d_{50}) and Brunauer–Emmett–Teller (BET) size with grinding time.

In this equation the SSA values of BET provided in Table 4 were considered and the BET size at each grinding time was determined by using the relation $f/k = \pi/6$. The results of Figure 5 show that in both cases the product particle size decreases with the grinding time, and very strong correlation between them is obtained with the use of inverse exponential function. However, the use of BET results in much finer particle sizes in comparison with LD. The results obtained from BET allow the determination of the true grinding limit as already mentioned in previous studies [63].

4.4. Modeling of Particle Size Distributions of Grinding Product

4.4.1. Rosin–Rammler, Gates–Gaudin–Schuhmann and Logistic Distributions

Rosin–Rammler, Gates–Gaudin–Schuhmann as well as Logistic distribution models were used to describe the particle size distribution of the slag products. Figure 6a–c shows the PSDs obtained after grinding for various times and the fitted curves to data points using the RR (Equation (3)), Logistic model (Equation (5)) and GGS (Equation (7)), respectively. Non-linear least square analysis using the Solver tool of Microsoft Excel was used to fit the experimental data and the values of model parameters were estimated, as seen in Table 5.


(a)

(b)

(c)
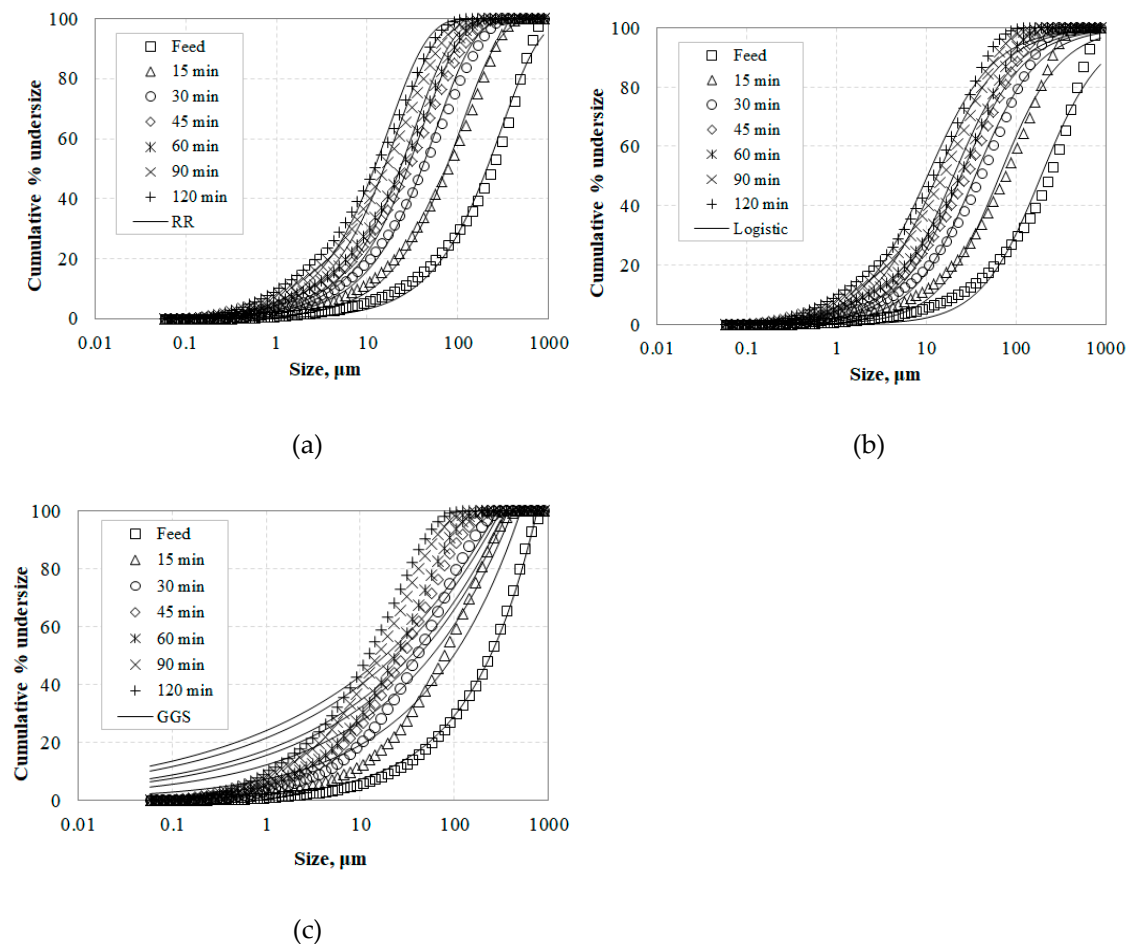
Figure 6. Particle size distribution of slag grinding products using the (**a**) Rosin–Rammler (RR) and (**b**) Logistic model, and (**c**) Gates–Gaudin–Schuhmann (GGS) distributions.

The accuracy of the model distributions was assessed using the adjusted correlation coefficient R^2 (Ads.). The results indicate that RR is a particularly suitable model for representing particle size distributions obtained after grinding in a ball mill, and fits the experimental data better than the GGS and Logistic models. It is known that the PSD of materials generated by comminution can be dependent on a variety of factors such as the initial particle size and the physical properties of the material, as well as the comminution mechanisms applied by the machines. In this regard, the comminution forces acting on the particles during grinding change depending on the machine type, and this affects the product particle size distribution. For example, Taşdemir and Taşdemir [45] mention that the GGS model describes better the PSDs obtained after grinding of chromite ores by low energy events, i.e., jaw and cone crushing, while the RR model is more suitable for PSDs obtained by high energy events, i.e., hammer crushing and ball milling.

Table 5. Model distribution parameters for the slag grinding products.

Model	Parameters	Grinding Time (min)					
		15	30	45	60	90	120
RR	N	1.10	1.42	1.66	1.81	2.16	2.41
	x'	116.8	81.5	66.5	60.1	47.6	41.7
	R^2 (Ads.)	0.998	0.998	0.998	0.998	0.997	0.997
Logistic	x_{50}	65.42	35.06	24.29	20.12	13.21	10.30
	Λ	1.28	1.24	1.22	1.23	1.18	1.18
	R^2 (Ads.)	0.993	0.996	0.996	0.995	0.996	0.995
GGS	K	506.8	418.0	373.5	349.4	310.5	286.9
	M	0.42	0.35	0.32	0.30	0.27	0.25
	R^2 (Ads.)	0.956	0.928	0.910	0.897	0.877	0.861

Size parameters such as size modulus and uniformity index were also determined with the use of the RR model to characterize particle size distribution of the slag grinding products. As shown in Figure 7, the size modulus decreases with increasing grinding time, while the uniformity index becomes higher as grinding proceeds. These results indicate that the finer the product size the higher is the *n* value, and the PSD becomes narrower. Very strong correlations (R^2 = 1.00) are obtained with the use of exponential functions between size modulus or uniformity index and grinding time.
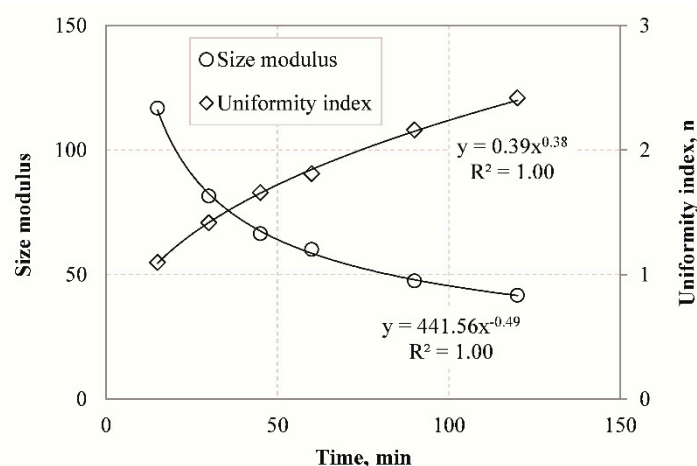
Figure 7. Size modulus and uniformity index versus grinding time using the RR model.

4.4.2. Fractal Features of Products PSD

Table 6 presents the estimated fractal dimensions *D* of grinding products obtained after different grinding times using Equations (7) and (8). Linear regression analysis using the Solver tool of Microsoft Excel was used to fit the experimental data and the goodness of fit was assessed using the correlation coefficient R^2. The results indicate that the values of *D* range between 2.58 and 2.75 which are consistent with the findings of Carpinteri and Pugno [64], who reported that the fractal dimension from comminution experiments ranges between 2 and 3. As reported by Taşdemir [48], the grinding products of chromite ore had different ranges of *D* values, depending on the type of machine used, which in turn affected their breakage mode. For example, in tumbling mills the ore is subjected to repeated forces and since the retention time is long they will eventually break. This results in higher *D* values, indicating wider particle size distribution and bigger proportion of fines in mill products compared to other machines. Table 6 also shows that the value of *D* increases with increasing grinding time, because as grinding proceeds more fines are produced. Due to fact that a large amount of energy is consumed for size reduction, especially for the production of very fine particles, the fractal dimension *D* is also considered a factor of comminution efficiency. However, the goodness-of-fit ($R^2 < 0.957$)

indicates that the single fractal model may not represent the entire range of measured particle sizes. The application of the fractal model to PSDs yielded a certain lack-of-fit which is more apparent during long grinding periods. This is also confirmed from the log-log plot of particle size distribution of slag after 15 min of grinding (Figure 8). It can be seen that the measured data points cannot be represented by a straight line and a significant increase in slope at finer sizes (below ~0.5 μm) is observed. To overcome this shortcoming, piecewise regression analysis by the quasi-Newton nonlinear estimation method was used to predict the size distributions derived. Figure 9 shows the presence of two different domains of particle sizes indicating that the PSDs of slag products may exhibit multi fractal character. These domains can be clearly identified by applying piecewise regression analysis, using Equation (9). Table 6 shows the estimated fractal dimensions D_1 and D_2 for the fine and coarse region of particle sizes, respectively. It is obvious that when piecewise regression analysis was applied to PSDs higher R^2 are obtained compared to single linear regression. The fractal dimension of coarse region (D_2) of particle sizes ranges between 2.29 and 2.49, and increases with increasing grinding time. However, the values of fractal dimension D_1 are negative and thus have no physical meaning. It is noted that Mandelbrot [65] introduced the fractal geometry to describe very irregular forms that cannot be represented by classical geometry. Fractal dimension is not necessarily an integer, and ranges between the values of Euclidean geometry for a point and volume and varies from 0 to 3 [48]. Thus, the fine region of particles cannot be represented by a fractal dimension and this may be due to limitations of the laser diffraction (LD) technique used, as already mentioned in previous studies [66,67]. The validity of particle size measurements in the submicron range using light scattering systems is questionable, and thus the slope of the fine region of particle size distributions may be misleading.

Table 6. Fractal dimensions calculated with the use of simple linear model and piecewise linear regression.

Grinding Time (min)	Linear Regression		Piecewise Regression		
	D	R^2	D_1	D_2	R^2
15	2.58	0.957	−0.64	2.29	0.993
30	2.65	0.929	−1.33	2.32	0.989
45	2.68	0.911	−1.39	2.34	0.988
60	2.70	0.899	−1.45	2.37	0.989
90	2.73	0.879	−1.73	2.44	0.982
120	2.75	0.863	−1.92	2.49	0.980
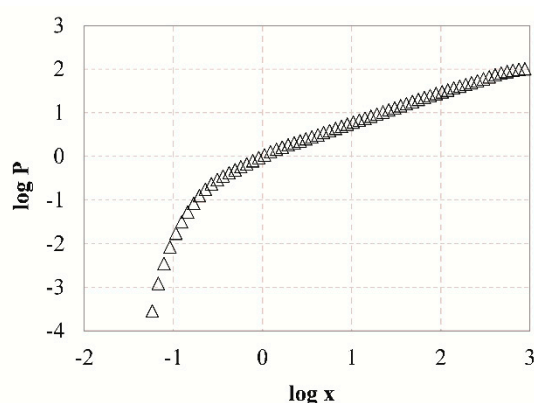
**Figure 8.** Log-log plot of particle size distribution of slag particles after 15 min of grinding.
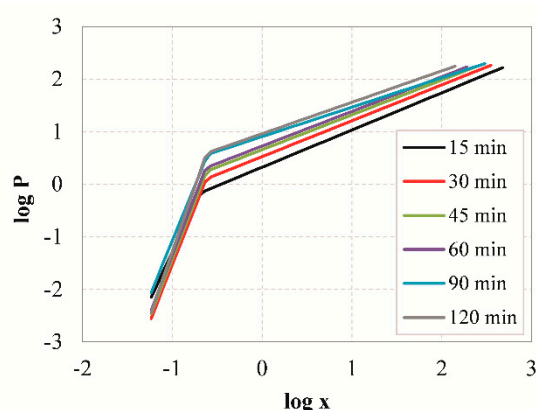
Figure 9. Log-log plots of particle size distributions of slag particles obtained after grinding for different times, using piecewise regression analysis.

4.5. Alkali-Activation of Slag

4.5.1. Effect of Slag Particle Size and Curing Temperature

In order to investigate the effect of slag particle size on the compressive strength of the produced AAMs, three different median sizes of slag particles were selected, namely 39.9, 23.4, and 11.9 μm, obtained after 30, 60, and 120 min of grinding, respectively. The equivalent particle sizes of slag products are presented in Table 4. The other AAM synthesis conditions were the H_2O/Na_2O molar ratio in the paste of 12.9, the curing period of 24 h and the ageing period of seven days. The setting time of the paste depends on the particle size of the slag product and ranges between 3 and 9 h for the different grinding products tested. It was observed that the paste consisting of finer particles requires much shorter setting time compared to the paste consisting of coarser particles. This is due to the fact that the finer particles have larger specific surface area and react faster with the activating solution [68]. Figure 10 shows the compressive strength of the AAMs produced as a function of particle size and curing temperature (60 or 80 °C).
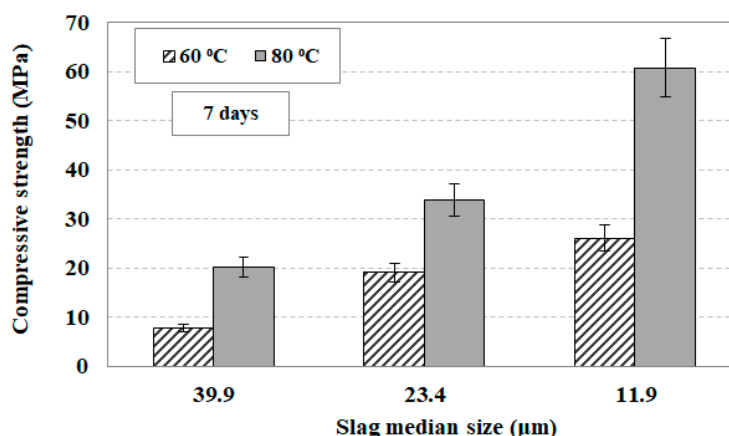
Figure 10. Effect of slag median size and curing temperature on the compressive strength of the produced alkali activated materials (AAMs). Synthesis conditions: molar ratio in the reactive paste H_2O/Na_2O 12.9, curing time 24 h, ageing period seven days; median sizes of 39.9, 23.4, 11.9 μm derived after 30, 60, and 120 min of grinding, respectively. Error bars indicate the standard deviation of three measurements.

It is seen from this data that at 60 °C when the median particle size of the slag grinding product decreases from 39.9 to 11.9 μm, and the compressive strength of the produced AAMs increases by 230%, from 7.9 to 26.2 MPa. On the other hand, when the curing temperature increases to 80 °C the

produced AAMs acquire much higher compressive strength which increases by 200%, from 20.2 MPa to 60.8 MPa, when the median particle size decreases from 39.9 to 11.9 µm. These results indicate that when the raw material is finer, and thus has larger surface area, the reactions with the activating solution proceed faster, and thus the produced AAMs are denser and stronger [69,70]. It is noted that the increase of ageing period from seven to 28 days increases the compressive strength slightly, but the results are not provided in this study.

Other selected properties of the produced AAMs, namely, apparent density (g/cm^3), porosity (%), and water absorption (%) when different slag particle sizes were used are presented in Table 7. This table also shows the compressive strength of the AAMs produced under the conditions: H_2O/Na_2O molar ratio in the reactive paste 12.9, curing temperature 80 °C, curing time 24 h, and ageing period seven days. It can be seen from this data that there is an evident difference in all properties when three median sizes of slag particles were used. The main difference was observed in porosity which decreased from 13.5 to 6.7% when the slag median size decreased from 39.9 to 11.9 µm, indicating that this property may have a significant effect on the compressive strength of the produced AAMs. A similar trend was observed for water absorption which decreased from 5.9 to 3.8% by taking into account the same median sizes. On the other hand, the apparent density of the AAMs increased from 2.28 g/cm^3 when slag with median size 39.9 µm was used to 2.54 g/cm^3 when the median size was 11.9 µm. It is mentioned that the shrinkage of AAMs after curing at 60 or 80 °C was negligible. The reactivity of different slag products, as denoted by the concentration of Al and Si in solution after 8 mole/L NaOH leaching, and the respective Si/Al ratios, is shown in Table 8. It is observed that when the slag median size decreases from 39.9 to 11.9 µm the concentration of Si and Al in solution increases from 216 to 550 mg/L and 57 to 101.5 mg/L, respectively. Thus, the Si/Al ratio also increases and reaches 5.4 when the median size of slag was 11.9 µm. These results justify the magnitude of the compressive strength values obtained.

Table 7. Selected properties of AAMs produced under the conditions 12.9 H_2O/Na_2O, curing temperature 80 °C, curing time 24 h, ageing period seven days.

| Slag Median Size	Compressive Strength	Apparent Density	Porosity	Water Absorption
µm	MPa	g/cm^3	%	%
39.9	20.2	2.28	13.5	5.9
23.4	33.8	2.37	10.6	4.5
11.9	60.8	2.54	6.7	3.8

Table 8. Concentration of Si and Al as well as Si/Al ratio in solution after leaching of slag with different particle size with NaOH.

Slag Median Size	Si	Al	Si/Al
µm	mg/L		
39.9	216.0	57.0	3.8
23.4	281.5	63.4	4.4
11.9	550.0	101.5	5.4

Figure 11 shows SEM-back-scattered electron (BSE) images of selected AAMs produced when different slag particle sizes were used, i.e., 39.9 µm, 23.4 µm, and 11.9 µm. Overall, significant differences in the microstructure and the associated EDS analyses were observed among the AAMs studied. More specifically, the AAMs produced using slag with median size of 39.9 µm, obtained after 30 min of grinding, exhibit heterogeneous structures consisting of elongated and large in size unreacted slag particles (mostly diaspore, quartz, hedenbergite, and fayalite, in accordance with XRD analyses) surrounded by a porous and spongy inorganic gel matrix formed during alkali-activation (Figure 11a). EDS analysis of the inorganic gel (P1) revealed the abundance of Ca, Al, Si, and Fe, as well as the

presence of Mg and Na in lower quantities (provided by the alkaline activators NaOH and Na_2SiO_3 as well as after partial solubilization of the raw slag). However, well-defined cracks and voids are seen in the microstructure of AAMs produced using slag with a median size of 39.9 µm due to incomplete gel formation, which probably explains the lower compressive strength obtained (20.2 MPa).
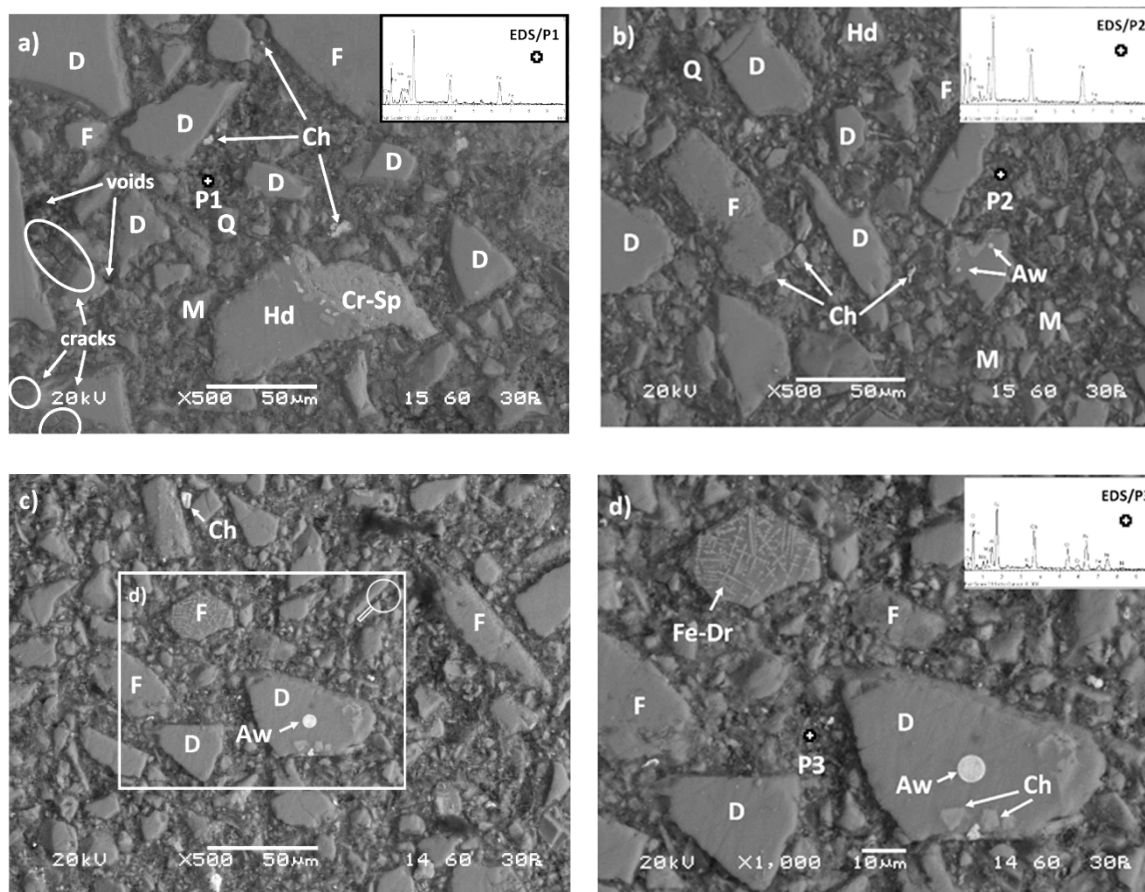
Figure 11. SEM-back-scattered electron (BSE) images of cross-sections of AAMs produced using slag particles with median size of (**a**) 39.9 µm, (**b**) 23.4 µm, and (**c,d**) 11.9 µm. The presence of unreacted compounds, crack propagation and void formation is seen in several spot locations. Q: Quartz (SiO_2), D: Diopside ($CaMgSi_2O_6$), M: Magnetite (Fe_3O_4), F: Fayalite (Fe_2SiO_4), Hd: Hedenbergite ($Ca(Fe,Mg)(SiO_3)_2$), Cr-Sp: Cr-Spinel, Fe-Dr: Ferrite dendrites, Ch: Chromite ($FeCr_2O_4$), Aw: Awaruite (Ni_3Fe).

On the other hand, after prolonged grinding of the slag and the production of finer particles, i.e., median size 23.4 µm and 11.9 µm, almost negligible crack propagation and a highly dense and uniform/homogeneous inorganic matrix can be observed along the cross-sectional interfaces of the produced AAMs (Figure 11b,c, respectively). This microstructure suggests the formation of strong bonds due to polymeric reactions that took place between the alumino–silicate particles of the raw slag and the alkaline activators. In this context, particles with rounded edges or deteriorated are visible, indicating excessive dissolution of the raw slag by the attack of the alkaline solution. It also appears that the presence of finer slag particles, enhanced the dissolution of calcium ions present in diopside and hedenbergite.

In both AAMs produced using material obtained after prolonged grinding times (60 min and 120 min), N-A-S-H and C-A-S-H gels coexist in the alkaline matrix and contribute to the formation of products with higher cohesion and strength [71,72]. As can be seen in Table 9, which shows the elemental composition and selected properties of AAMs, a greater conversion of the precursor material

(raw slag) to polymeric compounds is achieved in the prolonged grinding (median size 23.4 μm and 11.9 μm) compared to the AAMs produced from a slag median size of 39.9 μm due to the higher Ca/Si and Al/Si ratios present, as indicated by EDS analyses (P2 and P3, respectively). As a result, higher solubilization of Si and Al from the raw slag was attained that subsequently caused the formation of denser reaction products and the increase in compressive strength, up to 60.8 MPa. On the other hand, the lower content of Ca along with the higher Na content detected in AAMs produced when slag with median size of 39.9 μm was used, indicates that more N-A-S-H gel was formed, compared to C-A-S-H gel, and thus specimens with lower compressive strength was obtained (20.2 MPa). Finally, it is also interesting to mention that several other constituents were found in the alkaline matrix of the AAMs produced using slag particles with median size of 11.9 μm, such as Cr (up to 22%), and Ni (10%) due to dissolution of chromite ($FeCr_2O_4$) and awaruite (Ni_3F) particles, respectively. Figure 11d (zoom of rectangular area of Figure 11c) shows the presence of chromite and awaruite as small single intergrown drops and inclusions embedded in the clinopyroxene (diopside) matrix as well as the development of ferrite dendrites in the fayalite matrix [2,73].

Table 9. Elemental composition and selected properties of AAMs produced under the conditions H_2O/Na_2O ratio 12.9, curing temperature 80 °C, curing time 24 h, ageing period seven days.

Slag Median Size Used (μm)	Representative EDS Point	Ratios			Compressive Strength (MPa)
		Ca/Si	Al/Si	Na/Si	
39.9	P1	0.27	0.19	0.31	20.2
23.4	P2	0.51	0.32	0.19	33.8
11.9	P3	0.79	0.41	0.14	60.8

The AAMs produced using the same synthesis conditions were also characterized with XRD, as seen in Figure 12. The results indicate that the mineralogy of the AAMs produced using different slag median size have no significant differences. The specimens show a typical amorphous (broad hump between 20° and 40° 2θ) to semi-crystalline composition consisting of several crystalline phases, i.e., quartz (SiO_2), hedenbergite ($Ca(Fe,Mg)(SiO_3)_2$), fayalite (Fe_2SiO_4), diopside ($CaMgSi_2O_6$), magnetite (Fe_3O_4), and hatrurite (Ca_3SiO_5).
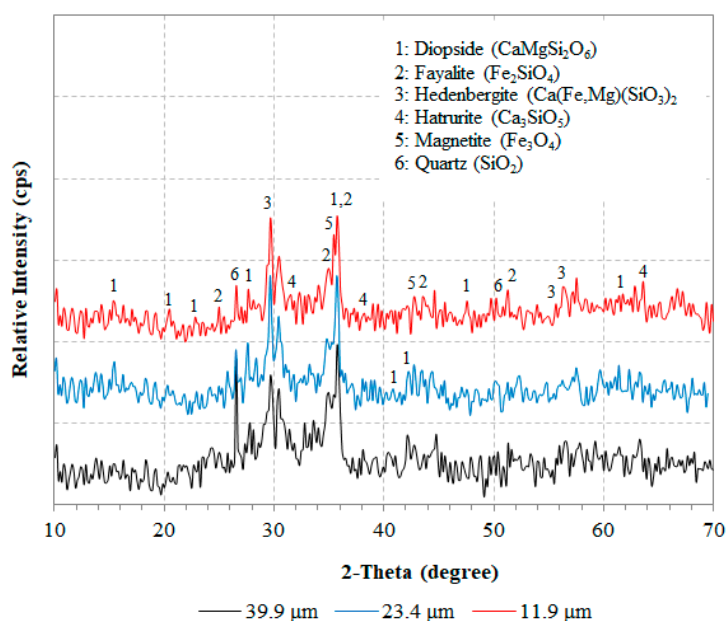
Figure 12. XRD patterns of produced AAMs when different median sizes of slag particles were used. Synthesis conditions were: molar ratio in the reactive paste H_2O/Na_2O 12.9, curing temperature 80 °C, curing time 24 h, ageing period seven days.

4.5.2. Prediction of the Compressive Strength of AAMs

Figure 13 shows the effect of d_{50} slag particle size and BET specific surface area (SSA) on the compressive strength (CS) of the AAMs produced under the conditions H_2O/Na_2O molar ratio 12.9, heating 80 °C, curing period 24 h, and ageing period seven days. Three different median sizes of slag were used, namely 39.9, 23.4 and 11.9 μm corresponding to raw material obtained after 30, 60, and 120 min of grinding, respectively. Table 4 shows the respective values of SSA of the slag grinding products. Simple regression analysis with the use of Excel software was carried out to establish potential correlations between CS and d_{50}, SSA and equations with the highest correlation coefficient R^2 were obtained. As seen in Figure 13, very strong correlation between CS and d_{50} is obtained using inverse exponential equation, while CS is correlated very well with SSA using linear equations. The experimental data were validated with the execution of additional experiments using as raw material slag with a median size 15.2 μm (90 min of slag grinding), and the results are given in Figure 13. The obtained equations are the following

$$CS = 660 \cdot d_{50}^{-0.95} \quad R^2 = 0.99 \tag{12}$$

$$CS = 0.04 \cdot SSA - 30 \quad R^2 = 0.99 \tag{13}$$

where CS, SSA, and d_{50} represent compressive strength (MPa), specific surface area (m^2/kg), and median size (μm), respectively.
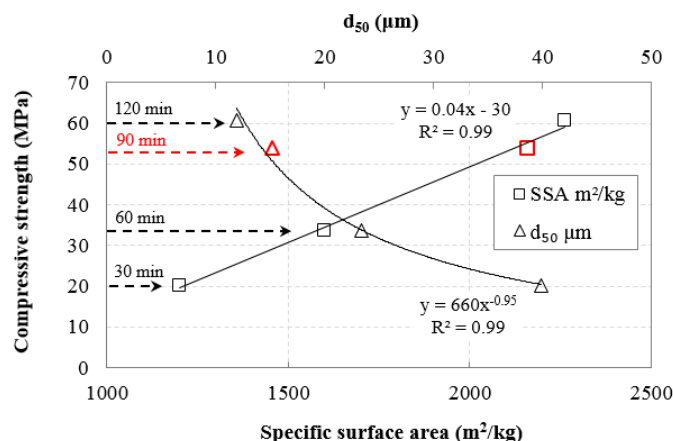
Figure 13. Correlations between compressive strength of AAMs produced and median size (d_{50}), BET specific surface area of slag.

5. Conclusions

The present experimental study studied the ball mill grinding kinetics of Polish slag in order to produce fractions that after alkali activation can be used for the production of AAMs with beneficial properties.

The results show that the particle size of slag products decreases with increasing grinding time, while particle agglomeration is not observed even after prolonged grinding (120 min). The equivalent particle sizes (EPSs) are very well correlated with grinding time, as derived through the use of inverse exponential functions. It is evident that the size reduction rate of particles is constantly decreasing and after prolonged grinding particle size can reach a constant value which is defined as the grinding limit. Among the different mathematical models used, i.e., Rosin–Rammler, Gates–Gaudin–Schuhmann, and Logistic distributions to simulate the particle size distribution, Rosin–Rammler was found to be the most suitable for the slag products. The piecewise regression analysis by the quasi-Newton nonlinear estimation method showed that the PSDs of slag products exhibit multifractal character. It is seen that

when piecewise regression analysis was applied to PSDs higher R^2 are obtained compared to single linear regression.

In addition, grinding of slag exhibits non-first-order behavior and the reduction rate of each size is time dependent. The deviation from the first order is more evident for the coarse particles indicating that these particles exhibit higher grinding efficiency than fine particles. Based on breakage rate constant *K* values, it is shown that grinding efficiency increases when the particle size increases, but drops sharply near zero after prolonged grinding.

The results also indicate that the compressive strength of the produced AAMs is significantly affected by the slag particle size used. The finer particles of the raw slag have larger surface areas and react faster with the activating solution, and thus the produced AAMs acquire higher compressive strength, the maximum value of which reached 60.8 MPa under the conditions slag median size 11.9 μm, H_2O/Na_2O 12.9 molar ratio, curing temperature 80 °C, curing period 24 h, and ageing period seven days. The results also indicate that the curing temperature is a crucial parameter during alkali activation, since higher temperatures accelerate activation reactions and thus AAMs with better mechanical properties are produced. The determination of selected properties of the produced AAMs revealed that porosity and water absorption decreased when the slag median size decreased, indicating that these properties have also an impact on the compressive strength. As expected, the apparent density (g/cm^3) showed an inverse trend. Finally, correlations between particle size/specific surface area of the raw material and compressive strength of the produced specimens were established.

Author Contributions: E.P. designed and performed the experiments, critically analyzed results and wrote the paper. V.K. carried out experiments and analytical techniques and analyzed data. G.B. carried out SEM analysis and reviewed the paper. K.K. critically reviewed the experimental design, the analysis of the results and wrote the paper.

Conflicts of Interest: The authors declare no conflict of interest.

References

1. Mo, L.; Zhang, F.; Deng, M.; Jin, F.; Al-Tabbaa, A.; Wang, A. Accelerated carbonation and performance of concrete made with steel slag as binding materials and aggregates. *Cem. Concr. Compos.* **2017**, *83*, 138–145. [CrossRef]

2. Komnitsas, K.; Bartzas, G.; Karmali, V.; Petrakis, E.; Kurylak, W.; Pietek, G.; Kanasiewicz, J. Assessment of alkali activation potential of a Polish ferronickel slag. *Sustainability* **2019**, *11*, 1863. [CrossRef]

3. Chen, C.; Habert, G.; Bouzidi, Y.; Jullien, A. Environmental impact of cement production: Detail of the different processes and cement plant variability evaluation. *J. Clean. Prod.* **2010**, *18*, 478–485. [CrossRef]

4. Ali, M.; Saidur, R.; Hossain, M. A review on emission analysis in cement industries. *Renew. Sustain. Energy Rev.* **2011**, *15*, 2252–2261. [CrossRef]

5. Maharaj, C.; White, D.; Maharaj, R.; Morin, C. Re-use of steel slag as an aggregate to asphaltic road pavement surface. *Cogent Eng.* **2017**, *4*, 1416889. [CrossRef]

6. Komnitsas, K. Potential of geopolymer technology towards green buildings and sustainable cities. *Procedia Eng.* **2011**, *21*, 1023–1032. [CrossRef]

7. Penpolcharoen, M. Utilization of secondary lead slag as construction material. *Cem. Concr. Res.* **2005**, *35*, 1050–1055. [CrossRef]

8. Komnitsas, K.; Zaharaki, D. Geopolymerisation: A review and prospects for the minerals industry. *Miner. Eng.* **2007**, *20*, 1261–1277. [CrossRef]

9. Komnitsas, K.; Zaharaki, D.; Perdikatsis, V. Geopolymerisation of low calcium ferronickel slag. *J. Mater. Sci.* **2007**, *42*, 3073–3082. [CrossRef]

10. Shi, C.; Meyer, C.; Behnood, A. Utilization of copper slag in cement and concrete. *Resour. Conserv. Recycl.* **2008**, *52*, 1115–1120. [CrossRef]

11. Komnitsas, K.; Zaharaki, D.; Perdikatsis, V. Effect of synthesis parameters on the compressive strength of low-calcium ferronickel slag inorganic polymers. *J. Hazard. Mater.* **2009**, *161*, 760–768. [CrossRef] [PubMed]

12. Mehta, A.; Siddique, R. Sustainable geopolymer concrete using ground granulated blast furnace slag and rice husk ash: Strength and permeability properties. *J. Clean. Prod.* **2018**, *205*, 49–57. [CrossRef]

13. Xu, H.; Van Deventer, J.S.J. The geopolymerisation of alumino-silicate minerals. *Int. J. Miner. Process.* **2000**, *59*, 247–266. [CrossRef]

14. Zaharaki, D.; Komnitsas, K.; Perdikatsis, V. Use of analytical techniques for identification of inorganic polymer gel composition. *J. Mater. Sci.* **2010**, *45*, 2715–2724. [CrossRef]

15. Perera, D.S.; Cashion, J.D.; Blackford, M.G.; Zhang, Z.; Vance, E.R. Fe speciation in geopolymers with Si/Al molar ratio of ∼2. *J. Eur. Ceram. Soc.* **2007**, *27*, 2697–2703. [CrossRef]

16. Zaharaki, D.; Galetakis, M.; Komnitsas, K. Valorization of construction and demolition (C&D) and industrial wastes through alkali activation. *Constr. Build. Mater.* **2016**, *121*, 686–693.

17. Arnold, M.C.; de Vargas, A.S.; Bianchini, L. Study of electric-arc furnace dust (EAFD) in fly ash and rice husk ash-based geopolymers. *Adv. Powder Technol.* **2017**, *28*, 2023–2034. [CrossRef]

18. Peys, A.; White, C.E.; Rahier, H.; Blanpain, B.; Pontikes, Y. Alkali-activation of $CaO-FeOx-SiO_2$ slag. Formation mechanism from in-situ X-ray total scattering. *Cem. Concr. Res.* **2019**, *122*, 179–188. [CrossRef]

19. Komnitsas, K.; Zaharaki, D.; Bartzas, G. Effect of sulphate and nitrate anions on heavy metal immobilisation in ferronickel slag geopolymers. *Appl. Clay Sci.* **2013**, *73*, 103–109. [CrossRef]

20. Alshaaer, M.; Zaharaki, D.; Komnitsas, K. Microstructural characteristics and adsorption potential of zeolitic tuff—Metakaolin geopolymers. *Desalin. Water Treat.* **2015**, *56*, 338–345. [CrossRef]

21. Djordjevic, N. Improvement of energy efficiency of rock comminution through reduction of thermal losses. *Miner. Eng.* **2010**, *23*, 1237–1244. [CrossRef]

22. Petrakis, E.; Stamboliadis, E.; Komnitsas, K. Identification of optimal mill operating parameters during grinding of quartz with the use of population balance modelling. *KONA Powder Part. J.* **2017**, *34*, 213–223. [CrossRef]

23. Herbst, J.A.; Fuerstenau, D.W. Scale-up procedure for continuous grinding mill design using population balance models. *Int. J. Miner. Process.* **1980**, *7*, 1–31. [CrossRef]

24. Austin, L.G.; Klimpel, R.R.; Luckie, P.T. *Process Engineering of Size Reduction: Ball Milling*; SME–AIME: New York, NY, USA, 1984.

25. Ipek, H.; Göktepe, F. Determination of grindability characteristics of zeolite. *Physicochem. Probl. Miner. Process.* **2011**, *47*, 183–192.

26. Gupta, V.K.; Sharma, S. Analysis of ball mill grinding operation using mill power specific kinetic parameters. *Adv. Powder Technol.* **2014**, *25*, 625–634. [CrossRef]

27. Katubilwa, F.M.; Moys, M.H. Effect of ball size distribution on milling rate. *Miner. Eng.* **2009**, *22*, 1283–1288. [CrossRef]

28. Deniz, V. The effects of ball filling and ball diameter on kinetic breakage parameters of barite powder. *Adv. Powder Technol.* **2012**, *23*, 640–646. [CrossRef]

29. Olejnik, T.P. Selected mineral materials grinding rate and its effect on product granulometric composition. *Physicochem. Probl. Miner. Process.* **2013**, *49*, 407–418.

30. Shin, H.; Lee, S.; Jung, H.S.; Kim, J.-B. Effect of ball size and powder loading on the milling efficiency of a laboratory-scale wet ball mill. *Ceram. Int.* **2013**, *39*, 8963–8968. [CrossRef]

31. Petrakis, E.; Komnitsas, K. Correlation between material properties and breakage rate parameters determined from grinding tests. *Appl. Sci.* **2018**, *8*, 220. [CrossRef]

32. Mulenga, F.K.; Gharehgheshlagh, H.H.; Chehreghani, S. Assessing the dependency of selection function parameters with batch mill design. *Adv. Powder Technol.* **2019**, *30*, 242–251. [CrossRef]

33. Gupta, V.K. An appraisal of the energy-size reduction relationships for mill scale-up design. *Adv. Powder Technol.* **2019**, *30*, 73–84. [CrossRef]

34. Rajamani, R.K.; Guo, D. Acceleration and deceleration of breakage rates in wet ball mills. *Int. J. Miner. Process.* **1992**, *34*, 103–118. [CrossRef]

35. Bilgili, E.; Scarlett, B. Population balance modeling of non-linear effects in milling processes. *Powder Technol.* **2005**, *153*, 59–71. [CrossRef]

36. Barani, K.; Balochi, H. First-order and second-order breakage rate of coarse particles in ball mill grinding. *Physicochem. Probl. Miner. Process.* **2016**, *52*, 268–278.

37. Harris, C.C. The Alyavdin-Weibull Plot of Grinding Data and the Order of Kinetics. *Powder Technol.* **1973**, *7*, 123–127. [CrossRef]

38. Beke, B. *Process of Fine Grinding*; Dr. W. Junk Publications: The Hague, The Netherlands, 1981.

39. King, R.P. *Modeling and Simulation of Mineral Processing Systems*; Butterworth-Heinemann: Oxford, UK, 2001; p. 416.

40. Allen, T. *Powder Sampling and Particle Size Determination*; Elsevier: Amsterdam, The Netherlands, 2003; p. 682.

41. Millán, H.; González-Posada, M.; Aguilar, M.; Domínguez, J.; Céspedes, L. On the fractal scaling of soil data. Particle-size distributions. *Geoderma* **2003**, *117*, 117–128. [CrossRef]

42. Zhong, W.; Yue, F.; Ciancio, A. Fractal behavior of particle size distribution in the rare earth tailings crushing process under high stress condition. *Appl. Sci.* **2018**, *8*, 1058. [CrossRef]

43. Menéndez-Aguado, J.M.; Peña-Carpio, E.; Sierra, C. Particle size distribution fitting of surface detrital sediment using the Swrebec function. *J. Soils Sediments* **2015**, *15*, 2004–2011. [CrossRef]

44. Osorio, A.M.; Menéndez-Aguado, J.M.; Bustamante, O.; Restrepo, G.M. Fine grinding size distribution analysis using the Swrebec function. *Powder Technol.* **2014**, *258*, 206–208. [CrossRef]

45. Taşdemir, A.; Taşdemir, T. A comparative study on PSD models for chromite ores comminuted by different devices. *Part. Part. Syst. Charact.* **2009**, *26*, 69–79. [CrossRef]

46. Lu, P.; Jefferson, I.F.; Rosenbaum, M.S.; Smalley, I.J. Fractal characteristics of loess formation: Evidence from laboratory experiments. *Eng. Geol.* **2003**, *69*, 287–293. [CrossRef]

47. Turcotte, D.L. Fractals and fragmentation. *J. Geophys. Res.* **1986**, *91*, 1921–1926. [CrossRef]

48. Taşdemir, A. Fractal evaluation of particle size distributions of chromites in different comminution environments. *Miner. Eng.* **2009**, *22*, 156–167. [CrossRef]

49. Petrakis, E.; Stamboliadis, E.; Komnitsas, K. Evaluation of the relationship between energy input and particle size distribution in comminution with the use of piecewise regression analysis. *Part. Sci. Technol.* **2017**, *35*, 479–489. [CrossRef]

50. Kierczak, J.; Neel, C.; Puziewicz, J.; Bril, H. The Mineralogy and weathering of slag produced by the smelting of lateritic Ni ores, Szklary, Southwestern Poland. *Can. Miner.* **2009**, *47*, 557–572. [CrossRef]

51. Ferraris, C.; Garboczi, E.J. Identifying improved standardized tests for measuring cement particle size and surface area. *Transport. Res. Rec.* **2013**, *2342*, 10–16. [CrossRef]

52. De Boer, G.B.J.; de Weerd, C.; Thoenes, D.; Goossens, H.W.J. Laser diffraction spectrometry: Fraunhofer diffraction versus Mie scattering. *Part. Part. Syst. Charact.* **1987**, *4*, 138–146. [CrossRef]

53. Xu, R. *Particle Characterization: Light Scattering Methods*; Kluwer Academic: Dordrecht, The Netherlands, 2002.

54. Kuila, U.; Prasad, M. Specific surface area and pore-size distribution in clays and shales. *Geophys. Prospect.* **2012**, *61*, 341–362. [CrossRef]

55. British Standards Institute. *BS EN 1936: Natural Stone Test Methods. Determination of Real Density and Apparent Density and of Total and Open Porosity*; NP EN 1936:2006; BSI: London, UK, 2007.

56. Kaya, E.; Hogg, R.; Kumar, S.R. Particle shape modification in comminution. *KONA Powder Part. J.* **2002**, *20*, 188–195. [CrossRef]

57. Hogg, R.; Turek, M.L.; Kaya, E. The Role of Particle Shape in Size Analysis and the Evaluation of Comminution Processes. *Part. Sci. Technol.* **2004**, *22*, 355–366. [CrossRef]

58. Petrakis, E.; Komnitsas, K. Effect of energy input in a ball mill on dimensional properties of grinding products. *Min. Metall. Explor.* **2019**, *36*, 803–816. [CrossRef]

59. Bailon-Poujol, I.; Bailon, J.-P.; L'Espérance, G. Ball-mill grinding kinetics of master alloys for steel powder metallurgy applications. *Powder Technol.* **2011**, *210*, 267–272. [CrossRef]

60. Zhao, J.; Wang, D.; Yan, P.; Li, W. Comparison of grinding characteristics of converter steel slag with and without pretreatment and grinding aids. *Appl. Sci.* **2016**, *6*, 237. [CrossRef]

61. Austin, L.G.; Bagga, P. An analysis of fine dry grinding in ball mills. *Powder Technol.* **1981**, *28*, 83–90. [CrossRef]

62. Fuerstenau, D.W.; Phatak, P.B.; Kapur, P.C.; Abouzeid, A.-Z.M. Simulation of the grinding of coarse/fine (heterogeneous) systems in a ball mill. *Int. J. Miner. Process.* **2011**, *99*, 32–38. [CrossRef]

63. Knieke, C.; Sommer, M.; Peukert, W. Identifying the apparent and true grinding limit. *Powder Technol.* **2009**, *195*, 25–30. [CrossRef]

64. Carpinteri, A.; Pugno, N. A fractal comminution approach to evaluate the drilling energy dissipation. *Int. J. Numer. Anal. Methods Geomech.* **2002**, *26*, 499–513. [CrossRef]

65. Mandelbrot, B.B. *The Fractal Geometry of Nature*; Freeman: New York, NY, USA, 1982.

66. Austin, L.G.; Yekeler, M.; Dumm, T.F.; Hogg, R. The kinetics and shape factors of ultrafine dry grinding in a laboratory tumbling ball mill. *Part. Part. Syst. Charact.* **1990**, *7*, 242–247. [CrossRef]

67. Hogg, R. Issues in particle size analysis. *KONA Powder Part. J.* **2008**, *26*, 81–93. [CrossRef]

68. Traven, K.; Češnovar, M.; Ducman, V. Particle size manipulation as an influential parameter in the development of mechanical properties in electric arc furnace slag-based AAM. *Ceram. Int.* **2019**, *45*, 22632–22641. [CrossRef]

69. Heah, C.Y.; Kamarudin, H.; Mustafa, A.L.; Bakri, A.M.; Binhussain, M.; Luqman, M.; Khairul Nizar, I.; Ruzaidi, C.M.; Liew, Y.M. Effect of Curing Profile on Kaolin-based Geopolymers. *Phys. Procedia* **2011**, *22*, 305–311. [CrossRef]

70. Yahya, Z.; Abdullah, M.M.A.B.; Hussin, K.; Ismail, K.N.; Razak, R.A.; Sandu, A.V. Effect of Solids-To-Liquids, Na_2SiO_3-To-NaOH and Curing Temperature on the Palm Oil Boiler Ash (Si+Ca) Geopolymerisation System. *Materials* **2015**, *8*, 2227–2242. [CrossRef]

71. Yip, C.K.; Lukey, G.C.; Van Deventer, J.S.J. Coexistence of geopolymeric gel and calcium silicate hydrate at the early stage of alkali activation. *Cem. Concr. Res.* **2005**, *35*, 1688–1697. [CrossRef]

72. Peng, H.; Cui, C.; Liu, Z.; Cai, C.S.; Liu, Y. Synthesis and reaction mechanism of an alkali-activated metakaolin-slag composite system at room temperature. *J. Mater. Civ. Eng.* **2019**, *31*, 04018345. [CrossRef]

73. Parbhakar-Fox, A.; Gilmour, S.; Fox, N.; Olin, P. Geometallurgical Characterization of Non-Ferrous Historical Slag in Western Tasmania: Identifying Reprocessing Options. *Minerals* **2019**, *9*, 415. [CrossRef]

Factors affecting co-valorization of fayalitic and ferronickel slags for the production of alkali activated materials

Konstantinos Komnitsas [a,*], Lourdes Yurramendi [b], Georgios Bartzas [c], Vasiliki Karmali [a], Evangelos Petrakis [a]

[a] Technical University of Crete, School of Mineral Resources Engineering, University Campus, Kounoupidiana, 73100 Chania, Greece
[b] Tecnalia, Energy and Environment Division, Mikeletegi Pasealekua 2, E-20009 San Sebastián, Spain
[c] National Technical University of Athens, School of Mining and Metallurgical Engineering, 9 Heroon Polytechniou str., 157 80 Zografos, Athens, Greece

HIGHLIGHTS

- Alkali-activated materials (AAMs) were produced using three metallurgical slags.
- Use of fayalitic slag (FS), after plasma treatment (FSP) and ferronickel slag (LS)
- Mechanical properties of AMMs were improved when FS and FSP were mixed with LS.
- AMMs from slag mixtures maintained very good structural integrity after firing.
- Alkali activation is a viable option for the co-valorization of different slags.

GRAPHICAL ABSTRACT
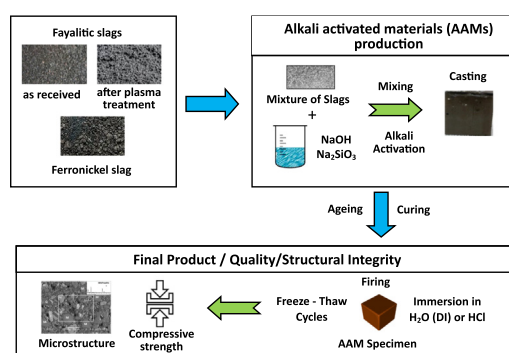
ARTICLE INFO

ABSTRACT

The first objective of this experimental study is the assessment of the alkali activation potential of two types of fayalitic slags, an as-received one (FS) and the one obtained after plasma treatment (FSP) of the initial FS, for the production of alkali activated materials (AAMs). Furthermore, the second objective is the elucidation of the co-valorization potential of FS and FSP slags when mixed with ferronickel (FeNi) slag (LS). The alkaline activating solution used was a mixture of sodium hydroxide (NaOH) and sodium silicate (Na_2SiO_3). The effect of various operating parameters, such as H_2O/Na_2O and SiO_2/Na_2O ratios present in the activating solution, curing temperature, curing period and ageing period on the compressive strength, density, water adsorption, porosity and toxicity of the produced AAMs was explored. The structural integrity of selected AAMs was investigated after firing specimens for 6 h at temperature up to 500 °C, immersion in distilled water and acidic solution or subjection to freeze-thaw cycles for a period of 7 or 30 days. The results of this study show that FS- and FSP-based AAMs acquire compressive strength of 44.8 MPa and 27.2 MPa, respectively. When FS and FSP were mixed with LS at 50:50%wt ratios the compressive strength of the produced specimens increased to 64.3 MPa and 45.8 MPa, respectively. Furthermore, selected AAMs produced after co-valorisation of slags retained sufficient compressive strength after firing at 500 °C, 45–68 MPa, and exhibited very low toxicity. These findings prove the alkali activation potential of fayalitic slags as well as their co-valorization with ferronickel slag for the production of AAMs, an approach which is in line with the principles of zero-waste and circular economy.

© 2020 Elsevier B.V. All rights reserved.

---

* Corresponding author.
E-mail address: komni@mred.tuc.gr (K. Komnitsas).

1. Introduction

The metallurgical industry produces worldwide large quantities of various types of slags that are mainly used in construction applications. Some slags may contain hazardous compounds and their direct use, or uncontrolled disposal, may cause environmental impacts (Agnello et al., 2018; Gee et al., 1997; Muñoz et al., 2018). On the other hand, it has to be underlined that several slags possess beneficial physical and chemical properties and thus their valorization, following the principles of zero waste and circular economy, results in environmental benefits and improves the sustainability of the metallurgical and construction sectors (Bartzas and Komnitsas, 2015; Liu et al., 2019; Mastali et al., 2020; Pasetto et al., 2017; Ouellet-Plamondon and Habert, 2014). Regarding the Portland cement industry, it is mentioned that the adoption of low-carbon binders, namely alkali-activated, carbonate, and belite-ye'elimite-based binders, will play a key role in reducing its carbon footprint (Shi et al., 2019).

Alkali activation is considered a feasible approach and has received great interest over the last 30 years for the valorization of various industrial wastes and the production of materials with amorphous or partially crystalline structure, beneficial physico-chemical properties and higher added value (Davidovits, 1991; Komnitsas et al., 2019a; Kriven et al., 2003; Krivenko and Kovalchuk, 2007; Xu and Van Deventer, 2000). However, it has to be mentioned that alkali activated cement based binders may exhibit some shortcomings that need to be clearly addressed before they effectively compete against Portland cement; these shortcomings mainly include production cost, CO_2 emissions and reduced durability due to efflorescence formation, alkali silica reaction and corrosion of reinforced steel (Pacheco-Torgal et al., 2017).

The use of alkali activated materials (AAMs), termed as inorganic polymers or geopolymers, contributes to considerable savings of virgin raw materials and a noticeable reduction of the environmental footprint of various industrial sectors (Duxson et al., 2007; Habert et al., 2011; Komnitsas and Zaharaki, 2007; Komnitsas, 2011; Komnitsas et al., 2019b; Palomo et al., 2014; Passuello et al., 2017). Recent studies on AAMs and various binders also explore their beneficial use in water and wastewater treatment (Alshaaer et al., 2015; Bumanis et al., 2019; Luukkonen et al., 2019), as well as in solidification/stabilization of contaminated sediments and municipal solid waste incinerator fly ash (Chen et al., 2019; Komnitsas, 2016; Wang et al., 2019). Successful alkali activation requires the use of aluminosilicate raw materials, strong alkaline solutions such as NaOH and KOH and a silicate solution such as Na_2SiO_3 that is usually added to balance the Si/Al ratio in the reactive paste, which after curing for a few hours at rather mild temperatures (30–90 °C) enables the formation of a matrix with beneficial properties (Bernal et al., 2010; Duxson and Provis, 2008; Khale and Chaudhary, 2007; Peys et al., 2019a; Yip et al., 2005).

During the last years, alkali activation of various types of slags has been widely studied and the results of efforts on upcycling these slags to produce sustainable cementitious binders have been reported in literature. The produced AAMs have various properties depending on the mineralogy and chemistry of the raw slags, the particle size, the synthesis conditions, the silicate modulus in the activating solution and the type of additives used to improve the properties of the produced matrix (Huang et al., 2017; Kaze et al., 2018; Petrakis et al., 2019; Traven et al., 2019; Tchadjie and Ekolu, 2018; Yan et al., 2017). In other studies, mixtures of slags with other waste types including fly ash from power stations, bauxite residues, construction and demolition wastes as well as aluminosilicate minerals such as kaolin or metakaolin in order to regulate the mineralogy of the raw materials have been successfully alkali activated (Furlani et al., 2018; Marjanović et al., 2015; Onisei et al., 2012; Pontikes et al., 2013; Provis and Bernal, 2014).

The ultimate objective of this study is the co-valorization of metallurgical slags with different mineralogy and the optimization of alkali activation conditions for the production of AAMs with beneficial properties.

2. Materials and methods

2.1. Materials

The raw materials used in this study were two types of slags, namely a fayalitic slag (FS) produced after pyrometallurgical treatment of copper concentrates in flash smelting furnace in Finland for the production of copper cathodes, copper sulphate and various metal concentrates (Saari et al., 2019) and a slag produced after plasma treatment (FSP) of the previous FS. The plasma treatment was carried out at Tecnalia, Spain, in a pilot plant furnace at 1650 °C with the use of coke as reducing agent and calcium hydroxide as flux. It is mentioned that apart from slag, two more materials were produced, a Zn-rich fly ash and an Fe-rich metallic fraction, which are both marketable products according to their composition (Fig. 1). In addition, in order to investigate the co-valorization potential of different slags for the production of AAMs, a third slag (LS) produced at Larco S.A, in Greece, after pyrometallurgical treatment of nickel laterites in electric-arc furnace for the production of ferronickel (FeNi) was used (Komnitsas et al., 2007).

Prior to use, all slags were pulverized using a Bico type pulverizer (Type UA, Fritsch, Dresden, Germany) and the particle size distribution was obtained with the use of a laser particle size analyzer (Mastersizer S, Malvern Instruments, Malvern, UK). The chemical analysis of the slags was carried out using a Bruker-AXS S2 Range Spectroscopic Fluorescence Spectrometer A (XRF-EDS, Bruker, Karlsruhe, Germany). The particle size distribution and chemical composition in the form of oxides of the three slags are presented in Tables 1 and 2, respectively.

It is observed from Table 1 that the 90% passing size (d_{90}) of all slags is less than 50 μm, which is considered adequately fine for efficient alkali activation and the production of AAMs, as indicated in previous studies (Komnitsas et al., 2015).

All slags contain sufficient amounts of SiO_2 and Al_2O_3 for alkali activation, while their F_2O_3 content is also high (Van De Sande et al., 2020). It is also observed that the CaO content in FSP and LS slags is higher compared to FS slag (Table 2).

2.2. Synthesis of AAMs

The alkali activating solution used for the synthesis of AAMs was a mixture of sodium hydroxide (NaOH, Sigma Aldrich) and sodium silicate (7.5–8.5 wt% NaOH and 25.5–28.5 wt% SiO_2, Merck). The sodium hydroxide solution was produced by dissolving anhydrous pellets of
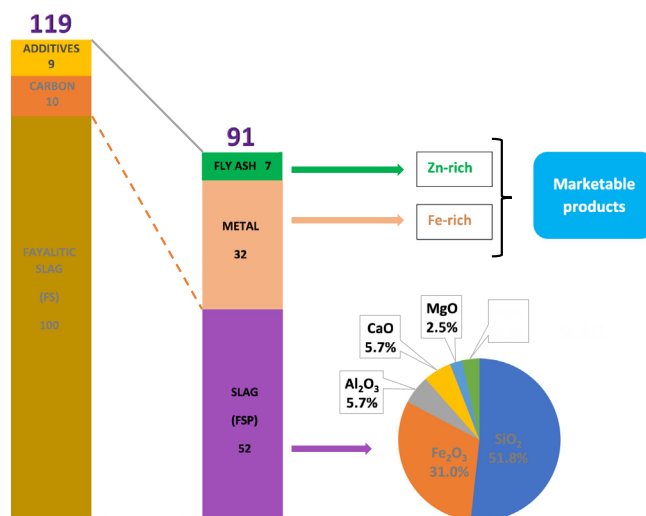
Fig. 1. Plasma treatment of FS slag for the production of FSP slag (and two other marketable products), carried out at Tecnalia, Spain (the main chemical composition of FSP slag is also indicated).

Table 1
Particle size distribution of the three slags.

Particle size (μm)	FS	FSP	LS
d_{90}	48.6	41.3	45.7
d_{50}	9.0	5.7	8.9

NaOH in distilled water so that solutions with different molarity (6–10 mol L^{-1}, M) were obtained.

The raw materials were mixed with the activating solution under continuous stirring in a laboratory mixer for about 15 min in order to produce a homogeneous paste. Then, the fresh paste was casted in metallic cubic molds (5 cm edge) which were vibrated for a few minutes to remove air. Pre-curing of the reactive paste was carried out at room temperature for 6 h until sufficient hardening was enabled. Then, the produced specimens were sealed in plastic bags to avoid moisture loss and placed in a laboratory oven (Jeio Tech ON-02G, Seoul, Korea) for curing at 40, 60 or 90 °C for 24 h. After curing the specimens were removed from the oven, allowed to cool at room temperature (~20 °C), demoulded and left for ageing for a period of 7 and 28 days. All tests were carried out in triplicate. The AAM codes, the mixing ratios for all materials used as well as the H$_2$O/Na$_2$O and SiO$_2$/Na$_2$O ratios in the activating solution are presented in Table 3.

The thermal response of selected AAMs was assessed after firing them at 250, 350 and 500 °C in a laboratory furnace (N – 8 L Selecta) for 6 h. Also, the structural integrity of selected AAMs was evaluated by immersing them in various solutions, namely distilled water and acidic solution (1 M HCl) for 7 and 30 days or subjecting them to freeze-thaw cycles using −18 ± 5 °C for 4 h and room temperature (20 ± 0.5 °C) for 12 h as temperature extremes over a period of 7 and 28 days (Standard C1262–10) (ASTM, 2018). Finally, the compressive strength as well as selected physical properties (i.e. porosity, water absorption and apparent density) of selected specimens after each treatment were determined.

2.3. Characterization of slags and AAMs

The reactivity of slags was evaluated through leaching tests carried out in 250 mL conical flasks under continuous stirring; 1.0 g of ground solids was added in 100 mL of 8 M NaOH solution and leaching was carried out for 24 h at room temperature (~20 °C). After leaching solid and liquid separation was done using 0.45 μm pore size membrane filters (PTFE, Chromafil). The concentration of Al and Si in solution was determined using an Inductively Coupled Plasma Mass Spectrometry (ICP MS, Agilent 7500 cx) equipped with an Agilent ASX-500 Autosampler.

The chemical analysis of raw materials and the produced AAMs was determined using a Bruker S2 Ranger – energy dispersive X-ray

Table 2
Chemical composition (wt%) of slags.

Oxide	FS	FSP	LS
Na$_2$O	0.5	0.6	–
Fe$_2$O$_3$	57.6	31.0	43.8
SiO$_2$	30.1	51.8	32.7
Al$_2$O$_3$	2.8	5.7	8.3
Cr$_2$O$_3$	0.06	0.40	3.1
MgO	1.3	2.5	2.8
CaO	1.0	5.7	3.7
NiO	0.2	–	–
K$_2$O	0.9	1.2	–
TiO$_2$	0.2	0.3	–
MnO	0.06	0.1	0.4
SO$_3$	0.4	0.5	0.2
ZnO	2.8	0.03	–
Total	97.9	99.8	95.0

Table 3
Test details and selected molar oxides in the activating solution.

AAM Code	NaOH (M)	Slag (wt %)	NaOH (wt %)	H$_2$O (wt %)	Na$_2$SiO$_3$ (wt%)	L/S ratio	H$_2$O/Na$_2$O	SiO$_2$/Na$_2$O
FS2	8	81.0	2.4	7.1	9.5	0.20	17.4	1.0
FS3	10	76.2	3.6	8.3	12.0	0.25	14.8	1.0
FS4	6	83.7	1.3	5.2	9.8	0.18	22.5	1.5
FS5	6	85.7	1.9	7.7	4.8	0.14	20.2	0.7
FSP1	6	82.7	2.6	10.4	4.3	0.17	19.5	0.4
FSP2	8	81.1	3.6	10.6	4.7	0.18	14.9	0.4
FSP3	10	80.3	4.5	10.2	4.9	0.18	11.9	0.4
FSP4	10	82.4	2.7	6.1	8.8	0.17	14.6	0.9
FSP5	10	81.4	3.6	8.1	7.0	0.18	13.1	0.6
LS	8	83.2	2.1	6.3	8.4	0.17	17.4	1.0
FS10LS90	8	83.5	2.1	6.2	8.2	0.17	17.4	1.0
FS30LS70	8	82.6	2.2	6.5	8.7	0.18	17.4	1.0
FS40LS60	8	81.9	2.3	6.8	9.0	0.19	17.4	1.0
FS50LS50	8	81.1	2.4	7.1	9.4	0.20	17.4	1.0
FSP10LS90	10	86.7	2.0	4.6	6.7	0.13	14.6	0.9
FSP30LS70	10	82.4	2.7	6.2	8.7	0.18	14.6	0.9
FSP40LS60	10	79.0	3.2	7.3	10.5	0.22	14.6	0.9
FSP50LS50	10	75.0	3.8	8.7	12.47	0.27	14.6	0.9

fluorescence spectrometer (ED-XRF, Bruker, Karlsruhe, Germany), while their mineralogical analysis was performed using an X-ray diffractometer with a Cu tube and scanning range from 4° to 70° 2theta (θ), with a step of 0.02°, and 0.2 s/step measuring time (D8-Advance type, Bruker AXS, Karlsruhe, Germany). Data were then qualitatively analyzed with the DiffracPlus Software (EVA v. 2006, Bruker, Karlsruhe, Germany) using the PDF database. Fourier transform infrared (FTIR) spectroscopy was carried out for the wavenumber range 400 to 4000 cm^{-1}, using a Perkin Elmer Spectrum 1000 spectrometer (Perkin Elmer, Akron, OH, USA), Pellets produced after mixing a pulverized sample of each specimen with KBr at a ratio of 1:100 w/w. The tests were carried out at atmospheric pressure under nitrogen atmosphere, with a flow rate of 100 mL min^{-1} and a heating rate of 10 °C min^{-1}. The morphology of the AAMs was assessed by Scanning electron microscopy (SEM) using a JEOL-6380LV scanning microscope (JEOL ltd., Tokyo, Japan) with an Oxford INCA Energy dispersive spectroscopy (EDS) micro analysis system (Oxford Instruments, Abingdon, UK). The compressive strength of the produced AAMs was determined using a MATEST C123N load frame (compression and flexural machine, Matest S.p.A, Treviolo, Bergamo, Italy). The other properties, namely apparent density, porosity and water absorption, of selected AAMs were determined according to the standard BS EN 1936 (BSI, 2007).

3. Results and discussions

3.1. Characterization of slags

The reactivity of slags which indicates their alkali activation potential was assessed after leaching with an 8 mol L^{-1} NaOH solution. Table 4 shows the concentration of Al and Si in the final solution derived after solid: liquid separation, as well as the respective Si/Al ratios. It is seen from this data that LS exhibits the highest reactivity, as indicated by the concentration of Si and Al in the leaching solution, which is 332.5 and 99.1 mg L^{-1}, respectively. The high reactivity of ferronickel slag has been also shown in earlier studies (Zaharaki and Komnitsas,

Table 4
Concentration of Si, Al and Si/Al ratios in solution after leaching[a].

Raw material	Si (mg L^{-1})	Al (mg L^{-1})	Si/Al
FS	139.5	14.5	9.6
FSP	100.0	23.9	4.2
LS	332.5	99.1	3.4

[a] Leaching with 8 mol L^{-1} NaOH solution for 24 h.

2009). The two fayalitic slags, namely FS and FSP, exhibit lower reactivity since the concentrations of Si and especially Al are much lower, compared to the respective concentrations obtained after leaching of the LS slag; however, their reactivity is considered sufficient for alkali activation. Based on this data, the Si/Al ratios in solution are 9.6, 4.2 and 3.4 for FS, FSP and LS, respectively.

The XRD patterns of all slags are presented in Fig. 2. Magnetite (Fe_3O_4) and fayalite (Fe_2SiO_4) were the main phases detected in FS, while clinoferrosilite ($FeSiO_3$) was mainly detected in FSP (the detected graphite (Gr) corresponds to traces of residual carbon from the addition made in the pilot for the carbo-reduction plasma reaction). The main mineralogical phases present in LS were magnetite (Fe_3O_4), quartz (SiO_2), anorthite ($CaAl_2Si_2O_8$), chromite ($FeCr_2O_4$), cristobalite (SiO_2), forsterite (Mg_2SiO_4), fayalite (Fe_2SiO_4) and tridymite (SiO_2). It is also mentioned that LS has high amorphous content (~50%) denoted by the broad hump shown between 2θ 25–40⁰, as also indicated in previous studies (Komnitsas et al., 2009; Zaharaki et al., 2010).

The FTIR spectra of slags FS, LS and FSP are presented in Fig. 3. Regarding FS, the rocking band at 457 cm^{-1} is characteristic of fayalitic slags and corresponds to in plane Si – O bending and Al – O linkages as well as bending Si – O– Si and O – Si – O vibrations (Komnitsas et al., 2013; Komnitsas et al., 2015; Yip et al., 2008). An additional peak associated with the stretching vibrations of T-O-T (T = Si, or Al) bonds is also seen at 575 cm^{-1}, while the bands at 689 cm^{-1} and 876 cm^{-1} are attributed to the bending modes of CO_3^{-2} (Komnitsas et al., 2019a, 2019b). The narrow band at 505 cm^{-1}, which is typical of the Fe—O stretching vibrations, is due to the presence of magnetite in LS, as also confirmed by XRD analysis (Muthuvel et al., 2019). The major band observed at 961 cm^{-1} represents the Si—O asymmetric stretching vibrations with its wide broadness indicating the high glassy/vitreous content present in FS and LS slags (Chen et al., 2020; Komnitsas et al., 2009). The FTIR spectrum of LS also shows two narrow bands at 2845 cm^{-1} and 2918 cm^{-1}, typical of symmetric and asymmetric –CH$_2$- stretching vibrations, respectively (Li et al., 2019), while the two bands at 1525 cm^{-1} and 2370 cm^{-1} in the FSP are attributed to the atmospheric carbonation (Gao et al., 2014; Komnitsas et al., 2015). Finally, the broad bands at 1382 cm^{-1} and 3423 cm^{-1}, which are related to the presence of water, are due to bending and stretching vibrations of O—H bonds, respectively (Maragkos et al., 2009).
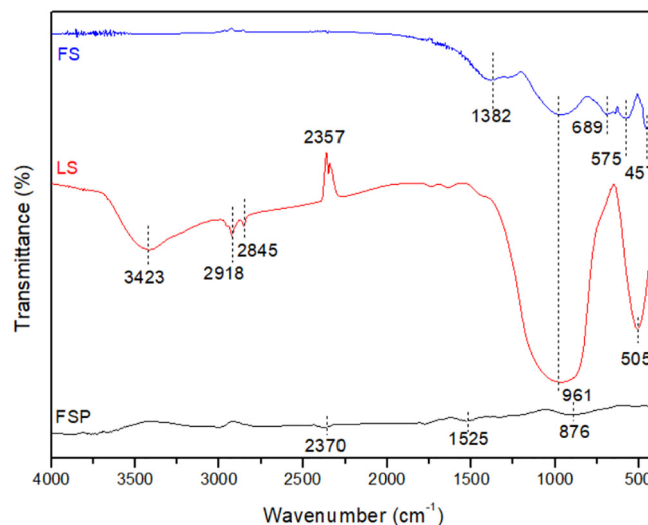
Fig. 3. FTIR spectra of FS, FSP and LS slags.

3.2. Factors affecting the compressive strength of the produced AAMs

3.2.1. Effect of H$_2$O/Na$_2$O molar ratio in the activating solution and ageing period

Fig. 4 presents the compressive strength of the AAMs produced from FS (Fig. 4a) and FSP (Fig. 4b), after curing at 90 °C, as a function of H$_2$O/Na$_2$O molar ratio in the activating solution and ageing period (7 or 28 days). The SiO$_2$/Na$_2$O molar ratio in the activating solution was kept constant at 1.00 in this series. It is seen that as the H$_2$O/Na$_2$O molar ratio decreases from 21.6 to 14.8, the compressive strength of the produced AAMs also decreases, while the increase of ageing period from 7 to 28 days has only a minor beneficial effect. The maximum compressive strength recorded after a curing period of 28 days, was 28.0 MPa, when the H$_2$O/Na$_2$O ratio was 21.6. On the other hand, when FSP was used as raw material (Fig. 4b), the decrease in H$_2$O/Na$_2$O molar ratio from 19.5 to 11.9, resulted in a noticeable increase in the compressive strength of the produced AAMs. The maximum
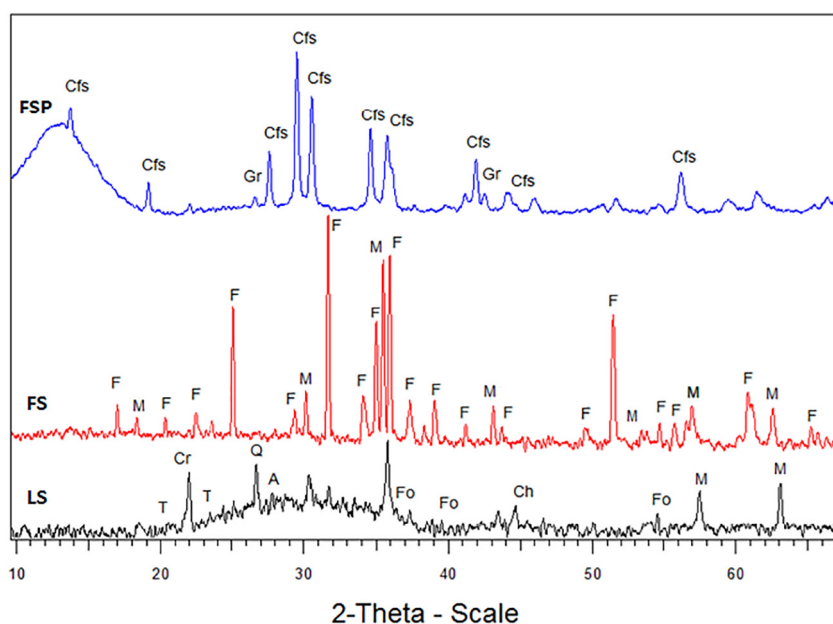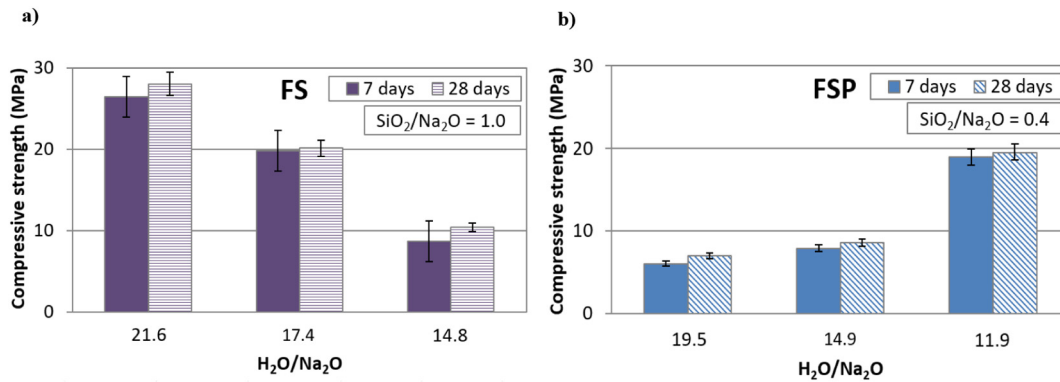
Fig. 2. XRD patterns of slags FS, FSP and LS. Phases identified are: anorthite (A), clinoferrosilite (Cfs), chromite (Ch), cristobalite (Cr), fayalite (F), forsterite (Fo), graphite (Gr), magnetite (M), quartz (Q), tridymite (T).

Fig. 4. Effect of H_2O/Na_2O molar ratio in the activating solution and ageing period on the compressive strength of (a) FS- and (b) FSP-based AAMs (pre-curing time 6 h, curing temperature 90 °C, curing period 24 h; error bars indicate the standard deviation of measurements obtained from three specimens).

compressive strength recorded was 19.5 MPa when the H_2O/Na_2O ratio was 11.9. It is noted that the SiO_2/Na_2O molar ratio in alkaline solution in this series was kept constant at 0.4. As in the previous case, the effect of the ageing period was negligible.

It is known that the H_2O/Na_2O ratios plays major role during alkali activation; low ratio indicates excess of OH^- ions which may remain unreacted and result in the production of specimens with lower strength, whereas high ratio may indicate either deficiency of OH^- ions or excess of water which may also remain unreacted under specific synthesis conditions. The optimum H_2O/Na_2O ratio in each case depends also on the mineralogy of the precursor and the rate of the reaction between the raw material and the alkaline solution, as indicated in earlier studies (Komnitsas et al., 2019a, 2019b; Soultana et al., 2019; Zaharaki and Komnitsas, 2009).

The results regarding alkali activation of these two slags may be explained by considering their mineralogy as well as the dissolution of Si and Al from the raw materials in alkaline conditions as presented in Table 4. FS exhibits higher activation potential since its Si/Al ratio in the alkaline solution is more than two times higher compared to the respective ratio obtained after leaching of FSP. It is also possible that the reactivity of FSP slag has reduced after plasma treatment.

3.2.2. Effect of curing temperature

The compressive strength of the produced AAMs, as a function of curing temperature (40, 60 or 90 °C), when FS or FSP was used as precursor is presented in Fig. 5a and b, respectively. In this series, the SiO_2/Na_2O molar ratio was kept at 1 and 0.4 for FS and FSP respectively, as shown in Fig. 4. It is seen from these results that temperature has a major beneficial effect on the compressive strength of the AAMs produced from both slags, which increases by more than 5 times when the curing temperature increases from 40 to 90 °C. The maximum

values of compressive strength obtained after an ageing period of 7 days were 26.5 and 18.9 MPa for FS- and FSP-based AAMs, respectively. It is also mentioned that the weight loss of the specimens during curing increases with increasing temperature from 2 wt% to almost 6 wt % over the temperature range investigated.

It is well known from previous studies, that higher curing temperature accelerates the rate of reactions between the precursors and the activating solution and improves condensation and re-solidification so that more aluminosilicate bonds are formed, a better microstructure is developed and the matrix acquires more beneficial mechanical properties (Soultana et al., 2019; Zaharaki et al., 2016). On the other hand, it should be mentioned that special care should be taken during curing at higher temperature in order to avoid fast evaporation of water which may result in incomplete alkali activating reactions (Gebregziabiher et al., 2016; Sindhunata et al., 2006; Yuan et al., 2016).
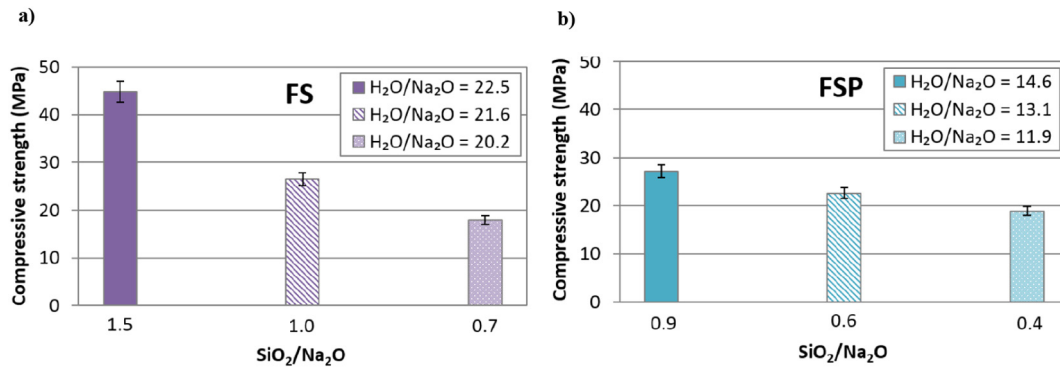
3.2.3. Effect of SiO_2/Na_2O molar ratio in the activating solution

Fig. 6 shows the compressive strength of the AAMs produced from FS (Fig. 6a) and FSP (Fig. 6b) as a function of SiO_2/Na_2O molar ratio in the alkaline solution, using a curing temperature of 90 °C and an ageing period of 7 days. The respective H_2O/Na_2O ratios are also shown for both series; these ratios are slightly different in each case as indicated in Table 3.

The maximum values of the compressive strength obtained were 44.8 MPa for FS-based AAMs with SiO_2/Na_2O molar ratio of 1.5, while when FSP was used the compressive strength was 27.2 MPa with SiO_2/Na_2O molar ratio of 0.9. It is seen in both cases that the compressive strength of the produced AAMs decreases with decreasing SiO_2/Na_2O molar ratios and this effect is more noticeable for FSP-based specimens. This is mainly due to the fact that when lower SiO_2/Na_2O molar ratios are used less Si ions are available to react and form Si-O-Si
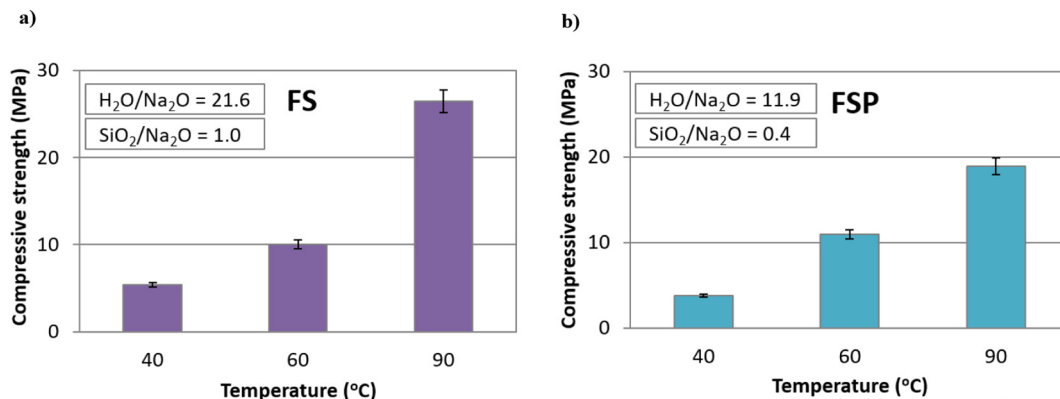
Fig. 5. Effect of curing temperature on the compressive strength of (a) FS- and (b) FSP-based AAMs (pre-curing time 6 h, curing period 24 h, ageing period 7 days; error bars indicate the standard deviation of measurements obtained from three specimens.

a)

b)

Fig. 6. Effect of SiO_2/Na_2O ratio in the activating solution on compressive strength of (a) FS- and (b) FSP-based AAMs (pre-curing time 6 h, curing temperature 90 °C, curing period 24 h, ageing period 7 days; error bars indicate the standard deviation of measurements obtained from three specimens).

bonds and thus specimens with decreased strength are obtained (Gao et al., 2014; Komnitsas et al., 2009). On the other hand, it is known that excess of NaOH in the activating solution may cause early precipitation of aluminosilicate gel or reduced dissolution of Si and Al from the precursor and formation of less oligomers, factors which reduce the compressive strength (Gao et al., 2014; Lee and van Deventer, 2002; Zhang et al., 2009). Also, excess of Na_2SiO_3, which is a liquid with high viscosity, may hinder the rate of reactions between the precursors and the activating solution so that the compressive strength is reduced (Yuan et al., 2016).

3.2.4. Potential of co-valorization of fayalitic and FeNi slags

In order to assess the potential of slag co-valorization through alkali activation, precursors obtained by mixing FS and FSP with different ratios of LS were used, since as mentioned earlier LS exhibits higher reactivity during alkali activation.

Fig. 7 presents the compressive strength obtained for specimens produced by mixing FS with LS at ratios 10:90, 30:70, 40:60 and 50:50. The synthesis conditions used for the alkali activation of the mixtures were pre-curing period 6 h, curing period 24 h, curing temperature 90 °C and ageing period 7 days. The ratios H_2O/Na_2O and SiO_2/Na_2O in the activating solution were 17.4 and 1.0 respectively. In the same figure the compressive strength of control specimens produced after alkali activation of each slag, namely FS and LS, are also given for comparison.

Experimental results prove the beneficial effect of LS addition in the initial mixture on the subsequent alkali activation, given that the AAMs produced after alkali activation of LS acquire a compressive strength of 80 MPa. It is seen that the specimens produced after alkali activation of all combinations examined acquire very high compressive strength which reaches 64.3 MPa also in the case when the mixing ratio FS:LS

is 50:50. This value is almost 70% higher compared to the value recorded for the AAM produced using only FS as precursor. It is also important to mention that almost no loss of strength is noted for the specimens produced from FS:LS mixing ratios 10:90 and 30:70.
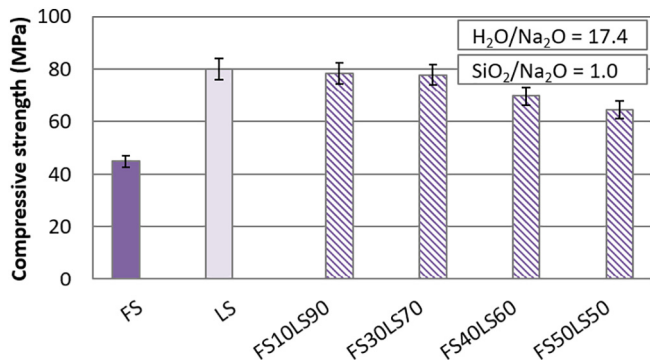
Fig. 8 presents the compressive strength obtained from specimens produced by mixing FSP with LS at ratios and synthesis conditions similar as in the previous case. In the same figure the compressive strength of control specimens produced after alkali activation of each slag, namely FSP and LS, are also given for comparison. The ratios H_2O/Na_2O and SiO_2/Na_2O in the activating solution were 14.6 and 0.9, respectively.

Experimental results also in this case prove the beneficial effect of LS addition in the initial mixture on the subsequent alkali activation. It is seen that the specimens produced after alkali activation of all combinations tested acquire very high compressive strength which reaches 45.8 MPa also in the case when the mixing ratio FSP:LS is 50:50. This value is 49% higher compared to the value recorded for the AAM produced from FSP only.

The results of this series prove the high co-valorization potential for both fayalitic and ferronickel slags. Based on this data, AAMs produced using a mixture consisting of 30 wt% FSP and 70 wt% LS, which was alkali activated under the optimum conditions, namely SiO_2/Na_2O 0.9, curing temperature 90 °C, curing period 24 h and ageing period 7 days were selected to study their structural integrity.

### 3.3. Structural integrity and toxicity of AAMs FS30LS70 and FSP30LS70

This section investigates the structural integrity of AAMs FS30LS70 and FSP30LS70 which represent specimens produced using the optimum synthesis conditions in the frame of slags co-valorization. In particular, Fig. 9 shows the evolution of the compressive strength of both

Fig. 7. Effect of mixing proportions of FS and LS on the compressive strength of FSLS-based AAMs (pre-curing time 6 h, curing period 24 h, curing temperature 90 °C, ageing period 7 days; error bars indicate the standard deviation of measurements obtained from three specimens).
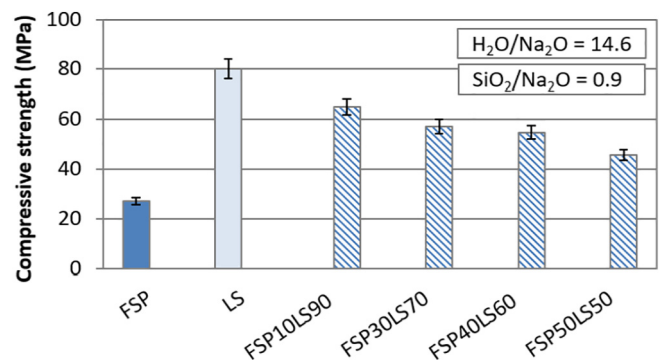
Fig. 8. Effect of mixing proportions of FSP and LS on the compressive strength of FSPLS-based AAMs (pre-curing time 6 h, curing period 24 h, curing temperature 90 °C, ageing period 7 days; error bars indicate the standard deviation of measurements obtained from three specimens).
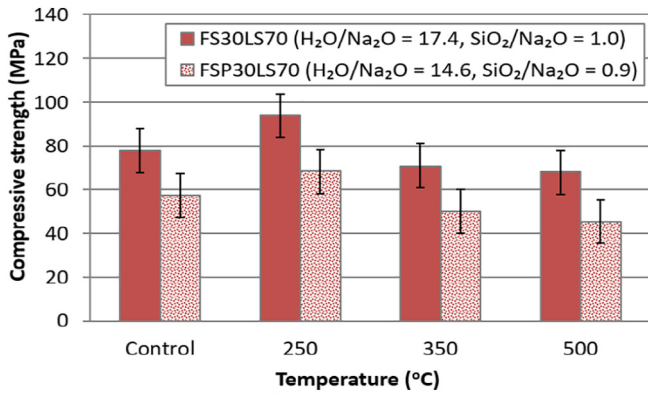
Fig. 9. Compressive strength of FS30LS70 and FSP30LS70 AAMs after firing between 250 and 500 °C; synthesis conditions: pre-curing time 6 h, curing period 24 h, curing temperature 90 °C, ageing period 7 days; error bars indicate the standard deviation of measurements obtained from three specimens.

AAMs after firing at 250, 350 and 500 °C for 6 h, while Fig. 10 presents the evolution of compressive strength after their immersion in distilled water and 1 M HCl for a period of 7 and 30 days as well as after the implementation of freeze-thaw cycles, using −18 ± 5 °C and room temperature (~24 ± 5 °C), as temperature extremes over a period of 7 and 28 days. The compressive strength of the control specimens is also shown for comparison.

Fig. 9 shows that the response of both AAMs to firing is good and FS30LS70 exhibits better behavior since its initial strength was higher. More specifically, the compressive strength of FS30LS70 specimen increases by ~20% to 94 MPa after firing at 250 °C, due to volumetric shrinkage (5.0%), and drops slightly by ~12% to 68 MPa after firing at higher temperatures up to 500 °C. Similar behavior is seen for FSP30LS70 which after firing at 500 °C retains a compressive strength of 45 MPa. The compressive strength after firing at higher temperatures, e.g. 800 °C, drops to less than 15 MPa (data not shown), due to phase transformations, deterioration of the structural integrity of the specimens as a result of the decomposition of Si–O–Al and Si–O–Si bonds, and the development of microcracks. It is thus deduced that AAMs produced after firing can be potentially used as medium fire-resistant materials (Abdel-Ghani et al., 2018; Zaharaki and Komnitsas, 2012; Komnitsas et al., 2019a, 2019b).

On the other hand, both specimens exhibit also very good to good behavior after immersion in distilled water or 1 M HCl, respectively for a period of 7 and 30 days. More specifically, immersion in distilled water affects only marginally the compressive strength of the specimens, even after a period of 30 days, whereas immersion in HCl solution

for 7 days results in a decrease of compressive strength to 65 MPa for FS30LS70 (Fig. 10a) and 45 MPa for FSP30LS70 (Fig. 10b), respectively. Additional retention of both AAMs in HCl solution for 30 days results in higher drop of compressive strength to 45 MPa and 30 MPa for FS30LS70 and FSP30LS70, respectively. Even though this loss of strength is considered big, it is important to mention that both specimens retain a substantial final strength under such harsh conditions.

Regarding the effect of freeze-thaw cycles for 7 and 30 days, it is seen that both specimens respond very well and that the decrease in strength after 30 cycles is only marginal to 67 MPa for FS30LS70 (14% decrease) and 50 MPa for FSP30LS70 (12% decrease), respectively.

Several studies pertinent to the structural integrity of AAMs using as precursors various types of slags or construction and demolition wastes (i.e. bricks and tiles) have been carried out. Komnitsas et al. (2015) showed that the final compressive strength of brick-based or concrete-based AAMs is slightly affected, while the final compressive strength of tile-based AAMs is severely affected when subjected to freeze–thaw cycles for 1 or 2 months. Mohamed (2019) showed that the alkali-activated slag concrete demonstrates generally better resistance to freeze-thaw compared to Ordinary Portland Concrete (OPC). Luukkonen et al. (2018) studied the freeze-thaw resistance of blast furnace slag mortar specimens and showed that they could withstand 120 cycles.

Finally, Table 5 shows the properties, namely porosity (%), water absorption (%) and density (kg m^{-3}) of selected AAMs, i.e. FS, FSP, LS, FS30LS70, FSP30LS70 as well as the last two after firing at 250 °C and 500 °C. All AAMs examined were produced using the optimum synthesis conditions, as shown in the previous graphs. In this table also the compressive strength of these AAMs is also shown.

It is seen from this data that the main differences were observed for porosity and density. It is observed that the porosity was 10.8% for FS4 specimen and decreased to 7.3% for FS30LS70 after firing at 250 °C. A similar trend was observed for water absorption which decreased from 3.8% to 3.2%. On the other hand, by taking into consideration the same AAMs the density increased from 2330 to 4330 kg m^{-3}.

Finally, it is mentioned that the solubilisation of heavy metals from FSP, LS and all produced AAMs is well below all available limits, as indicated by the application of TCLP (US EPA, 1992), EN 12457-3 (2002) and NEN 7341 (1995) tests. The only raw material that exhibited some toxicity was the original fayalitic slag (FS) and only in terms of Zn, due to its relatively high content of ZnO (2.80%wt), as shown in Table 2. The application of the TCLP test on FS indicated that Zn concentration in the extract was 10.8 mg L^{-1} but no limit is indicated for this metal by this specific test. The application of the EN 12457-3 test indicated that Zn solubilisation was 63 mg kg^{-1} and based on this value FS as a waste can be only disposed at a landfill that accepts hazardous wastes. The application of NEN test indicates that Zn exhibits noticeable solubilisation,
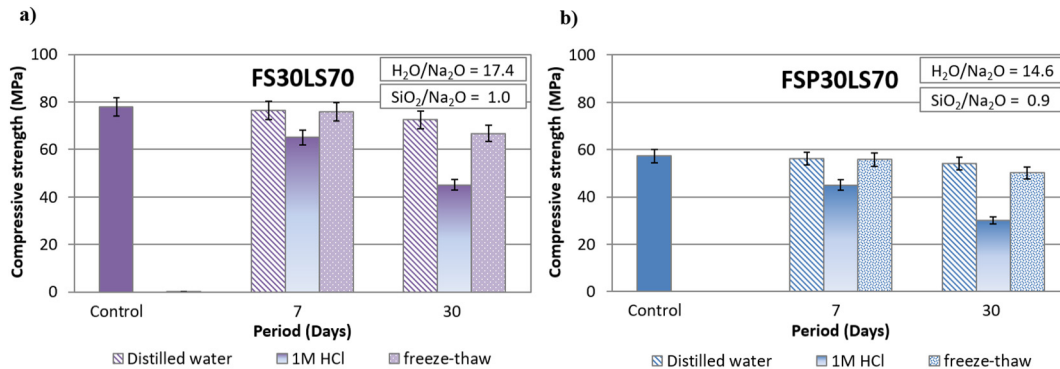
Fig. 10. Compressive strength of (a) FS30LS70 and (b) FSP30LS70 AAMs after immersion in distilled water and 1 M (mol L^{-1}) HCl and implementation of freeze-thaw cycles for 7 and 30 days; synthesis conditions: pre-curing time 6 h, curing period 24 h, curing temperature 90 °C, ageing period 7 days; error bars indicate the standard deviation of measurements obtained from three specimens.

Table 5
Physical properties of selected AAMs.

AAM code	Compressive strength (MPa)	Water absorption (%)	Porosity (%)	Density (kg/m^3)
FS	44.8	3.8	10.8	2330
FSP	27.2	4.0	9.4	2400
LS	80.1	3.0	8.0	2580
FS30LS70 (control)	77.9	3.2	8.6	2640
FS30LS70 after firing at 250 °C	93.9	3.2	6.3	4330
FS30LS70 after firing at 500 °C	67.2	3.9	10.3	2650
FSP30LS70 (control)	57.3	2.3	8.5	3754
FSP30LS70 after firing at 250 °C	68.3	3.8	8.8	3800
FSP30LS70 after firing at 500 °C	45.4	3.8	9.2	3428

since its concentration in the leachate is 355 mg kg^{-1} at pH 4 and 238,355 mg kg^{-1} at pH 7; however, it has to be taken into account that this test is carried out using high L/S ratio, 50:1, and that no limit is again indicated for this metal. So, alkali activation of these wastes apart of their co-valorisation and the synthesis of new products that can be used as binders or construction materials, also results in reduction of their toxicity, in case that such toxicity exists.

3.4. Mineralogy – microstructure of selected AAMs

3.4.1. XRD analysis

Fig. 11 presents the XRD patterns of selected AAMs, namely FS30LS70 before and after firing at 250 °C for 6 h, as well as the patterns of raw FS and LS for comparison. It is observed that the main mineral phases, namely magnetite (Fe$_3$O$_4$) and fayalite (Fe$_2$SiO$_4$) present in FS30LS70 are also present after its firing. It is also observed that silicon containing phases, such as quartz, cristobalite and tridymite present in the raw materials are not detected in the produced AAMs, due to their dissolution after the attack of the raw materials by the activating solution. Finally, it is seen that the intensities of the crystalline phases of fayalite and magnetite present in the produced AAMs are in general lower than the ones present in the raw slags. The lower intensities of these dominant phases identified in the AMMs indicate that they partially participate in the reactions and thus confirm to some extent the degree of polymerization (Peys et al., 2019b).

3.4.2. FTIR analysis

Fig. 12 presents the FTIR spectra of selected AAMs, namely FS30LS70 before and after firing at 250 °C for 6 h, as well as the FS and LS for comparison. The FTIR spectra of the AAMs indicated that polymerization took place and has resulted in the increase of the compressive strength. In this context and in line with XRD results (Fig. 11), the disappearance of major bands in the 450–650 cm^{-1} range, which are attributable to characteristic T–O–T (T = Si, or Al) deformation vibrations, suggests that the activating solutions were effective in attacking the glassy content of the raw slags and thus, most part of the dissolved aluminosilicate content has participated in the synthesis of the AAMs (Bernal et al., 2011). Moreover, the FTIR spectra of the AMMs show a slight shift to higher wavenumbers for most vibration bands compared to raw slags, which is typically attributed to the higher Si content in the C–S–H gel and the higher degree of polymerization (Ravikumar and Neithalath, 2012). In particular, a shift of the rocking band at 457 cm^{-1} in the FS towards higher wavenumber (465 cm^{-1}) along with a significant reduction in its intensity in the examined AAMs is observed. Another explanation that is proposed, apart from the higher Si content of the inorganic matrix, is that the Fe present in the raw slag partly oxidizes to Fe^{3+} after alkali activation and subsequently decreases the amount of non-bridging oxygens available for the silicate network (Peys et al., 2019a, 2019b; Van De Sande et al., 2020). In this case, higher degree of silicate polymerization is achieved and the Si—O stretching band at 961 cm^{-1} present in the spectra of the raw slags shifts to higher wavenumbers in FS30LS70, i.e. 1017 cm^{-1} and 1021 cm^{-1} before and after firing at 250 °C for 6 h, respectively. Finally, the weaker bands present at 1630 cm^{-1} and 3423 cm^{-1} in the raw LS and attributed to the characteristic H–OH– bending and stretching vibrations of O—H are shifted to broader and more intense bands located at 1633 cm^{-1} and 3450 cm^{-1} in both AAMs, respectively.

3.4.3. SEM analysis

Back-scattered electron (BSE) images of selected AAMs, namely FS30LS70 before and after firing at 250 °C for 6 h are shown in Fig. 13 (a-d). As shown in XRD patterns, SEM analysis of the polished AAM surfaces along with EDS point analyses revealed that fayalite and magnetite particles were the major mineralogical phases identified after alkali activation. Other phases such as chromite occurred as drop-like inclusions, while silicates such as forsterite and quartz were also detected in some places (Fig. 13 b and d). Regarding the microstructure of both AAMs, no
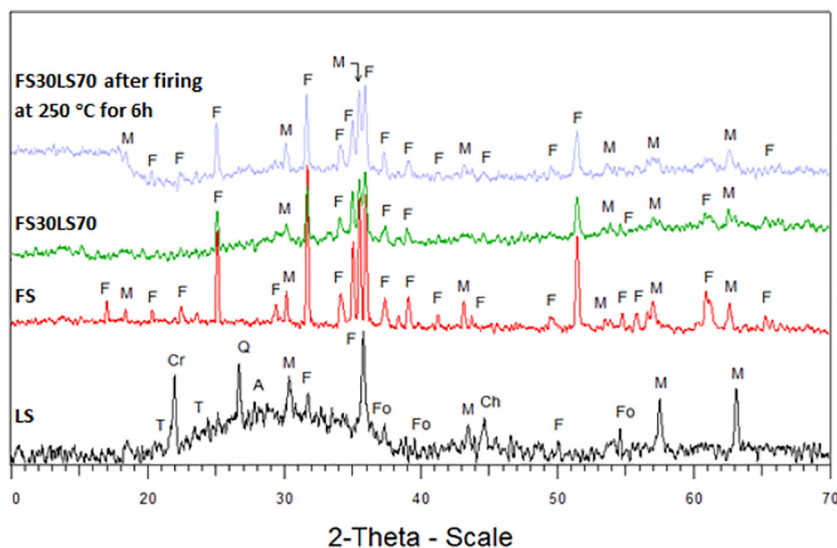

Fig. 11. XRD patterns of raw LS and FS slags, as well as AAMs FS30LS70 before and after firing at 250 °C for 6 h - phases identified are: anorthite (A), chromite (Ch), cristobalite (Cr), fayalite (F), forsterite (Fo), magnetite (M), quartz (Q), tridymite (T).
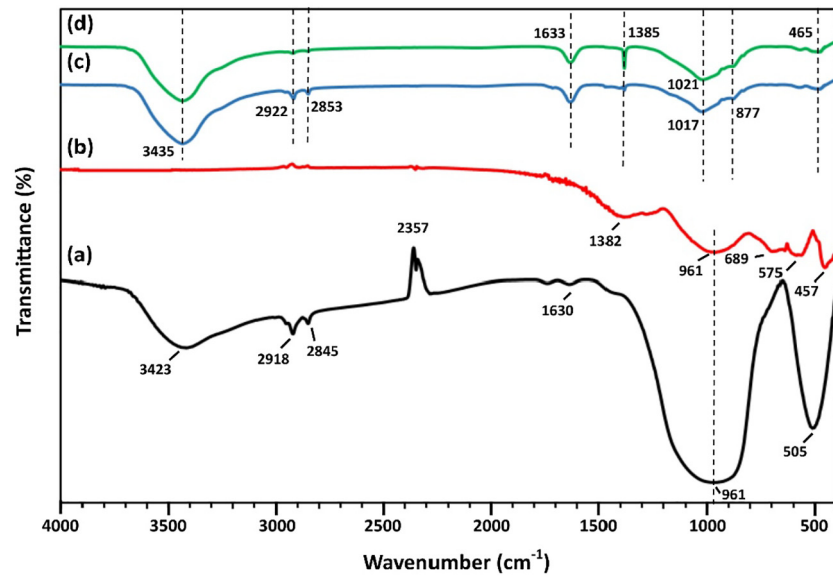
Fig. 12. FTIR spectra of raw slags, namely (a) LS and (b) FS, as well as AAMs (c) FS30LS70 before and (d) FS30LS70 after firing at 250 °C for 6 h.

signs of cracks were observed along the cross sectional interfaces examined as a result of the strong bonds that formed after the reactions between the slag particles (mostly fayalite) and the alkaline activators (Na_2SiO_3 and NaOH). In this context, the presence of inorganic

polymeric gels (G1 and G2) containing Ca, Al, Si, Fe, Mg and Na and surrounded by radically dissolved particles of fayalite and quartz after alkali-activation were identified in FS30LS70 before (Fig. 13b) and after firing (Fig. 13d), respectively. However, the FS30LS70 AAM
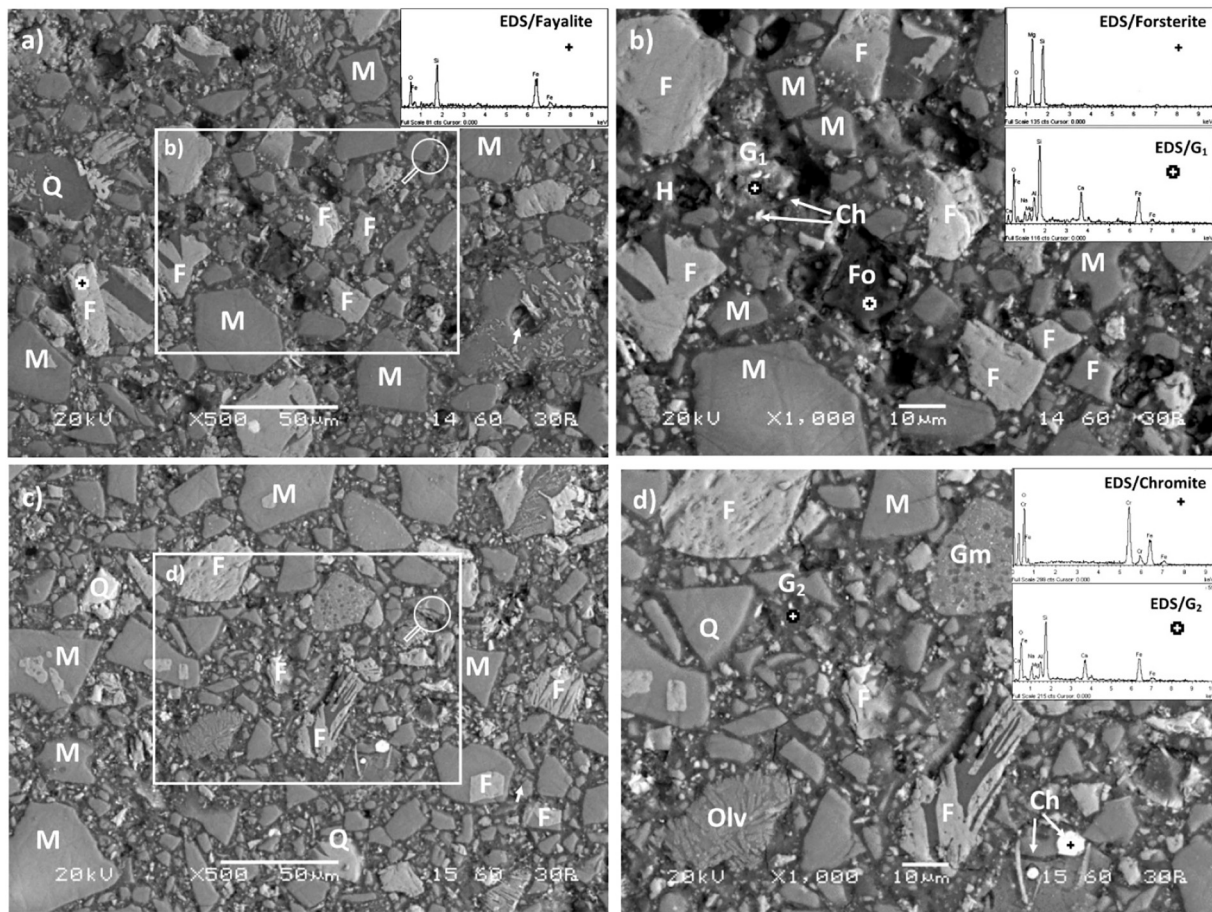
Fig. 13. SEM-BSE images of polished cross-sections of selected AAMs (a,b) FS30LS70 and (c,d) FS30LS70 after firing at 250 °C for 6 h. EDS spectra show in several spot locations the presence of metallic and oxide phases, the formation of mixed aggregates and newly formed inorganic gels (Q: Quartz, Fo: Forsterite, F: Fayalite, M: Magnetite, Olv: Olivine, Ch: Chromite, Gm: Glassy matrix, G1:Gel, G2: Gel).

presents a microstructure which is characterized by several holes/pores scattered in the inorganic matrix and a greater proportion of unreacted or partially reacted larger particles compared to FS30LS70 after firing at 250 °C for 6 h.

After firing, it seems that holes were filled with inorganic gel as result of dehydration reactions that took place along with sintering of the unreacted aluminosilicate content (Rincón et al., 2018; Xu et al., 2019) and therefore a denser and more homogenous microstructure was finally formed with a continuous and embedded gel matrix. This well-established microstructure justifies the higher compressive strength obtained for the fired AAM (94 MPa). Fig. 13d (zoom of rectangular area of Fig. 13c) shows in detail the presence of columnar elongated of olivine particles (mixed forsterite/fayalite) and fine to coarse-sized euhedral crystals of anorthite and fayalite embedded in a glassy matrix (Gm) (Lemonis et al., 2015).

4. Conclusions

The present study explored the alkali activation potential of fayalitic slags as well as their co-valorization potential, when mixed with ferronickel slag, for the production of AAMs.

The experimental results show that under the synthesis conditions: pre-curing period 24 h, curing temperature 90 °C, curing period 24 h and ageing period 7 days, the maximum values of the compressive strength obtained were 44.8 MPa and 27.2 MPa for FS- and FSP-based AAMs, respectively. The SiO_2/Na_2O molar ratios used in the activating solution were 1.5 and 0.9 in each case, respectively.

The results also show the noticeable co-valorization potential of FS and FSP slags when mixed with LS slag. It is seen that the AAMs produced after alkali activation of FS-LS and FSP-LS mixtures at ratio 50:50, using the same as above synthesis conditions, acquire compressive strength of 64.3 MPa and 45.8 MPa, respectively; the SiO_2/Na_2O molar ratio in the activating solution was 1.0 and 0.9 in each case respectively.

Furthermore, the AAMs produced after alkali activation of slag mixtures maintained sufficient structural integrity after firing for 6 h at temperature up to 500 °C, immersion in distilled water and acidic solution or subjection to freeze-thaw cycles for a period of 7 or 30 days. Finally, all produced AAMs exhibit very low toxicity, as indicated by the application of TCLP, EN 12457-3 and NEN 7341 tests.

The results of this study proved that alkali activation is a viable option for the co-valorization of different slags and the production of AAMs with beneficial properties, thus enabling the minimization of these wastes and the reduction of the environmental footprint of the metallurgical sector.

CRediT authorship contribution statement

Konstantinos Komnitsas: Conceptualization, Methodology, Project administration, Supervision, Writing - review & editing. **Lourdes Yurramendi:** Methodology, Resources, Writing - review & editing. **Georgios Bartzas:** Investigation, Methodology, Data curation, Writing - review & editing. **Vasiliki Karmali:** Investigation, Methodology, Data curation, Writing - original draft. **Evangelos Petrakis:** Investigation, Methodology, Data curation, Writing - original draft.

Declaration of competing interest

The authors declare that they have no known competing financial interests or personal relationships that could have appeared to influence the work reported in this paper.

Acknowledgments

References

Abdel-Ghani, N.T., Elsayed, A.H., AbdelMoied, S., 2018. Geopolymer synthesis by the alkali-activation of blast furnace steel slag and its fire-resistance. HBRC J. 14 (2), 159–164. https://doi.org/10.1016/j.hbrcj.2016.06.001.

Agnello, A.C., Potysz, A., Fourdrin, C., Huguenot, D., Chauhan, P.S., 2018. Impact of pyrometallurgical slags on sunflower growth, metal accumulation and rhizosphere microbial communities. Chemosphere 208, 626–639. https://doi.org/10.1016/j.chemosphere.2018.06.038.

Alshaaer, M., Zaharaki, D., Komnitsas, K., 2015. Microstructural characteristics and adsorption potential of zeolitic tuff – metakaolin geopolymers. Desalin. Water Treat. 56, 338–345. https://doi.org/10.1080/19443994.2014.938306.

ASTM (American Society for Testing and Materials), 2018. C1262 – 10 Standard Test Method for Evaluating the Freeze-Thaw Durability of Dry Cast Segmental Retaining Wall Units and Related Concrete Units. ASTM International, West Conshohocken, PA 2018. Retrieved from. www.astm.org.

Bartzas, G., Komnitsas, K., 2015. Life cycle assessment of ferronickel production in Greece. Resour. Conserv. Recycl. 105, 113–122. https://doi.org/10.1016/j.resconrec.2015.10.016.

Bernal, S.A., de Gutierrez, R.M., Provis, J.L., Rose, V., 2010. Effect of silicate modulus and metakaolin incorporation on the carbonation of alkali silicate-activated slags. Cem. Concr. Res. 40, 898–907. https://doi.org/10.1016/j.cemconres.2010.02.003.

Bernal, S.A., Provis, J.L., Rose, V., Gutierrez, R.M., 2011. Evolution of binder structure in sodium silicate-activated slag-metakaolin blends. Cem. Concr. Compos. 33, 46–54. https://doi.org/10.1016/j.cemconcomp.2010.09.004.

BSI (British Standards Institute), 2007. BS EN 1936: Natural Stone Test Methods. Determination of Real Density and Apparent Density and of Total and Open Porosity; NP EN 1936:2006. 2007. BSI, London, UK.

Bumanis, G., Novais, R.M., Carvalheiras, J., Bajare, D., Labrincha, J.A., 2019. Metals removal from aqueous solutions by tailored porous waste-based granulated alkali-activated materials. Appl. Clay Sci. 179, 105147. https://doi.org/10.1016/j.clay.2019.105147.

Chen, L., Wang, L., Cho, D.-W., Tsang, D.C.W., Tong, L., Zhou, Y., Yang, J., Hu, Q., Poon, C.S., 2019. Sustainable stabilization/solidification of municipal solid waste incinerator fly ash by incorporation of green materials. J. Clean. Prod. 222, 335–343. https://doi.org/10.1016/j.jclepro.2019.03.057.

Chen, W., Peng, R., Straub, C., Yuan, B., 2020. Promoting the performance of one-part alkali-activated slag using fine lead-zinc mine tailings. Constr. Build. Mater. 236, 117745. https://doi.org/10.1016/j.conbuildmat.2019.117745.

Davidovits, J., 1991. Geopolymers—inorganic polymeric new materials. J. Therm. Anal. Calorim. 37, 1633–1656. https://doi.org/10.1007/BF01912193.

Duxson, P., Provis, J.L., 2008. Designing precursors for geopolymer cements. J. Am. Ceram. Soc. 91, 3864–3869. https://doi.org/10.1111/j.1551-2916.2008.02787.x.

Duxson, P., Provis, J.L., Lukey, G.C., van Deventer, J.S.J., 2007. The role of inorganic polymer technology in the development of 'green concrete'. Cem. Concr. Res. 37, 1590–1597. https://doi.org/10.1016/j.cemconres.2007.08.018.

EN12457-3:2002, 2002. Characterization of Waste – Compliance Test for Leaching of Granular Waste Materials and Sludges – Part 3: Two Stage Batch Test at a Liquid to Solid Ratio of 2 l/kg and 8 l/kg for Materials with High Solid Content and with Particle Size below 4 mm. CEN, Brussels.

Furlani, E., Maschio, S., Magnan, M., Aneggi, E., Andreatta, F., Lekka, M., Lanzutti, A., Fedrizzi, L., 2018. Synthesis and characterization of geopolymers containing blends of unprocessed steel slag and metakaolin: the role of slag particle size. Ceram. Int. 44, 5226–5232. https://doi.org/10.1016/j.ceramint.2017.12.131.

Gao, K., Lin, K.-L., Wang, D., Hwang, C.-L., 2014. Effects SiO_2/Na_2O molar ratio on mechanical properties and the microstructure of nano-SiO_2 metakaolin-based geopolymers. Constr. Build. Mater. 53, 503–510. https://doi.org/10.1016/j.conbuildmat.2013.12.003.

Gebregziabiher, B.S., Thomas, R.J., Peethamparan, S., 2016. Temperature and activator effect on early-age reaction kinetics of alkali-activated slag binders. Constr. Build. Mater. 113, 783–793. https://doi.org/10.1016/j.conbuildmat.2016.03.098.

Gee, C., Ramsey, M.H., Maskallh, J., Thornton, I., 1997. Mineralogy and weathering processes in historical smelting slags and their effect on the mobilisation of lead. J. Geochem. Explor. 58, 249–257. https://doi.org/10.1016/s0375-6742(96)00062-3.

Habert, G., Lacaillerie, J.B.E., Russel, N., 2011. An environmental evaluation of geopolymer based concrete production: reviewing current research trends. J. Clean. Prod. 19, 1229–1238. https://doi.org/10.1016/j.jclepro.2011.03.012.

Huang, Y., Wang, Q., Shi, M., 2017. Characteristics and reactivity of ferronickel slag powder. Constr. Build. Mater. 156, 773–789. https://doi.org/10.1016/j.conbuildmat.2017.09.038.

Kaze, C.R., Djobo, J.N.Y., Nana, A., Tchakoute, H.K., Kamseu, E., Melo, U.C., Leonelli, C., Hubert Rahier, H., 2018. Effect of silicate modulus on the setting, mechanical strength and microstructure of iron-rich aluminosilicate (laterite) based-geopolymer cured at room temperature. Ceram. Int. 44 (17), 21442–21450. https://doi.org/10.1016/j.ceramint.2018.08.205.

Khale, D., Chaudhary, R., 2007. Mechanism of geopolymerization and factors influencing its development: a review. J. Mater. Sci. 42, 729–746. https://doi.org/10.1007/s10853-006-0401-4.

Komnitsas, K., 2011. Potential of geopolymer technology towards green buildings and sustainable cities. Procedia Engineering 21, 1023–1032. https://doi.org/10.1016/j.proeng.2011.11.2108.

Komnitsas, K., 2016. Co-valorization of marine sediments and construction & demolition wastes through alkali activation. J. Environ. Chem. Eng. 4, 4661–4669. https://doi.org/10.1016/j.jece.2016.11.003.

Komnitsas, K., Zaharaki, D., 2007. Geopolymerisation. A review and prospects for the minerals industry. Miner. Eng. 20, 1261–1277. https://doi.org/10.1016/j.mineng.2007.07.011.

Komnitsas, K., Zaharaki, D., Perdikatsis, V., 2007. Geopolymerisation of low calcium ferronickel slags. J. Mater. Sci. 42 (9), 3073–3082. https://doi.org/10.1007/s10853-006-0529-2.

Komnitsas, K., Zaharaki, D., Perdikatsis, V., 2009. Effect of synthesis parameters on the compressive strength of low-calcium ferronickel slag inorganic polymers. J. Hazard. Mater. 161, 760–768. https://doi.org/10.1016/j.jhazmat.2008.04.055.

Komnitsas, K., Zaharaki, D., Bartzas, G., 2013. Effect of sulphate and nitrate anions on heavy metal immobilisation in ferronickel slag geopolymers. Appl. Clay Sci. 73, 103–109. https://doi.org/10.1016/j.clay.2012.09.018.

Komnitsas, K., Zaharaki, D., Vlachou, A., Bartzas, G., Galetakis, M., 2015. Effect of synthesis parameters on the quality of construction and demolition wastes (CDW) geopolymers. Adv. Powder Technol. 26, 368–376. https://doi.org/10.1016/j.apt.2014.11.012.

Komnitsas, K., Bartzas, G., Karmali, V., Petrakis, E., Kurylak, W., Pietek, G., Kanasiewicz, J., 2019a. Assessment of alkali activation potential of a Polish ferronickel slag. Sustainability 11, 1863. https://doi.org/10.3390/su11071863.

Komnitsas, K., Petrakis, E., Bartzas, G., Karmali, V., 2019b. Column leaching of low-grade saprolitic laterites and valorization of leaching residues. Sci. Tot. Environ. 665, 347–357. https://doi.org/10.1016/j.scitotenv.2019.01.381.

Kriven, W.M., Bell, J.L., Gordon, M., 2003. Microstructure and microchemistry of fully-reacted geopolymers and geopolymer matrix composites. Ceram. Trans. 153, 227–250. https://doi.org/10.1002/9781118406892.ch15.

Krivenko, P.V., Kovalchuk, G.Y., 2007. Directed synthesis of alkaline aluminosilicate minerals in a geocement matrix. J. Mater. Sci. 42, 2944–2952. https://doi.org/10.1007/s10853-006-0528-3.

Lee, W.K.W., van Deventer, J.S.J., 2002. The effects of inorganic salt contamination on the strength and durability of geopolymers. Colloids Surf. A. Physicochem. Eng. Aspects 211, 115–126. https://doi.org/10.1016/s0927-7757(02)00239-x.

Lemonis, N., Tsakiridis, P.E., Katsiotis, N.S., Antiohos, S., Papageorgiou, D., Katsiotis, M.S., Beazi-Katsioti, M.S., 2015. Hydration study of ternary blended cements containing ferronickel slag and natural pozzolan. Constr. Build. Mater. 81, 130–139. https://doi.org/10.1016/j.conbuildmat.2015.02.046.

Li, Q., Yang, Y., Yang, K., Chao, Z., Tang, D., Tian, Yi, Wu, F., Basheer, M., Yang, C., 2019. The role of calcium stearate on regulating activation to form stable, uniform and flawless reaction products in alkali-activated slag cement. Cem. Concr. Res. 103, 242–251. https://doi.org/10.1016/j.cemconcomp.2019.05.009.

Liu, Z., Wang, J., Jiang, Q., Cheng, G., Li, L., Kang, Y., Wang, D., 2019. A green route to sustainable alkali-activated materials by heat and chemical activation of lithium slag. J. Clean. Prod. 225, 1184–1193. https://doi.org/10.1016/j.jclepro.2019.04.018.

Luukkonen, T., Abdollahnejad, Z., Yliniemi, J., Kinnunyn, P., Illikainen, M., 2018. Comparison of alkali and silica sources in one-part alkali-activated blast furnace slag mortar. J. Clean. Prod. 187, 171–179. https://doi.org/10.1016/j.jclepro.2018.03.202.

Luukkonen, T., Heponiemi, A., Runtti, H., Pesonen, A., Yliniemi, J., Lassi, U., 2019. Application of alkali-activated materials for water and wastewater treatment: a review. Rev. Environ. Sci. Biotechnol. 18 (2), 271–297. https://doi.org/10.1007/s11157-019-09494-0.

Maragkos, I., Giannopoulou, P.I., Panias, D., 2009. Synthesis of ferronickel slag-based geopolymers. Miner. Eng. 22, 196–203. https://doi.org/10.1016/j.mineng.2008.07.003.

Marjanović, J.N., Komljenović, M., Baščarević, Z., Nikolić, V., Petrović, R., 2015. Physical-mechanical and microstructural properties of alkali-activated fly ash-blast furnace slag blends. Ceram. Int. 41, 1421–1435. https://doi.org/10.1016/j.ceramint.2014.09.075.

Mastali, M., Shaad, K.M., Abdollahnejad, Z., Falah, M., Kinnunen, P., Illikainen, M., 2020. Towards sustainable bricks made with fiber-reinforced alkali-activated desulfurization slag mortars incorporating carbonated basic oxygen furnace aggregates. Constr. Build. Mater. 232, 117258. https://doi.org/10.1016/j.conbuildmat.2019.117258.

Mohamed, O.A., 2019. A review of durability and strength characteristics of alkali-activated slag concrete. Materials 12 (8), 1198. https://doi.org/10.3390/ma12081198.

Muñoz, I., Cifrian, E., Andrés, A., SanMiguel, G., Ruiz, D., Viguri, J.R., 2018. Analysis of environmental benefits associated with the incorporation of Waelz slag into fired bricks using LCA. Constr. Build. Mater. 168, 178–186. https://doi.org/10.1016/j.conbuildmat.2018.02.108.

Muthuvel, I., Gowthami, K., Thirunarayanan, G., Suppuraj, P., Krishnakumar, B., do Nascimento Sobral, J.F., Swaminathan, M., 2019. Graphene oxide–Fe2V4O13 hybrid material as highly efficient hetero-Fenton catalyst for degradation of methyl orange. Int. J. Ind. Chem. 10, 1–11. https://doi.org/10.1007/s40090-019-0173-8.

NEN 7341, 1995. Leaching Characteristics of Solid Earthy and Stony Building and Waste Materials-leaching Tests: Determination of the Availability of Inorganic Components for Leaching. 1st ed. Nederlands Normalisatie Instituut (NNI), Delft, the Netherlands ICS 13.030-70;91.100.

Onisei, S., Pontikes, Y., Van Gerven, T., Angelopoulos, G.N., Velea, T., Predica, V., Moldovan, P., 2012. Synthesis of inorganic polymers using fly ash and primary lead slag. J. Hazard. Mater. 205–206, 101–110. https://doi.org/10.1016/j.jhazmat.2011.12.039.

Ouellet-Plamondon, C., Habert, G., 2014. Life cycle analysis (LCA) of alkali-activated cements and concretes. Handbook of Alkali-activated Cements, Mortars and Concretes. WoodHead Publishing-Elsevier, Cambridge, pp. 663–686.

Pacheco-Torgal, F., Abdollahnejad, Z., Miraldo, S., Kheradmand, M., 2017. Alkali-activated cement-based binders (AACBs) as durable and cost-competitive low-CO2 binder materials: some shortcomings that need to be addressed, chapter 9. Handbook of Low Carbon Concrete. Butterworth-Heinemann, Oxford, pp. 195–216. https://doi.org/10.1016/B978-0-12-804524-4.00009-9.

Palomo, A., Krivenko, P., Garcia-Lodeiro, I., Kavalerova, E., Maltseva, O., Fernández-Jiménez, A., 2014. A review on alkaline activation: new analytical perspectives. Mater. Constr. 64 (315), 22. https://doi.org/10.3989/mc.2014.00314.

Pasetto, M., Baliello, A., Giacomello, G., Pasquini, E., 2017. Sustainable solutions for road pavements: a multi-scale characterization of warm mix asphalts containing steel slags. J. Clean. Prod. 166, 835–843. https://doi.org/10.1016/j.jclepro.2017.07.212.

Passuello, A., Rodríguez, E.D., Hirt, E., Longhi, M., Bernal, S.A., Provis, J.L., 2017. Evaluation of the potential improvement in the environmental footprint of geopolymers using waste-derived activators. J. Clean. Prod. 166, 680–689. https://doi.org/10.1016/j.jclepro.2017.08.007.

Petrakis, E., Karmali, V., Bartzas, G., Komnitsas, K., 2019. Grinding kinetics of slag and effect of final particle size on the compressive strength of alkali activated materials. Minerals 9, 714. https://doi.org/10.3390/min9110714.

Peys, A., Douvalis, A.P., Siakati, C., Rahier, H., Blanpain, B., Pontikes, Y., 2019a. The influence of air and temperature on the reaction mechanism and molecular structure of Fe-silicate inorganic polymers. J. Non-Cryst. Solids 526, 119675. https://doi.org/10.1016/j.jnoncrysol.2019.119675.

Peys, A., Douvalis, A.P., Hallet, V., Rahier, H., Blanpain, B., Pontikes, Y., 2019b. Inorganic polymers from CaO-FeOx-SiO2 Slag: the start of oxidation of Fe and the formation of a mixed valence binder. Front. Mater. Sci. 6, 212. https://doi.org/10.3389/fmats.2019.00212.

Pontikes, Y., Machiels, L., Onisei, S., Pandelaers, L., Geysen, D., Jones, P.T., Blanpain, B., 2013. Slags with a high Al and Fe content as precursors for inorganic polymers. Appl. Clay Sci. 73, 93–102. https://doi.org/10.1016/j.clay.2012.09.020.

Provis, J.L., Bernal, S.A., 2014. Geopolymers and related alkali-activated materials. Annu. Rev. Mater. Res. 44, 229–327. https://doi.org/10.1146/annurev-matsci-070813-113515.

Ravikumar, D., Neithalath, N., 2012. Effects of activator characteristics on the reaction product formation in slag binders activated using alkali silicate powder and NaOH. Cem. Concr. Compos. 34, 809–818. https://doi.org/10.1016/j.cemconcomp.2012.03.006.

Rincón, A., Desideri, D., Bernardo, E., 2018. Functional glass-ceramic foams from 'inorganic gel casting' and sintering of glass/slag mixtures. J. Clean. Prod. 187, 250–256. https://doi.org/10.1016/j.jclepro.2018.03.065.

Saari, V., Latostenmaa, P., Yliniemi, J., Ohenoja, K., 2019. Boliden Harjavalta copper and nickel smelter – review of smelter operations, slags and slag valorization studies. 6th International Slag Valorisation Symposium, 1–5 April 2019, Mechelen, Belgium Retrieved from. www.slag-valorisation-symposium.eu.

Shi, C., Qu, B., Provis, J.L., 2019. Recent progress in low-carbon binders. Cem. Concr. Res. 122, 247–250. https://doi.org/10.1016/j.cemconres.2019.05.009.

Sindhunata van Deventer, J.S.J., Lukey, G.C., Xu, H., 2006. Effect of curing temperature and silicate concentration on fly-ash-based geopolymerization. Ind. Eng. Chem. Res. 45, 3559–3568. https://doi.org/10.1021/ie051251p.

Soultana, A., Valouma, A., Bartzas, G., Komnitsas, K., 2019. Properties of inorganic polymers produced form brick waste and metallurgical slag. Minerals 9, 551. https://doi.org/10.3390/min9090551.

Tchadjie, L.N., Ekolu, S.O., 2018. Enhancing the reactivity of aluminosilicate materials toward geopolymer synthesis. Mater. Sci. 53, 4709–4733. https://doi.org/10.1007/s10853-017-1907-7.

Traven, K., Češnovar, M., Ducman, V., 2019. Particle size manipulation as an influential parameter in the development of mechanical properties in electric arc furnace slag-based AAM. Ceram. Int. 45 (17), 22632–22641. https://doi.org/10.1016/j.ceramint.2019.07.296.

US EPA, 1992. TCLP (Toxicity Characteristics Leaching Procedure), Method 1311, Revision 2, July 1992.

Van De Sande, J., Peys, A., Hertel, T., Rahier, H., Pontikes, Y., 2020. Upcycling of non-ferrous metallurgy slags: identifying the most reactive slag for inorganic polymer construction materials. Resour. Conserv. Recycl. 154, 104627. https://doi.org/10.1016/j.resconrec.2019.104627.

Wang, L., Chen, L., Tsang, D.C.W., Zhou, Y., Rinklebe, J., Song, H., Kwon, E.E., Baek, K., Ok, Y.S., 2019. Mechanistic insights into red mud, blast furnace slag, or metakaolin-assisted stabilization/solidification of arsenic-contaminated sediment. Environ. Int. 133, 105247. https://doi.org/10.1016/j.envint.2019.105247.

Xu, H., Van Deventer, J.S.J., 2000. The geopolymerisation of alumino-silicate minerals. Int. J. Miner. Process. 59, 247–266. https://doi.org/10.1016/s0301-7516(99)00074-5.

Xu, Y., Yang, B., Liu, X., Gao, S., Li, D., Mukiza, E., Li, H., 2019. Investigation of the medium calcium based non-burnt brick made by red mud and fly ash: durability and hydration characteristics. Int. J. Min. Met. Mater. 26, 983. https://doi.org/10.1007/s12613-019-1814-9.

Yan, B., Yu, Q.L., Brouwers, H.J.H., 2017. Evaluation of slag characteristics on the reaction kinetics and mechanical properties of Na2CO3 activated slag. Constr. Build. Mater. 131, 334–346. https://doi.org/10.1016/j.conbuildmat.2016.11.074.

Yip, C.K., Lukey, G.C., van Deventer, J.S.J., 2005. The coexistence of geopolymeric gel and calcium silicate hydrate at the early stage of alkaline activation. Cem. Concr. Res. 35, 1688–1697. https://doi.org/10.1016/j.cemconres.2004.10.042.

Yip, C.K., Lukey, G.C., Provis, J.L., Van Deventer, J.S.J., 2008. Effect of calcium silicate sources on geopolymerisation. Cem. Concr. Res. 38, 554–564. https://doi.org/10.1016/j.cemconres.2007.11.001.

Yuan, J., He, P., Jia, D., Yang, C., Zhang, Y., Yan, S., Yang, Z., Duan, X., Wang, S., Zhou, Y., 2016. Effect of curing temperature and SiO2/K2O molar ratio on the performance of metakaolin-based geopolymers. Ceram. Int. 42, 16184–16190. https://doi.org/10.1016/j.ceramint.2016.07.139.

Zaharaki, D., Komnitsas, K., 2009. Effect of additives on the compressive strength of slag-based inorganic polymers. Glob. Nest J. 11, 137–146. https://doi.org/10.30955/gnj.000585.

Zaharaki, D., Komnitsas, K., 2012. Long term behaviour of ferronickel slag inorganic polymers in various environments. Fresenius Environ. Bull. 21, 2436–2440.

Zaharaki, D., Komnitsas, K., Perdikatsis, V., 2010. Use of analytical techniques for identification of inorganic polymer gel composition. J. Mater. Sci. 45, 2715–2724. https://doi.org/10.1007/s10853-010-4257-2.

Zaharaki, D., Galetakis, M., Komnitsas, K., 2016. Valorization of construction and demolition (C&D) and industrial wastes through alkali activation. Constr. Build. Mater. 121, 686–693. https://doi.org/10.1016/j.conbuildmat.2016.06.051.

Zhang, Z.H., Yao, X., Zhu, H.J., 2009. Role of water in the synthesis of calcined kaolin-based geopolymer. Appl. Clay Sci. 43, 218–223. https://doi.org/10.1016/j.clay.2008.09.003.

Article

Factors Affecting Alkali Activation of Laterite Acid Leaching Residues

Konstantinos Komnitsas [1,*], Georgios Bartzas [2], Vasiliki Karmali [1] and Evangelos Petrakis [1]

[1] School of Mineral Resources Engineering, Technical University of Crete, 73100 Chania, Greece; vkarmali@isc.tuc.gr (V.K.); vpetraki@mred.tuc.gr (E.P.)

[2] School of Mining and Metallurgical Engineering, National Technical University of Athens, 15780 Zografos, Greece; gbartzas@metal.ntua.gr

* Correspondence: komni@mred.tuc.gr; Tel.: +30-28210-37686

Abstract: In this experimental study, the alkali activation of acid leaching residues using a mixture of sodium hydroxide (NaOH) and alkaline sodium silicate solution (Na_2SiO_3) as activators is investigated. The residues were also calcined at 800 and 1000 °C for 2 h or mixed with metakaolin (MK) in order to increase their reactivity. The effect of several parameters, namely the H_2O/Na_2O and SiO_2/Na_2O ratios present in the activating solution, the pre–curing time (4–24 h), the curing temperature (40–80 °C), the curing time (24 or 48 h), and the ageing period (7–28 days) on the properties of the produced alkali activated materials (AAMs), including compressive strength, porosity, water absorption, and density, was explored. Analytical techniques, namely X-ray diffraction (XRD), Fourier transform infrared (FTIR) spectroscopy, scanning electron microscopy (SEM), and elemental mapping analysis were used for the identification of the morphology and structure of the final products. The experimental results show that the laterite acid leaching residues cannot be alkali activated in an unaltered state, and the compressive strength of the produced AAMs barely reaches 1.4 MPa, while the mixing of the residues with 10 wt% metakaolin results in noticeably higher compressive strength (41 MPa). Moreover, the calcination of residues at 800 and 1000 °C has practically no beneficial effect on alkali activation. Alkali activated materials produced under the optimum synthesis conditions were subjected to high temperature firing for 2 h and immersed in distilled water or acidic solution (1 mol L^{-1} HCl) for 7 and 30 days in order to assess their structural integrity under different environmental conditions. This study explores the potential of alkali activation of laterite leaching residues amended with the addition of metakaolin for the production of AAMS that can be used as binders or in several construction applications in order to enable their valorization and also improve the environmental sustainability of the metallurgical sector.

Keywords: alkali activated materials (AAMs); laterite acid leaching residues; metakaolin; compressive strength

1. Introduction

Heap leaching is one of the oldest low-cost hydrometallurgical processes that can be used for the extraction of base and precious metals, mainly from low-grade ores and secondary resources [1–4]. The recovery of the metals from the pregnant leach solution (PLS) generated after leaching is mainly accomplished with the use of solvent extraction and electrowinning (SX/EW). Heap leaching can be applied for the treatment of various sulphide and oxide ores, while its efficiency depends on the mineralogical characteristics of the raw materials, the overall design of the process, and the selectivity of the leaching agent [5–9]. One of the major environmental concerns associated with heap leaching is the management of the final leaching residues, the so-called spent ore, which may contain residual metal values and chemicals. The current industrial practice indicates that these residues are mainly disposed/stockpiled on site or leached at later periods for additional metal extraction. However, if residues are not properly managed, e.g., are left

un-lined or unmonitored, they may cause severe contamination of nearby soils and water resources, especially in regions with favorable climatic conditions (e.g., high precipitation and temperature). So far, only a few studies have been carried out to predict or assess risk in waste disposal areas, while no studies are available for their valorization [10–13].

Laterite ores consist mainly of iron oxides (goethite (FeO(OH)) and hematite (Fe_2O_3)), aluminum oxides (Al_2O_3), quartz (SiO_2), kaolinite ($Al_2Si_2O_5(OH)_4$), nontronite ($Na_{0.3}Fe_2((Si, Al)_4O_{10}(OH)_2.nH_2O)$), serpentine ($((Mg,Fe,Ni,Al,Zn,Mn)_{2-3}.(Si,Al,Fe)_2O_5(OH)_4)$), and chlorite ($((Mg,Fe,Al)_6(Si,Al)_4O_{10}(OH)_8)$). They account for more than 70% of the world's nickel reserves and more than 50% of total Ni production [14–16]. In Greece, the major laterite deposits are located on the island of Evia and the Lokris region in central Greece, as well as in Kastoria in northwestern Greece [17]. These deposits are classified into two main types, namely limonitic, with high iron and low magnesium content (on Evia and in Lokris), and saprolitic, with high magnesium and low iron content (in Kastoria). Greek laterites have been treated pyrometallurgically for over 50 years for the production of ferronickel (FeNi) at the Larco General Mining & Metallurgical Co. S.A (LARCO) plant, located in Larymna (central Greece) [18]. Due to the decreasing grade of the Greek laterite ores and the urgent need to reduce environmental impacts, several studies have been carried out over the last 35 years for the development of alternative treatment techniques involving atmospheric [19,20], pressure [21], and heap leaching [22–24]. Geopolymers, inorganic polymers, or alkali activated materials (AAMs) are partially amorphous materials that are produced by chemical reactions between aluminosilicate raw materials, alkaline (NaOH and KOH), and/or silicate solutions. They contain Si-O-Al bonds, while the tetrahedral AlO_4 and SiO_4 units are built in three dimensional structures [25–29].

Alkali activated materials are partially amorphous and consist of a network of SiO_4 and AlO_4 tetrahedra, which are linked alternately by sharing all oxygen atoms. Their production requires reactions between aluminosilicate raw materials and concentrated alkaline and silicate solutions, often at ambient temperature. The release of Si and Al ions results in the formation of $Mx(AlO_2)y(SiO_2)z.nMOH.mH_2O$ gel (M: K^+ or Na^+), which hardens within a few hours. The degree of polymerization of silicate species is mainly affected by the alkalinity of the activating solution, the temperature, and the liquid to solid ratio in the starting mixture [30,31]. Raw materials and reagents are mixed together in order to optimize the $SiO_2:Al_2O_3$ ratio in the reactive paste and then cast and cured for a few hours at mild temperature so that matrices with the desired microstructure and properties are obtained [32–36]. Several factors affect the efficiency of alkali activation and the production of AAMs with beneficial properties, mainly the H_2O/Na_2O and the SiO_2/Na_2O molar ratios present in the alkali activating solution [33,36,37] and the curing temperature [38–40]. Alkali activation can be used for the valorization of several industrial wastes and the production of end-products with tailored physical and chemical properties, which can be used as building elements or binders, or in several other applications in various sectors [41–46].

So far, several studies have been carried out, mainly by African scientists, in order to investigate the alkali activation potential of lateritic soils, which are often used for the construction of roads and houses in African countries [47,48]. On the other hand, only a few studies pertinent to valorization of leaching residues through alkali activation are available [49]. Thus, the objective of the present study was to explore the alkali activation potential of laterite acid leaching residues in the presence of metakaolin (MK) and develop an integrated approach that will result in their valorization and the production of high added value products that can be used as binders or construction elements, in line with the zero-waste approach and circular economy principles.

2. Materials and Methods

2.1. Materials

The leaching residues (LR) were obtained after the implementation of laboratory column leaching tests using Greek laterites and H_2SO_4 as a leaching medium. The exper-

imental conditions used are similar to those described in previous recent studies [24,49]. For the production of AAMs, the leaching residues that were used as precursors were first subjected to solid:liquid separation and were then washed to remove any remaining acidity and dried at 80 °C for 1 day. In addition, in order to study the effect of calcination of the precursors on alkali activation, the LR were calcined at 800 and 1000 °C for 2 h. In order to regulate the Si/Al ratio in the precursors and thus increase their reactivity during alkali activation, metakaolin (MK) was mixed with the residues in different proportions, e.g., 5 and 10 wt%. Metakaolin was obtained after calcination of kaolin ($Al_2Si_2O_5(OH)_4$, Fluka) at 750 °C for 2 h in a laboratory oven (N–8L Selecta, Abrera, Spain). The use of metakaolin is considered beneficial during alkali activation due to its high amorphous content and its pozzolanic nature. Care should be taken during the selection of the kaolin's calcination temperature because, if the temperature is lower than 700 °C, the produced metakaolin contains unreactive kaolin and exhibits low reactivity, while, if the calcination temperature exceeds 850 °C, crystallization occurs and, as a result, lower amorphicity and reactivity are anticipated [50–52].

The chemical composition of the raw materials used, in the form of oxides, and their particle size (expressed as percentage smaller than a specific size) are presented in Table 1. Loss on ignition (LOI) was determined by heating the materials at 1050 °C for 4 h. Particle size analysis was determined using a laser particle size analyzer (Mastersizer S, Malvern Instruments, Malvern, UK).

Table 1. Chemical composition (wt%) and particle size distribution of raw materials.

Component (wt%)	Leaching Residues (LR)	Metakaolin (MK)
SiO_2	30.8	54.2
Al_2O_3	2.3	40.3
Cr_2O_3	2.5	0.02
Na_2O	-	1.3
Fe_2O_3	50.9	0.6
MgO	2.1	0.3
NiO	0.1	-
K_2O	-	2.4
TiO_2	0.6	0.4
CoO	0.02	<0.00097
MnO	0.3	0.01
CaO	3.7	0.1
P_2O_5	-	0.5
SO_3	-	0.3
ZnO	-	<0.00003
LOI *	6.2	-
Total	99.5	100.1
Particle Size	**μm**	**μm**
d_{90}	48.2	25.5
d_{50}	9.9	8.8

* LOI: Loss on ignition.

As seen from this table, the leaching residues mainly consist of SiO_2 and Fe_2O_3, while their low content in Al_2O_3 (2.7 wt%) indicates poor potential for successful alkali activation. Thus, the addition of metakaolin with high SiO_2 (54.2 wt%) and Al_2O_3 (40.3 wt%) content is anticipated to regulate the SiO_2/Al_2O_3 ratio and increase the reactivity of the starting mixture. Table 1 also shows that both raw materials have adequate and compatible size for alkali activation because their d_{90} values are lower than 50 μm [43].

2.2. Synthesis AAMs

The alkali activating solution used for the synthesis of AAMs consisted of sodium hydroxide (NaOH) and sodium silicate (7.5–8.5 wt% Na_2O and 25.5–28.5 wt% SiO_2, Merck) solutions. Sodium hydroxide was prepared by dissolving anhydrous pellets of NaOH

(Sigma–Aldrich, St. Louis, MO, USA) in distilled water so that solutions with different molarity (6−10 mol L^{-1}, M) were obtained. The alkali activating solution was left overnight prior to use.

The synthesis of AAMs was carried out by continuous mixing of the raw materials and the activating solution for about 10 min in a laboratory mixer until a homogenous paste was obtained, which was then cast in cubic molds $50 \times 50 \times 50$ mm^3. The molds were mechanically vibrated for 5 min to eliminate the air voids and then left at room temperature for 4 to 24 h (pre-curing time) to enable initiation of alkali activating reactions and early solidification of the paste. The sufficiently hardened specimens were removed from the molds, wrapped in plastic bags to avoid fast evaporation of water, and cured at 40, 60, and 80 °C for 24 or 48 h in a laboratory oven (Jeio Tech ON−02G, Seoul, Korea). After curing, the specimens were allowed to cool at room temperature for a period of 7 and 28 days. The AAM codes of all tests carried out, the mixing proportions, and the different H$_2$O/Na$_2$O and SiO$_2$/Na$_2$O ratios in the activating solution are given in Table 2.

Table 2. Alkali activated material (AAM) codes, raw material used, and selected molar ratios in the activating solution.

AAM Code	Solids (wt%)	NaOH (M)	NaOH (wt%)	H$_2$O (wt%)	Na$_2$SiO$_3$ (wt%)	L/S Ratio *	H$_2$O/Na$_2$O **	SiO$_2$/Na$_2$O **
LR1	78.1	6	2.2	8.8	10.9	0.25	21.2	1
LR2	75.6	8	3.1	9.1	12.2	0.27	17.4	1
LR3	73.4	10	4.0	9.3	13.3	0.29	14.8	1
MK	52.0	8	6.0	18.0	24.0	0.92	17.4	1
800LR 1000LR	76.0	8	3.0	8.9	12.0	0.26	17.4	1
LR95MK5 800LR95MK5 1000LR95M5	74.6	8	3.2	9.5	12.7	0.29	17.4	1
LR90MK10 800LR90MK10 1000LR90MK10	75.8	8	3.1	9.0	12.1	0.27	17.4	1
LR90MK10-1	82.7		3.5	10.4	3.4	0.16	14.8	0.3
LR90MK10-2	80.8	8	3.4	10.2	5.6	0.19	14.8	0.5
LR90MK10-3	75.0		2.0	7.0	16.0	0.30	21.2	1.6

* Liquid-to-solid ratio in the starting mixture, ** Molar ratios in the activating solution. LR1: AAMs produced from laterite leaching residues using 6 mol L^{-1} NaOH. 800LR: AAMs produced from calcined at 800 °C laterite leaching residues. LR95MK5: AAMs produced from laterite leaching residues and metakaolin using mass ratio 95:5. LR90MK10-1: AAMs produced from laterite leaching residues and metakaolin using mass ratio 90:10 and SiO$_2$/Na$_2$O molar ratio 0.3.

For all specimens, the determined properties were compressive strength (MPa), porosity (%), water absorption (%), and density (g cm^{-3}). The durability of the selected AAMs was evaluated after firing them at 200, 400, 600, and 800 °C for 2 h in a laboratory furnace (N–8L Selecta) as well as after immersion in distilled water or 1 mol L^{-1} HCl solution for 7 and 30 days.

All tests were carried out in triplicate, and the values given for each parameter are average; it is mentioned that the difference in measurements was marginal and did not exceed ± 3.8%.

2.3. Characterization of Raw Materials and the Produced AAMs

The laterite leaching residues were first pulverized using a Bico type pulverizer (Type UA, Fritsch, Dresden, Germany). Prior to alkali activation, their reactivity of raw materials was assessed through the leaching of 1.0 g of each raw material with 100 mL of 8 mol L^{-1} (M) NaOH solution for 24 h at room temperature (~20 °C) in 250 mL conical flasks under continuous stirring. After solid and liquid separation with the use of 0.45 μm pore size membrane filters (PTFE, Chromafil), the Al and Si concentration in the eluate was determined using an Inductively Coupled Plasma Mass Spectrometry (ICP MS, Agilent 7500cx) equipped with an Agilent ASX–500 Autosampler (Agilent, Santa Clara, CA, USA).

The chemical composition of the raw materials and the produced AAMs was determined using a Bruker S2 Ranger–energy dispersive X–ray fluorescence spectrometer (ED–XRF, Bruker, Karlsruhe, Germany), while their mineralogical analysis using an X-ray diffractometer (Bruker AXS, D8–Advance, Bruker, Karlsruhe, Germany) with a Cu tube and a scanning range from 4° to 70° 2theta (θ) and a step of 0.02°, and 0.2 s/step measuring time. The crystalline phases present in the raw materials and the produced specimens were identified with the use of the DiffracPlus Software (EVA v. 2006, Bruker, Karlsruhe, Germany) and the PDF database. Fourier transform infrared (FTIR) analysis was carried out using pellets produced by mixing the pulverized raw material or AAM with KBr at a ratio of 1:100 *w/w*. The analysis was carried out at atmospheric pressure under nitrogen atmosphere, with a flow rate of 100 mL min^{-1} and heating rate of 10 °C min^{-1} using a PerkinElmer 1000 spectrometer (PerkinElmer, Akron, OH, USA), in the spectra range of 400 to 4000 cm^{-1}. Microstructural analysis of the produced AAMs was performed with the use of scanning electron microscopy (SEM) and energy dispersive X–ray spectroscopy (EDS). For that purpose, a JEOL–6380LV scanning microscope (JEOL Ltd., Tokyo, Japan), operating at an accelerating voltage of 20 kV equipped with an Oxford INCA EDS microanalysis system (Oxford Instruments, Abingdon, UK), was used.

The Brunauer–Emmett–Teller (BET) nitrogen adsorption method (using a Quantachrome Nova 2200 analyser (Anton Paar QuantaTec Inc., Boynton Beach, FL, USA) was considered for the determination of the specific surface area of the raw materials. The compressive strength of the produced AAMs was determined with the use of a MATEST C123N load frame (compression and flexural machine, Matest S.p.A, Treviolo, Bergamo, Italy) with dual range 500/15 kN. Finally, the apparent density (g cm^{-3}), the porosity (%), and the water absorption (%) of the selected AAMs were determined according to the BS EN 1936 standard; 3 measurements using specimens 50 ± 5 mm × 50 ± 5 mm × 50 ± 5 mm were taken, and average values are given in the paper [53].

3. Results

3.1. Reactivity of Raw Materials

So far, most studies carried out to assess the reactivity and subsequently the potential of various raw materials (i.e., virgin materials, by-products, and wastes) for alkali activation focused on the calculation of SiO_2/Al_2O_3 molar ratios in the raw materials (precursors) [54–58]. However, this ratio provides only an indication of the reactivity rather than defines the actual dissolution of the Si and Al that participate during alkali activation in the formation of Si-O-Al bonds [59–63]. The concentration of Al and Si (in mg L^{-1}) in the eluate after alkaline leaching, using 8 mol L^{-1} NaOH solution, indicates the reactivity of the raw materials used in the present study (Table 3); in the same Table, the Si/Al molar ratio in the eluate is also provided.

Table 3. Concentration of Si, Al, and Si/Al molar ratios in the eluate.

| Raw Material	Si (mg L^{-1})	Al (mg L^{-1})	Si/Al (Molar Ratio)
Leaching residue	20.1 ± 1.7	2.4 ± 0.4	8.4 ± 2.2
Leaching residue calcined at 800 °C	12.9 ± 0.9	0.6 ± 0.1	21.5 ± 5.1
Leaching residue calcined at 1000 °C	2.0 ± 0.3	0.4 ± 0.1	5.4 ± 2.0
Metakaolin	58.7 ± 3.2	41.9 ± 2.3	1.4 ± 0.2

It is observed from this data that, after alkaline leaching of laterite residues, the concentrations of Si and Al in the eluate were 20.1 and 2.4 mg L^{-1}, respectively. Calcination of laterite residues at 800 °C significantly reduced the concentration of Si and Al in the eluate to 12.9 and 0.6 mg L^{-1}, respectively, while the increase of the calcination temperature to 1000 °C resulted in a much lower concentration of both elements in the eluate. Previous studies have shown that, after calcination of laterite at temperature higher than 800 °C, structural modifications occur, mainly due to the formation of spinels ($Si_3Al_4O_{12}$) [64,65].

On the other hand, metakaolin exhibits much higher reactivity, as also indicated in earlier studies [66–68]. In our case, the concentration of Si and Al in the eluate after alkaline leaching of metakaolin was 58.7 and 41.9 mg L^{-1}, respectively, values that indicate high reactivity during alkali activation and provision of sufficient Si and Al ions that can participate in the formation of aluminosilicate bonds.

3.2. Properties of AAMs

3.2.1. Alkali Activation of Laterite Leaching Residues

Figure 1 shows the compressive strength of laterite residue based AAMs as a function of curing temperature (40, 60, and 80 °C) in relation to the H_2O/Na_2O molar ratios (21.2 for LR1, 17.4 for LR2, and 14.8 for LR3) in the activating solution. The difference in H_2O/Na_2O molar ratios is due to the slightly different S/L ratios used in each case to obtain a paste with optimum flowability. In all tests, the curing and ageing periods were 24 h and 7 days, respectively, while the SiO_2/Na_2O molar ratio in the activating solution was kept constant at 1. It can be seen from this figure that the effect of temperature is important for all H_2O/Na_2O molar ratios tested, but the maximum compressive strength recorded is only 1.4 MPa for LR2 (curing temperature, 80 °C, and H_2O/Na_2O molar ratio in the activating solution, 17.4). It is therefore evident that the laterite leaching residues cannot be effectively alkali activated in an unaltered state, mainly due to their low content of Al_2O_3 (2.7 wt%.), as shown in Table 1. As a result of this, the concentration of Al ions in the alkaline solution is low and, thus, the Si/Al molar ratio in the produced paste is unfavorable for alkali-activation (Table 3). It is also important to note that the increase of the ageing period from 7 to 28 days has only a marginal beneficial effect on the compressive strength of the produced specimens, which increases slightly to 1.7 MPa (data not shown).
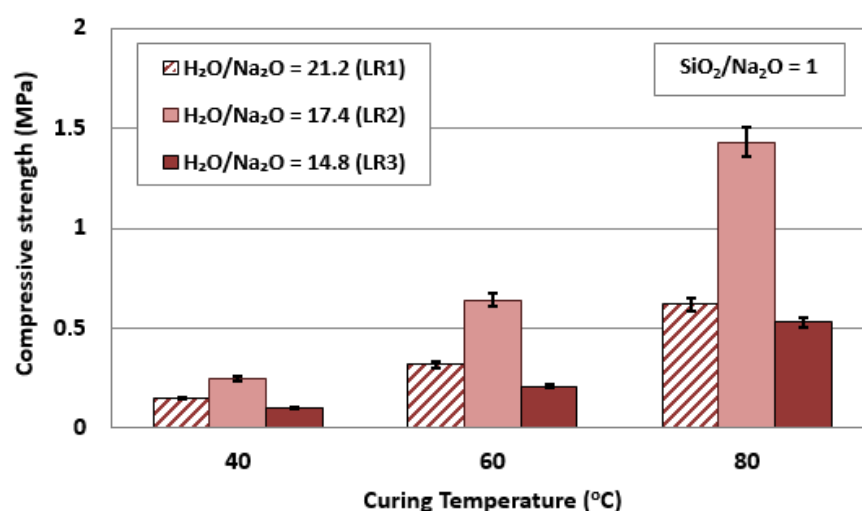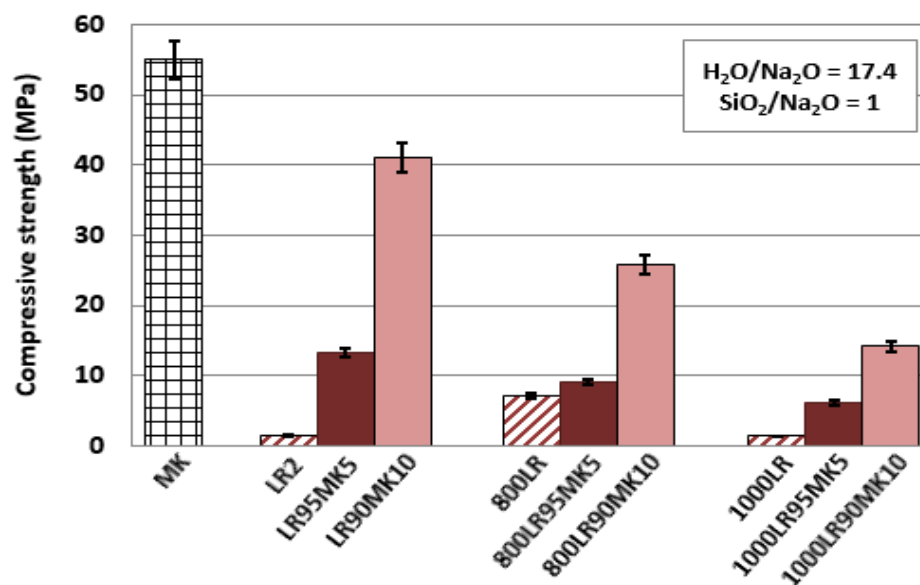

Figure 1. Effect of curing temperature in relation to H_2O/Na_2O molar ratios in the activating solution on the compressive strength of laterite based AAMs (pre-curing time, 4 h; curing time, 24 h; ageing period, 7 days; error bars denote standard deviation of measurements obtained from three specimens).

3.2.2. Effect of the Addition of Metakaolin—Calcination of Leaching Residues

Figure 2 shows the effect of the addition of metakaolin in the starting mixture as well as th effect of the calcination of leaching residues on the compressive strength of the produced AAMs. It is seen from this data that the compressive strength of the LR95MK5 specimen, for which the metakaolin addition in the staring mixture was only 5 wt%, increased from 1.4 MPa to 12 MPa. When the metakaolin addition increased to 10 wt% (LR90MK10 specimen), a much higher compressive strength value was recorded, i.e., 41 MPa. This is due to the high alkali activation potential of metakaolin for which the compressive strength of the respective AAM (MK specimen) reached 55 MPa. The beneficial effect of the addition of metakaolin on the compressive strength of the produced AAMs was anticipated by

taking into consideration its chemical analysis, as shown in Table 1 (SiO_2, 54.2 wt%; Al_2O_3, 40.3 wt%) as well as the concentration of Si and Al in the eluate produced after its alkaline leaching, as shown in Table 3 (58.7 mg L^{-1} Si and 41.9 mg L^{-1} Al, respectively).


Figure 2. Effect of calcination temperature and addition of MK (5 wt% and 10 wt%) to LR on the compressive strength of the produced AAMs (pre-curing time, 4 h; curing temperature, 80 °C; curing period, 24 h; ageing period, 7 days; error bars denote standard deviation of measurements obtained from three specimens).

Another issue that has to be underlined is that both laterite residues and metakaolin had similar grain size, as shown in Table 1, a factor that is considered beneficial during alkali activation. The specific surface area of laterite leaching residues was 2.1 m²/g, while that of metakaolin was 2.4 m²/g, similar to the value determined in another recent study [68]. On the other hand, it is seen that calcination of the laterite leaching residues has a detrimental effect on the compressive strength of the produced specimens. This is mainly due to the decreased dissolution of Si and Al ions from the calcined residues (Table 2), which does not enable efficient alkali activation and production of a matrix with beneficial properties. It is mentioned that the specific surface area of calcined laterite leaching residues increased to 15 m²/g, but its reactivity was not increased due to the occurred phase transformations; it is also noted that materials with high surface areas often require more water during alkali activation and, thus, higher liquid to solid ratios need to be used to obtain a paste with beneficial properties. The only specimens (800LR90MK10 and 1000LR90MK10) that retained a good to moderate compressive strength were the ones produced after alkali activation of mixtures containing 90 wt% laterite residues calcined at 800 °C or 1000 °C and 10 wt% metakaolin; the respective compressive strength values recorded were 26 and 13 MPa.

3.2.3. Effect of SiO_2/Na_2O and H_2O/Na_2O Molar Ratios in the Activating Solution

The effect of SiO_2/Na_2O molar ratio in relation to the corresponding H_2O/Na_2O molar ratios in the alkali activating solution on the compressive strength of LR90MK10 AAM are shown in Figure 3. The H_2O/Na_2O ratios shown in this figure are the optimum ones for each case examined. The use of a starting mixture containing 90 wt% laterite leaching residue and 10 wt% metakaolin was selected because the respective AAM acquired the highest compressive strength (41 MPa), as shown in Figure 2.
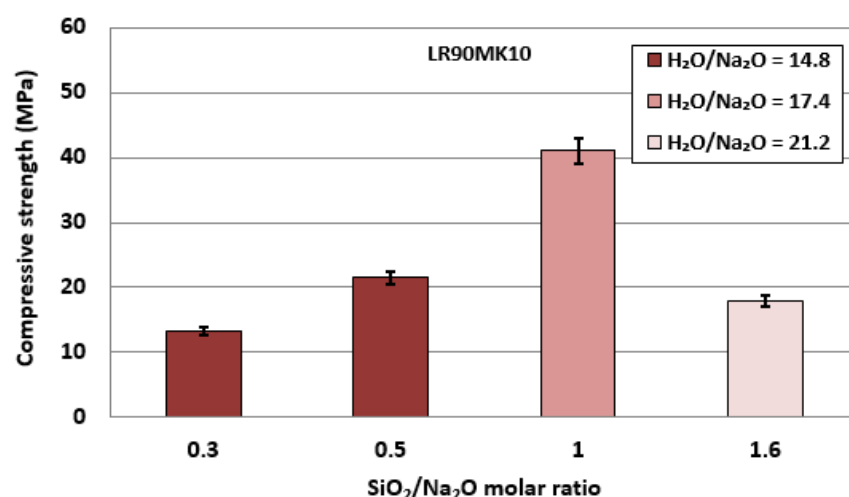
Figure 3. Effect of SiO_2/Na_2O molar ratios in relation to the corresponding H_2O/Na_2O molar ratios in the activating solution on the compressive strength of LR90MK10 AAMs (pre-curing time, 4 h; curing temperature, 80 °C; curing period, 24 h; ageing period, 7 days; error bars denote standard deviation of measurements obtained from three specimens).

The results indicate that the maximum compressive strength (41 MPa) was obtained for a SiO_2/Na_2O molar ratio equal to 1.0. Higher or lower SiO_2/Na_2O molar ratios resulted in the production of specimens with lower strength, which did not exceed 21 MPa, a value 50% lower compared to the maximum one obtained. This may be explained by the presence of deficient or excessive alkalinity in the reactive paste, which affects the formation of aluminosilicate bonds and, thus, the microstructure and the strength of the produced specimens. Optimum alkalinity in the reactive paste results in the formation of sufficient $Si(OH)_4$ and $Al(OH)_4$ oligomers and enables polycondensation, which improves the strength of the produced specimens. On the other hand, lower alkalinity, expressed by high SiO_2/Na_2O molar ratios, slows down the rate of alkali activation reactions while very high alkalinity, expressed by lower SiO_2/Na_2O molar ratios, results in early precipitation of aluminosilicate gel and increased viscosity of the paste.

The trend shown in the evolution of the compressive strength vs. the SiO_2/Na_2O molar ratio in this study is very similar to the trend shown in an earlier study investigating the effect of the SiO_2/K_2O molar ratio on the performance of metakaolin based geopolymers [69].
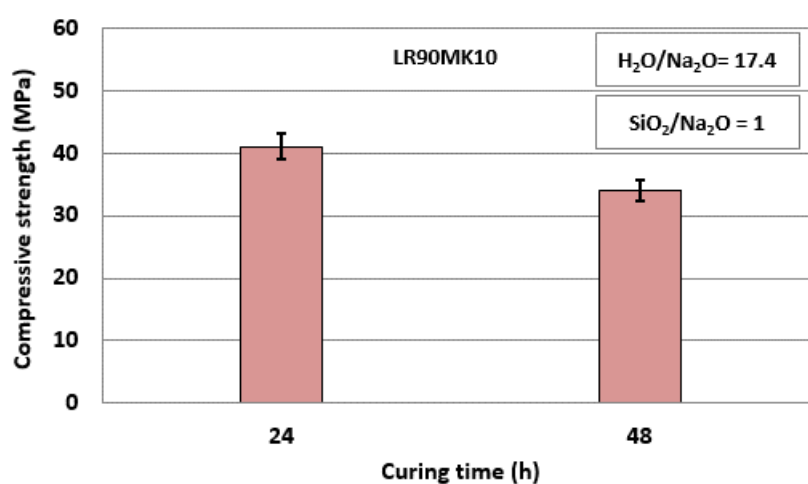
3.2.4. Effect of Pre-Curing and Curing Time

Figure 4a,b shows the effect of pre-curing (4 to 24 h) and curing time (24 to 48 h) on the compressive strength of LR90MK10 AAM, respectively.

It is seen from these results that the compressive strength decreases with increasing pre-curing and curing time. The maximum value obtained was 41 MPa after a pre-curing period of 4 h and a curing period of 24 h. The duration of the pre-curing period of the paste defines the extent to which alkali activation reactions proceed so that bonds are developed and specimens acquire sufficient early strength. Longer pre-curing periods may cause higher evaporation of water, which in turn results in incomplete reactions, development of internal stresses, and voids, which hinder the development of high strength during curing. Similar issues are anticipated after prolonged curing periods. It is mentioned that optimum pre-curing and curing periods, which play a major role in the properties of the produced AAMs, depend on the characteristics of the precursors, the S/L ratio during mixing, and the curing temperature, need to be carefully defined during alkali activation [36,70–73].
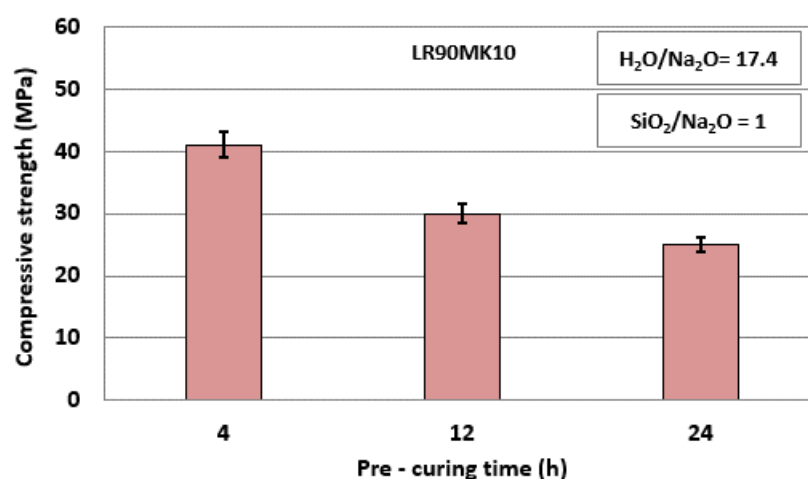
(a)

(b)

Figure 4. Effect of (**a**) pre-curing time and (**b**) curing time on the compressive strength of LR90MK10 AAM (curing temperature, 80 °C; ageing period, 7 days; error bars denote standard deviation of measurements obtained from three specimens).

3.2.5. Porosity, Water Absorption, and Apparent Density of Selected AMMs

Table 4 shows the porosity (%), water absorption (%), and apparent density (g cm^{-3}) of the selected AMMs, i.e., LR2, LR95MK5, and LR90MK10; the compressive strength values are also given. It can be observed from this data that the LR90MK10 specimen, which acquires the maximum compressive strength (41 MPa), has the lowest porosity (21.3%) and water absorption (5.1%), while its apparent density (2.3 g cm^{-3}) is almost identical to the one obtained by LR95MK5. The LR2 specimen, produced by alkali activation of laterite residues using a H_2O/Na_2O molar ratio in the 17.4activating solution is characterized by the highest porosity (36.8%) and water adsorption (30.7%) and the lowest apparent density (1.8 g cm^{-3}). These values are anticipated by considering the poor alkali activation potential of leaching residues and the very low compressive strength acquired by the respective AAM.

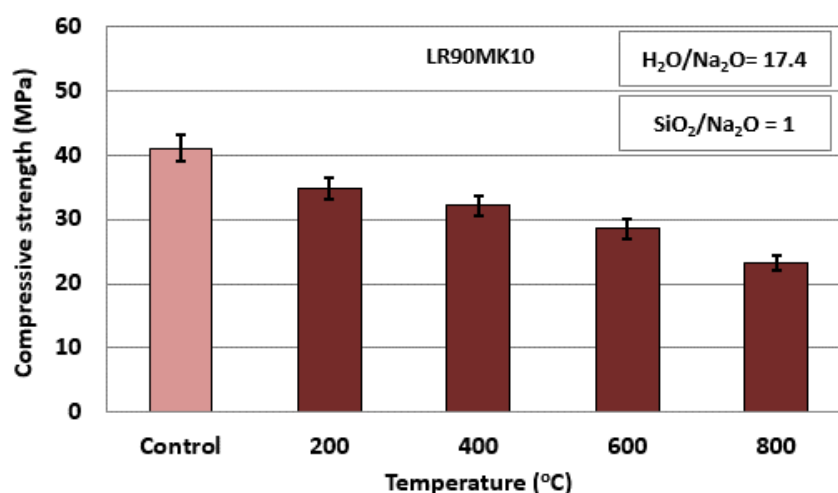**Table 4.** Porosity, water absorption, and apparent density of selected AAMs.

AAM Code	Compressive Strength (MPa) *	Porosity (%)	Water Absorption (%)	Apparent Density (g cm^{-3})
LR2	1.43	36.8	30.7	1.8
LR95MK5	13.3	27.9	13.1	2.2
LR90MK10	41.0	21.3	5.1	2.3

* Curing temperature, 80 °C; curing time, 24 h; ageing period, 7 days.

3.2.6. Structural Integrity of LR90MK10 AAM

The structural integrity of LR90MK10 AAMs was assessed after firing for a period of 2 h at a broad temperature range varying between 200 and 800 °C and after immersion in distilled water and acidic solution (1 mol L^{-1} HCl) for 7 and 30 days. All AAMs tested were produced under the optimal conditions, i.e., H_2O/Na_2O molar ratio, 17.4; curing temperature, 80 °C; and ageing period, 7 days.

Figure 5 presents the evolution of the compressive strength of LR90MK10 AAMs after firing. The compressive strength of the control specimen, which was not subjected to firing, is also shown for comparison. It is seen from this data that the compressive strength decreases gradually with the increase of firing temperature and finally drops to 23.1 MPa at 800 °C, which is considered sufficient for the use of these AAMs as fire resistant materials. It is mentioned for comparison that thermal-stressing (from ambient temperature to 1000 °C) results in a reduction of the unconfined compressive strength (UCS) of high-strength concrete by 96%, from about 110 MPa to about 5 MPa [74].
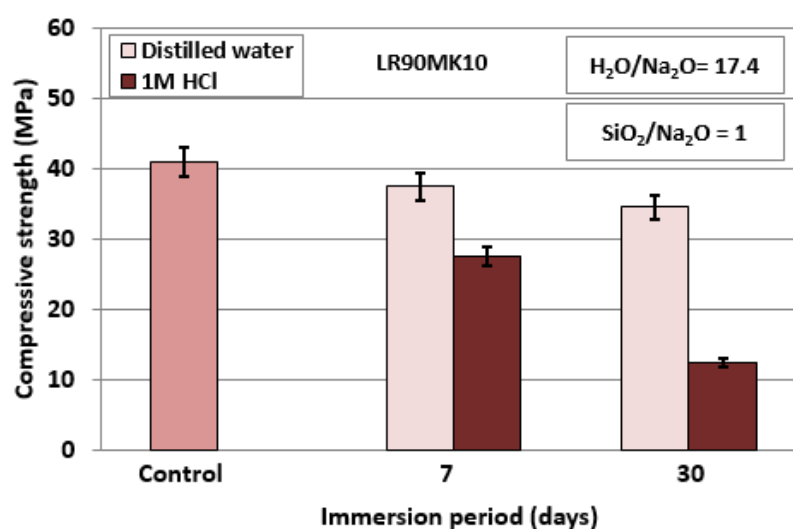

Figure 5. Evolution of the compressive strength of LR90MK10 AAMs after firing between 200 and 800 °C for 2 h (pre-curing time, 4 h; curing time, 24 h; curing temperature, 80 °C; ageing period, 7 days; error bars indicate the standard deviation of measurements obtained from three specimens.

Table 5 presents the evolution of weight loss (%), volumetric shrinkage (%), porosity (%), water absorption (%), and apparent density (g cm^{-3}) of the fired AAMs. It is seen from this data that the specimens after firing at 800 °C acquire the lowest compressive strength (23.1 MPa) and apparent density (1.8 g cm^{-3}), and on the other hand the highest weight loss (12. 1%), shrinkage (7.5%), porosity (27.2%), and water adsorption (14.8%). As Duxson et al. [75] mention, the increase of shrinkage takes place stepwise in four temperature regions: in Region I, at temperatures below 100 °C, which is attributed to the release of free water; at Region II, between 100–250 °C, due to pore water released from the formed gel; at Region III, between 250–600 °C, due to the loss of bound hydroxyls; and at Region IV, at temperatures higher than 700 °C due to a viscous sintering–like process. As a result of these processes, the specimens also acquire the lowest density.

Table 5. Selected properties of LR90MK10 AAMs after firing at high temperatures.

Temperature (°C)	Compressive Strength (MPa)	Weight Loss (%)	Shrinkage (%)	Apparent Density (g cm^{-3})	Porosity (%)	Water Absorption (%)
Control AAM	41.0	-	-	2.3	21.3	5.1
200	34.8	6.3	3.2	2.0	24.8	8.2
400	32.1	7.6	4.3	2.1	25.1	10.8
600	28.5	11.2	7.3	1.8	25.0	11.3
800	23.1	12.1	7.5	1.8	27.2	14.8

Figure 6 shows the compressive strength of LR90MK10 AAMs after immersion in distilled water or acidic solution (1 mol L^{-1} HCl) for 7 and 30 days. The compressive strength of the control specimen is also provided for comparison. As seen from this data, the compressive strength of the specimens drops slightly to 37.5 MPa and 34.5 MPa (23.3% decrease) after their immersion in distilled water for 7 and 30 days, respectively. A bigger decrease in compressive strength is observed, as anticipated, when specimens are immersed in 1 mol L^{-1} HCl. The recorded values are 27.5 MPa and 12.5 MPa (72.3% decrease), when the specimens are immersed for 7 and 30 days, respectively. It is also mentioned that a slight to moderate increase of solution pH is noted after immersion for 30 days. Immersion in distilled water results in an increase of pH from 7.6 to 10.8, while immersion in 1 mol L^{-1} HCl results in a pH increase from 1.3 to 2.3, as also shown in earlier studies with the use of AAMs produced from different precursors [36,40].

Figure 6. Compressive strength of LR90MK10 AAMs after immersion in distilled water and 1 mol L^{-1} HCl for 7 and 30 days; synthesis conditions: pre-curing time, 4 h; curing period, 24 h; curing temperature, 80 °C; ageing period, 7 days; error bars indicate the standard deviation of measurements obtained from three specimens.

3.2.7. Comparison with Other Studies

Table 6 compares the results of this study to those obtained from other studies that investigated the production of laterite soil-based AAMs using pre-cursors with different mineralogical composition that were not subjected to acid leaching that affects their nature.

Gualtieri et al. [76] produced AAMs by alkali activation of calcined laterite (700 °C for 2 h) and metakaolin with the use of phosphoric acid, sodium hydroxide, and sodium silicate solutions as activators. The results showed that the highest compressive strength achieved was low, more specifically, 4 MPa, when the curing temperature was 60 °C and the ageing period was 28 days. Phummipham et al. [77] produced AAMs by mixing marginal lateritic soil with fly ash at a mass ratio of 70:30, using sodium hydroxide and sodium silicate solutions as activators. The produced specimens acquired slightly higher compressive

strength, 7.1 MPa, after curing at 30 °C and ageing for 7 days. Furthermore, Nkwaju et al. [78] investigated the potential of sugar cane bagasse as reinforcement of laterite soil-based geopolymer cement. The laterite soil, which was the precursor, was calcined at 700 °C for 4 h prior to use. The produced specimens acquired compressive strength that varied between 15 and 50 MPa, after curing at room temperature and ageing for 28 days. Lemougna et al. [67] produced AAMs using a mixture of calcined laterite (700 °C for 2 h) and ground granulated blast furnace slag (50 wt% by weight) as precursors, while the activators were sodium hydroxide and sodium silicate solutions. The paste cured at 25 °C and, after ageing for 28 days, the produced specimens acquired a compressive strength of 65 MPa. This high value is due to the beneficial effect of slag, which is a by-product with noticeable alkali activation potential. Kaze et al. [73] produced AAMs using laterite calcined at 600 °C and meta–halloysite as precursors and sodium hydroxide and sodium silicate solutions as activators. Meta-halloysite was produced by calcining halloysite at 600 °C for 4 h. The produced AMMs acquired a compressive strength of 45 MPa after curing at 25 ± 3 °C and ageing for 28 days. Finally, Obonyo et al. [79] investigated the geopolymerization potential of two lateritic soils, also after calcination at 700 °C for 4 h in the presence of river sand, also using sodium hydroxide and sodium silicate solutions as alkali activators. The paste was pressed and cured at room temperature for 7 days in order to produce disks of 40 mm diameter and 6–9 mm thickness. The authors studied in depth the mechanisms involved in the process as well as the mineralogy and morphology of the produced specimens.

Table 6. Comparison of results of various studies using laterite-based AAMs.

| Raw Materials	Sio$_2$/Na$_2$O Molar Ratio	Conditions		Compressive Strength (MPa)	Reference
		Temperature (°C)	Ageing Period (Days)		
Laterite (calcined at 700 °C for 2 h) and metakaolin	3.0	60	28	4	[76]
Marginal lateritic soil and fly ash	5.6	27–30	7	7.1	[77]
Iron-rich laterite (calcined at 700 °C for 4 h) and bagasse fibers	1.4	25	28	14–50	[78]
Laterite (calcined at 700 °C for 2 h) and slag	1.6	25	28	65	[67]
Laterite (calcined at 600 °C) and metahalloysite (calcined halloysite clay at 600 °C)	0.75	25 ± 3	28	45	[73]
Laterite leaching residues and metakaolin	1.0	80	7	45	This study

In the present study, the produced AAMs, after alkali activation of laterite leaching residues amended with 10 wt% metakaolin, acquired a relatively high compressive strength of 41 MPa. The SiO$_2$/Na$_2$O molar ratios used varied from 0.3 to 1.6 due to the different configurations used. The results show that the use of metakaolin enables the successful alkali activation of a by-product that has very low inherent alkali activation potential.

3.3. Mineralogy-Morphology of AAMs

3.3.1. XRD Analysis

The XRD patterns of laterite leaching residues and selected AAMs are shown in Figure 7. It is observed that the main mineralogical phases present in the leaching residues

are quartz (SiO_2) and hematite (Fe_2O_3), while other minor phases are goethite (FeO(OH)), clinochlore (($Mg,Fe)_5Al(Si_3Al)O_{10}(OH)_8$), and lizardite (($Mg,Fe)_3Si_2O_5(OH)_4$) (Figure 7a). The main Ni-bearing phases detected in the leaching residues are chromite (Cr_2O_3 NiO) and willemseite (($Ni,Mg)_3Si_4O_{10}(OH)_2$). As a result of the acid column leaching of limonitic laterite (CaO content, 3.7 wt%; Table 1) with the use H_2SO_4 solution, gypsum was also detected in the residues. On the other hand, the main mineralogical phases present in the XRD pattern of metakaolin are quartz and muscovite with a broad amorphous hump seen between 17° and 40° 2-Theta (Figure 7b).
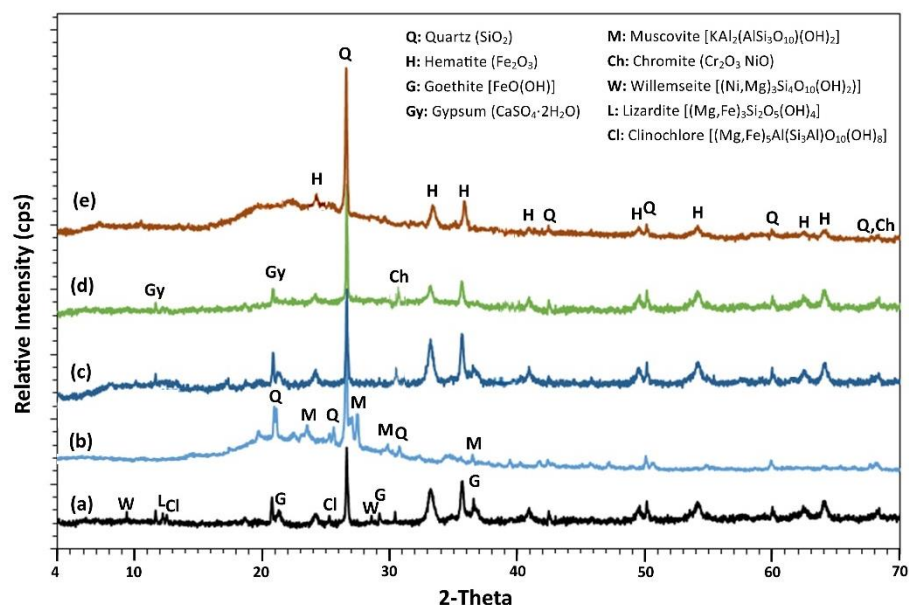
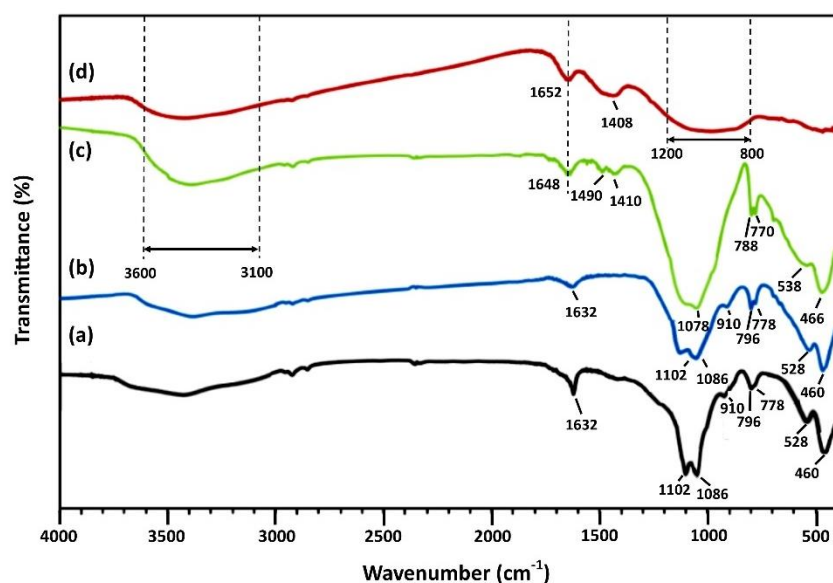**Figure 7.** XRD patterns of (**a**) laterite leaching residues, (**b**) metakaolin, and (**c**) AAMs produced using only leaching residues (LR2 AAM) as well as by mixing (**d**) leaching residues and metakaolin at mass ratio 90:10 (LR90MK10) and (**e**) LR90MK10 after firing at 800 °C for 2 h.

After alkali activation (LR2 AAM), which, as explained earlier in this paper, is poor due to the low content of Al_2O_3, a slight increase in the intensity of the peaks of the crystalline phases such as quartz and hematite is observed, compared to the ones present in the laterite leaching residues (Figure 7c). This observation confirms that these phases do not participate in the alkali activation reactions [67].

On the contrary, the intensity of the peaks of the crystalline phases present in LR90MK10 AAM is significantly lower compared to the ones present in the leaching residues; this is due to metakaolin addition, which has a high alkali activation potential as a result of the dissolution of sufficient number of Si and Al ions that participate in alkali activated reactions and the development of the geopolymeric network (Figure 7d). Thus, a broad hump between 17 and 40° 2-Theta in the XRD pattern, which represents the amorphous content typical for metakaolin-based AAMs, is seen [80], which justifies the high compressive strength acquired by LR90MK10 AAM (45 MPa). After firing the leaching residues at 800 °C, the amorphous hump of the LR90MK10 AAM is more apparent (Figure 7e). However, the center of the hump shifts towards lower 2-Theta, i.e., from 27° 2-Theta to 26.5° 2-Theta for the specimen before and after firing of the laterite leaching residues, respectively. This slight decrease implies partial depolymerization of metakaolin after firing at 800 °C and the subsequent reorganization of its structure resulting in partial reduction of compressive strength (23.1 MPa), as has also been reported in earlier studies [81]. In all laterite leaching residue based AAMs (before firing), minor but detectable quantities of crystalline chromite and gypsum were detected in the corresponding XRD patterns, indicating their partial dissolution after alkali activation.

3.3.2. FTIR Analysis

The FTIR spectra, over the range 4000–400 cm^{-1}, of the leaching residues and the AAMs produced by mixing them (unaltered or after firing) with metakaolin at mass ratio 90:10 (LR90MK10 AAM) are presented in Figure 8. In line with the XRD results, FTIR spectra of leaching residues show the characteristic bands at 460 cm^{-1} and 694 cm^{-1}, the double bands at 778 cm^{-1} and 796 cm^{-1}, and 1086 cm^{-1} and 1145 cm^{-1}, which are attributed to quartz [82], and small shoulders at 528 cm^{-1} and 910 cm^{-1}, which are attributed to hematite and goethite, respectively (Figure 8a) [24,49,67]. After alkali activation, the bands of the major crystalline phases (quartz and hematite) present in the laterite leaching residues remained almost unaffected in the LR2 AAM (Figure 8b), which confirms the low reactivity of the leaching residues during alkali-activation.

Figure 8. FTIR spectra of (**a**) laterite leaching residues and AAMs produced using (**b**) only leaching residues (LR2 AAM) as well as by mixing (**c**) leaching residues and metakaolin at mass ratio 90:10 (LR90MK10) and (**d**) LR90MK10 after firing at 800 °C for 2 h.

However, compared to LR2 AAM, a clear difference in the shape, position, and depth of the bands can be seen in the spectrum of the LR90MK10 AAM in the region of 450–1250 cm^{-1} (Figure 8c). This is a result of the different vibrations belonging to the Al–, Fe–, and Si– containing phases in the raw material/binder (leaching residues and metakaolin) and the respective Si–O–Si, Fe–O–Si, and Si–O–Al bonds in the produced alkali activated matrices. In this context, the rocking band seen at 460 cm^{-1} in the leaching residues and the LR2 AAM (Figure 8a,b), which was slightly shifted to 466 cm^{-1} in LR90MK10 AAM (Figure 8c), is attributed to the bending motions of the Al- and Si-containing phases [24,67]. The band present in LR2 AAM at 528 cm^{-1} was shifted to higher frequency, i.e., 538 cm^{-1}, in LR90MK10 AAM, while the one observed at 910 cm^{-1} disappeared, possibly due to enhanced dissolution of Fe ions from the crystalline phase of hematite and goethite, respectively, that were present in the laterite leaching residues and their subsequent participation in the alkali-activated reactions [73,83]. Moreover, the major difference between LR2 and LR90MK10 AAMs is due to the shifting of the pair of strong bands at 778 cm^{-1} and 796 cm^{-1} observed in the LR2 (as well as in the leaching residues), which is associated with the asymmetric stretching vibrations of the Si–O–Al bonds towards lower wavenumbers (770 cm^{-1} and 788 cm^{-1}), thus indicating the formation of inorganic gel in LR90MK10 AAM [73,84]. The displacement of the band shown at 1086 cm^{-1} in LR2 AAM to a lower wavelength (1080 cm^{-1}) in LR90MK10 AAM indicates the dissolution of aluminosilicate phases present in the laterite leaching residues and their subsequent polymerization during alkali-activation. The intense absorption

bands at ~1410 cm^{-1} and ~1490 cm^{-1}, shown only in the LR90MK10 AAM, are attributed to asymmetric stretching vibrations of O-C-O bonds due to the formation of carbonation products from the reaction between the alkali activated silicates and the atmospheric CO$_2$ during the curing period [73]. The weaker band located at 1632 cm^{-1} in the LR2 AAM, which shifted as a sharper peak at 1648 cm^{-1} in the LR90MK10 AAM, corresponds to the characteristic bending vibrations of H-O-H [85]. The presence of water is more evident in LR90MK10 AAM because a relatively wide absorption band region appeared between 3000 cm^{-1} and 3700 cm^{-1} belonging to stretching vibrations of the OH groups as a result of the hydration processes that took place during alkali activation. After firing the laterite leaching residues at 800 °C, a structural reorganization of the LR90MK10 AAM was noticed, which is indicated by the very broad band shown in the region of 800–1200 cm^{-1} as result of the stretching vibrations of the Si(Al)–O groups (Figure 8d) [67]. This change in the polymeric matrix, along with the incomplete dihydroxylation, represented by a narrower band region between 3000 cm^{-1} and 3700 cm^{-1} compared to LR90MK10 AAM, results in lower compressive strength [86].
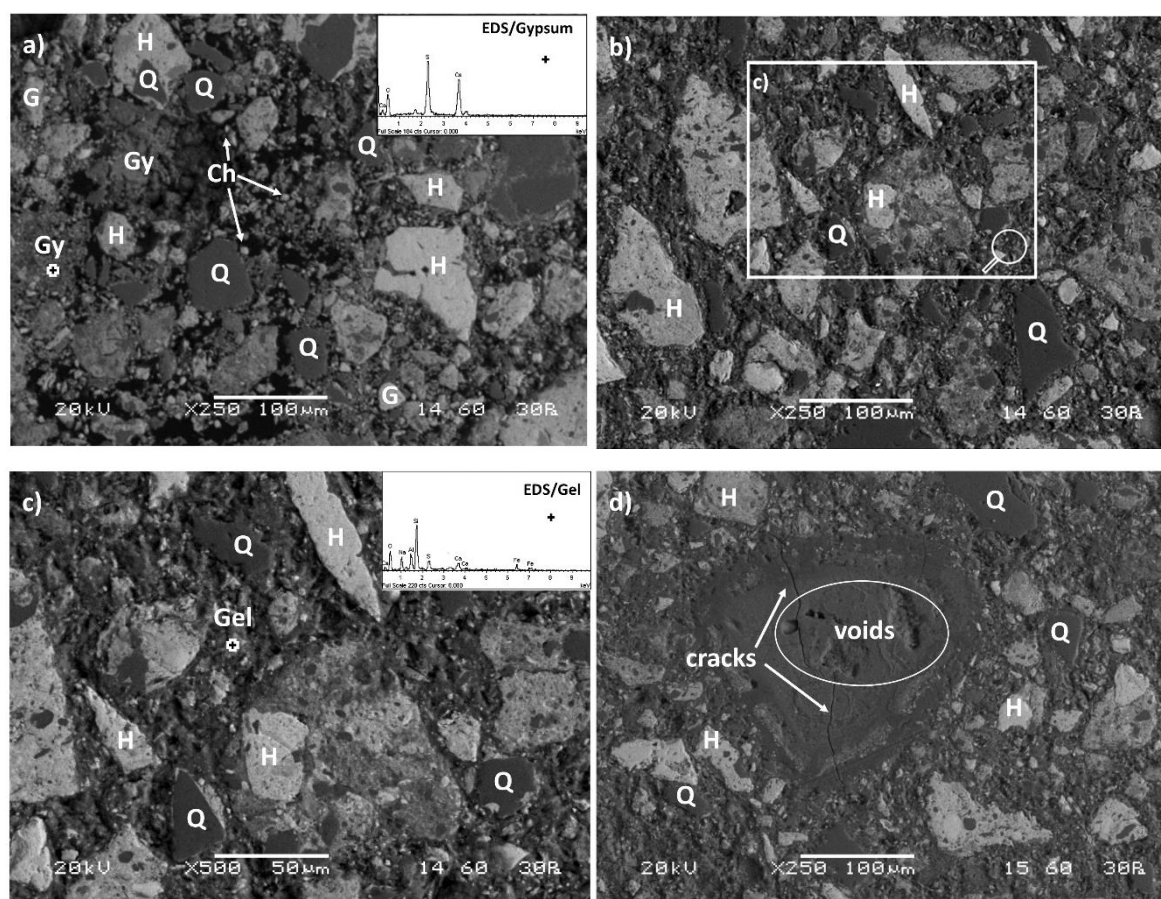
3.3.3. SEM Analysis

Figure 9 shows SEM-back-scattered electron (BSE) images of selected AAMs produced using only laterite leaching residues (LR2) as well as by mixing leaching residues and metakaolin at mass ratio 90:10 (LR90MK10) both as is and after firing at 800 °C for 2 h. Among the AAMs examined, significant differences in the microstructure and the associated EDS analyses were noticed, depending on the nature of the starting raw materials/binders used. As also shown in the XRD analysis, the examination of LR2 AAM by SEM/EDS (Figure 9a) revealed a heterogeneous and porous structure with a poor cohesion between the paste and the raw material that is dominated by large quartz and hematite crystals (>30 µm) with sharp edges, along with small tabular crystals (<10 µm) of gypsum and some grains of goethite. It is important to note that some chromite particles with loose connections were also present inside the pore cavities of the inorganic matrix (dark areas) of the LR2 AAM. The large number of hollow cavities, irregular voids, and un-reacted or partially reacted particles indicate a low alkali activation degree, which is confirmed by the low compressive strength acquired by this specimen (1.3 MPa) [87].

On the other hand, as shown in Figure 9b,c, the microstructure of the AAMs produced by mixing laterite leaching residues and metakaolin at mass ratio 90:10 (LR90MK10) is mainly characterized by a more dense and homogeneous polymeric network when compared to LR2 AAM. Additionally, less voids and fewer unreactive particles, mainly round in shape, that exhibit better cohesion with the inorganic matrix of the LR90MK10 AAM as well as the presence of mixed aggregates, are shown (Figure 9b). As the alkali-activation reactions progressed, gel products filled the hollow cavities and voids and strongly bonded the solid particles together with the precursors to form a compact matrix, with significantly reduced porosity and water absorption, as shown in Figure 9c (zoom of rectangular area of Figure 9b). SEM-EDS analyses confirmed the formation of (N,C)–A–S–H gel with high ratios of Al/Si and Na/Si, 0.32 and 0.43, respectively, and a Ca/Si ratio of 0.15. This microstructure justifies the higher compressive strength of the LR90MK10 AAM (41 MPa) among all specimens examined in this study (Table 4).

The microstructure of the LR90MK10 AAM was further evaluated using EDS elemental mapping analysis in order to elucidate the alkali activation mechanisms and the subsequent formation of reaction products in the polymeric matrix (Figure 10). The results of elemental mapping show a quite homogenous distribution of the main elements Ca, Fe, Al, Si, S, and Na throughout the polymeric matrix, thus suggesting the formation of strong bonds due to reactions between leaching residues, metakaolin, and alkaline activators (NaOH and Na$_2$SiO$_3$ solutions). In this context, the elemental maps of Al, Ca, and S indicate that the high Al content of metakaolin (40.3% as oxide) as well as gypsum formed during the column acid leaching of the limonitic laterite with the use of H$_2$SO$_4$ were evenly distributed in the formed gel. The uniform distribution of gypsum inside the polymeric network indicates

the synergistic interaction with the metakaolin added in the starting mixture, which results in the production of specimens with beneficial mechanical properties [88]. However, and in line with the XRD results, elemental mapping shows that some unreacted particles of quartz, hematite, and chromite are still present (bright spot areas) in the produced AAMs. It is important here to note that, despite the fact that laterite leaching residues have a relatively high content of Cr_2O_3 (2.5 wt%), as shown in Table 1, elemental distribution of Cr indicates that its dissolution from the raw material is extremely limited.

Figure 9. SEM-back-scattered electron (SEM-BSE) images of selected AAMs produced using (**a**) only laterite leaching residues (LR2 AAM) as well as by mixing (**b**,**c**) leaching residues and metakaolin at mass ratio 90:10 (LR90MK10) and (**d**) LR90MK10 fired at 800 °C. Energy dispersive X–ray spectroscopy (EDS) spectra show in several spot locations the presence of crystalline phases, the formation of mixed aggregates, and newly formed products (Q: Quartz, H: Hematite, G: Goethite, Gy: Gypsum, Ch: Chromite, Gel: (N,C)–A–S–H gel).

Regarding the produced LR90MK10 AAM after firing at 800 °C (Figure 9d), SEM analysis indicated the presence of a polymeric matrix filled with rounded particles, mostly hematite, seen in the center of the map. Even though firing at 800 °C resulted in a glassy structure, extensive cracking and noticeable formation of voids due to the evaporation of free water and shrinkage are visible in the fired specimen [89]. The co-existence of cracking and voids/shrinkage detected in the LR90MK10 AAM after firing is a major contributor to its 54% reduction in compressive strength (i.e., 23.1 MPa) compared to the LR90MK10 specimen.
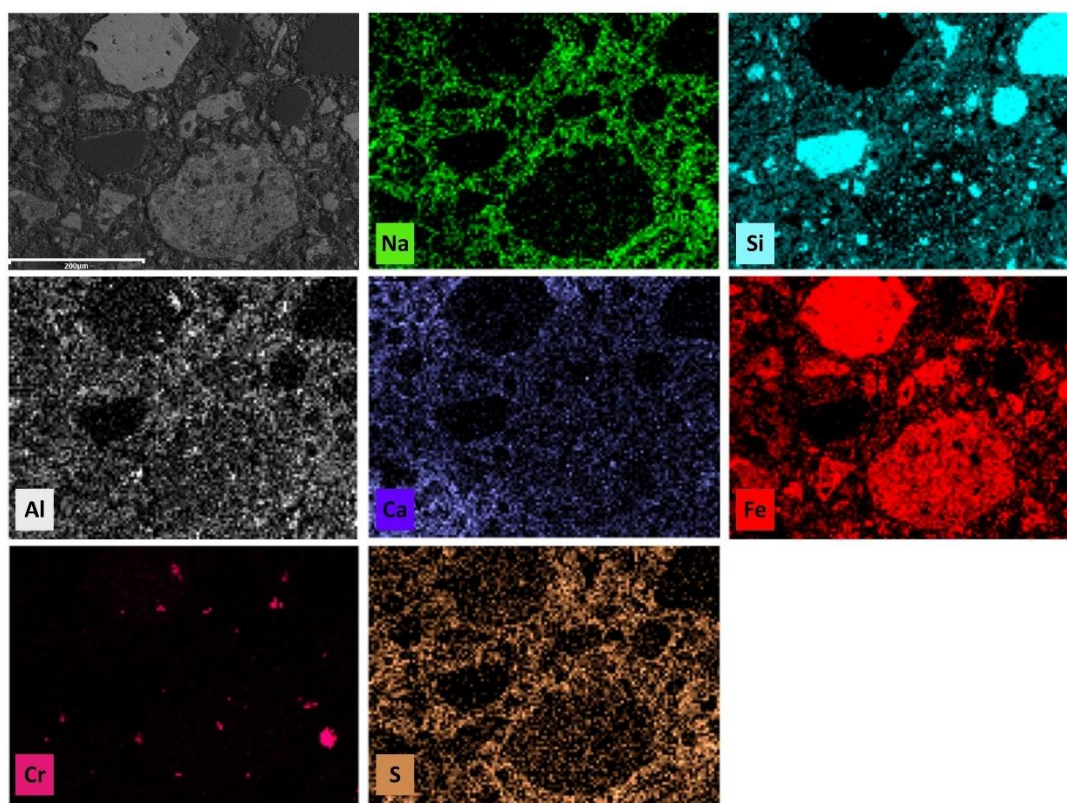
Figure 10. Elemental mapping analysis of LR90MK10 AAM produced by mixing laterite residues and metakaolin at mass ratio 90:10.

4. Conclusions

The present study is novel because it is the first one that explores the potential of, and investigates the main factors affecting, the alkali activation of laterite acid leaching residues. In order to accomplish this, the residues obtained after column leaching tests of Greek laterites were alkali activated without alteration, after calcination at 800 and 1000 °C, or after the addition of metakaolin at mass ratios leaching residues: metakaolin 95:5 and 90:10, in order to increase the reactivity of the starting mixture.

The experimental results show that the unaltered leaching residues cannot be practically alkali activated and the compressive strength of the produced AAMs hardly reaches 1.4 MPa, while the addition of 10 wt% metakaolin in the starting mixture results in the production of AAMs with noticeably higher compressive strength (41 MPa). The use of metakaolin is considered beneficial during alkali activation due to its high amorphous content and its pozzolanic nature, provided that the calcination of kaolin takes place at the most suitable temperature (around 750 °C). On the other hand, calcination of the residues at 800 and 1000 °C has little or no beneficial effect on alkali activation. The produced AAMs under the optimum synthesis conditions (using molar ratios H_2O/Na_2O, 17.4 and SiO_2/Na_2O, 1.0 in the alkali activation solution consisting of NaOH and Na_2SiO_3 solutions; pre-curing time, 4 h; curing temperature, 80 °C; curing time, 24 h; ageing period, 7 days) also exhibited good structural integrity when subjected to high temperature firing for 2 h and after immersion in distilled water or acidic solution (1 mol L^{-1} HCl) for 7 and 30 days.

The use of analytical techniques, including XRD, FTIR, and SEM-EDS, provided useful insights on the beneficial effect of metakaolin addition towards the improvement of the alkali activation potential of laterite acid leaching residues.

The results of this study can be used for the development of an integrated approach, which involves leaching residue valorization for the production of much higher added value products that can be used as binders or construction elements, in line with the zero-waste approach and circular economy principles.

References

1. Oraby, E.A.; Eksteen, J.J.; Karrech, A.; Attar, M. Gold extraction from paleochannel ores using an aerated alkaline glycine lixiviant for consideration in heap and in-situ leaching applications. *Miner. Eng.* **2019**, *138*, 112–118. [CrossRef]
2. Petersen, J. Heap leaching as a key technology for recovery of values from low-grade ores—A brief overview. *Hydrometallurgy* **2016**, *165*, 206–212. [CrossRef]
3. Thenepalli, T.; Chilakala, R.; Habte, L.; Tuan, L.Q.; Kim, C.S. A Brief Note on the Heap Leaching Technologies for the Recovery of Valuable Metals. *Sustainability* **2019**, *11*, 3347. [CrossRef]
4. Spooren, J.; Breemersch, K.; Dams, Y.; Mäkinen, J.; Lopez, M.; González-Moya, M.; Tripiana, M.; Pontikes, Y.; Kurylak, W.; Pietek, G.; et al. Near-zero-waste processing of low-grade, complex primary and secondary ores: Challenges and opportunities. *Resour. Conserv. Recy.* **2020**, *160*, 104919. [CrossRef]
5. Arpalahti, A.; Lundström, M. The leaching behavior of minerals from a pyrrhotite-rich pentlandite ore during heap leaching. *Miner. Eng.* **2018**, *119*, 116–125. [CrossRef]
6. Komnitsas, C.; Pooley, F.D. Mineralogical characteristics and treatment of refractory gold ores. *Miner. Eng.* **1989**, *2*, 449–457. [CrossRef]
7. Oxley, A.; Smith, M.E.; Caceres, O. Why heap leach nickel laterites? *Miner. Eng.* **2016**, *88*, 53–60. [CrossRef]
8. Ram, R.; Beiza, L.; Becker, M.; Pownceby, M.I.; Chen, M.; Yang, Y.; Yang, S.; Petersen, J. Study of the leaching and pore evolution in large particles of a sulfide ore. *Hydrometallurgy* **2020**, *192*, 105261. [CrossRef]
9. Ulrich, B.; Andrade, H.; Gardner, T. Lessons learnt from heap leaching operations in South America—An update. *J. S. Afr. Inst. Min. Metall.* **2003**, *103*, 23–28.
10. Catalan, L.J.J.; Li, M.G. Decommissioning of copper heap-leach residues by rinsing with water and alkaline solutions—A pilot scale study. *Environ. Eng. Sci.* **2000**, *17*, 191–202. [CrossRef]
11. Gaulier, C.; Billon, G.; Lesven, L.; Falantin, C.; Superville, P.J.; Baeyens, W.; Gao, Y. Leaching of two northern France slag heaps: Influence on the surrounding aquatic environment. *Environ. Pollut.* **2020**, *257*, 113601. [CrossRef] [PubMed]
12. Lupo, J.F. Sustainable issues related to heap leaching operations. *J. S. Afr. Inst. Min. Metall.* **2012**, *112*, 1021–1030.
13. McDonald, G.R.; Li, J.; Austin, P.J. High temperature pressure oxidation of a low-grade nickel sulfide concentrate with control of the residue composition. *Minerals* **2020**, *10*, 249. [CrossRef]
14. Zevgolis, E.; Zografidis, C.; Halikia, I. The reducibility of the Greek nickeliferous laterites: A review. *Miner. Process. Ext. Metall.* **2010**, *119*, 9–17. [CrossRef]
15. Petrakis, E.; Karmali, V.; Komnitsas, K. Factors affecting nickel upgrade during selective grinding of low–grade limonitic laterites. *Miner. Process. Ext. Metall.* **2018**, 1–10. [CrossRef]
16. Putzolu, F.; Balassone, G.; Boni, M.; Maczurad, M.; Mondillo, N.; Najorka, J.; Pirajno, F. Mineralogical association and Ni-Co deportment in the Wingellina oxide-type laterite deposit (Western Australia). *Ore Geol. Rev.* **2018**, *97*, 21–34. [CrossRef]
17. Komnitsas, K.; Petrakis, E.; Pantelaki, O.; Kritikaki, A. Column leaching of saprolitic laterites with sulphuric acid. In Proceedings of the 10th European Metallurgical Conference, EMC 2019, Dusseldorf, Germany, 23–26 June 2019; Volume 1, pp. 273–284.
18. Bartzas, G.; Komnitsas, K. Life cycle assessment of ferronickel production in Greece. *Resour. Conserv. Recy.* **2015**, *105*, 113–122. [CrossRef]
19. Panagiotopoulos, N.; Agatzini, S.; Kontopoulos, A. Extraction of nickel and cobalt from serpentinic type laterites by atmospheric pressure sulfuric acid leaching. In Proceedings of the 115th TMS-AIME Annual Meeting, New Orleans, LA, USA, 2–6 March 1986; p. A86-30.

20. Mystrioti, C.; Papassiopi, N.; Xenidis, A.; Komnitsas, K. Counter-Current Leaching of Low-Grade Laterites with Hydrochloric Acid and Proposed Purification Options of Pregnant Solution. *Minerals* **2018**, *8*, 599. [CrossRef]

21. Kontopoulos, A.; Komnitsas, K. Sulphuric acid pressure leaching of low-grade Greek laterites. In Proceedings of the 1st International Symposium on Hydrometallurgy, Beijing, China, 12–15 October 1988; Zheng, Y., Xu, J., Eds.; Pergamon Press: Oxford, UK, 1988; pp. 140–144.

22. Agatzini-Leonardou, S.; Zafiratos, J.G.; Spathis, D. Beneficiation of a Greek serpentinic nickeliferous ore: Part I. Mineral processing. *Hydrometallurgy* **2004**, *74*, 259–265. [CrossRef]

23. Agatzini-leonardou, S.; Tsakiridis, P.E.; Oustadakis, P.; Karidakis, T.; Katsiapi, A. Hydrometallurgical process for the separation and recovery of nickel from sulphate heap leach liquor of nickeliferrous laterite ores. *Miner. Eng.* **2009**, *22*, 1181–1192. [CrossRef]

24. Komnitsas, K.; Petrakis, E.; Pantelaki, O.; Kritikaki, A. Column leaching of Greek low-grade limonitic laterites. *Minerals* **2018**, *8*, 377. [CrossRef]

25. Davidovits, J. Geopolymers—Inorganic polymeric new materials. *J. Therm. Anal. Calorim.* **1991**, *37*, 1633–1656. [CrossRef]

26. Duxson, P.; Lukey, G.C.; van Deventer, J.S.J. Thermal evolution of metakaolin geopolymers: Part 1–Physical evolution. *J. Non Cryst. Solids* **2006**, *352*, 5541–5555. [CrossRef]

27. Khale, D.; Chaudhary, R. Mechanism of geopolymerization and factors influencing its development: A review. *J. Mater. Sci.* **2007**, *42*, 729–746. [CrossRef]

28. Palomo, A.; Grutzeck, M.W.; Blanco, M.T. Alkali—Activated fly ashes, a cement for the future. *Cem. Concr. Res.* **1999**, *29*, 1323–1329. [CrossRef]

29. Komnitsas, K.; Zaharaki, D. Geopolymerisation. A review and prospects for the minerals industry. *Miner. Eng.* **2007**, *20*, 1261–1277. [CrossRef]

30. Zaharaki, D.; Komnitsas, K.; Perdikatsis, V. Use of analytical techniques for identification of inorganic polymer gel composition. *J. Mater. Sci.* **2010**, *45*, 2715–2724. [CrossRef]

31. Duxson, P.; Fernández-Jiménez, A.; Provis, J.L.; Lukey, G.C.; Palomo, A.; Van Deventer, J.S.J. Geopolymer technology: The current state of the art. *J. Mater. Sci.* **2007**, *42*, 2917–2933. [CrossRef]

32. Bernal, S.A.; de Gutierrez, R.M.; Provis, J.L.; Rose, V. Effect of silicate modulus and metakaolin incorporation on the carbonation of alkali silicate-activated slags. *Cem. Concr. Res.* **2010**, *40*, 898–907. [CrossRef]

33. Lemougna, P.N.; Wang, K.-T.; Tang, Q.; Melo, U.C.; Cui, X.-M. Recent developments on inorganic polymers synthesis and applications. *Ceram. Int.* **2016**, *42*, 15142–15159. [CrossRef]

34. Peys, A.; Douvalis, A.P.; Hallet, V.; Rahier, H.; Blanpain, B.; Pontikes, Y. Inorganic polymers from CaO-FeOx-SiO$_2$ Slag: The start of oxidation of Fe and the formation of a mixed valence binder. *Front. Mater. Sci.* **2019**, *6*, 212. [CrossRef]

35. Yip, C.K.; Lukey, G.C.; van Deventer, J.S.J. The coexistence of geopolymeric gel and calcium silicate hydrate at the early stage of alkaline activation. *Cem. Concr. Res.* **2005**, *35*, 1688–1697. [CrossRef]

36. Komnitsas, K.; Bartzas, G.; Karmali, V.; Petrakis, E.; Kurylak, W.; Pietek, G.; Kanasiewics, J. Assessment of alkali activation potential of a Polish ferronickel slag. *Sustainability* **2019**, *11*, 1863. [CrossRef]

37. Azevedo, A.G.D.S.; Strecker, K. Brazilian fly ash based inorganic polymers production using different alkali activator solutions. *Ceram. Int.* **2017**, *43*, 9012–9018. [CrossRef]

38. Hounsi, A.D.; Gisèle, L.-N.; Djétéli, G.; Blanchart, P. Kaolin–based geopolymers: Effect of mechanical activation and curing process. *Constr. Build. Mater.* **2013**, *42*, 105–113. [CrossRef]

39. Rovnaník, P. Effect of curing temperature on the development of hard structure of metakaolin–based geopolymer. *Constr. Build. Mater.* **2010**, *24*, 1176–1183. [CrossRef]

40. Soultana, A.; Valouma, A.; Bartzas, G.; Komnitsas, K. Properties of Inorganic Polymers Produced from Brick Waste and Metallurgical Slag. *Minerals* **2019**, *9*, 551. [CrossRef]

41. Alshaaer, M. Synthesis and characterization of self-healing geopolymer composite. *Constr. Build. Mater.* **2020**, *245*, 118432. [CrossRef]

42. Hertel, T.; Pontikes, Y. Geopolymers, inorganic polymers, alkali-activated materials and hybrid binders from bauxite residue (red mud)–Putting things in perspective. *J. Clean. Prod.* **2020**, *258*, 120610. [CrossRef]

43. Komnitsas, K.; Zaharaki, D.; Vlachou, A.; Bartzas, G.; Galetakis, M. Effect of synthesis parameters on the quality of construction and demolition wastes (CDW) geopolymers. *Adv. Powder Technol.* **2015**, *26*, 368–376. [CrossRef]

44. Palankar, N.; Ravi Shankar, A.U.; Mithun, B.M. Studies on eco–friendly concrete incorporating industrial waste as aggregates. *Int. J. Sustain. Built Environ.* **2015**, *4*, 378–390. [CrossRef]

45. Peys, A.; Douvalis, A.P.; Siakati, C.; Rahier, H.; Blanpain, B.; Pontikes, Y. The influence of air and temperature on the reaction mechanism and molecular structure of Fe-silicate inorganic polymers. *J. Non Cryst. Solids* **2019**, *526*, 119675. [CrossRef]

46. Provis, J.L.; Bernal, S.A. Geopolymers and related alkali-activated materials. *Annu. Rev. Mater. Res.* **2014**, *44*, 229–327. [CrossRef]

47. Lemougna, P.N.; MacKenzie, K.J.D.; Melo, U.F.C. Synthesis and thermal properties of inorganic polymers (geopolymers) for structural and refractory applications from volcanic ash. *Ceram. Int.* **2011**, *37*, 3011–3018. [CrossRef]

48. Oyelami, C.A.; Van Rooy, J.L. A review of the use of lateritic soils in the construction/development of sustainable housing in Africa: A geological perspective. *J. Afr. Earth Sci.* **2016**, *119*, 226–237. [CrossRef]

49. Komnitsas, K.; Petrakis, E.; Bartzas, G.; Karmali, V. Column leaching of low–grade saprolitic laterites and valorization of leaching residues. *Sci. Total Environ.* **2019**, *665*, 347–357. [CrossRef]

50. Konan, K.L.; Peyratout, C.; Smith, A.; Bonnet, J.-P.; Rossignol, S.; Oyetola, S. Comparison of surface properties between kaolin and metakaolin in concentrated lime solutions. *J. Colloid Interface Sci.* **2009**, *339*, 103–109. [CrossRef]

51. Kakali, G.; Perrraki, T.; Tsivilis, S.; Badogiannis, E. Thermal Treatment of Kaolin: The Effect of Mineralogy on the Pozzolanic Activity. *Appl. Clay Sci.* **2001**, *20*, 73–80. [CrossRef]

52. Shvarzman, A.; Kovler, K.; Grader, G.S.; Shter, G.E. The effect of dehydroxylation/amorphization degree on pozzolanic activity of kaolinite. *Cem. Concr. Res.* **2003**, *33*, 405–416. [CrossRef]

53. British Standards Institute. *BS EN 1936: Natural Stone Test Methods. Determination of Real Density and Apparent Density and of Total and Open Porosity*; NP EN 1936:2006; BSI: London, UK, 2007.

54. Ascensão, G.; Marchi, M.; Segata, M.; Faleschini, F.; Pontikes, Y. Reaction kinetics and structural analysis of alkali activated Fe–Si–Ca rich materials. *J. Clean. Prod.* **2020**, *246*, 119065. [CrossRef]

55. Aughenbaugh, K.L.; Williamson, T.; Juenger, M.C.G. Critical evaluation of strength prediction methods for alkali-activated fly ash. *Mater. Struct.* **2015**, *48*, 607–620. [CrossRef]

56. Bumanis, G.; Vitola, L.; Bajare, D.; Dembovska, L.; Pundiene, I. Impact of reactive SiO_2/Al_2O_3 ratio in precursor on durability of porous alkali activated materials. *Ceram. Int.* **2017**, *43*, 5471–5477. [CrossRef]

57. He, P.; Wang, M.; Fu, A.; Jia, D.; Yan, S.; Yuan, J.; Xu, J.; Wang, P.; Zhou, Y. Effects of Si/Al ratio on the structure and properties of metakaolin based geopolymer. *Ceram. Int.* **2016**, *42*, 14416–14422. [CrossRef]

58. Lahoti, M.; Wong, K.K.; Yang, E.-H.; Tan, K.H. Effects of Si/Al molar ratio on strength endurance and volume stability of metakaolin geopolymers subject to elevated temperature. *Ceram. Int.* **2018**, *44*, 5726–5734. [CrossRef]

59. Sun, J.; Zhang, Z.; Zhuang, S.; He, W. Hydration properties and microstructure characteristics of alkali–activated steel slag. *Constr. Build. Mater.* **2020**, *241*, 118141. [CrossRef]

60. Tennakoon, C.; De Silva, P.; Sagoe-Crentsil, K.; Sanjayan, J.G. Influence and role of feedstock Si and Al content in Geopolymer synthesis. *J. Sust. Cem Based Mater.* **2014**, *4*, 129–139. [CrossRef]

61. Wang, Y.; Liu, X.; Zhang, W.; Li, Z.; Zhang, Y.; Li, Y.; Ren, Y. Effects of Si/Al ratio on the efflorescence and properties of fly ash based geopolymer. *J. Clean. Prod.* **2020**, *244*, 11852. [CrossRef]

62. Wang, R.; Wang, J.; Dong, T.; Ouyang, G. Structural and mechanical properties of geopolymers made of aluminosilicate powder with different SiO_2/Al_2O_3 ratio: Molecular dynamics simulation and microstructural experimental study. *Constr. Build. Mater.* **2020**, *240*, 117935. [CrossRef]

63. Zhang, Q.; Ji, T.; Yang, Z.; Wang, C.; Wu, H.-C. Influence of different activators on microstructure and strength of alkali-activated nickel slag cementitious materials. *Constr. Build. Mater.* **2020**, *235*, 117449. [CrossRef]

64. Kpinsoton, G.M.R.; Karoui, H.; Richardson, Y.; Koffi, B.N.D.S.; Yacouba, H.; Motuzas, J.; Drobek, M.; Lawane Gana, A. New insight into the microstructure of natural calcined laterites and their performance as heterogeneous Fenton catalyst for methylene blue degradation. *Reac. Kinet. Mech. Cat.* **2018**, *124*, 931–956. [CrossRef]

65. Mascarin, L. Characterization and Thermodynamic Modelling of Alkali-Activated Calcined Clays: Potentiality of Cameroon's Laterites as Eco-Sustainable Binders. Master's Thesis, Department of Geosciences, University of Padua, Padova, Italy, 19 July 2018.

66. Komnitsas, K.; Zaharaki, D.; Perdikatsis, V. Effect of synthesis parameters on the compressive strength of low-calcium ferronickel slag inorganic polymers. *J. Hazard. Mater.* **2009**, *161*, 760–768. [CrossRef] [PubMed]

67. Lemougna, P.N.; Wang, K.-T.; Tang, Q.; Kamseu, E.; Billong, N.; Melo, U.C.; Cui, X.-M. Effect of slag and calcium carbonate addition on the development of geopolymer from indurated laterite. *Appl. Clay Sci.* **2017**, *148*, 109–117. [CrossRef]

68. Vogt, O.; Ukrainczyk, N.; Ballschmiede, C.; Koenders, E. Reactivity and microstructure of metakaolin based geopolymers: Effect of fly ash and liquid/solid contents. *Materials (Basel)* **2019**, *12*, 3485. [CrossRef] [PubMed]

69. Yuan, J.; He, P.; Jia, D.; Yang, C.; Zhang, Y.; Yan, S.; Yang, Z.; Duan, X.; Wang, S.; Zhou, Y. Effect of curing temperature and SiO_2/K_2O molar ratio on the performance of metakaolin-based geopolymers. *Ceram. Int.* **2016**, *42*, 16184–16190. [CrossRef]

70. Jackson, P.R.; Radford, D.W. Effect of initial cure time on toughness of geopolymer matrix composites. *Ceram. Int.* **2017**, *43*, 9884–9890. [CrossRef]

71. Lemougna, P.N.; Chinje Melo, U.F.; Delplancke, M.-P.; Rahier, H. Influence of the activating solution composition on the stability and thermo-mechanical properties of inorganic polymers (geopolymers) from volcanic ash. *Constr. Build. Mater.* **2013**, *48*, 278–286. [CrossRef]

72. Zhang, M.; Zhao, M.; Zhang, G.; Sietins, J.M.; Granados-Focil, S.; Pepi, M.S.; Yan Xu, Y.; Tao, M. Reaction kinetics of red mud-fly ash based geopolymers: Effects of curing temperature on chemical bonding, porosity, and mechanical strength. *Cem. Concr. Comp.* **2018**, *93*, 175–185. [CrossRef]

73. Kaze, C.R.; Venyite, P.; Nana, A.; Juvenal, D.N.; Tchakoute, H.K.; Rahier, H.; Kamseu, E.; Melo, U.C.; Leonelli, C. Meta–halloysite to improve compactness in iron–rich laterite–based alkali activated materials. *Mater. Chem. Phys.* **2020**, *239*, 122268. [CrossRef]

74. Heap, M.J.; Lavallée, Y.; Laumann, A.; Hess, K.-U.; Meredith, P.G.; Dingwell, D.B.; Huismann, S.; Weise, F. The influence of thermal-stressing (up to 1000 °C) on the physical, mechanical, and chemical properties of siliceous-aggregate, high-strength concrete. *Constr. Build. Mater.* **2013**, *42*, 248–265. [CrossRef]

75. Duxson, P.; Provis, J.L.; Lukey, G.C.; van Deventer, J.S.J. The role of inorganic polymer technology in the development of 'green concrete'. *Cem. Concr. Res.* **2007**, *37*, 1590–1597. [CrossRef]

76. Gualtieri, M.L.; Romagnoli, M.; Pollastri, S.; Gualtieri, A.F. Inorganic polymers from laterite using activation with phosphoric acid and alkaline sodium silicate solution: Mechanical and microstructural properties. *Cem. Concr. Res.* **2015**, *67*, 259–270. [CrossRef]

77. Phummiphan, I.; Horpibulsuk, S.; Sukmak, P.; Chinkulkijniwat, A.; Arulrajah, A.; Shen, S.-L. Stabilisation of marginal lateritic soil using high calcium fly ash–based geopolymer. *Road Mater. Pavement Des.* **2016**, *17*, 877–891. [CrossRef]

78. Nkwaju, R.Y.; Djobo, J.N.Y.; Nouping, J.N.F.; Huisken, P.W.M.; Deutou, J.G.N.; Courard, L. Iron–rich laterite-bagasse fibers based geopolymer composite: Mechanical, durability and insulating properties. *Appl. Clay Sci.* **2019**, *183*, 105333. [CrossRef]

79. Obonyo, E.A.; Kamseu, E.; Lemougna, P.N.; Tchamba, A.B.; Melo, U.C.; Leonelli, C.A. Sustainable approach for the geopolymerization of natural iron–rich aluminosilicate. *Sustainability* **2014**, *6*, 5535–5553. [CrossRef]

80. Yi, C.; Boluk, Y.; Bindiganavile, V. Enhancing alkali-activation of metakaolin-based geopolymers using dry water. *J. Clean. Prod.* **2020**, *258*, 120676. [CrossRef]

81. Tchakouté, H.K.; Rüscher, C.H.; Kong, S.; Kamseu, E.; Leonelli, C. Comparison of metakaolin-based geopolymer cements from commercial sodium waterglass and sodium waterglass from rice husk ash. *J. Sol Gel Sci. Technol.* **2016**, *78*, 492–506. [CrossRef]

82. Criado, M.; Aperador, W.; Sobrados, I. Microstructural and Mechanical Properties of Alkali Activated Colombian Raw Materials. *Materials* **2016**, *9*, 158. [CrossRef]

83. Kaze, C.R.; Djobo, J.N.Y.; Nana, A.; Tchakoute, H.K.; Kamseu, E.; Melo, U.C.; Leonelli, C.; Rahier, H. Effect of silicate modulus on the setting, mechanical strength and microstructure of iron-rich aluminosilicate (laterite) based-geopolymer cured at room temperature. *Ceram. Int.* **2018**, *44*, 21442–21450. [CrossRef]

84. Kaze, C.R.; Tchakoute, H.K.; Mbakop, T.T.; Mache, J.R.; Kamseu, E.; Melo, U.C.; Leonelli, C. Synthesis and properties of inorganic polymers (geopolymers) derived from Cameroon–meta–halloysite. *Ceram. Int.* **2018**, *44*, 18499–18508. [CrossRef]

85. Ricciotti, L.; Molino, A.J.; Roviello, V.; Chianese, E.; Cennamo, P.; Roviello, G. Geopolymer Composites for Potential Applications in Cultural Heritage. *Environments* **2017**, *4*, 91. [CrossRef]

86. Adesanya, E.; Ohenoja, K.; Yliniemi, J.; Illikainen, M. Mechanical trans-formation of phyllite mineralogy toward its use as alkali-activated binderprecursor. *Miner. Eng.* **2020**, *145*, 106093. [CrossRef]

87. Song, W.; Zhu, Z.; Pu, S.; Wan, Y.; Huo, W.; Song, S.; Zhang, J.; Yao, K.; Hu, L. Efficient use of steel slag in alkali-activated fly ash-steel slag-ground granulated blast furnace slag ternary blends. *Constr. Build. Mater.* **2020**, *259*, 119814. [CrossRef]

88. Vimmrová, A.; Keppert, M.; Michalko, O.; Černý, R. Calcined gypsum–lime–metakaolin binders: Design of optimal composition. *Cem. Concr. Comp.* **2014**, *52*, 91–96. [CrossRef]

89. Rickard, W.D.A.; Gluth, G.J.G.; Pistol, K. In-situ thermo-mechanical testing of fly ash geopolymer concretes made with quartz and expanded clay aggregates. *Cem. Concr. Res.* **2016**, *80*, 33–43. [CrossRef]